# STRUCTURAL IMPACTS OF INFLATABLE AERODYNAMIC DECELERATOR DESIGN

A Thesis
Presented to
The Academic Faculty

by

Lin Li

In Partial Fulfillment
of the Requirements for the Degree
Doctor of Philosophy in the
Daniel Guggenheim School of Aerospace Engineering

Georgia Institute of Technology
August 2020

# STRUCTURAL IMPACTS OF INFLATABLE AERODYNAMIC DECELERATOR DESIGN

Approved by:


Dr. Julian Rimoli, Advisor
Daniel Guggenheim School of
Aerospace Engineering
*Georgia Institute of Technology*

Dr. John Dec
Daniel Guggenheim School of
Aerospace Engineering
*Georgia Institute of Technology*

Dr. Robert Braun, Co-Advisor
Planetary Exploration Programs
*NASA Jet Propulsion Laboratory*

Dr. Neil Cheatwood
Atmospheric Flight and Entry
Systems Branch
*NASA Langley Research Center*

Dr. Graeme Kennedy
Daniel Guggenheim School of
Aerospace Engineering
*Georgia Institute of Technology*


Date Approved: May 11, 2020

# ACKNOWLEDGEMENTS

I would like to recognize all of the individuals who have helped me during my time researching at Georgia Tech. I would first like to thank my advisers, Dr. Robert Braun and Dr. Julian Rimoli, for their support and guidance. Dr. Braun, I appreciate your advice and guidance in formulating this research and also for connecting me to the invaluable opportunities and engineers at NASA. These opportunities provided many of the foundations for this thesis. Dr. Rimoli, I sincerely appreciate you taking me as your student mid-way through my studies and allowing me continuing my research. I would also like to thank Michael Lindell at NASA Langley for providing great insight into the construction and debugging of the stacked tori finite element models. Your suggestions, along with the validation data sets you helped provide, directly enabled my simplified modeling contributions and greatly strengthened this dissertation. I would also like to thank the remaining members of my committee, Dr. Graeme Kennedy, Dr. John Dec, and Dr. Neil Cheatwood for their guidance on this research.

I would like to acknowledge both the National Science Foundation Graduate Research Fellowship Program and the NASA Pathways program for their financial support of my graduate studies and for the opportunities they provided for my academic and professional growth. Thank you to both the NASA Langley Hypersonic Air-breathing Propulsion Branch and Vehicle Analysis Branch for supporting my research and providing access to NASAs resources and engineers. Thank you very much to the entire HIAD team for keeping me informed of the current state-of-the-art of inflatable decelerator technologies and helping to answer any questions I had. I would also like to acknowledge my lab mates in the Space Systems Design Laboratory for their support.

Finally, I would like to thank my parents, Keir, Isaac, and Evelyn. Your love and support were like rainbows after the thunderstorm, guiding me and helping push me through all challenges. Isaac and Evelyn, you may have extended my graduation date by a couple years, but you have made the extra time that much more fulfilling.

# TABLE OF CONTENTS

# LIST OF TABLES

# LIST OF FIGURES

# NOMENCLATURE

## Symbols

| | | |
|---|---|---|
| $\beta$ | Ballistic coefficient | $[\frac{kg}{m^2}]$ |
| $\epsilon$ | Ratio of shoulder torus to structural torus cross-sectional radii | |
| $\lambda$ | Stress ratio (ratio of circumferential stress to meridional stress) | |
| $\nu$ | Poisson's ratio | |
| $\rho$ | Density | [m] |
| $\sigma$ | Stress | [Pa] |
| $\theta$ | IAD half-cone angle | [deg] |
| $a$ | Ratio of centerbody overlap to torus radius | |
| $A_{ref}$ | Aerodynamic reference area | $[m^2]$ |
| $b$ | Ratio of torus overlap to torus radius | |
| $B^2$ | Tension cone shape factor | |
| $C_D$ | Drag coefficient | |
| $D$ | Diameter | [m] |
| $L$ | Decelerator side length | [m] |
| $m$ | Mass | $[kg]$ |
| $N$ | Number of tori | |
| $P$ | Pressure | [Pa] |

| | | |
|---|---|---|
| $R$ | IAD major radius | [m] |
| $r$ | Torus cross-sectional radius | [m] |
| $R_{TS}$ | Tension skirt radius | [m] |
| $SA$ | Surface area | [m] |
| $t$ | Torus fabric thickness | [m] |
| $T_X$ | Torus number | |
| $V$ | Volume | [$m^3$] |

**Superscripts and Subscripts**

| | |
|---|---|
| $\phi$ | Property of meridional direction |
| $\theta$ | Property of circumferential direction |
| $aero$ | Property of aerodynamic loading |
| $Cen$ | Property of the centerbody |
| $fabric$ | Property of the fabric |
| $gas$ | Property of the inflation gas |
| $inf$ | Property of inflation |
| $s$ | Property of the shoulder torus |

**Acronyms**

| | |
|---|---|
| DGB | Disk-gap band parachute |
| EDL | Entry, descent, and landing |
| EDL:SA | Entry, Descent, and Landing: Systems Analysis |

| | |
|---|---|
| FFT | Fast Fourier Transform |
| FTPS | Flexible thermal protection systems |
| IAD | Inflatable aerodynamic decelerator |
| IRVE | Inflatable Reentry Vehicle Experiment |
| MSL | Mars Science Laboratory |
| NASA | National Aeronautics and Space Administration |
| NFAC | National Full-Scale Aerodynamics Complex |

# SUMMARY

In order to land larger payloads to Mars, more capable decelerators are required to advance beyond the performance limitations of traditional heritage entry, descent, and landing technologies. One potential technology is an inflatable aerodynamic decelerator (IAD), a flexible aeroshell that can be folded and stowed in a rocket fairing during launch and inflated prior to entry. IADs allow for larger drag areas with minimal mass increase in comparison to traditional rigid aeroshells and, thus, enable improved deceleration performance. However, minimal insight is available regarding the impact of detailed IAD configuration design on their structural performance. Future missions involving IADs will require this structural performance information early in the design cycle in order to develop IADs that have high structural and mass performance and are tailorable to specific mission requirements.

This thesis advances the state of the art of inflatable aerodynamic decelerator design by investigating the implications of IAD configuration on their structural and mass performance and developing data analysis techniques to assess an IAD's global dynamic response. These methodologies and results improve future IAD design efforts by enabling estimates of structural performance information in conceptual design, exploring the configurational impacts of novel decelerator designs, and providing new test methodologies to better evaluate those designs. This research, therefore, starts to explore the next phases in the IAD development process, as inflatable decelerator technology maturation transitions from early-stage concept demonstration to applications on future missions that require expanded capabilities beyond the current configurational design space.

In order to inform conceptual design efforts, simplified models of traditional stacked tori and tension cone decelerators are developed that strategically eliminate complexity in the IAD design to enable rapid simulation of the structural response. These computationally efficient models are used to evaluate the entire configurational design space and enable assessments of the IAD design on their structural and mass performance. A new hybrid decelerator is also developed, leveraging the benefits of the stacked tori and tension cone designs, to provide configurations that better balance mass efficiency with reduced deflection compared to the traditional stacked tori and tension cone designs.

New data analysis methodologies are also developed to extract information on an IAD's dynamic response from photogrammetry data. These methodologies allow for visualization of the global IAD dynamic response along with an evaluation of the frequency content of motion. The analysis routines are applied to existing photogrammetry data sets to highlight fundamental characteristics of the decelerator dynamic response and fluid-structure resonance phenomena.

# CHAPTER I

# INTRODUCTION

## *1.1 Background*

The National Aeronautics and Space Administration (NASA) has explored the Mars surface with eight robotic landing missions: Viking I and II, Mars Pathfinder, Mars Exploration Rovers, Phoenix, Mars Science Laboratory (MSL), and InSight. These missions relied on entry, descent, and landing technologies that were initially developed during the Viking program [1]. One of the most recent missions, MSL, was capable of delivering an approximately 1 t payload to a maximum of 0 km surface elevation [2]. Future robotic missions plan to land 1 to 2 t payloads at landing elevations as high as +2 km while human exploration missions may require landed masses of 40 to 80 t with high landing accuracy [1, 3]. Such requirements cannot be met with the current Viking heritage-based entry, descent, and landing (EDL) technologies. Therefore, new EDL technologies require development for future Mars missions.

## *1.2 Mars Entry, Descent, and Landing*

During the EDL phase of Mars missions, the vehicle must autonomously decelerate from hypersonic speed to zero in less than ten minutes. Past EDL architectures generally rely on a 70° half-angle sphere cone rigid aeroshell, a disk-gap band (DGB) parachute, and a touchdown system such as landing legs. This architecture was formulated and qualified during the technology program prior to the Viking mission and has been generally used since on all U.S. missions. An example EDL sequence for the Mars Science Laboratory mission is seen in Fig. 1.

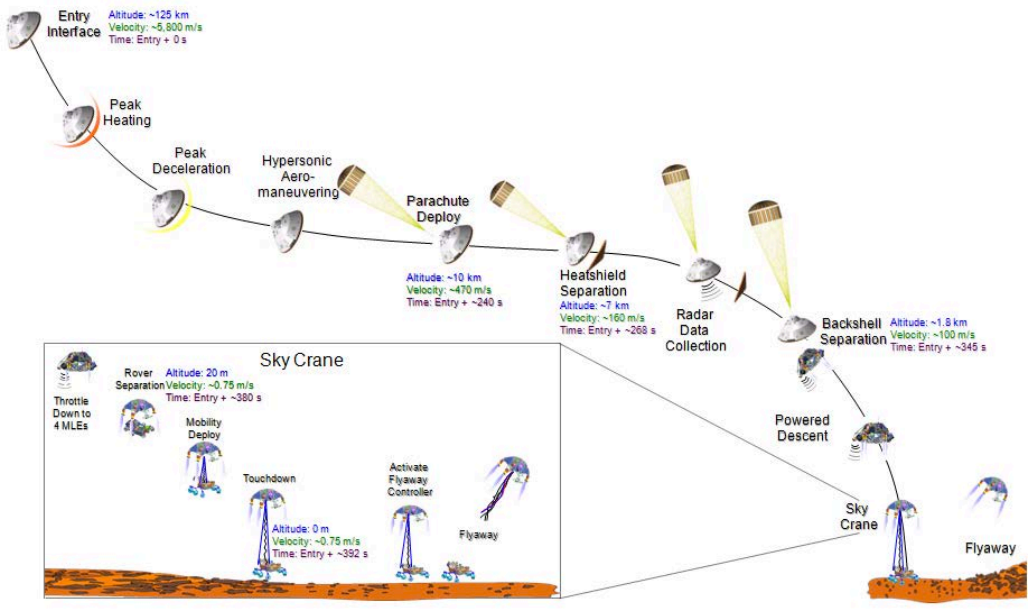


**Figure 1: Diagram of the entry, descent, and landing sequence for MSL [4]**

Spacecraft traveling to Mars enter the planet's atmosphere at speeds exceeding 5 $\frac{km}{s}$ and need to dissipate all their kinetic energy prior to landing. The vast majority of this dissipation is achieved through aerodynamic decelerators. During hypersonic and supersonic deceleration, the aeroshell removes greater than 90% of the initial spacecraft kinetic energy [5, 6, 7]. Achieving this performance with other means, such as chemical propulsion, is challenging due to the propellant mass fraction required and the payload capabilities of existing launch vehicles.

### 1.2.1 Mars Entry, Descent, and Landing Challenges

Mars has an atmosphere which is thick enough to induce significant aerothermal heating during entry. However, the atmosphere of Mars is also extremely sparse, having a density approximately 1% that of Earth. As a result, without special treatment, vehicles will decelerate at low altitude on Mars, leaving little time for subsequent critical events. The ballistic coefficient, $\beta$, is defined as the vehicle mass, $m$, over the drag area ($C_D$ times the aerodynamic reference area, $A_{ref}$) as in Eq. 1. Along with

vertical lift, this parameter is one of the primary controls of the altitude of hypersonic deceleration, as evidenced by Fig. 2.

$$\beta = \frac{m}{C_D A_{ref}} \tag{1}$$

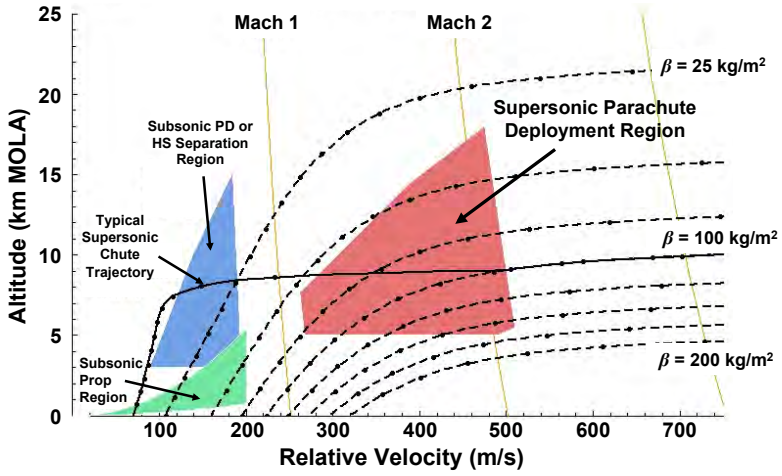


**Figure 2: Mars entry trajectories for varying ballistic coefficient vehicles along with limits for parachute and subsonic propulsion initiation [1].**

The high-altitude regions of the Mars surface in Fig. 3 have significant scientific interest but reaching them is difficult with current EDL technologies and payload masses. For such missions, entry systems that can reduce the ballistic coefficient, thereby decelerating higher in the atmosphere to provide more mission timeline, may be preferred [1]. MSL, with a ballistic coefficient of 145 $\frac{kg}{m^2}$, passes through the bottom right-hand corner of the DGB parachute deployment region in Fig. 2 [8]. Because ballistic coefficients tend to increase with increased payload mass, future high-mass Mars missions may decelerate too low in the Mars atmosphere and be unable to achieve the requisite parachute deployment conditions using traditional rigid aeroshell technologies.

Reduction of the entry vehicle's ballistic coefficient requires either a reduction in vehicle mass or an increase in drag area. Unfortunately, increasing the rigid aeroshell drag area is challenging as it requires an increase in launch vehicle fairing diameters

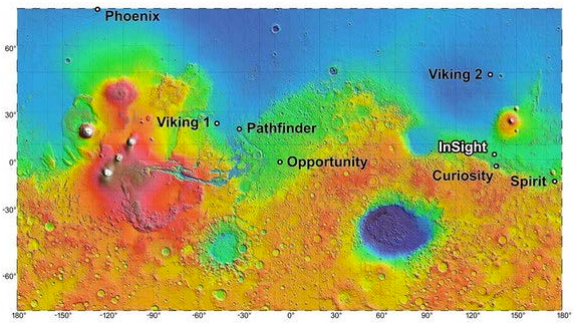


**Figure 3: Landing sites for past Mars missions [9]**

[8]. Future high mass missions will require either a much larger launch vehicle fairing or an aeroshell design that can fit inside the current launch vehicle but also meet the ballistic coefficient requirements for the specific mission.

### 1.2.2 Alternate Mars Entry, Descent, and Landing Technologies

One particular technology option for high mass Mars missions is an inflatable aerodynamic decelerator (IAD), or flexible aeroshell that can be inflated prior or during entry. Hypersonic IADs are an attractive option because they:

- allow for a drastic increase in drag area with minimal increase in mass, thus reducing the ballistic coefficient
- can be stowed during launch and inflated during interplanetary transit and are therefore not constrained by the diameter of the rocket fairing
- allow the vehicle to decelerate higher in altitude and, as a result, decrease the peak heat flux experienced during the EDL sequence and provide access to landing sites at higher altitudes
- increase the subsequent descent timeline to provide more time for precision landing or other critical descent and landing events

## *1.3 Inflatable Aerodynamic Decelerators*

Inflatable Aerodynamic Decelerators (IADs) are devices made of flexible, lightweight materials, which can be deployed in space prior to entry or during the EDL sequence to improve the performance characteristics of an entry vehicle. While they are typically used to increase drag, inflatable decelerators can also provide lift, decrease heating, and improve stability. IADs have the potential to provide significant benefit because, to first order, their size is not limited by the launch vehicle shroud diameter, allowing for much larger drag areas and, as a result, improved performance. Because IADs are composed of flexible materials, which can sustain minimal compressive loading, their shape is maintained by enclosing pressurized gas within the inflatable volume. Structural stiffness is driven by the inflation pressure, which must maintain fabric tension even under the application of aerodynamic loading [10]. IADs typically achieve gas pressure using internal gas generators, ram-air inlets, or through a combination of both methods.

### 1.3.1 General Classes of IADs

IADs can be categorized based on their operating flight regime, location relative to the payload, and structural shape. IADs deployed prior to entry are referred to as hypersonic IADs since they are responsible for hypersonic deceleration; whereas, IADs deployed supersonically are denoted supersonic IADs. If the inflatable decelerator is structurally attached to the entry vehicle it is called an attached IAD; whereas, if it is attached via a riser or suspension lines, it is called a trailing IAD. Attached IADs can be further categorized as aft-body attached or forebody attached based on their attachment location and both attached and trailing IADs can be further categorized based on their specific shape. Most IADs contain similar common elements in their designs including inflated compartments, gores, and straps. Attached IAD components include the rigid nose cone; whereas, trailing IAD components include the riser

or suspension lines. Hypersonic IADs generally require TPS. It is important to note that the term inflatable aerodynamic decelerator has arisen recently in the literature. Historical studies referred to IADs as ballutes, but that term has evolved since to refer to a specific configuration [5].

One of the earliest proposed IAD shapes was the trailing torus, seen in Fig. 4(a), because the shape's simplicity allowed for easy analysis and behavior modeling. Another common IAD shape is the trailing isotensoid, or ballute, seen in Fig. 4(b). The advantage of the isotensoid shape is that it maintains uniform tension throughout the fabric under internal pressure and external aerodynamic loading. Both the trailing torus and trailing isotensoid have been adapted to attached IADs in the form of the tension cone (Fig. 4(d)) and isotensoid (Fig. 4(e)), respectively. The idea of an inflatable torus was further modified to produce the stacked tori design in Fig. 4(g), which has been approximated by geometrically combining the tori as seen in Fig. 4(h). In addition, designs have taken ideas from mechanically deployed aerodynamic decelerators, mimicking their structural members with inflatable components, seen with the spar and rim design in Fig. 4(f).

For simplicity, trailing IAD designs proposed so far have generally employed a single inflated volume which is further simplified by an attachment to the spacecraft using lines that do not interfere with the vehicle's operation. Typically, trailing IADs are used as drag or stability devices and have similar functionality to parachutes, with the spacecraft separating from the IAD by cutting the lines at the desired trajectory point. Attached IADs are primarily drag modulation devices; however, the attachment is generally more complicated. Aft-body decelerators attach at the back of the payload while forebody decelerators attach to the aeroshell using it as a rigid nosecone. While more complicated, attached IADs can provide benefits above trailing configurations by introducing lift and avoiding the aeroshell wake flow field.

(a) Trailing torus [11]

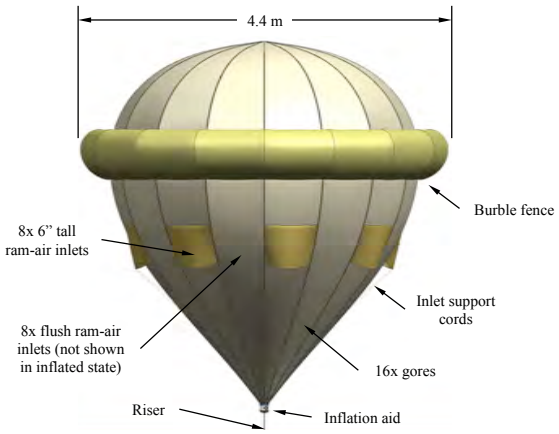


(b) Trailing isotensoid (ballute) [12]

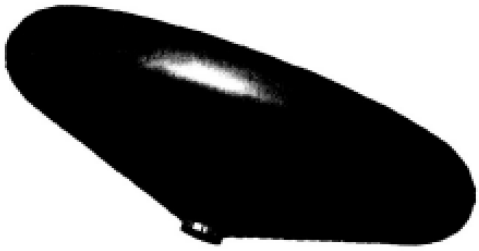

(c) Aft-body attached IAD [13]

(d) Forebody attached isotensoid [14]

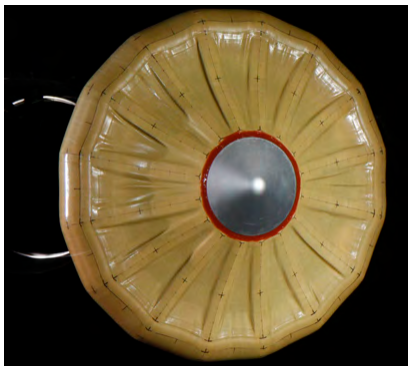

(e) Forebody attached tension cone [15]

(f) Forebody attached spar and rim [10]

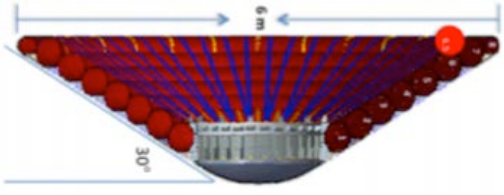


(g) Forebody attached stacked tori [16]

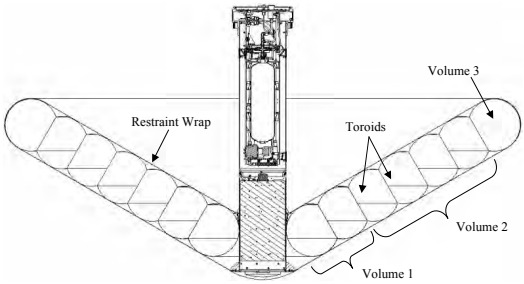


(h) Forebody attached stacked tori with geometrically joined bladders [17]

**Figure 4: Classifications of IADs**

### 1.3.2 IAD Structural Configurations

Two of the most cited IAD designs found in the literature are the tension cone and stacked tori, each featuring a different structural configuration. The motivation behind the tension cone IAD is the simplicity of an inflatable torus. In fact, the trailing torus and tension cone IADs have similar structural members. They differ in the supporting attachment members, with the trailing torus featuring suspension lines and attachment lines and tension cones featuring a fabric tension shell to support loading. Multiple methods have been discussed for attaching the tension shell, each with different structural implications. These include directly joining the tension shell and torus or wrapping the tension shell around the torus. Tension cones generally utilize gas inflation due to the limited surface area for installing ram-air inlets.

The torus is also the basis of the stacked tori configuration. Instead of increasing the drag area with a tension shell, the stacked tori configuration increases the decelerator area using successively larger tori. In this way, rigidity can be maintained to much larger scales while supporting higher loading. Since stacked tori IADs are typically larger than tension cones, the tori structures are reinforced with circumferential cords to help maintain their shape. The tori are conjoined using straps and are also bonded together to form a single cohesive structure. To prevent excessive heating from the scalloped surface, an aerocover is added. The stacked tori configuration has been approximated by joining sets of adjacent tori into a single inflatable volume, with geometric shape enforced by internal spars utilizing gaps to equilibrate pressure. The separate inflatable volumes are held together with a restraint wrap that encloses the entire structure. The restraint wrap, in this case, replaces the straps used in the traditional stacked tori configuration. All stacked tori configurations have utilized gas inflation due to the multiple inflatable volumes and complexity of maintaining consistent pressures.

### 1.3.3 Hypersonic IAD Materials

The materials used in hypersonic inflatable aerodynamic decelerator construction must meet certain requirements. They should be flexible and able to withstand tight folding while being stored inside the rocket fairing prior to deployment. The materials should also perform well in the low temperatures encountered during transit in space and high temperatures that occur during atmospheric entry. The fabrics need to be lightweight in order to capitalize on mass savings and ensure a low ballistic coefficient (low mass with a high drag), but they must be strong enough to withstand internal and external loading during the entry and descent phases. In addition, hypersonic IAD materials need to withstand vibration, outgassing, radiation, and abrasion. The flexible materials can be separated into two major categories, the first being for the inflatable decelerator itself and the other for the added thermal protection system.

Hypersonic IADs are typically constructed from either polyimide films or synthetic fibers [18, 19, 20, 21, 22, 23]. Polyimide films have good thermal and mechanical properties; whereas, synthetic fibers have high strength and additional durability and degradation resistance. While the flexible materials have promising structural properties, they have relatively high cloth permeability, a significant problem since their primary purpose is to contain the pressurized inflation gas [24]. As a result, IAD structural fabrics are typically coated to decrease their permeability and maintain the inflated shape [25, 26]. These coatings have historically included polyester, neoprene, or rubber but recently developed polyether and silicon have significantly reduced weight and improved temperature and degradation resistance. Coating materials have significantly improved the capabilities of flexible fabrics and their combined performance has contributed to the decreased total mass of IADs.

Recent advances in flexible materials with improved thermal capabilities have allowed for the development of flexible thermal protection systems (FTPS), which extend the capabilities of inflatable decelerators by performing the role of traditional,

rigid aeroshells [27, 28, 29, 5]. Unlike the flexible, structural materials, FTPS can withstand the heat rate and heat load associated with planetary entry and, as a result, enable the use of hypersonically or exoatmospherically deployed IADs of reasonable size. Since IADs are packed in a stowed configuration during launch, FTPS must also be capable of withstanding folding and high-density packing. The FTPS currently being developed is created by stacking multiple layers of fabric including Nextel, pyrogel, kapton, and kevlar to ensure sufficient insulation and thermal resistance.

## *1.4 Inflatable Structure Technology Maturation*

Historically, structural considerations have not been incorporated in the entry system conceptual design phase [30]. However, structural aspects and material selection have the potential to significantly impact the system performance and influence the initial design. Structural technology maturation is a complex process involving both numerical analysis and experimental testing to better characterize and improve the performance of emerging technologies. IAD maturation has involved numerical simulation to explore different designs and applications and experimental testing to validate designs against realistic physics. Novel test instrumentation and test techniques have evolved to better characterize flexible structures, which can exhibit more complex, multiple degree-of-freedom motion than traditional aerospace structures.

### 1.4.1 Experimental Testing

Experimental structural testing is necessary to validate the performance of future vehicles in relevant flight environments and at realistic vehicle scales. Testing is also a key component of the design phase since it provides the data used to validate numerical models. Experimental testing generally falls into one of two categories: ground testing or flight testing.

#### *1.4.1.1 Ground Testing*

Ground testing is an invaluable way to further understanding of the inflatable decelerator structural properties. Ground test rigs are often custom made for a specific test or class of test articles. Since ground tests are less expensive than flight tests, they are also useful for more rapid assessment of vehicle subcomponents or proposed designs.

Early tension cone ground testing was predominantly focused on evaluating torus buckling as a function of torus and tension shell geometry [31]. Multiple modes were identified including localized wrinkling, in-plane buckling, and out-of-plane buckling, with failure onset being dependent on the tension shell pressure distribution [32]. Similarly, studies were performed to evaluate the required inflation pressure to fully deploy the IAD under applied loading.

Ground testing of stacked tori vehicles was utilized to validate predictive finite element modeling. These tests included tensile testing of the cords, straps, and fabric in addition to tension and bending tests of single tori and straight beam inflatable volumes [33, 21]. The testing also involved full-model static loading to observe the deflected shape and structural stresses [34, 33].

Wind tunnel testing of IADs has been utilized as a relatively inexpensive way to understand their properties in a flight-like environment. Since wind tunnels have finite test sections, subscale models are required, but flight loads are often well approximated.

Tension cone wind tunnel testing was also performed to evaluate the effects of model configuration and aerodynamic conditions on supersonic and subsonic drag coefficient [35, 36, 37, 38, 39]. Increasing cone angles provided improved drag but with diminishing returns at high angles due to flow separation. More recent testing involved photogrammetry and particle image velocimetry to understand the unsteady tension shell shape and wake flow in order to validate fluid-structure interaction models [40].

Seen in Fig. 5, this was one of the first uses of photogrammetry as a non-intrusive test technique to assess IAD structural performance.

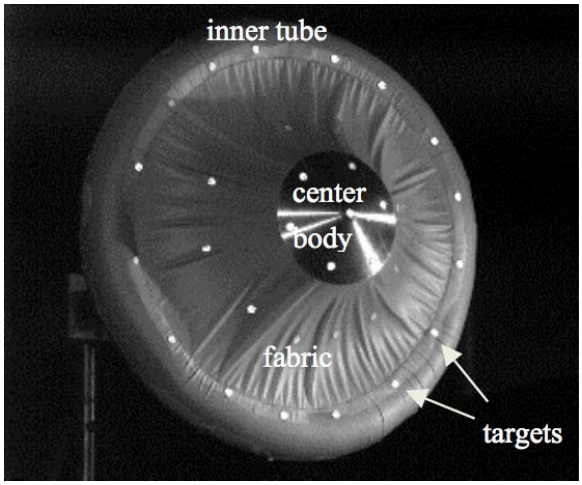


**Figure 5: Photograph of tension cone test article (from [40])**

Like the recent tension cone tests, stacked tori wind tunnel testing also implemented structural instrumentation techniques such as photogrammetry, strain gauges, and load pins to measure the test article deflection and fabric and strap loading [41, 42]. These results were used to validate CFD and FEA modeling as well as provide insight into the dynamic structural response behavior as a function of IAD configuration.

#### *1.4.1.2 Flight Testing*

Flight testing allows for full system investigations in a relevant flight environment. The many forms of flight tests include dropping from a helicopter or high-altitude balloon, being launched on a sounding rocket, or even riding as a secondary payload on a rocket. Reaching applicable Mars flight conditions on the Earth, however, requires deployment in the upper atmosphere. As a result, flight testing, particularly in hypersonic conditions, is often expensive.

A series of stacked tori hypersonic flight tests were successfully conducted by

NASA [17, 43]. During these sounding rocket tests, the flight experiment successfully demonstrated many aspects required of hypersonic inflatable technologies including exoatmospheric inflation, inflatable structure performance, flexible thermal protection system performance, aerodynamic stability, and structural integrity during atmospheric entry. The second flight test further demonstrated the potential capabilities of hypersonic IAD technology, including the use of a center of gravity offset to generate lift and survival in a more severe heating environment. Prior flight tests conducted in Europe were largely unsuccessful due to a range of structural and thermal anomalies [44, 45, 46].

### 1.4.2 Structural Analysis

The structural performance of inflatable decelerators is critical. Early in their development, it was recognized that wrinkling and other structural effects could induce localized stress, undesirable aeroelastic effects, and localized heating [47]. As a result, early investigations studied how to mitigate against wrinkling using analytically derived models of the inflatable decelerators. A desire to better predict the structural behavior of the inflatables motivated the use of higher-fidelity analysis. These analyses have included modeling of complex geometries, incorporation of realistic manufacturing implications, and use of non-uniform loading.

#### *1.4.2.1 Analytic Structural Analysis*

Analytic structural analysis of isotensoid, or ballute-like, decelerators has been performed since the 1960's, due to their simple, idealized design [48, 49, 50]. Analytical analysis of non-isotensoid inflatable decelerators, such as the tension cone and stacked tori configurations, was less prolific due to their more complicated shape. As a result, these analyses focused on simplified subcomponents, such as single inflatable beams, which could be analytically described. Equations were developed to characterize inflatable beams and calculate their deflection under loading [51, 52]. Because tension

cone IADs involve an inflated torus, analytical equations were also developed to understand their deflection under loading [53, 54, 55, 56]. These equations were used to understand buckling phenomena and determine critical buckling parameters. Advanced theories were later developed that described non-ideal beams and accounted for inflation effects [57, 58, 59]. Work was also performed to estimate the stress in the tension shell under applied aerodynamic and inertial loading [60].

#### *1.4.2.2 Numerical Structural Analysis*

The introduction of increasingly complicated IAD designs, in conjunction with a desire for higher fidelity predictive capabilities, has pushed analysis requirements beyond the applicability of analytical methods. As such, inflatable decelerator structural analysis has been progressively transitioning to numerical computations. Numerical modeling offers many other benefits, allowing for predictive capabilities when testing is too expensive or when available facilities lack the desired capabilities, and enabling trade studies for iterative designs.

Starting in the early 2000's, finite element analysis was used to study the deformation of a spar-and-rim IAD inflatable structure and aerocover [61]. Deflection results of the study were promising but specific limitations, such as the difficulty in evaluating surface wrinkling and buckling, were noted. Numerical modeling to predict the onset of buckling of tension cone IADs, validated against static load and wind tunnel tests, showed favorable agreement [15].

The structural response of the stacked tori configuration under applied loading is much more complicated than single-torus tension cone decelerators. This is primarily because the decelerator not only contains the inflatable tori but also the associated radial straps, parent loops, cords, and bonding material, with the additional components being critical to the system performance [33]. Braided fibers are used to enclose the tori and provide structural strength while cords are bonded to the fibers

to provide additional stiffness and bending strength. Radial straps are used to distribute the loads among all tori and parent loops are used to share loads between two adjacent tori. To complicate analysis, each component of the inflatable structure may have different material properties. FEA, validated with experimental testing, has had success in predicting the decelerator structural deflection and stress [33, 21]. However, in these cases, the geometry was simplified to either a 2D axisymmetric or 3D wedge model to reduce computational expense [17, 42].

Many of the difficulties associated with numerical modeling of inflatable decelerators arise from the thin, flexible fabric membranes. As a result, IAD structural modelers have started incorporating some of the membrane modeling advances made by the solar sail community into IAD analysis. One of the earliest examples of such analysis involved studying the effects of element formulation and analysis type on the deformations of solar sail membranes [62]. Similar studies have been conducted to investigate the formation of highly nonlinear wrinkled deformations in thin-film membranes and have shown that FEA is sufficient to capture the phenomena [63, 64, 65].

Other investigations have attempted to reduce the computational cost of simulating inflatable decelerators by employing faster, lower fidelity modeling techniques. Models approximating inflatable structural members as simplified beam elements have been developed to simulate straight inflatable tubes and single tori and have also been adapted to estimate full-scale decelerators [66, 67, 68]. These methods saw significant reduction in simulation times at the expense of accuracy but could be used to enable early-phase design space exploration.

#### *1.4.2.3 Structural Optimization of Inflatable Aerodynamic Decelerators*

Traditionally, IAD designs have been proposed based on engineering intuition. Following initial development, optimization has been used to determine configurations

that provided the best structural and performance characteristics. Early optimization of tension cone shapes was used to investigate the optimal drag and mass as a function of cone angle [36, 69]. For a given capsule size and loading condition, the IAD mass fraction was optimized over a range of cone angles, with the mass of the fabric and torus based on the applied stress and material strength. Tension shell shapes were also optimized to maximize drag [37, 38, 69]. While the simplified analyses neglected flow separation, which caused significant deviation from experimental results, it provided valuable first insights into the influence of IAD design choices.

Later efforts expanded this work by minimizing IAD mass as a function of cone angle for various IAD configurations including the tension cone, trailing torus, and single-volume attached IAD (such as stacked tori) designs [70]. Unlike the previous effort, the IAD mass was assumed to be dominated by the inflation gas and hardware instead of fabric mass. As a result, methods were developed to estimate the inflation pressure and gas mass. Results of the simulation confirmed the previous optimization results while also providing insight into the effect of IAD configuration.

#### *1.4.2.4 Aerodynamic Decelerator Comparison Studies*

Initial comparisons between decelerators was conducted through empirical extrapolation from past experience. Early studies adopted a structural efficiency index of merit, defined as the mass per pound of drag, to allow for an objective comparison independent of decelerator size or configuration [71, 47]. Seen in Fig. 6, these studies found IADs to be favorable in supersonic conditions. Studies conducted later adopted a more formalized approach that calculated the decelerator mass as a function of geometry, including the mass of the tension elements and fabric [72, 73, 50, 74, 75]. These studies confirmed the previous results, that IADs had favorable structural efficiency relative to parachutes in supersonic conditions.

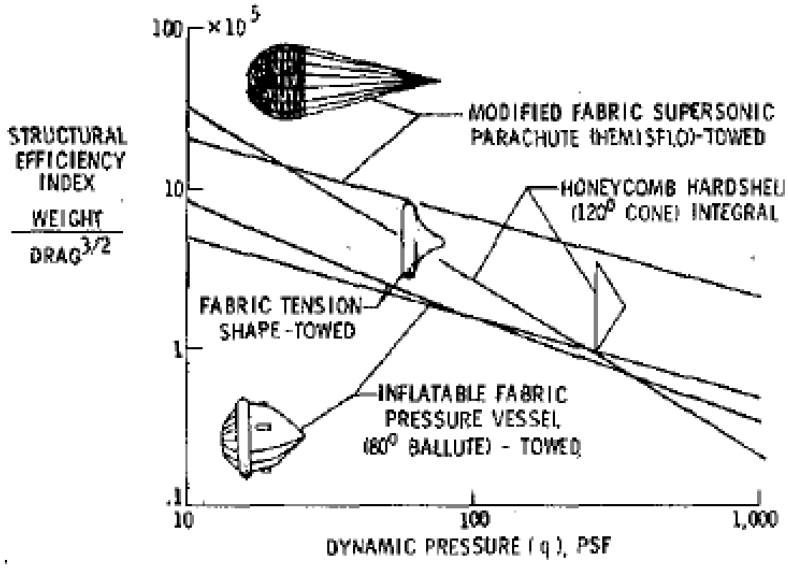


**Figure 6: Aerodynamic decelerator structural efficiency as a function of flight regime [47]**

In an effort to evaluate the required improvements in EDL technological capabilities for large robotic and human-scale missions to Mars, NASA conducted an expansive systems study to compare a wide range of potential decelerator options, assessing their mass as a function of the vehicle dimensions, maximum deceleration, and maximum heat load [76, 77, 78]. In this study, hypersonic IADs were shown to be efficient relative to rigid aeroshells. In addition, similar trends were observed for hypersonic decelerator structural efficiency. The parametric models also showed good agreement with high-fidelity finite element models. The methodologies employed in these studies, along with those of the previous efforts, can be advanced in future analyses such as those described in this thesis.

### 1.4.3 Photogrammetry Data Acquisition for Structural Analysis

Photogrammetry has emerged as a valuable data acquisition methodology for inferring the structural performance of a test article. Unlike strain gauges or load cells, which interfere with the model and take point-wise measurements, photogrammetry techniques collect data optically over the entire test article, giving insight into global

phenomena. In addition, photogrammetry systems do not attach to the model or significantly alter structural performance and, therefore, may mitigate errors due to temperature, model vibration, or other factors associated with contact measurements.

Photogrammetry, or the process of calculating a 3D shape from a series of 2D images, was first developed in the 1850's for remotely measuring the positions of surface points in a static scene for topographical applications [79, 80]. Modern close-range photogrammetry has improved by incorporating digital photography and computer data analysis, often tracking up to hundreds or thousands of object points [81, 82]. In addition, modern algorithms have been developed to extract the 3D surface from image data.

Photogrammetry has also been adapted to measure the 3D positions of time-varying surfaces, known as dynamic photogrammetry, videogrammetry, or videometrics [83]. Dynamic photogrammetry is favorable compared to other non-intrusive dynamic measurement techniques such as laser vibrometry because it measures deformations over a large area instead of a single point. Static surface measurements are the simplest to make, requiring a minimum of two stationary photos of the structure from convergent viewing directions while dynamic measurements require synchronized image sequences from multiple cameras. Challenging measurements include quantifying the unsteady dynamic characteristics of inflating or deploying flexible structures because this involves large geometry changes, target obstructions, and analyzing a time series of images [84].

Flexible structures are particularly difficult to analyze due to their large number of degrees of freedom. However, accurate test data is necessary to validate analytical and numerical predictions of static shape, vibrational modes, and deployment dynamics. Both static and dynamic photogrammetry have been utilized to measure the structural responses of lightweight and inflatable space structures, as seen in Fig. 7 [85, 86, 87, 88, 89, 90, 91, 92, 93, 94, 95, 96, 97, 98, 99, 100, 101, 102, 103, 104]. Dot

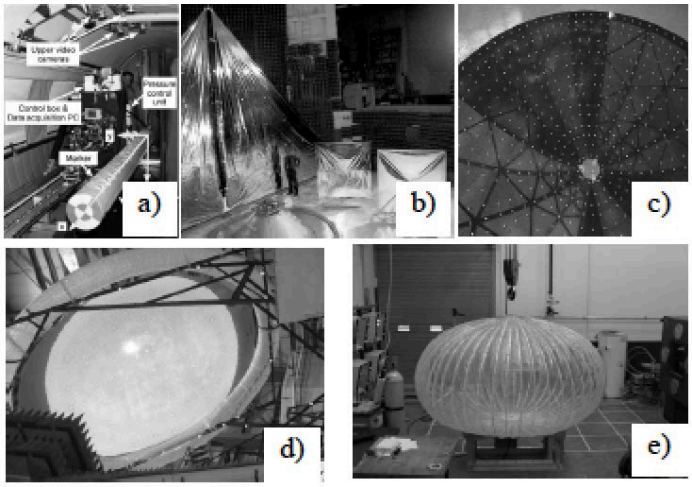


**Figure 7: Applications of photogrammetry to flexible structures [85]**

projection techniques have also been used to measure the static shape of reflective membrane surfaces and vibration control experiments, and to measure distributed, small-amplitude wrinkles on a lightly tensioned membranes [105, 100].

## *1.5 Research Goals*

### 1.5.1 Motivation

Based on a thorough literature review of the development and advancement of inflatable aerodynamic decelerators, a few insights can be made.

The first observation is that a significant amount of testing and analysis has been conducted to understand the performance benefits of IADs. However, there is significantly less insight on how to design an IAD system. This includes the lack of trade studies to probe the design space and understand which designs perform best for a specific mission. Rather, IAD design has historically been based on engineering intuition. For example, one study pointed out that the torus diameter chosen for a tension shell model was based on a scale law rather than being optimized for that specific decelerator [106]. Another example is the recent IRVE-3 flight test, which employed a stacked tori design with 7 structural tori but did not systematically evaluate the implications of different numbers of tori or tori diameters.

The second observation is that test instrumentation and analysis is a critical part of the IAD design process and a strong driver of IAD maturation. In particular, test instrumentation has enabled a greater understanding of IAD structural phenomena in flight environments and provided valuable data for predictive modeling. Photogrammetry has recently been used in several ground and wind tunnel test campaigns to study the static deformed shape and has been shown to be particularly useful for investigating flexible structures because it is non-invasive and does not artificially influence the test article's structural stiffness. A key characteristic of inflatable decelerators is the unsteady components of their deformation. However, despite multiple photogrammetry data sets being available, such methods have not been used to study the IAD dynamic structural response.

### 1.5.2 Summary of Contributions

This thesis advances the state of the art of inflatable aerodynamic decelerator design and analysis by providing a systematic investigation into the implications of IAD configuration on their structural and mass performance along with establishing photogrammetry as a valid test instrumentation technique for assessing an IAD's global dynamic response. Specific contributions are made in the following areas.

**Development of a photogrammetric analysis methodology for the experimental determination of an IAD's dynamic response and the identification of structural-forcing coupling and resonance.** Photogrammetry has been shown to be a valuable non-invasive test technique for calculating test article deflection and inferring structural performance. However, photogrammetric analysis of inflatable vehicles has so far been limited to validation of the static response of finite element analysis models and understanding the effects of different flight parameters. This thesis develops a methodology to analyze the dynamic response of an IAD during experimental testing by utilizing a series of 3D photogrammetric point cloud

data sets. The methodology allows for an expansion of the current photogrammetric data reduction capabilities by providing quantitative information on the motion of the entire decelerator surface as well determining coupling between the dynamic IAD structural response and cyclic external forcing. The surface motion data can enable improved insight into the decelerator dynamic response and sensitivity to design parameters while the dynamic structural coupling is an important factor in the decelerator performance and provides a data set for higher-fidelity structural modeling. A case study is presented, which demonstrates the methodology while leveraging existing photogrammetry data sets, and test improvements are proposed to allow future ground-based efforts to better capture unsteady phenomena.

**Development of simplified IAD models that enable assessments of IAD configurational design impacts in conceptual design.** Assessing IAD structural performance, either through testing or numerical simulation, is expensive and time-consuming. As a result, IAD development has traditionally revolved around isolated designs of a particular configuration, often sized based on engineering intuition. Otherwise, past development efforts have taken the practical approach of simplifying the multi-dimensional IAD design space in order to capture aggregate performance estimates of disparate families of configurations. However, these approaches obscure the performance variability within a particular configuration and fail to provide insight into the impacts of individual design parameters on the IAD performance. This thesis develops novel, simplified FEA models of the traditional stacked tori and tension cone decelerators that enable rapid exploration of the IAD parameter design space to inform structural design trades in conceptual design. Leveraging the efficiency of the simplified models, full-factorial exploration of the multi-dimensional design spaces is performed to understand the relative impact of each design parameter and its influence on the decelerator's structural and mass performance. Response surface

equations are also developed and presented for both configurations to enable estimation of their structural and mass performance without the use of computational simulation tools.

**Formulation and evaluation of a hybrid stacked tori/tension cone IAD configuration enabling the optimization of higher performant IAD designs across various mission scales.** The stacked tori and tension cone decelerators have both been studied and developed extensively in the literature but they are limited in their configurational flexibility and applicability to a broad range of mission classes. The stacked tori decelerator, with its multiple structural members, can withstand the higher loading hypersonic deceleration environments at the cost of a large decelerator mass, whereas the tension cone decelerator, with its mass-efficient tension skirt, has a small decelerator mass at the expense of being restricted to the lower loading supersonic deceleration environments. This thesis improves the state-of-the-art of IAD design by introducing a configurationally flexible hybrid stacked tori/tension cone decelerator design that bridges the previously disparate design spaces. This hybrid design leverages the structural benefits of the stacked tori decelerator's multiple tori along with the mass benefits of the tension cone's tension skirt and enables greater tailoring of the IAD design for each particular mission. The IAD configurational design spaces are evaluated for large robotic, human, and intermediate mission-classes to assess the performance of the three decelerator designs across the various mission-scales.

The methodologies and results developed in this thesis improve future IAD design efforts by enabling estimates of structural performance information in conceptual design, exploring the configurational impacts of novel decelerator designs, and providing new test methodologies to better evaluate those designs. This research, therefore, starts to explore the next phases in the IAD development process, as inflatable decelerator technology maturation transitions from early stage concept demonstration to

applications on future missions that require expanded capabilities beyond the current configurational design space.

# CHAPTER II

# PHOTOGRAMMETRY ANALYSIS DEVELOPMENT TO DETERMINE THE DYNAMIC CONTENT OF IAD DEFLECTION

## *2.1 Background*

The dynamic response of a vehicle is an important component of overall mission performance. The dynamic response encompasses many phenomena including characterization of the structural resonant modes and mode shapes, decelerator dynamic stability, and global characteristics of motion. Poor decelerator dynamics can have drastic impacts on mission success and can cause vehicle instability and loss of structural integrity. As a result, a significant portion of flight qualification efforts revolve around characterizing the structural dynamics of a vehicle. This is particularly true for inflatable decelerators because they can be subject to much larger and more complicated deformation than traditional rigid structures [107].

The dynamics of IADs are particularly difficult to characterize due to the flexible nature of inflatables and the difficulty of instrumentation. Given the low stiffness and large deformations inherent in IAD structures, traditional instrumentation, such as strain gauges, are problematic because they may artificially influence the structure. Photogrammetry is an appealing solution to this problem because it can simultaneously observe the global deformation without significantly interfering with the structure and can also resolve large deflections.

Analysis of existing wind tunnel data sets can enable the extraction of structural dynamics information and improve the utility of current and future ground and wind

tunnel test programs. This data can be used in conjunction with finite element analysis as a verification dataset for high-fidelity predictive models. This study expands the capabilities of current photogrammetric data analysis by developing a methodology to characterize the dynamic content inherent in the deflection of inflatable aerodynamic decelerators. Data from wind tunnel testing of a 6 m stacked tori IAD is used to demonstrate the methodology.

## *2.2 The Photogrammetric Method*

Photogrammetry is the process of using stereo camera imaging of a surface to calculate its three-dimensional coordinates. The photogrammetric method starts with calibrating the camera system to a known set of target points prior to testing the model. Next, targets are placed on the test article to facilitate accurate tracking with minimal error. Solid colored, circular targets that have high contrast with the test article are preferred since they are easily identified in the image. If large geometric changes occur during testing, such as the deployment or inflation of a flexible structure, solid targets are generally preferred since they are visible over a wide range of angles. If less dramatic geometric changes occur, retro-reflective targets can improve target visibility in low light conditions by providing higher contrast.

In addition to physical targets, dot patterns can also be projected onto the article for fast or low-cost applications [85]. In this way, the target size, spacing, and positioning can be automatically controlled and adapted to the individual run requirements. This is also beneficial in the case of ultra-light structures where physical targets would add a non-trivial amount of mass or stiffness. Target projection is not possible, however, for vibration analysis because it cannot track a fixed point and is also infeasible for test articles constructed out of materials with high absorptivity or transparency [101].

During testing, photogrammetry cameras take synchronized pictures of the test

article, which are saved for post-processing. The images are imported into a data analysis software that identifies sets of reference targets in each image. The reference targets are used to reorient and scale the images and to correlate individual targets among each image in order to assess that target's motion over time. The photogrammetry software then computes the 3D coordinates of each target over time based on the saved image sequences and the known spatial locations and orientations of the cameras. These points can be scaled to the physical size of the test article and rotated into a desired coordinate system for structural analysis.

When employing photogrammetry as test instrumentation, it is important to clearly define the test objectives. Because photogrammetry is based on image processing with finite size targets and sensor resolution, the accuracy of the camera calibration and camera distance to the target can significantly influence the error in the positional results. Global imaging of large test articles also requires multiple camera pairs to view the entire surface, known as stereophotogrammetry, and time accurate measurements require cameras with high temporal as well as spatial resolution. There is no single camera system that can satisfy all the requirements. Therefore, judicious designing of the photogrammetry setup is critical to ensure successful testing.

## *2.3 Methodology*

In this investigation, an analysis suite is developed to extract dynamic information from the photogrammetry data. Specific computations and expected results are described below.

### 2.3.1 Analysis

As seen in Fig. 8, the dynamic photogrammetry analysis methodology is composed of four steps, categorized as either preprocessing or analysis. The inputs to the methodology are the raw datafiles produced by the photogrammetry system. These inputs files contain point cloud data representing the test article surface at a given

instant of time. As a result, the spatial and temporal resolution of the data is set based on the photogrammetry system. The data is represented as a set of (x, y, z) coordinates for each point, describing their position in 3-dimensional space, along with a set of (1, 2, 3) indices, which are used as unique identifiers. The identifiers allow for a way to correlate the locations of each point throughout the sequence of input files. The time sequence of data is critical to this analysis, as it allows for the characterization of the surface motion.

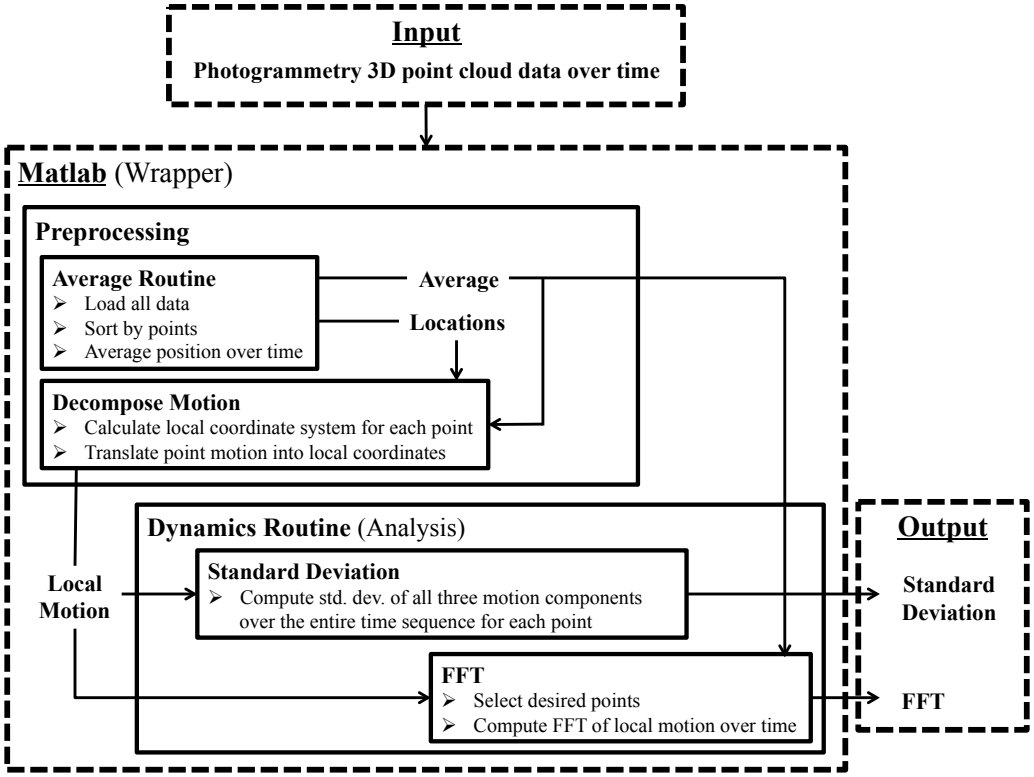


**Figure 8: Design structure matrix of the dynamic photogrammetry analysis methodology**

The averaging routine takes the input files and processes them for use in later analyses. The first step is to compile the individual photogrammetry data files into a single dataset so that it can be manipulated. The routine then sorts the data by point index, grouping data with like identity indices, in order to isolate individual surface points. The script iterates through each point and averages the set of 3D

positions over time to produce an averaged position. The average is calculated using Eq. 2, taking into account the total number of frames that contain the given point. In cases where the photogrammetry system does not identify a point in one or more frames, these frames do not contribute to that points averaged position because the corresponding identity set would also be missing. The two outputs of the averaging routing are the 3D positions over time grouped by each point on the surface and the averaged location of those points.

$$x_{ave} = \frac{1}{N}\sum_{i=1}^{n} x_i \tag{2a}$$

$$y_{ave} = \frac{1}{N}\sum_{i=1}^{n} y_i \tag{2b}$$

$$z_{ave} = \frac{1}{N}\sum_{i=1}^{n} z_i \tag{2c}$$

Analyses conducted in the global reference frame can be applied directly to the location and average output files generated by the averaging routine. However, in certain instances, it is beneficial to perform the analysis in a local reference frame defined by the instantaneous geometry of the local surface. The justification for the use of local and global frames is discussed in section 2.4.2. For these cases, before performing the analysis, it is necessary to first convert the location of the surface points from the global to the local coordinate frames using the decompose motion routine. The first step in the transformation is to define the local coordinates based on the local surface contour. The routine then computes the difference between the instantaneous locations of the points at each instant in time with their averaged locations to determine the points motion, expressed in the global coordinate system. The time history of motion is transformed from the global to local coordinates by taking the dot product between the motion vector and the vectors defining each of the local coordinate axes. The motion information in both the local and global

coordinates are saved to output files for use in the various analyses.

The first dynamic analysis routine is the positional standard deviation analysis. This analysis calculates the standard deviation of the set of motion vectors (instantaneous position minus the averaged position) for each point, as described in Eq. 3. The analysis is performed independently for each coordinate axis to isolate trends of motion in the various directions. Calculations are also performed on the absolute motion (magnitude of the motion vector) to provide an aggregate metric. The standard deviation results are saved for future use and are plotted to visualize the global characteristics. The plots can be used to understand trends in the data and infer the dynamic response of the test article, for example, by visualizing the mode shapes.

$$\sigma_x = \sqrt{\frac{1}{N}\sum_{i=1}^{n}(x_i - x_{ave})^2} \tag{3a}$$

$$\sigma_y = \sqrt{\frac{1}{N}\sum_{i=1}^{n}(y_i - y_{ave})^2} \tag{3b}$$

$$\sigma_z = \sqrt{\frac{1}{N}\sum_{i=1}^{n}(z_i - z_{ave})^2} \tag{3c}$$

The second of the dynamic analyses is the Fourier Transform, or FFT, calculations. This analysis computes the Fourier Transform of the motion of selected points. The Fourier Transform is a reversible, linear transform that calculates the frequency content of a time domain signal. This is useful for diagnosing cyclic phenomena, such as vibration, in order to understand the resonance and frequency response of the test article. For discretely sampled signals, a Discrete Fourier Transform is used, shown in Eq. 4. This is implemented using the Fast Fourier Transform algorithm, which significantly reduces computational time by decomposing the n-point time domain signal into n single-point signals and synthesizing the overall frequency spectrum from the

spectra of the individual points.

$$X(\omega)_k = \sum_{j=0}^{N-1} x(t)_j e^{-2\pi i j k/N} \tag{4}$$

The analysis is applied in two different ways, the first to understand the underlying coupling of the structural and fluid frequency responses and the second to observe global trends in the surface motion. In both instances, the vast amount of information makes data visualization difficult. This is because each n-point time domain signal produces amplitude information for $n/2$ different frequencies. As a result, fluid-structure interactions are inferred from the frequency response of the surface at discrete locations. This limits the information produced by the analysis to two dimensions so that the results can be easily visualized. Trends in the motion are independently assessed for a single characteristic dimension of the structure. Points are chosen, evenly spaced along the dimension, and results are visualized both as bubble and surface plots. The bubble plots display the point location and frequency range along the y- and x-axes, respectively, and represent signal amplitude in the color and size of the plot markers. The surface plots display the point location along the y-axis and the frequency and amplitude signals along the x- and z-axes, respectively. The combination of both the bubble and surface plots allow for clear inspection of the trends as well as relative magnitudes of the signals.

### 2.3.2 Analysis Applications

The specific analyses developed contribute to an improved understanding of unique aspects of the test article's dynamic response and, combined, provide insight into the overall decelerator dynamics. The positional standard deviation analysis enables a global visualization of the magnitude of motion (defined as the magnitude of the dispersion of positions over time) across the entire structure. As a result, it allows for visualization of global mode shapes as well as locations of increased motion. The

results have important structural design implications by helping to visualize how the configuration influences regions of high and low motion, which could contribute to structural fatigue or uncertainty in aerodynamic calculations based on the static shape. Since the positional standard deviation is a single metric, it also enables rapid characterization of the dynamic response and is useful in comparisons between different configurations and test conditions.

While the positional standard deviation analysis provides global insight into the degree of motion at each point on the inflatable structure, the FFT analysis provides information on the frequency content of motion at those points. Many of the phenomena in wind tunnel or ground test experiments are inherently cyclical, including vibration of the inflatable structure and vortex shedding around the test article. The FFT analysis extracts the frequency information from photogrammetry data to investigate the system resonance arising from the dynamic coupling of the inflatable structure and surrounding fluid. Other test methods have been developed to calculate the resonance of an isolated inflatable structure from cyclic forcing using discrete shakers and accelerometers [108]. These tests noted that the lack of realistic aerodynamic loading of the structure was a drawback of the method and suggested this area for future work. Another survey of instrumentation challenges for inflatable vehicles noted the dynamic structural response as one of the six key areas of interest [109]. This survey commented that "measurements of the lAD's dynamic response are desired to understand the relative significance of the aerodynamic forcing function coupling into the inflatable structure. These measurements can also provide estimates of global oscillations and inflatable shedding frequencies" [109]. The FFT analysis specifically addresses both aforementioned challenges, allowing for calculation of the coupling between the aerodynamic and structural forcing for an inflatable structure under applied aerodynamic loading. To the author's knowledge, this has

not been previously implemented on an inflatable ground test article with an aerodynamic load. The FFT analysis calculates the frequency response of the surface motion at several points. By analyzing the frequency content of motion, distinct peaks can be identified, corresponding to fundamental resonance modes of the inflatable and surrounding flow field. These peaks can inform structural designers of the fluid-structure coupling and identify if unsteady dynamics could potentially occur in flight. Through the application of this methodology, with a specifically designed test program, the fluid-structure coupling can be diagnosed and characterized for use in numerical fluid-structure interaction modeling.

The preceding analyses can be performed in any arbitrary coordinate system. The most convenient of which is the coordinate system used by the photogrammetry system, denoted here as the global coordinates, which typically coincides with the wind-tunnel axial, vertical, and horizontal directions. The output of the photogrammetry data is presented with respect to the global coordinates and, as a result, minimal processing is needed to perform the analyses. Results of the standard deviation and FFT analyses, presented in the global coordinate system, will provide a single metric of the overall motion because each of the coordinate axes is equally arbitrary. Most inflatable test articles will have a set of characteristic directions that parameterize their overall shape, with deformation in these various directions constituting different possible modes. For example, a cylinder can be described by the radial, angular, and axial directions, with axial motion corresponding to elongation, angular motion corresponding to twist, and radial motion corresponding to expansion, contraction, or bending. If the motion is instead decomposed into these local coordinates, it will provide valuable insight into the independent characteristic directions. As a result, the principal direction standard deviation and FFT analyses will be able to identify if the inflatable structure is being excited in any subset of the possible fundamental modes, which is a much more useful result for structural designers.

The analyses developed in this thesis improve the observation of test article dynamic phenomena and can leverage existing ground test programs and datasets. The data can provide useful information that goes beyond the inflatable's static response in order to better analyze various structural configurations and flight environments. The information obtained from testing can also be used to support high-fidelity structural modeling and analysis as a validation case study. These analyses can also be expanded in the future to couple with force and moment data to calculate other phenomena such as the dynamic stability of the structure.

## *2.4 Case Study: Stacked Tori Wind-Tunnel Testing*

This case study applies the methodology developed in section 2.3 to data from a wind tunnel test conducted at the NASA Ames National Full-Scale Aerodynamics Complex (NFAC) 40- by 80- ft test section. A photogrammetry instrumentation setup was installed to observe the deformation of a 6 m stacked tori decelerator under applied loading. While the primary objectives of the test were to understand the IAD static deformation, this dataset provides a valuable opportunity to evaluate the effectiveness of the dynamic analysis methodology in characterizing the IAD dynamic response.

### 2.4.1 Wind Tunnel Test Set-Up

The stacked tori configuration tested in this study is composed of two major components: a rigid center-body made of aluminum and several tori composed of fiber reinforced thin films. The IAD also had an aerodynamic skin cover that mimicked the structure of a flexible TPS [110]. Two configurations were tested, seen in Fig. 9. The Baseline configuration is composed of seven structural tori ($T_1$-$T_7$) and one shoulder torus ($T_8$). The second configuration, called the Tri-tori, builds upon the Baseline configuration by adding an additional torus located between $T_6$ and $T_7$, $T_{6.5}$ (seen in Fig. 9 as the red circle), and was developed to investigate whether this addition substantially improved rigidity. The test article was mounted upon a test rig,

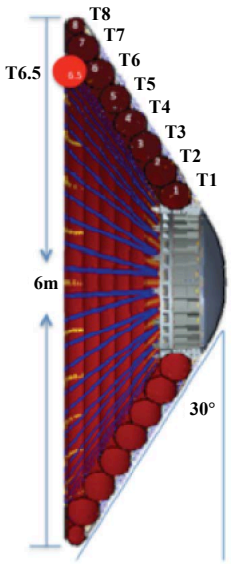


**Figure 9: Stacked tori configuration [16]**

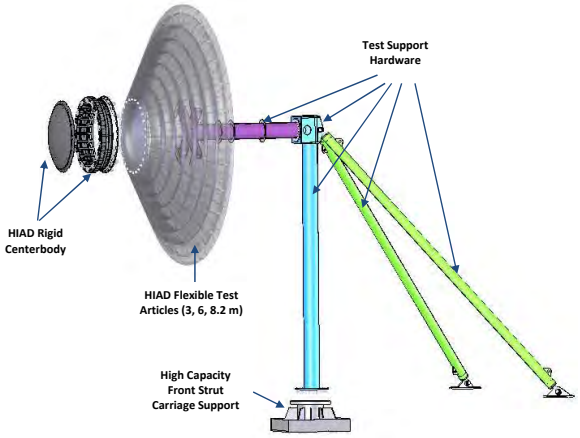


**Figure 10: Diagram of the stacked tori mounting rig [110]**

seen in Fig. 10, that included a center sting and supporting legs offset behind the decelerator.

The photogrammetry instrumentation featured four pairs of stereoscopic cameras mounted in the center, lower, and upper sections of the east wall as well as on the floor and ceiling [110]. The set-up, shown in Fig. 11, was chosen to provide a full view of the stacked tori between all the camera pairs and to permit 3D tracking. Each camera acquired data at 15 Hz for 10 seconds, producing 150 frames, and was synchronized by a signal pulse from the facility data acquisition system. Camera

placement was determined before testing by using virtual imaging software in order to meet the design and resource constraints in the wind tunnel environment [111]. SVIEW photogrammetry software was used to stitch together each camera view and ARAMIS generated the full 3D model.

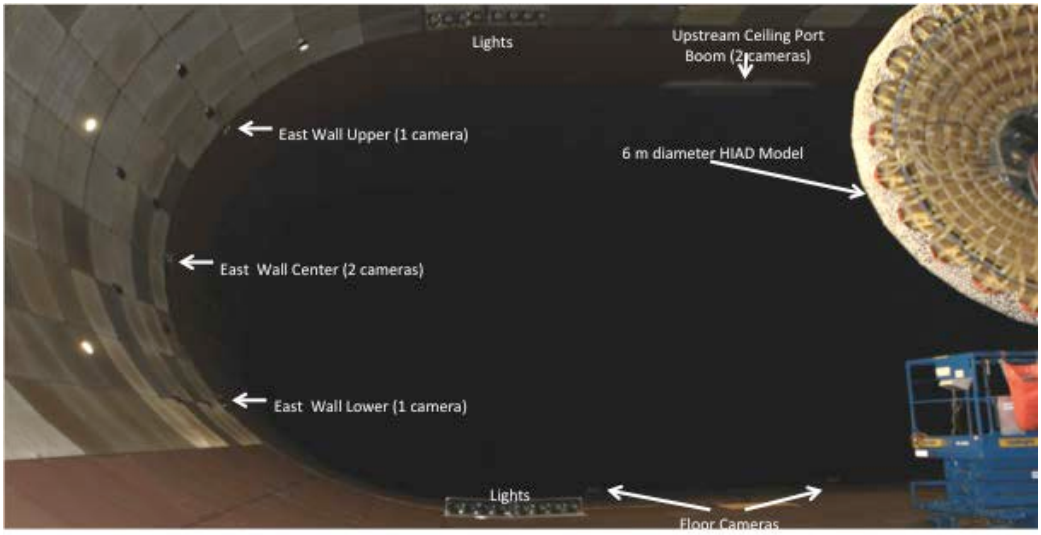


**Figure 11: Photogrammetry camera setup [41]**

In order to develop a deflection data set sufficient to validate aero-elastic models, three parameters were studied: yaw angle, free-stream dynamic pressure, and inflation pressure. The test matrix can be seen in Table 1. Note, English units were used for this test program. For consistency, the original unit system is retained in the discussion of this case study.

**Table 1: Test matrix for stacked tori NFAC wind tunnel testing**

| Yaw Angle (deg) | Dynamic Pressure (psf) | Inflation Pressure (psi) | |
|---|---|---|---|
| -25, -15, -5, 0, 5, 10 | 8, 40, 50, 65, 70 | $I_2$ | 15 (all tori) |
| | | $I_3$ | 10 ($T_{3-6,8}$), 15 ($T_{1,2,7}$) |
| | | $I_4$ | 8 ($T_{3-6}$), 15 ($T_{1,2,7}$) |

The yaw angle was modulated to simulate an angle of attack during actual flight. Positive yaw angles were defined as a clockwise rotation when looking down upon the wind tunnel. Dynamic pressure was changed by adjusting the freestream air velocity.

The maximum wind tunnel dynamic pressure was limited to 70 psf by NFAC safe operating procedures. The last parameter analyzed was the inflation pressure of the individual tori. Three settings were used to investigate the sensitivity of the stacked tori stiffness to inflation pressure [110].

### 2.4.2 Analysis Implementation

The dynamic photogrammetry analyses described in section 2.3.1 are applied to the photogrammetry data obtained during testing. Due to the specifics of the data files and test article geometry, several steps are taken to implement the methodologies. The details of the implementation and a discussion of how to apply the analyses to conical shaped test vehicles is described below.

Each implementation of the dynamic analyses for test articles of a different shape will have a unique routine for decomposing the motion into the local coordinates due to those vehicles having unique local coordinate definitions. In the case of the NFAC test, the IAD can be approximately described as a cone with a truncated nose. Therefore, the most appropriate set of local coordinates to describe the motion of the surface is the normal, radial, and tangential system. Seen in Fig. 12, the normal direction points towards the outward normal of the local surface, the radial direction points in the direction of a radial line extending from the virtual nose of the cone, and the tangential direction is orthogonal to the first two directions, pointing in the angular direction parallel to the plane defined by the base of the cone. In these coordinates, the normal direction corresponds to pure angular deflection of the surface (motion 1), the radial direction corresponds to a pure elongation of the inflatable side (motion 2), and the tangential direction corresponds to a pure twist of the surface about the IAD symmetry axis (motion 3).

The coordinate system is described as a local coordinate because the specific axis vectors are unique for points distributed among different locations on the conical

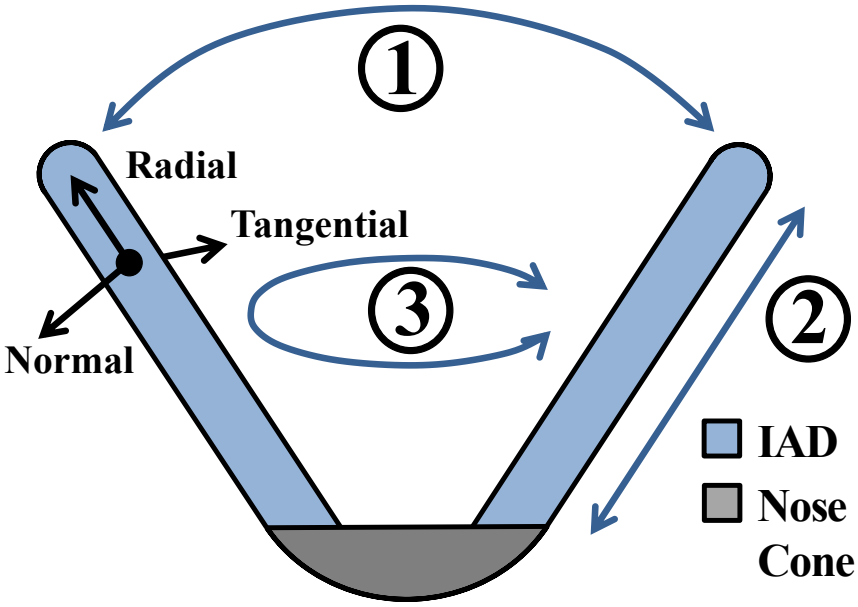


**Figure 12: Depiction of the IAD local coordinate system and possible modes of motion.**

surface. Therefore, a processing routine is developed to identify the local coordinate system for each point. Because the local coordinate vectors are the same for all points located within an angular slice of the IAD (similar values of azimuthal angle), the local direction vector routine first expresses each of the data points in cylindrical coordinates. Points are isolated for processing by segmenting the IAD surface into 5-degree wedges, with all points in that wedge being assigned a single set of local coordinates. A wedge of five degrees is chosen for two reasons: it reduces the computational cost by limiting the number of iterations and improves robustness to uncertainty in the data by providing a sufficiently large population. A best fit line is fit to all points within the wedge using singular value decomposition, a method to identify the dimensions along which the data points exhibit the most variability and to reduce the dimensionality of the data. In this case, the three-dimensional wedge of points is reduced to a single dimensional line approximation. Singular value decomposition reduces the rectangular matrix $A$, containing the three dimensional locations of all points within the wedge, into the product of matrices $U$ and $V$, containing orthonormal columns,

and diagonal $S$, containing positive real entries, as seen in Eq. 5. The largest entry of $S$ denotes the eigenvalue of the dimension of largest variation and its corresponding eigenvector is the parameterization of the best fit line.

$$A_{mn} = U_{mp} S_{pq} V_{nq}^{T} \tag{5}$$

The tangential direction lies parallel to the plane of the conical base and is perpendicular to the best fit vector. This vector can therefore be computed easily by calculating the orthogonal vector to the current angular slice of datapoints, expressed in the 2-dimensional radius and theta coordinates of the original cylindrical coordinate system. Because both the tangential vector and the best fit vector are located in the plane of the instantaneous surface segment, the surface normal is computed by taking their cross product. Finally, the radial vector, which is orthogonal to the normal and tangential vectors, is computed by taking their cross product. The same process is repeated for every wedge segment so that the local coordinates are defined for each point. This method is developed to minimize the variability in the local coordinate definition due to uncertainty or non-uniformity in the test data.

The full 3D photogrammetry dataset is constructed by stitching together data obtained from at least two camera-pairs. Figure 13 shows an example of the data captured by the four stereoscopic camera-pairs during a run. The data in this figure is represented by colors while gray is an area of no information. When processing the data, it is apparent that there are discrepancies between the results observed by different camera pairs in overlapping regions. As a result, a second copy of each script is created specifically to handle the independent camera pair data. An extra routine is included in the new script that isolates points from the different camera pairs and writes out each datafile individually. Subsequent analyses incorporate an additional loop that iterates through each set of camera data to independently calculate the results.

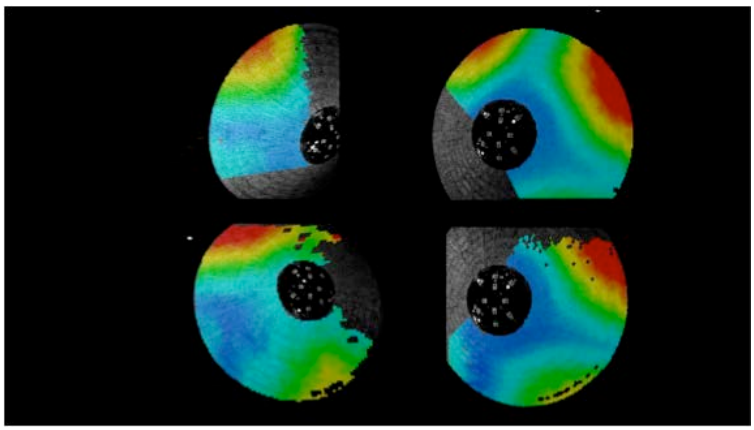

**Figure 13: Images from separate camera pairs taken from ARAMIS**

### 2.4.3 Results

#### *2.4.3.1 Characterization of Stacked Tori Global Oscillations*

Oscillation of the stacked tori test article resulted in significant deviation between the positions of the IAD surface at different points in time. It is important to globally characterize this motion as it can provide valuable insight into the structural performance of the decelerator as well as quantify the uncertainty in surface deflection calculations. This is achieved by calculating the standard deviation in position of each point over all 150 frames of a run. Because the standard deviation is a metric describing the overall dispersion of sample data, regions of high standard deviation correlate with a significant degree of motion while regions of low standard deviation indicate limited motion. Motion, here, is defined as the overall amount of change in position from the averaged response. Therefore, both large changes in position over a short interval of time as well as small changes in position over extended periods of time contribute to an increase in motion.

The standard deviation analysis is first performed in the global coordinate frame, calculating the standard deviation in absolute position for each point (absolute position being the magnitude of the vector extending from that point's average position

to its instantaneous position). Figure 14 shows a top down view the stacked tori depicting the absolute positional standard deviation results with the standard deviation (in mm) being represented by the color of each data point (this standard will be used for all plots in this section). This run was conducted at 70 psf dynamic pressure with a 0° yaw angle and $I_3$ inflation setting.

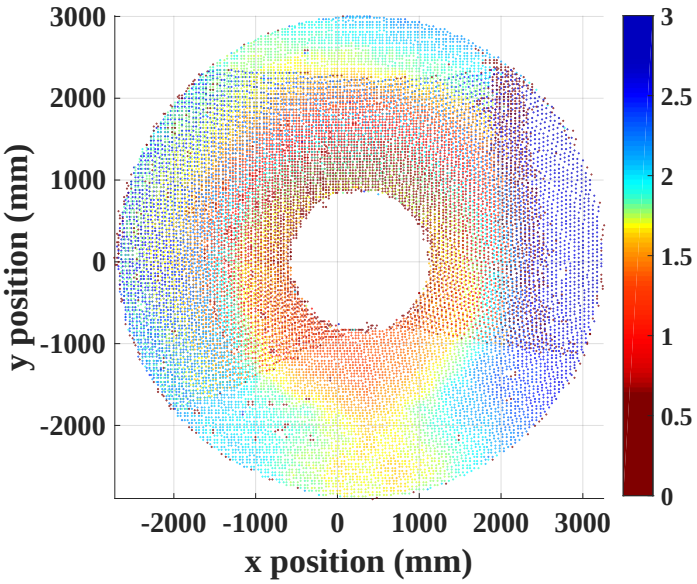


**Figure 14: Standard deviation of the absolute position of all points on the stacked tori. Standard deviation (in mm) is represented by color of the data points. Run is conducted 70 psf, 0° yaw angle, $I_3$ inflation setting.**

As seen in the figure, the positional standard deviation increases when moving radially outward from the center and is approximately uniform azimuthally around the stacked tori. These characteristics mirror that of a rigid oscillator, where the points on the perimeter have more motion than points near the center and thus have a higher standard deviation in their position. The fact that there is no clear axis of low standard deviation indicates that the test article is rotating about the cone center point rather than any preferred linear axis. There is one region of points along the 180° radial (down) that have lower deviation than other points at the same radius. This could be an effect of the sting used to hold the test article, which was located in this region.

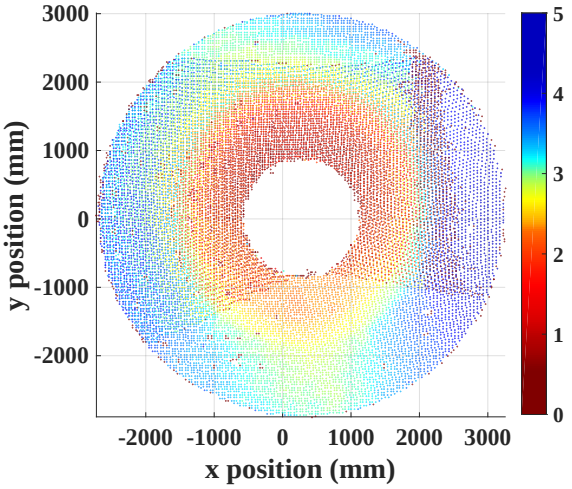


(a) Positional standard deviation of the IAD surface in the local normal direction

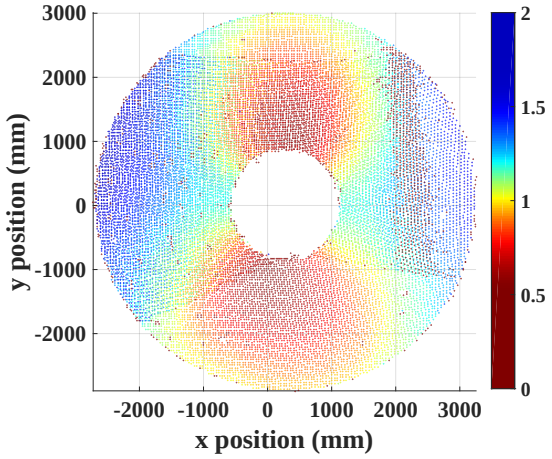


(b) Positional standard deviation of the IAD surface in the local tangential direction

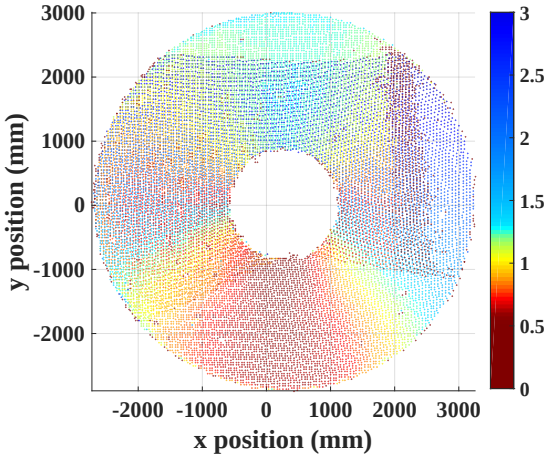


(c) Positional standard deviation of the IAD surface in the local radial direction

**Figure 15: Positional standard deviation of stacked tori in the local coordinate system (70 psf, 0° yaw angle, $I_3$ inflation setting)**

The standard deviation analysis is repeated for the same run, seen in Fig. 15, this time applying the calculations in the local (normal, tangential, radial) coordinate frame. The normal standard deviation plot in Fig. 15(a) looks similar to that of the absolute position, which indicates that the normal motion dominates the overall response. This is to be expected and is also evidenced by the much higher deviation exhibited in the normal deviation plot in Fig. 15(a) than the tangential or radial plots in Figs. 15(b) and 15(c), respectively. However, due to the discrepancy in

the magnitude of motion in the different local directions, the tangential and radial information is lost in the absolute position standard deviation analysis.

The shape of the positional standard deviations in Fig. 15 are similar to the overall normal, tangential, and radial responses seen across all test conditions. Therefore, given the diverse set of parameters and ranges tested, it can be seen that these responses are fundamental characteristics of the HIAD test article. The normal positional standard deviation tends to produce circles with motion increasing with increasing radius. Due to the absolute position confounding the normal response with the tangential and radial results, the normal deviation graph exhibits circles similar to the absolute deviation graph, but clearer and with less distortion. The low deviation along the 180° (down) radial is preserved, however, confirming that this is likely due to the influence of the sting.

The tangential graph produces an interesting shape, with circular petal-like structures emerging along the 0° (up) and 180° (down) radial directions. These petals correspond to regions of low tangential (twist) motion. Given that the analyzed run is at 0° yaw, it is expected that any results would be symmetric about the vertical axis, but the reason as to why the structures do not follow any of the conical characteristic dimensions (along a radial or azimuthal line) is uncertain. The radial deviation plot displays bands of constant deviation extending radially outward from the IAD center. The lowest radial motion is seen along the 180° (down) radial direction, which is likely due to interactions with the sting, and motion increases away from that direction.

The shapes of the local positional standard deviation graphs are investigated by calculating the displacement of each point in the normal, tangential, and radial directions at each instant in time and combining the consecutive frames into a video. The videos are viewed both holistically and frame-by-frame to understand the global deformed mode shapes and to correlate the overall motion with the graphs from Fig.

15. The results in all videos are chaotic, which is to be expected with a flexible structure in this environment. However, certain trends do persist. Note that the plots of the video frames do not show standard deviation, or motion, information and instead show the difference between instantaneous and average locations of each point (in mm) oriented along the local direction (represented as a blue color) or in opposition to the local direction (represented as a red color).

The deflection in the normal direction tends to correlate with a rigid body-like rocking motion, with one side moving in the positive normal direction and the other side moving in the negative normal direction, separated by an axis of no normal deflection, as seen in Fig. 16. This shape is observed to occur around multiple axes, as seen in Figs. 16(a) and 16(b), which gives rise to the circular structure in Fig. 15(a). It is important to note that the normal direction is oriented towards the exterior of the cone for all points, so a blue color corresponds to deflection towards the freestream flow and a red color corresponds to deflection in the direction of the freestream flow.

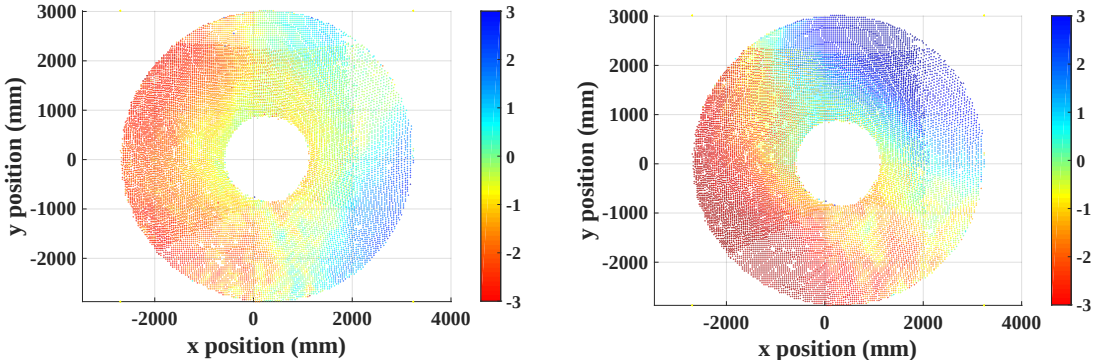


(a) Deflection (in mm) in the normal direction indicating a rocking motion about the vertical axis

(b) Deflection (in mm) in the normal direction indicating a rocking motion about a diagonal axis

**Figure 16: IAD deflection in the normal direction indicating a rocking motion about various axes (Run conducted at 70 psf, 0° yaw angle, $I_3$ inflation setting)**

Specific instances of other modes are also observed, such as a breathing mode

(all points cohesively moving in either the positive or negative direction), or a bell mode (points on opposite sides having the same positive or negative deflection with adjacent sides moving in the opposite direction). An example of the bell mode is seen in Fig. 17.

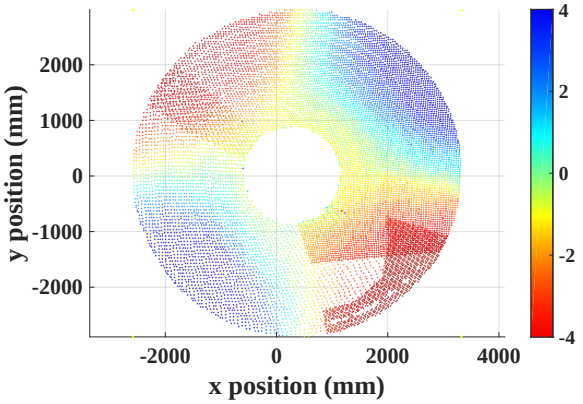


**Figure 17: IAD deflection (in mm) in the normal direction indicating a bell mode (Run conducted at 70 psf, -25° yaw angle, $I_4$ inflation setting)**

The instantaneous frames of the radial video typically show an asymmetric plot, with one side of the IAD exhibiting deflection in the positive radial direction and the other side exhibiting deflection in the negative direction. However, the transition between the regions often occurred along non-radial lines, as seen in Fig. 18(a). These transitions are seen to sweep around the test article in an azimuthal pattern. The region of low deviation in Fig. 15(c) appears to correlate with the overall locations of the transition regions across all instantaneous frames.

The instantaneous frames of the tangential deviation movie do not show any petal structures, which is to be expected, but did not show any definable structures that would logically produce the petal shapes either. Seen in Fig. 18(b), certain frames of the tangential video do exhibit regions of low deviation (yellow, green color) around the location of the petals however, none of these frames displays their circular shape. Nevertheless, the petal structure is evident in the standard deviation plots of many different runs and is clearly a characteristic feature of the test article motion. These

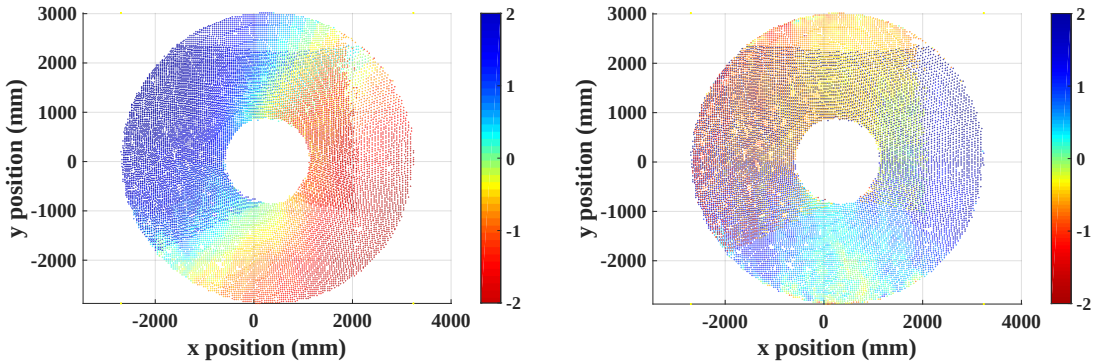


(a) Instantaneous deflection (in mm) in the radial direction

(b) Instantaneous deflection (in mm) in the tangential direction

**Figure 18: IAD instantaneous deflection in the tangential and radial directions (Run conducted at 70 psf, 0° yaw angle, $I_3$ inflation setting)**

phenomena demonstrates the importance of the standard deviation analysis, not only as a quick comparison of the global motion, but also as a way to aggregate the chaotic instantaneous motion of the IAD and discover the underlying characteristics of the structure's dynamics.

The standard deviation analysis is also a valuable way to assess how different configurations and flight environments influence the IAD dynamic response. Therefore, the analysis is applied to several runs that vary a single test parameter in order to capture these effects. Varying the test article yaw angle is shown to increase normal motion (blue) on the left side, 270° radial, of the IAD for positive yaw angles, as seen in Fig. 19(b), and increase motion on the right side, 90° radial, for negative yaw angles, as seen in Fig. 19(a). This is interesting because, for a positive yaw angle, the right side of the article is exposed to the flow (side with lower overall positional deviation, or motion). Therefore, while the side exposed to the flow experiences higher deformation, the side shielded from the flow experiences higher movement, or variation in deflection. This could potentially be due to the reduced pressure differential across the inflatable wall, resulting in less resistance to increased or decreased deflection.

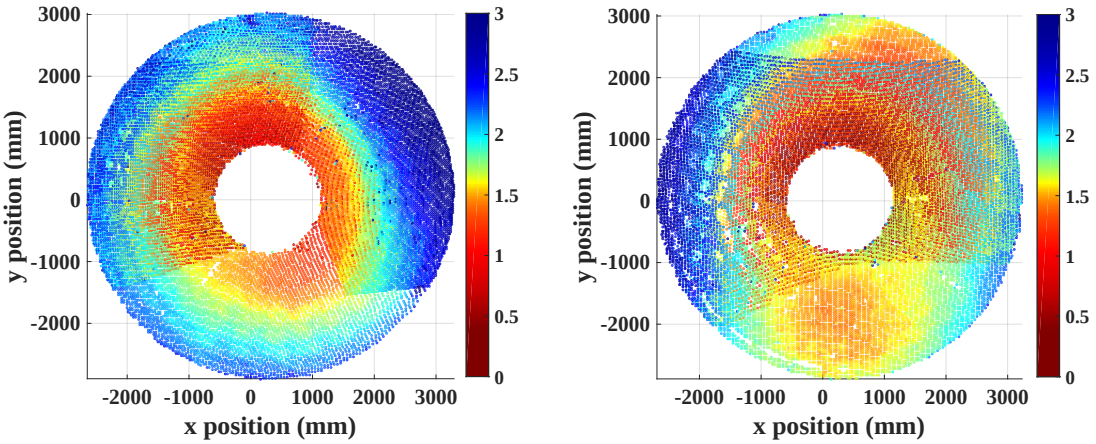


(a) Positional standard deviation of normal deflection with a negative yaw. (Run at -15° yaw, 50 psf dynamic pressure, $I_3$ inflation pressure)

(b) Positional standard deviation of normal deflection with a positive yaw. (Run at +10° yaw, 50 psf dynamic pressure, $I_3$ inflation pressure)

**Figure 19: Change in the positional standard deviation in the normal direction due to a variation in yaw angle**

Yaw also affects the tangential deviation by rotating the low-deviation petals counter-clockwise for positive yaw (seen in Fig. 20(b)) and clockwise for negative yaw (seen in Fig. 20(a)). The low deviation regions rotate towards the freestream on

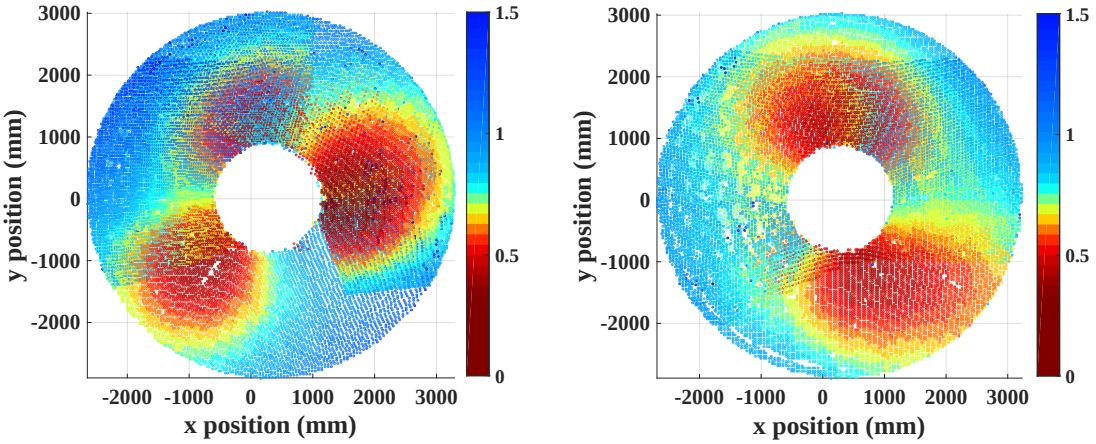


(a) Positional standard deviation of tangential deflection with a negative yaw. (Run at -15° yaw, 50 psf dynamic pressure, $I_3$ inflation pressure)

(b) Positional standard deviation of tangential deflection with a positive yaw. (Run at +10° yaw, 50 psf dynamic pressure, $I_3$ inflation pressure)

**Figure 20: Change in the positional standard deviation in the tangential direction due to a variation in yaw angle**

the bottom of the article and away on the top. This is likely due to the interactions of the wind tunnel sting that holds the test article, seen in Fig. 10. The decelerator is held out in front of the sting so that at 0° yaw its influence is primarily on the 180° (down) radial (because the sting extends below the test article). As the test fixture rotates with positive yaw, the sting projection onto the test article shifts to the positive x-values. This corresponds to a counterclockwise rotation about the inflatable cone's symmetry axis, which is seen in the tangential response. The opposite petal likely rotates counterclockwise as well due to the symmetry of the test article. This same phenomenon is seen with the radial standard deviation response, with the low deviation region rotating based on the yaw angle and interaction of the sting.

Variations in dynamic pressure also have significant influence on the IAD motion. Figure 21 shows the effect of dynamic pressure on the normal motion for low dynamic pressure (Fig. 21(a)) and high dynamic pressure (Fig. 21(b)) cases. It is clear from the figures that the overall normal motion significantly increases with increasing dynamic pressure. This is intuitive, as more energy in the flow likely translates to

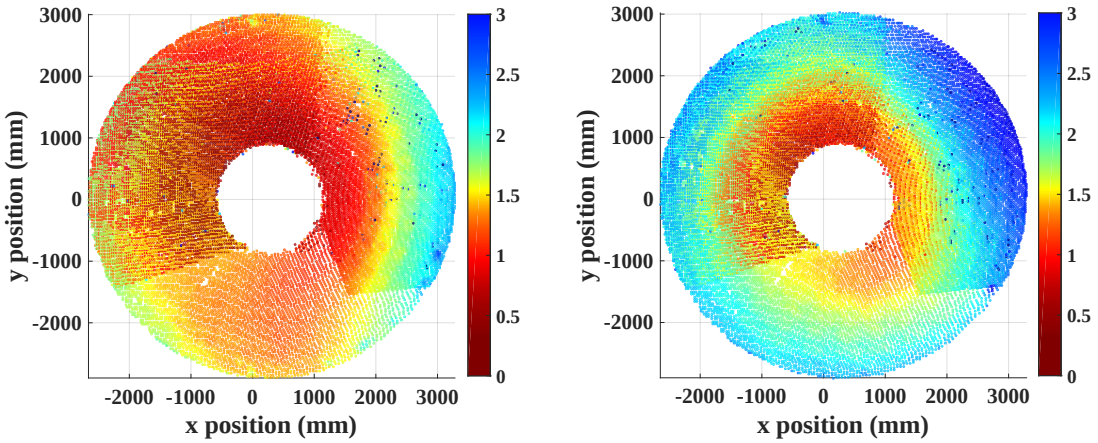


(a) Positional standard deviation of normal deflection under low dynamic pressure. (Run at -15° yaw, 40 psf dynamic pressure, $I_3$ inflation pressure)

(b) Positional standard deviation of normal deflection under high dynamic pressure. (Run at -15° yaw, 50 psf dynamic pressure, $I_3$ inflation pressure)

**Figure 21: Change in the positional standard deviation in the normal direction due to variation in dynamic pressure**

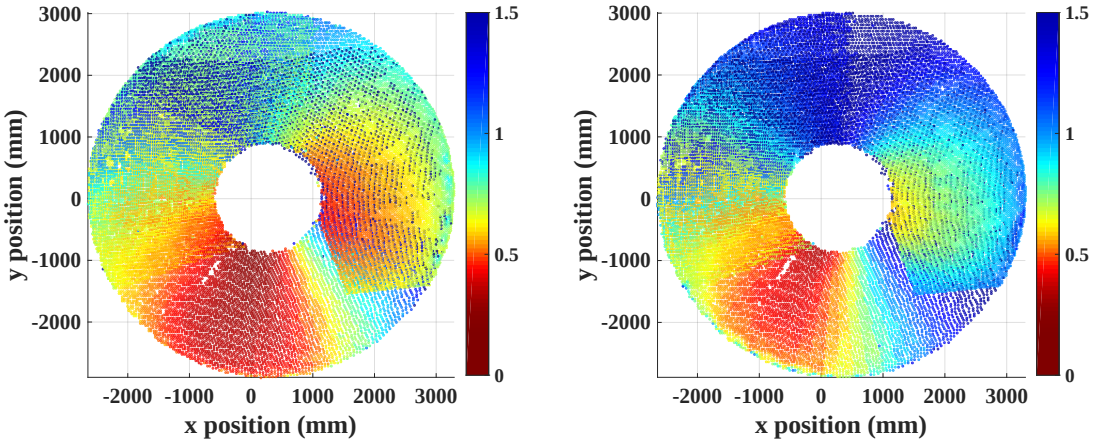


(a) Positional standard deviation of radial deflection under low dynamic pressure. (Run at -15° yaw, 50 psf dynamic pressure, $I_3$ inflation pressure)

(b) Positional standard deviation of radial deflection under high dynamic pressure. (Run at -15° yaw, 70 psf dynamic pressure, $I_3$ inflation pressure)

**Figure 22: Change in the positional standard deviation in the radial direction due to variation in dynamic pressure**

more energy in the structural motion. The same is true for motion in all directions, with increases in both tangential and radial (seen in Fig. 22) positional standard deviation being observed for increasing dynamic pressure.

The inflation pressure has a more subtle effect on the positional standard deviation response. Increasing the inflation pressure results in a reduction in normal motion, seen in Fig. 23, but with standard deviation contours that are less circular. The shape of the high inflation pressure contours in Fig. 23(b) reflect a cohesive rocking mode about the vertical axis whereas the low inflation pressure contours in Fig. 23(a) do not indicate motion in any particular axis. Instead, the lower inflation pressure of the middle tori are seen to deflect uniformly around the decelerator circumference.

The tangential positional standard deviation response is similar to the normal response, with decreased motion, although to a lesser degree, with increasing inflation pressure. The radial standard deviation, however, exhibits increased motion with increase in inflation pressure, seen in Fig. 24. This could be due to the higher inflation pressure maintaining a more rigid decelerator shape and contributing to a

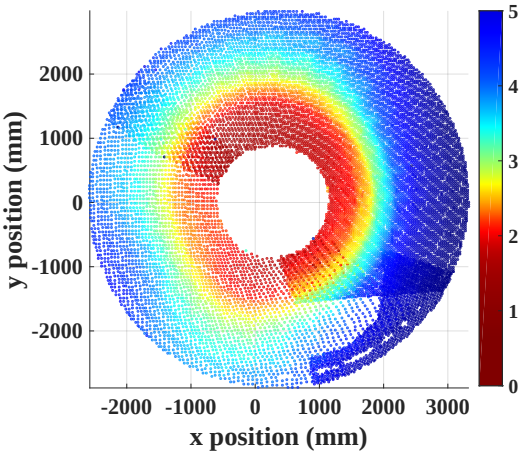


(a) Positional standard deviation of normal deflection under low inflation pressure. (Run at -25° yaw, 70 psf dynamic pressure, $I_4$ inflation pressure)

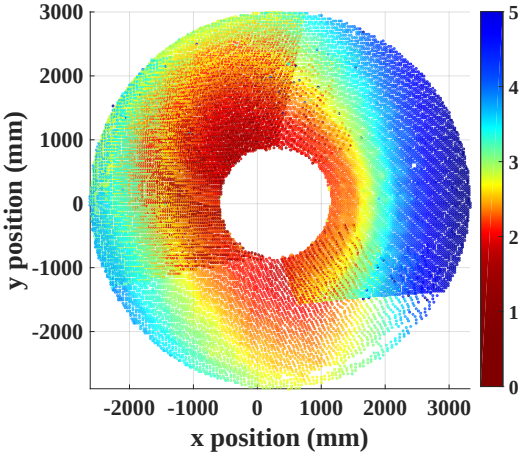


(b) Positional standard deviation of normal deflection under high inflation pressure. (Run at -25° yaw, 70 psf dynamic pressure, $I_2$ inflation pressure)

**Figure 23: Change in the positional standard deviation in the normal direction due to variation in inflation pressure**

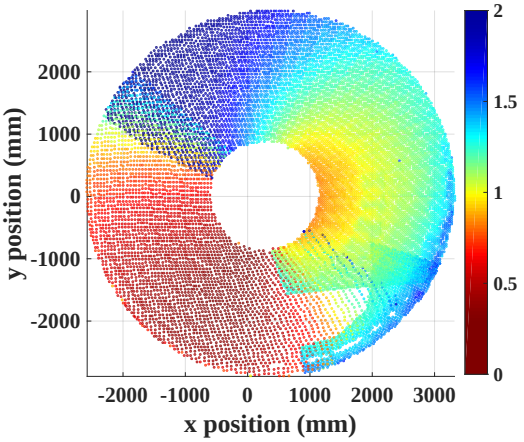


(a) Positional standard deviation of radial deflection under low inflation pressure. (Run at -25° yaw, 70 psf dynamic pressure, $I_4$ inflation pressure)

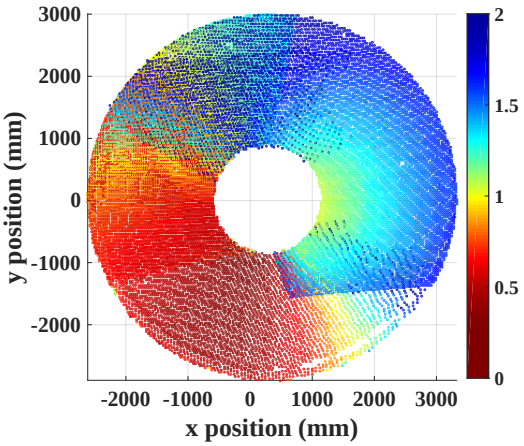


(b) Positional standard deviation of radial deflection under high inflation pressure. (Run at -25° yaw, 70 psf dynamic pressure, $I_2$ inflation pressure)

**Figure 24: Change in the positional standard deviation in the radial direction due to variation in inflation pressure**

greater radial forcing function from the oncoming airflow.

The final test parameter studied is the influence of the tri-torus configuration, which adds an additional structural torus near shoulder of the decelerator. Seen in Fig. 25, the tri-torus configuration results in more circular contours in the normal standard deviation plot. However, it also results in higher deviation values. This effect is similar to the results observed with normal standard deviation response subject to inflation pressure variation, likely due to their both increasing the inflatable's structural rigidity.

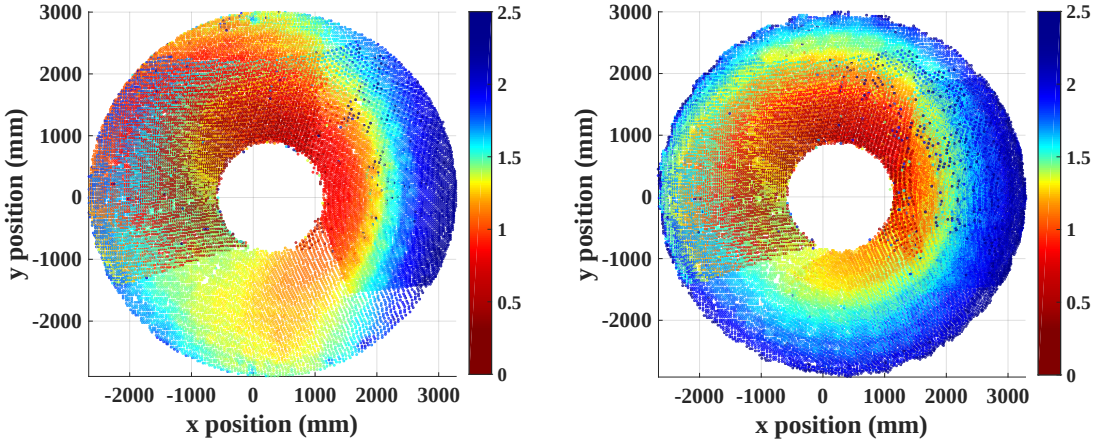


(a) Positional standard deviation of normal deflection for the baseline configuration. (Run at -15° yaw, 40 psf dynamic pressure, $I_3$ inflation pressure)

(b) Positional standard deviation of normal deflection for the tri-tori configuration. (Run at -15° yaw, 40 psf dynamic pressure, $I_3$ inflation pressure)

**Figure 25: Change in the positional standard deviation in the normal direction due to variation in stacked tori configuration**

The addition of the tri-torus also contributes to a slight increase in motion in the tangential direction, seen in Fig. 26. It has limited influence however, on the radial response. Unlike the inflation pressure, which affects the shape of the individual tori cross sections, the tri-torus appears to add primarily deflection support in the normal direction and, as a result, does not interfere with radial motion.

Many of the previous figures exhibit discontinuities in the results in different locations. Figure 14, for example, displays a distinct change in standard deviation along

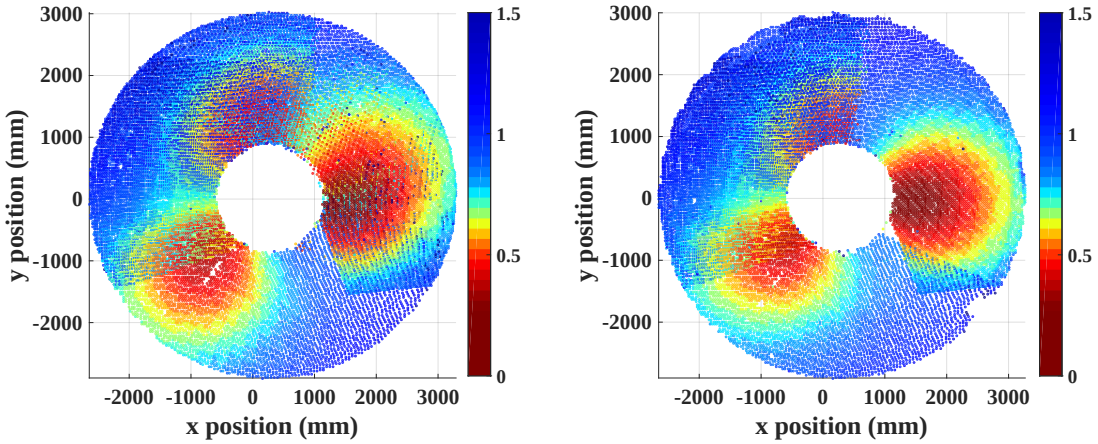


(a) Positional standard deviation of tangential deflection for the baseline configuration. (Run at -15° yaw, 50 psf dynamic pressure, $I_3$ inflation pressure)

(b) Positional standard deviation of tangential deflection for the tri-tori configuration. (Run at -15° yaw, 50 psf dynamic pressure, $I_3$ inflation pressure)

**Figure 26: Change in the positional standard deviation in the tangential direction due to variation in stacked tori configuration**

bands near $y = 2000$, $y = -1000$ and $x = 2000$. These discontinuities correspond to the overlay of images from different camera pairs. The fact that different cameras do not observe the same deviation at their interface could potentially be caused by differing resolutions of each camera pair. All cameras used for photogrammetry had the same sensor and lens setup. Therefore, differences in resolution are a function of distance between the camera and the test article, with the closer cameras having the highest resolution and thus minimizing the error due to uncertain tracking of the stacked tori surface.

This phenomenon is also seen in a different run, tested at 40 $psf$ with a 0° yaw angle and $I_3$ inflation setting. As seen in Fig. 27, the standard deviation in absolute position observed from the wall camera pair is much lower than that observed from the bottom pair. When the two views are stitched together (shown in Fig. 27(c)), the datasets are simply overlaid. Figure 27(b) shows a higher positional standard deviation compared to Fig. 27(a) for points in the same location. This discrepancy matches the hypothesis that the floor camera pair yields a lower resolution relative

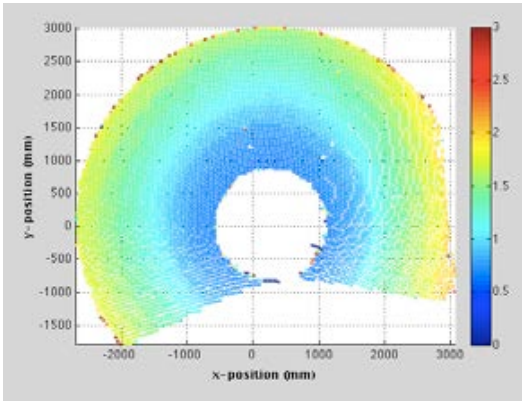


(a) View from wall camera pair

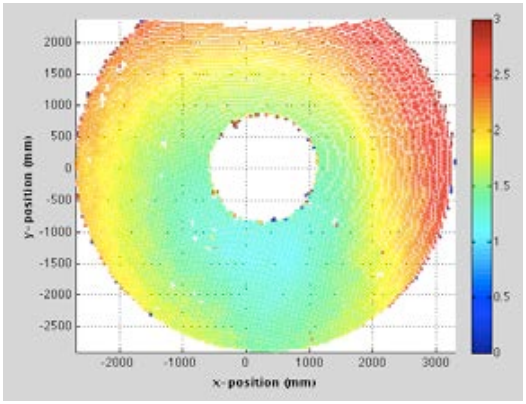


(b) View from bottom (floor) camera pair

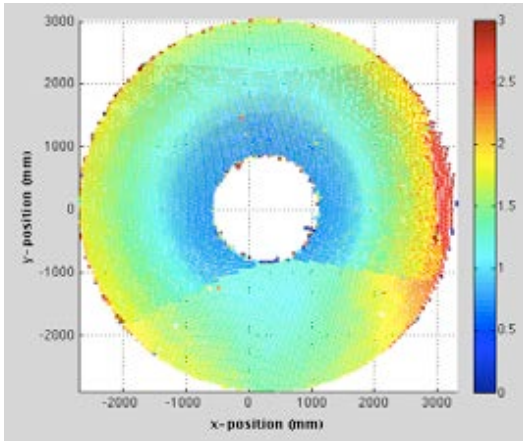


(c) View of overlapping data sets

**Figure 27: Standard deviation of stacked tori photogrammetry data including views from each individual camera**

to the wall pair due to their further distance from the test article. The standard deviation in Fig. 27(a) varies radially while that of Fig. 27(b) varies with radius and y-position. The wall camera pair was mounted at the same height as the stacked tori, so resolution is a weak function of y-position. However, the floor cameras were located below the stacked tori. Therefore, their resolution was highly dependent on the y-position of the tracked points. In this case, the data from the top camera pair has less uncertainty and is expected to portray a more representative measure of the stacked tori oscillation. For a more accurate assessment, the positional uncertainty due to the camera sensing should be evaluated for each point to understand the uncertainty

in the standard deviation measurements presented.

#### *2.4.3.2 Characterization of Stacked Tori Fluid - Structure Coupling*

There is significant interest in describing the vibrational modes of inflatable structures under loading and understanding the coupled response of the structure and surrounding fluid. As a result, analysis is conducted to extract the frequency content of motion from the inflatable surface to identify these phenomena during testing.

In the wind tunnel, aerodynamic loading induces vortex shedding around the test article. This vortex shedding results in a quasi-cyclic forcing that is dependent on the test article geometry and orientation and the instantaneous flow conditions. The inflatable structure can be approximately described as a linear system. Therefore, it is expected to have a set of discrete vibrational resonant frequencies. When forced by a constant cyclic forcing at the resonant frequencies, the inflatable structure oscillations will grow and diverge. When forced by constant cyclic forcing off of the resonant frequency, the structure will oscillate with a reduced amplitude and modulated frequency.

Given that the inflatable structure will undergo significant deflection under load and that the vortex shedding is dependent on the instantaneous geometry of the test article, these two phenomena have a highly complex coupling. In instances where the structural and fluid dynamics interfere with each other, it is expected that the resulting surface motion will be chaotic and unpredictable, without an easily discernible structure. Because this case would result in no definable frequency of structural vibration or forcing, an FFT of the surface position over time would likely look chaotic and noisy. However, in instances where the structural and fluid dynamics constructively coalesce, the resulting surface motion would likely oscillate at a single, or discrete set of frequencies. As a result, an ideal FFT of this case would show distinct, isolated peaks at the resonant frequencies and minimal signal elsewhere.

The frequency analysis is first performed on a single point using its position data over time. For each run, 4 points are chosen along each of the 0° (N), 90° (E), 180° (S), and 270° (W) radial directions. The locations of these points are shown in Fig. 28 as red dots.

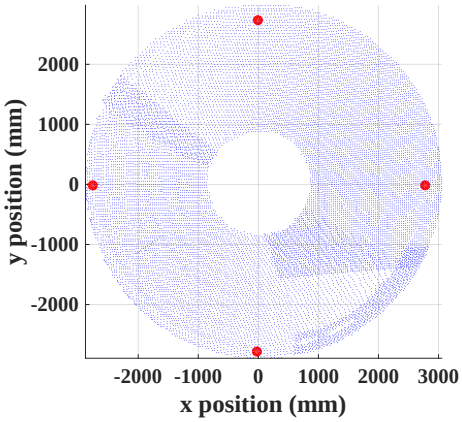


**Figure 28: Locations of points chosen for the FFT analysis**

For each point, a Discrete Fast Fourier Transform is taken of its position over the 150 frames (over time) to determine the frequency content of motion. The FFT results are shown in Figs. 29 and 30 for a run conducted at -25° yaw (IAD nose rotated

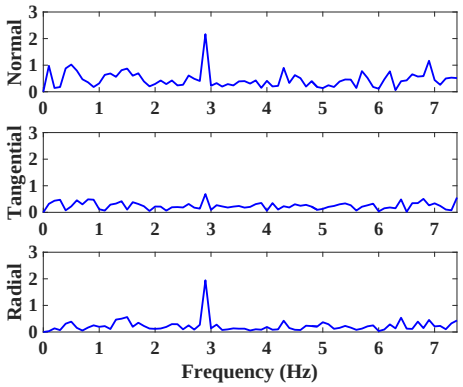


(a) FFT of motion in the normal, tangential, and radial directions of a single point along the 0° radial direction

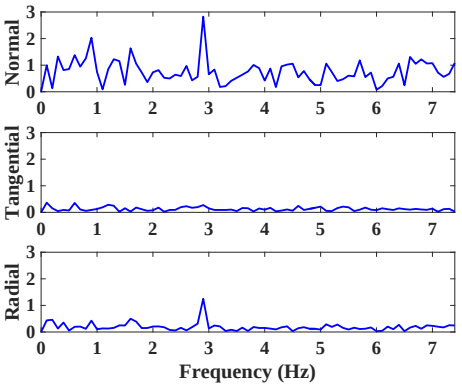


(b) FFT of motion in the normal, tangential, and radial directions of a single point along the 90° radial direction

**Figure 29: FFT of the motion of surface points showing a distinct peak at around 3 Hz (run conducted at -25° yaw, 70 psf dynamic pressure, and $I_3$ inflation pressure)**

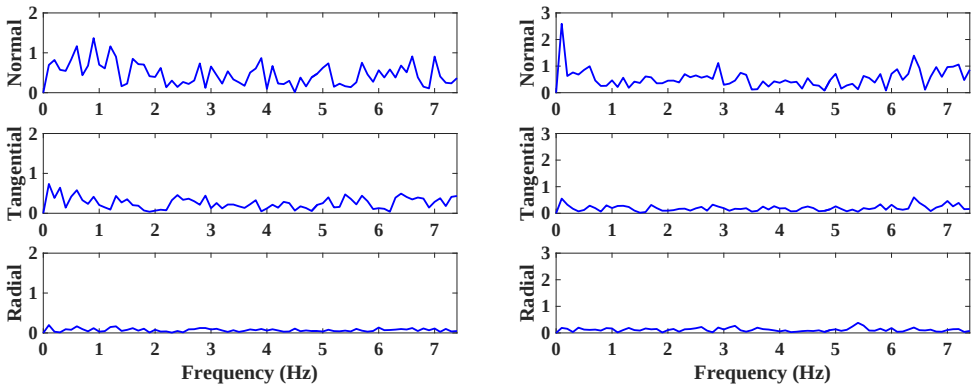


(a) FFT of motion in the normal, tangential, and radial directions of a single point along the 180° radial direction

(b) FFT of motion in the normal, tangential, and radial directions of a single point along the 270° radial direction

**Figure 30: FFT of the motion of surface points without a distinct peak (run conducted at -25° yaw, 70 psf dynamic pressure, and $I_3$ inflation pressure)**

towards the 90° (E) radial), 70 psf inflation pressure, and an $I_3$ inflation setting. A clear peak is seen in the FFT graphs at around 3 Hz for points located along the 0° (N) (Fig. 29(a)) and 90° (E) (Fig. 29(b)) radial directions. Pre-test calculations of the vortex shedding around the inflatable predicted the shedding frequency to be approximately 2-3 $Hz$ [112]. Therefore, this peak is most likely attributed to the aerodynamic forcing on the test article.

The distinct 3 Hz peak is not apparent in the 180° (S) (Fig. 30(a)) or 270° (W) (Fig. 30(b)) plots. Therefore, it appears as if the dynamic coupling is isolated to the upper-right portion of the test article. This is likely due to two phenomena. The first is that this specific run was conducted at a large, -25° yaw angle. As a result, the 270° (W) radial was directed into the flow and the 90° (E) radial was directed away from the flow. As discussed in section 2.4.3.1, when the test article is rotated, the side directed towards the flow experiences higher overall deflection while the side away from the flow experiences higher overall motion. Therefore, at this dynamic pressure, inflation pressure, and local surface orientation, the vibrational response of the inflatable reinforces the vortex shedding around the article on the 90° (E) radial

side and results in a cyclic motion whereas the local surface angle and vibrational response on the 270° (W) side disrupts the periodic forcing. The second phenomenon is likely the influence of the test article sting. As discussed in section 2.4.3.1, regions of reduced motion are observed in the vicinity of the sting. Therefore, it appears that the sting disrupts the vortex shedding along the 180° (S) radial. The combination of these effects causes the axis of coupled fluid-structure vibration to shift toward the 45° (NE) radial direction.

These graphs also confirm the results observed in section 2.4.3.1 on the distribution of motion in the different directions. In both Figs. 29 and 30 the overall vibrational response is dominated by motion in the normal direction. This is to be expected as the inflatable structure is most likely to deflect in the normal direction under load. Nevertheless, the relative magnitude of the tangential and radial response is inconsistent between Fig. 29 and Fig. 30. Figure 29 represents points on the inflatable directed away from the freestream flow. As a result, because the surface is more aligned with the flow, the fluid travels in the radial direction, resulting in a large influence of the vortex shedding on the radial response. Figure 30 represents points on the inflatable directed almost perpendicular to the freestream flow. In these regions the fluid can most easily deflect around the surface in the tangential direction, resulting in a larger response for this coordinate. However, because the cyclic vortex shedding is disrupted on this side, the tangential vibrational response is more dispersed among many frequencies instead of excited at a single frequency as is seen with the radial response in Fig. 29.

Variations in the test parameters are observed to have a significant influence on the fluid-structure coupling. Figure 31 shows the frequency response of points along the 0° (N) radial for a series of tests conducted with different inflation pressures. Figure 31(c) is the run discussed above that exhibits a clear peak at around 3 Hz. Both Figs. 31(a) (reduction in inflation pressure) and 31(b) (increase in inflation

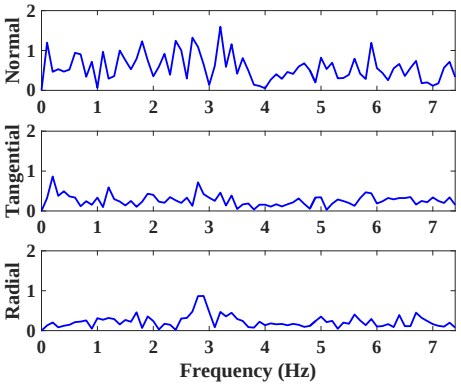


(a) FFT of motion in the normal, tangential, and radial directions of a single point along the 0° radial direction for a run with decreased inflation pressure (run conducted with an $I_4$ inflation setting)

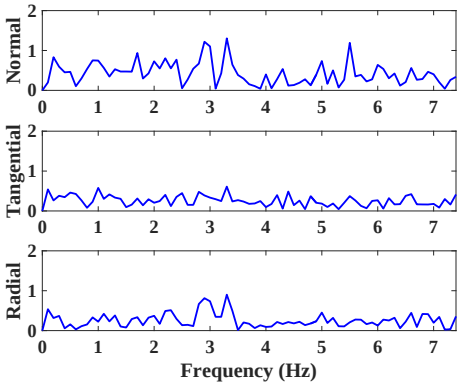


(b) FFT of motion in the normal, tangential, and radial directions of a single point along the 0° radial direction for a run with increased inflation pressure (run conducted with an $I_2$ inflation setting)

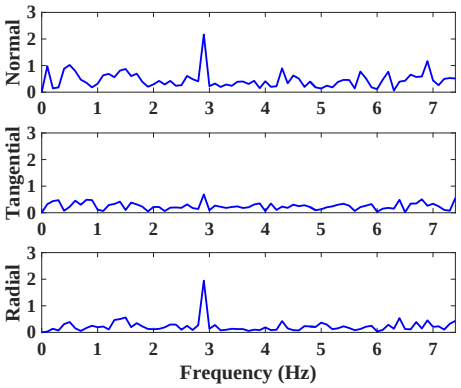


(c) FFT of motion in the normal, tangential, and radial directions of a single point along the 0° radial direction showing a distinct peak around 3 Hz (run conducted with an $I_3$ inflation setting)

**Figure 31: Change in frequency response due to changes in inflation pressure (all runs conducted at -25° yaw and 70 psf dynamic pressure)**

pressure) show approximate peaks in the normal and radial directions around 3 Hz. Both graphs, however, are much more distorted and exhibit normal oscillations both above and below 3 Hz. These same phenomena are evident in the radial response, with the single peak in Fig. 31(c) bifurcating into two peaks distributed around 3 Hz. It is interesting that both a reduction of inflation pressure and increase in inflation pressure result in similar, rather than opposite, responses. The pressure reduction likely lowers the vibrational resonance mode, which would intuitively correspond to a shift in the 3 Hz peak to lower frequencies. The pressure increase likely increases the vibrational resonance mode as well as contributes to a greater coupling between the 90° (E) and 270° (W) sides of the test article, which would intuitively result in the 3 Hz peak shifting to higher frequencies. The fact that these shifts do not occur demonstrates the complexity of fluid-structure interactions for inflatables and the importance of this analysis.

Changes in yaw are also observed to disrupt the fluid-structure coupling. Figure 32 shows the results for the run with a distinct 3 Hz peak discussed above compared to a similar run with 0° yaw. It is evident from the figure that the change in yaw disrupts the cyclic forcing. In the original run conducted at -25° yaw, 70 psf dynamic pressure, and with an $I_3$ inflation setting, the 90° (E) side of the inflatable experiences constructive fluid-structure interactions while the 270° (W) side experiences destructive. The constructive and destructive interference is, in part, due to the relative angle between the inflatable surface and the freestream flow. In this run, the 90° (E) side is nominally at a 35° relative angle to the wind direction while the 270° side is nominally at an 85° relative angle. For the 0° yaw run, both sides are nominally at relative angles of 60°, half-way between the previous 35° and 85°. Given the sensitivity of the coupled oscillations, this large of a relative angle change is expected to disruption the coupling. Similar FFT results are also seen for changes in dynamic pressure, with no clear peak being evident. The variation in dynamic pressure is

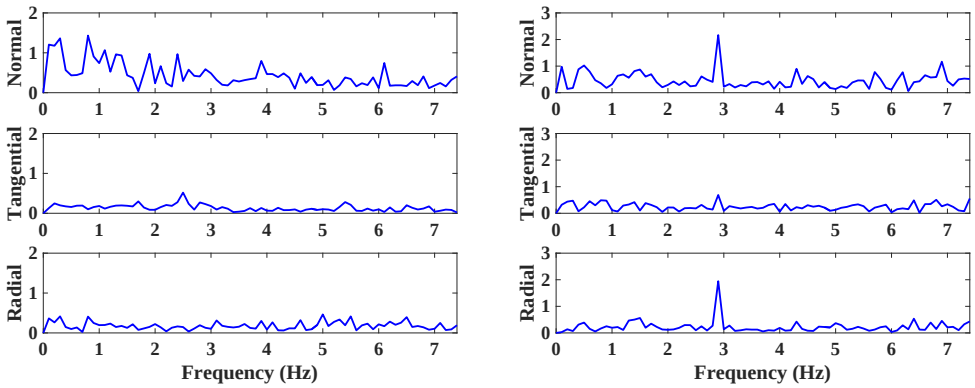


(a) FFT of motion in the normal, tangential, and radial directions of a single point along the 0° radial direction for a run with zero yaw

(b) FFT of motion in the normal, tangential, and radial directions of a single point along the 0° radial direction showing a distinct peak around 3 Hz (run conducted at -25° yaw)

**Figure 32: Change in frequency response due to change in yaw (both runs conducted at 70 psf dynamic pressure with $I_3$ inflation pressure)**

particularly complex because it not only influences the vortex shedding frequency, but also changes the relative angle between the inflatable surface and the wind due to variation in surface deflection.

Two additional analyses are performed to estimate the global frequency response of the stacked tori. Instead of calculating the FFT of the motion of isolated points, the frequency response is calculated for a set of points along characteristic dimensions of the inflatable: radially, along a single radial direction, and azimuthally, along a constant radius circle. Motion of the surface is assessed by comparing the relative response of adjacent points to understand how the motion evolves around the decelerator.

Figure 33 shows the FFT results along the 0° radial direction (+y direction) (points chosen shown in Fig. 33(c)) for the run conducted at -25° yaw, 70 psf dynamic pressure, and with an $I_3$ inflation setting. Figure 33(a) plots the percentage distance away from the nose versus the frequency content of motion. Marker size and color is determined by the amplitude of the signal at that frequency (based on the FFT).

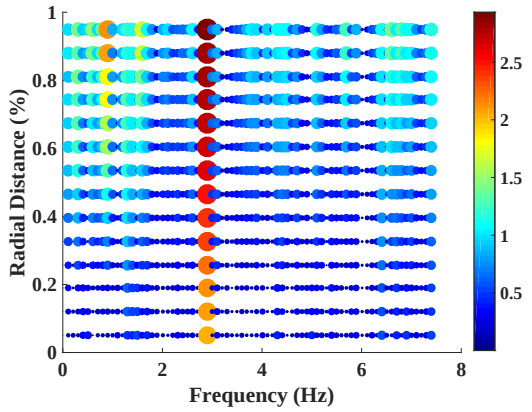


(a) Scatter plot of FFT frequency vs distance along the radial direction with signal amplitude visualized as the marker size and color

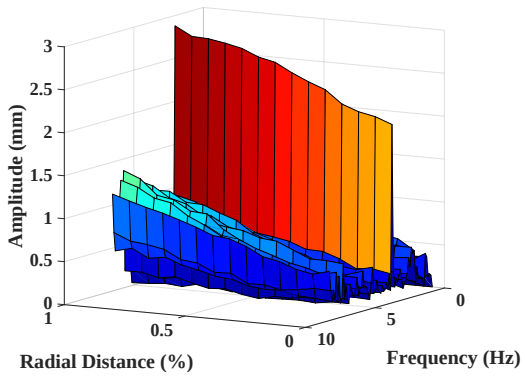


(b) Surface plot of FFT frequency vs distance along the radial direction with signal amplitude visualized as the height along the z-axis

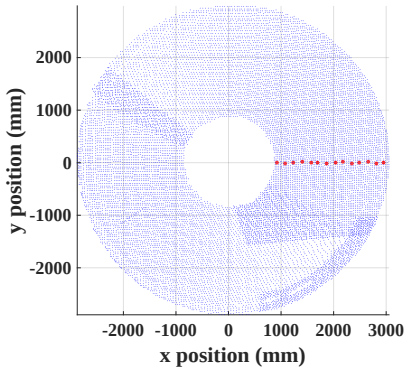


(c) Location of points used for the analysis

**Figure 33: Frequency content of deflection along the 0° radial direction for a run conducted at -25° yaw, 70 psf inflation pressure, and with $I_3$ inflation setting**

The 3 Hz peak is observed in the FFT response of all surface points and all other signal amplitudes appear to be continuous with radial distance (seen in the vertical lines spanning Fig. 33(a)). This shows that each point along the radial direction acts cohesively and oscillates at the same frequency. Figure 33(b) also depicts the oscillation frequency versus distance away from the nose (y and x-axes, respectively), and portrays the amplitude of motion at each frequency on the z-axis. The peak frequencies at each distance away from the nose all align. Furthermore, the amplitude increases while moving outwards from the nose cone so points on the outer tori have

greater displacement than points on inner tori. This indicates that movement along a single radial direction behaves like a rigid rod constrained by the aluminum nose cone.

The motion of the stacked tori along the azimuthal direction is investigated by selecting points distributed uniformly in 10-degree increments near the edge of the test article, all at the same radius (seen in Fig. 34(c)). FFT plots are shown for the run conducted at -25° yaw, 70 psf dynamic pressure, and with an $I_3$ inflation setting. The scatter plot depicts the frequency content of motion for each radial

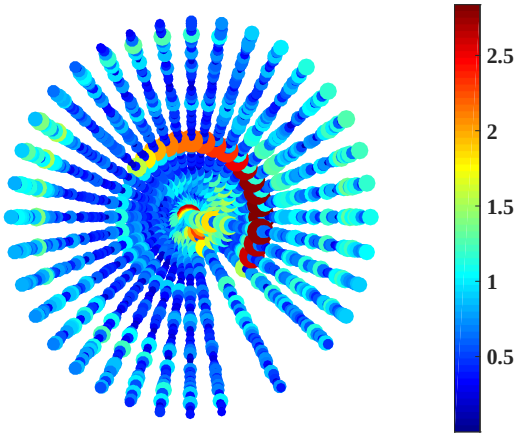


(a) Scatter plot of FFT frequency vs azimuthal angle with signal amplitude visualized as the marker size and color

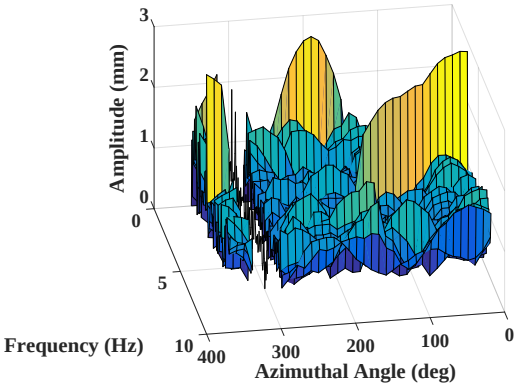


(b) Surface plot of FFT frequency vs azimuthal angle with signal amplitude visualized as the height along the z-axis

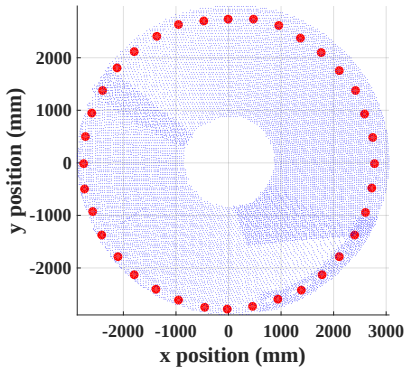


(c) Location of points used for the analysis

**Figure 34: Frequency content of deflection when traveling azimuthally around near the inflatable outer edge for a run conducted at -25° yaw, 70 psf inflation pressure, and with $I_3$ inflation setting**

direction plotted in a polar graph with low frequencies towards the center and higher frequencies found radially outward (Fig. 34(a)). Higher amplitude signals are shown via colors and larger markers. The surface plot also shows frequency content of motion versus azimuthal angle (y and x-axes, respectively) and includes signal amplitude on the z-axis (Fig. 34(b)).

The surface plot in Fig. 34(b) shows a continuous peak at 3 Hz spanning the 300° - 180° azimuthal angles (encompassing 0°). The amplitude is greatest between 0° and 90° and smallest between 180° and 270°, as is observed with the original FFT analysis. However, the other peaks are not as cohesive as in the radial analysis. Therefore, while each radial direction appears to act as a single member, different radial directions appear to move quite chaotically, with both the amplitude and frequency components of the signals shifting as the azimuthal angle travels around the test article. There is also a distinct change in the graph between the 150° and 300° radial directions. When comparing Figs. 34(c) and 34(a), the locations of the discontinuities match with where the camera pair views overlap (denoted by intensity of color in Fig. 34(c)). Therefore, the FFT graphs seem to be continuous for individual camera pairs, but discontinuous in overlapping regions. This is also observed in the standard deviation analysis.

Care must be taken to ensure that the inflatable surface is sampled with sufficient accuracy when conducting the wind tunnel experiments. Accuracy, in this context, refers to both the camera spatial and temporal resolution. For this test campaign, the cameras imaged the surface with a resolution between 6 - 13 pixels/inch, corresponding to a resolution of approximately 2 - 4 mm/pixel [113]. The data processing software, ARAMIS, utilizes subpixel accuracy calculations, which have been demonstrated to improve resolution by up to 100 times [114]. Even with a 10-time resolution increase, the uncertainty in the position measurements would be less than a half millimeter. Figure 35 displays the time history of the normal, tangential, and radial

displacements of a point along the 0° radial for the run conducted at -25° yaw, 70 psf dynamic pressure, and with an $I_3$ inflation pressure. As seen in the figure, the range of displacements vary between 10 and 20 mm. As a result, there is more than an order of magnitude separation between the sample values and their uncertainties, which demonstrates that the measurements are taken with sufficient spatial accuracy.

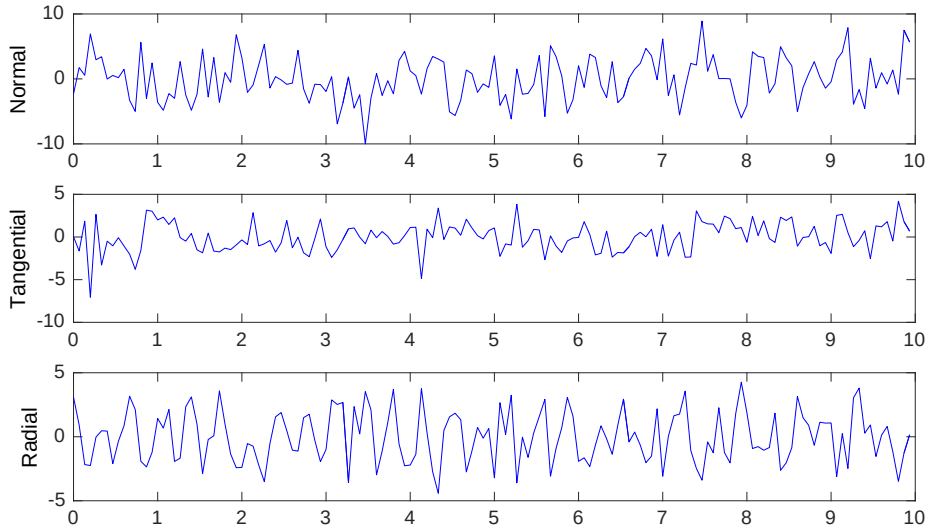


**Figure 35: Time signals of the normal, tangential, and radial displacements of a point along the inflatable 0° radial direction for a run conducted at -25° yaw, 70 psf dynamic pressure. and with $I_3$ inflation pressure**

The photogrammetry cameras also sample data with a 15 $Hz$ temporal resolution. In order for a Discreet Fourier Transform to avoid aliasing of a signal, the sampling frequency must be at least twice that of the highest frequency of that signal [115, 116]. It is expected that the dominant forcing frequency would be due to vortex shedding at approximately 3 Hz, which is less than half of the camera sampling frequency. However, it is possible that oscillations higher than 7.5 Hz did occur. If this did happen, the higher frequency signals would be aliased into the lower frequency data, which could be a contributing factor to some of the noise in the results. Nevertheless, the clear peak near the expected vortex shedding frequency observed during testing lends credibility to the methodology and accuracy of the photogrammetry system.

## *2.5 Summary and Implications*

This investigation explores the ability of photogrammetry to analyze the dynamic response of inflatable structures during ground testing. A data reduction methodology is developed that calculates the positional standard deviation and frequency spectrum of the inflatable surface to allow for characterization of the global surface motion and experimental determination of the structural-fluid coupling. These new analysis routines allow insight into the IAD dynamic characteristics and provide data that has not be previously available for inflatable decelerators. Additional capabilities are developed that also decompose the global motion observed by the photogrammetry system into local surface coordinates. In this way, the IAD dynamic response can be interpreted based on its contribution from each characteristic mode of the system.

These analyses leverage existing ground test program data and are applied to wind tunnel testing of a stacked tori IAD configuration. Motion under a range of configurations and flight environments is assessed, providing insight into the structural response. This information can be used to support high-fidelity structural modeling as a validation case study. Future analyses can incorporate force and moment data to calculate other phenomena such as the dynamic stability of the structure.

Future test programs that wish to employ this methodology should take care to ensure that the photogrammetry system has sufficient spatial and temporal resolution. In this way, the full frequency spectrum of the inflatable surface can be captured. Specific procedures should also be implemented for future test programs dedicated to understanding the fluid-structure coupling of inflatable structures. Given that constructive interference of the vortex shedding and structural vibration is a complex function that is sensitive to all test parameters, each of these parameters needs to be tested with high enough resolution in order to achieve the resonant conditions. Therefore, it is recommended that, for a given decelerator configuration and yaw angle, the dynamic pressure be varied incrementally over a wide range and held

at a constant value for a period of time. It is observed that the coupling is least sensitive to the inflation pressure. Therefore, if it is possible to modulate the inflation pressure in mid-test, this may prove to be a more robust method to isolate resonant conditions. It is also recommended to instrument pressure sensors along many radial directions behind the vehicle to observe the vortex shedding. This may also provide useful information for understanding the forcing frequencies and diagnosing when constructive fluid-structure vibrations are occurring.

# CHAPTER III

# SIMPLIFIED INFLATABLE DECELERATOR MODELING DEVELOPMENT TO ENABLE STRUCTURAL PERFORMANCE CHARACTERIZATION IN CONCEPTUAL DESIGN

## *3.1 Background*

The conceptual design phase is a critical part of the mission development process. In conceptual design, decisions are made concerning the overall vehicle architecture and what decelerator technologies to incorporate. These decisions propagate through the entire mission development process, with changes to the vehicle design become increasingly expensive as the process progresses. Conversely, knowledge of the design increases over time with analysis and study of the proposed architecture. Due to the uncertainties in critical aspects of the design, conceptual design is often reliant on extrapolation or high-level estimation of candidate technology performance due to the lack of existing data in the environments of interest. Without sufficient information, it is difficult to perform successful architecture trades during conceptual design as technology performance can be grossly misunderstood. As a result, techniques that can improve estimates of technology performance during the conceptual design phase, especially for difficult parameters such as structural performance, are invaluable, as they enable more representative assessments of the technologies.

Design space studies are useful tools for exploring technology performance outside of their qualified environments and use-cases. Design studies are able to extrapolate component capabilities while grounding estimates in physics-based simulations such

as finite element analysis. However, design space studies typically require many simulations to establish trends and to properly evaluate system performance across the appropriate ranges of environmental and configurational parameters, which can be prohibitively expensive for high-fidelity, physics-based models.

Representative models of inflatable aerodynamic decelerators, in particular, can be exceedingly complex, involving structural members composed of flexible fabrics stiffened by an inflation gas and complicated strap patterns to constrain the decelerator geometry and distribute external loads. The structural fabrics have nonlinear material properties and are typically stitched or bonded together, with multiple adjacent components simultaneously in contact throughout the entire system. Finite element modeling of inflatable decelerators also involves capturing the large deflections that are characteristic of IAD loading. The combination of the flexible structural fabrics, nonlinear material properties, numerous contact points between multiple components, and the large deflections results in finite element models of inflatables that involve nonlinear solvers, numerous contact sets, and many different components and material properties. This not only leads to computationally expensive models, but often results in non-convergence of the model due to the sensitive coupling of all the component responses.

In order for design space studies of IAD structural performance to be leveraged in conceptual design studies, an FEA model is required that is computationally efficient, flexible enough to geometrically encompass all designs, and which provides robust solutions for all possible sets of configuration parameters. Full fidelity models, tailored to a given design, are not suited to such analysis. Therefore, it is necessary to develop a simplified finite element model, validated against data from the existing traditional designs. The reduction of complexity allows for the rapid solution of the many designs necessary to generate the design space and improves the reliability of the model solutions.

## *3.2 Simplified Stacked Tori Model Validation*

Simplified finite element models are able to rapidly estimate realistic system responses because they remove complexity from full-fidelity models, ignoring or replacing features with simplified approximations. In many instances, the simulated model performance can be sensitive to the implementation of the simplifying substitutions, requiring tuning parameters to adjust the response. Therefore, in order to retain accuracy and ensure confidence in the simulated results, simplified models must be validated against test data. Without a sufficient validation basis, the models cannot be expected to reliably estimate actual system responses and will not be useful for conceptual design space exploration studies.

### 3.2.1 Stacked Tori Validation Data Sets

Stacked tori inflatable decelerators are one of the candidates for landing high mass payloads on Mars and other planets with an atmosphere and are featured in both the NASA Inflatable Reentry Vehicle Experiment (IRVE) and EDL: Systems Analysis study (EDL:SA) [16, 117, 118, 76, 77]. Being a relatively new and more complicated design, there are few literature studies developing analytical structural models of stacked tori decelerators. Nevertheless, some test data sets are available of stacked tori IADs, which can be used to validate simplified numerical models. These test datasets include the NASA Inflatable Reentry Vehicle Experiment and HIAD test programs of the last decade. In particular, the NFAC wind tunnel and static load test programs, which utilized photogrammetry in conjunction with an instrumented test article, are useful for this validation effort [16, 117, 118]. Despite only a fraction of the data being available at this time, the compilation of the multiple data sets allows for a robust validation of the simplified stacked tori finite element model.

#### *3.2.1.1 Validation Data Set: HIAD Static Load Test Program*

The static load test program was one of the ground test efforts conducted by the NASA HIAD team to demonstrate the structural integrity of stacked tori IADs under various loading conditions [118]. Testing was performed on full scale articles, which were supported by their nose cone and placed in an air-tight tub and vacuum bag, seen in Fig. 36. During testing, a partial vacuum was pulled on the underside (leeward side) of the test article to apply a uniform, static load across the outer (windward) surface that approximates the aerodynamic loading experienced during reentry. This form of testing is advantageous because it is relatively inexpensive and can elucidate the static structural response of the decelerator under various loading conditions.

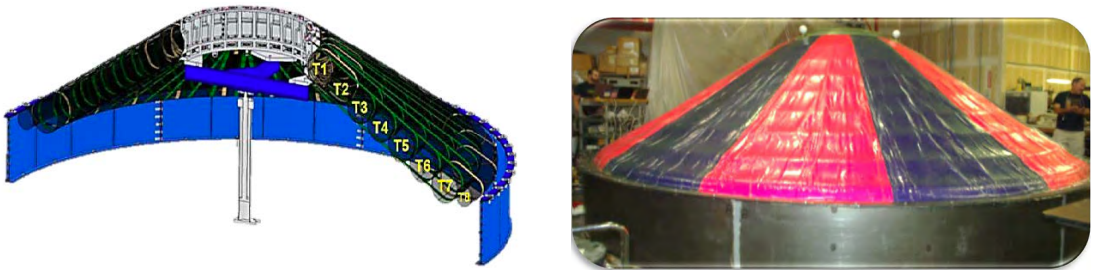


(a) Cross section depiction of installed test article [118]

(b) Test article in air-tight tub with vacuum bag [118]

**Figure 36: Setup of the static load test**

The test instrumentation suite involved both global and point-wise sensors. A laser scanner was used to image the entire outer surface and determine the post-inflation test article shape and post-loading deformed shape. Point-wise measurements of the axial deflection were also taken using a string pot located on the underside of torus T7, shown as a blue circle in Fig. 37. Loads carried by the radial strap were measured with a load pin placed at the interface to the mock nose cone, depicted by the red circle in Fig. 37. A ram loadcell was included in the nose cone support to measure the total applied load. The global laser scanning allows for an accurate characterization of the HIAD shape for use in generating the finite element model geometry and the

high-fidelity deflection and load data allow for precise, scalar calibration data to use in model validation.

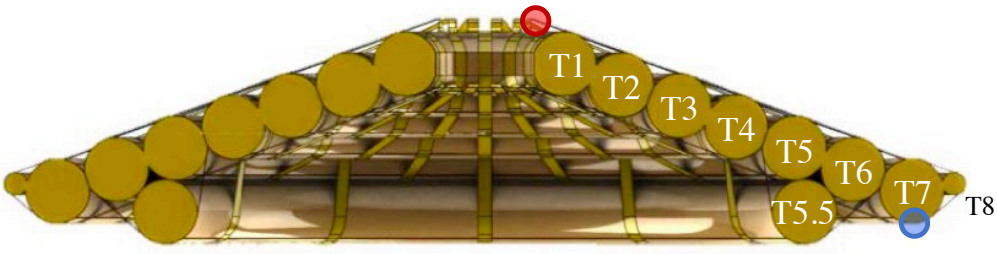


**Figure 37: Instrumentation locations for static load test. Blue circle is location of string pot displacement sensor and red circle is location of load pin radial strap force sensor. Image shown is for instrumentation location information only and depicts an alternate stacked tori design with an additional "tri-torus" (T5.5) that is not used in this analysis.** [118]

Two separate static load test programs were conducted, the first with a 6.0 m, 60° half-cone angle test article and the second with a 3.7 m, 70° half-cone angle article with newer, higher performant materials. Data from the 6.0 m test series is not accessible however, a subset of the data from the second-generation 3.7 m test series is available for articles with 10, 12, and 15 psi inflation pressures, allowing for a direct comparison of the inflation pressure effects.

#### *3.2.1.2 Validation Data Set: HIAD Wind Tunnel Ground Test Program*

The second validation data set used by the simplified model is the NFAC wind tunnel ground test program, introduced in section 2.4. The NFAC wind tunnel testing involved placing a stacked tori decelerator in a subsonic freestream flow to measure its structural response. Photogrammetric imaging of the test article under load is available from this test series, characterizing the deformed shape of the entire HIAD windward surface. The global deflection test data provides unique insight and fills gaps in the static load test validation data, which is otherwise limited to validating deflection at a single point. More so than just providing deflection information along the entire HIAD, being able to validate the shape of the windward surface is much

more valuable than a point-wise deflection measurement on the aft-side of a single torus, as the windward surface determines the decelerator aerodynamic performance.

The NFAC wind tunnel test was performed using a 6.0 m, 60° test article with an older iteration of the inflatable structure materials. The 3.7 m static load testing instead employed a 70° half-cone angle and the newest iteration of structural fabrics with improved structural and thermal material properties. The simplified model developed in this thesis also utilizes the current-generation material properties. As a result, the NFAC wind tunnel testing is useful for qualitative validation of the simplified model deflected shape, but is somewhat less applicable for specific tailoring of model parameters.

### 3.2.2 Reference High Fidelity Finite Element Analysis Models

Unpublished high-fidelity stacked tori models have been generated as part of the NASA HIAD technology advancement program [108]. These models simulate the inflatable tori, pairing loop straps constraining adjacent tori, and radial and chevron straps distributing the load from the outer tori to the nose cone, all shown in Fig. 38. These models also simulate contact between adjacent components to allow for the tori and straps to shift under load. To reduce computational expense, the high-fidelity FEA model leverages the symmetry of the tori and strap pattern to simulate a smaller wedge section.

The high-fidelity models were developed and validated based on the static load test data from Section 3.2.1.1 and were also extrapolated to 6.0 m and 12.0 m base diameter decelerators. Therefore, the high fidelity stacked tori models can also serve as a validation data set that can fill in the gaps in the static load and wind tunnel ground test data and allow for better tailoring of the simplified model at different decelerator scales.

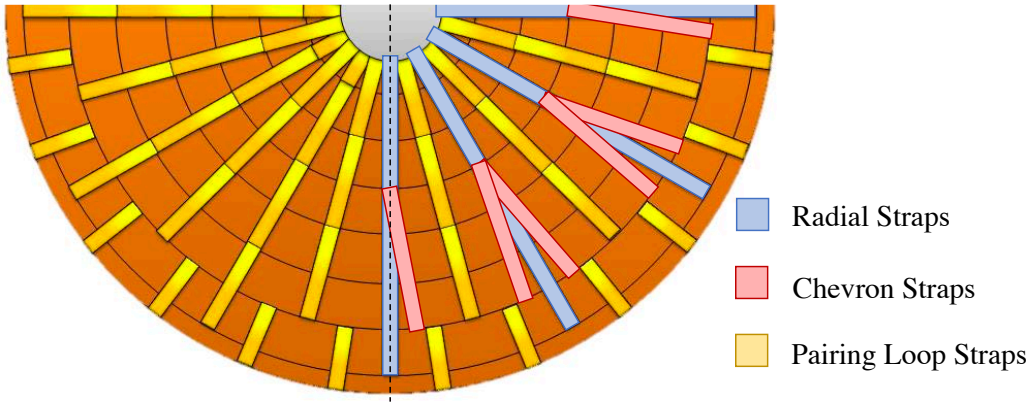


**Figure 38: HIAD test article strap pattern depicting the pairing loop, radial, and chevron strap configuration [118].**

The high-fidelity models have solutions for multiple geometries and loading conditions. 6.0 m, 70° half-cone angle, 15 psi inflation pressure and 12.0 m, 70° half-cone angle, 20 psi inflation pressure models are available at various, uniform-pressure aerodynamic loads. The models provide information on the predicted global deflected shape. However, like the simplified model developed in this thesis, the high-fidelity models were validated solely based on the static load test deflection data from the string pot located on T7 and the radial strap loading from the load pin located near the centerbody. Therefore, only the T7 deflection data from these models is used as a validation metric for the simplified model.

### 3.2.3 Simplified Stacked Tori Validation Model Development

The simplified stacked tori validation model, shown in Fig. 39, is based on the high fidelity FEA model discussed in Section 3.2.2. The geometry of both models mirrors the static load test HIAD, the most recent stacked tori configuration as of the writing of this thesis and the basis of the vast majority of available test data. The models are designed to the as-built geometry of the 3.7 m static load test article to minimize potential sources of deviation. The as-build geometry is determined from laser scans of the entire static load test article surface following inflation, which was synthesized into the geometric design parameters such as the tori center locations, structural and

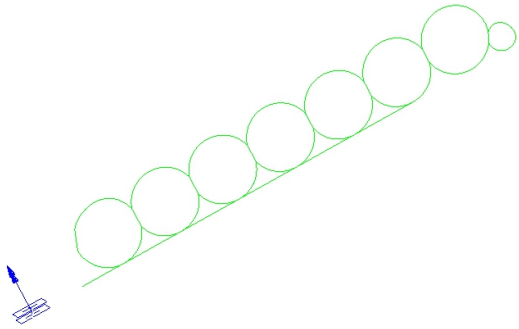

(a) Simplified stacked tori model cross section

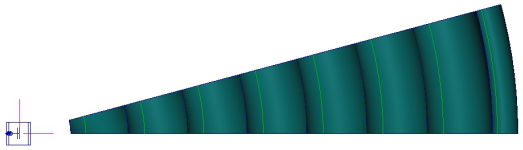

(b) Simplified stacked tori model cross section revolved around axis of symmetry to generate wedge model

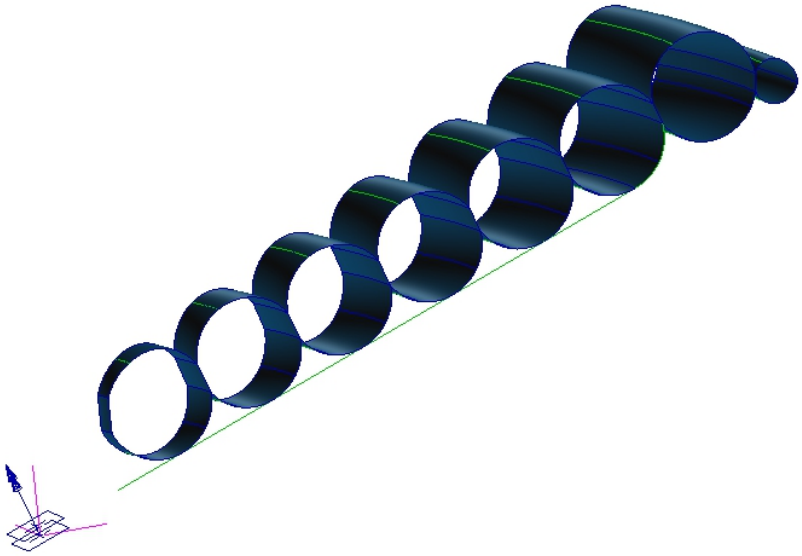

(c) Simplified stacked tori wedge model

**Figure 39: Generation of the simplified finite element stacked tori model geometry. Image shown is of a 3.7 m, 70° configuration with 7 structural tori and 1 shoulder torus**

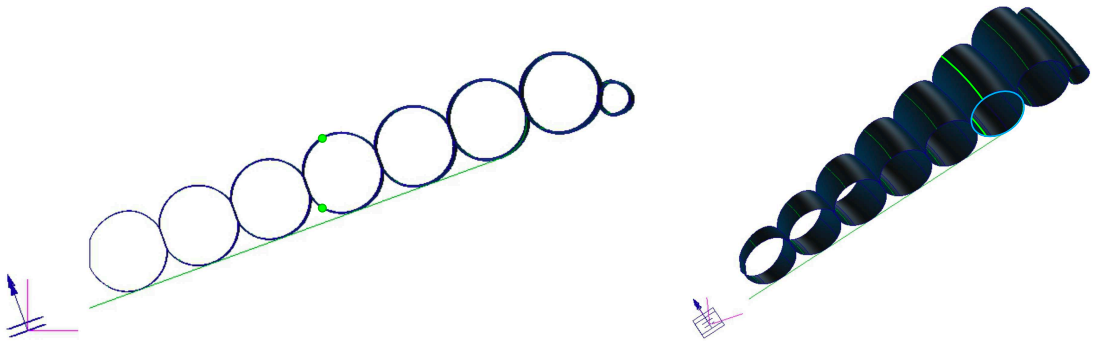

(a) Location of the cords in the stacked tori model 2D cross-section. Cord locations are depicted by green circles.

(b) Location of the cords in the full 3D stacked tori wedge model. Cord locations are depicted by green lines.

**Figure 40: Simplified finite element stacked tori model showing cord locations**

shoulder tori major and minor radii, and tori overlap lengths. The simplified model also utilizes the same material properties as the high-fidelity model, those properties being determined from structural testing of the inflatable fabrics.

The simplified model emulates the high-fidelity FEA modeling in most aspects and strategically simplifies certain aspects of the model to reduce computational complexity and cost. As a result, the majority of simulated components, boundary conditions, and load cases are retained from the high-fidelity model. The simplified model is, therefore, intended to reproduce high-fidelity simulation results with significant reductions to computational complexity. Specific model features and deviations from the high-fidelity model are explicitly addressed in the following discussion.

#### *3.2.3.1 Simplified Stacked Tori Validation Model: Geometry*

The simplified stacked tori model is first constructed by generating the cross-sectional profile. The cross section, seen in Fig. 39(a), is composed of seven structural tori ($T_1$ - $T_7$) and one shoulder torus. The first torus is flat on the inside surface to represent the interaction with the central nose cone. Cords are also incorporated into the tori models and help to distribute the stresses generated from inflation loads and maintain

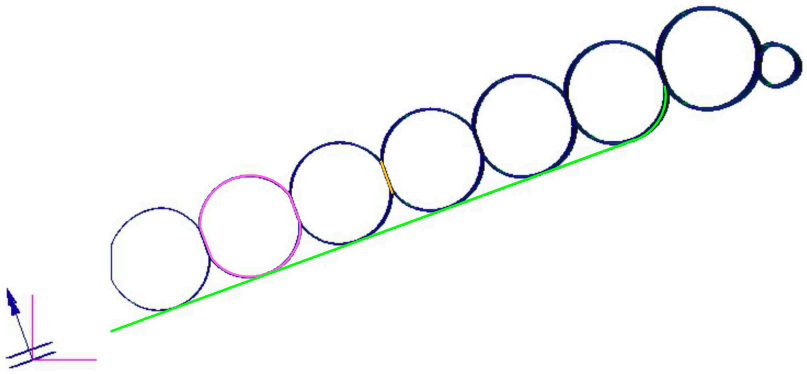

**Figure 41: 2D section of the simplified stacked tori model, showing the cross section along the 0° radial. An example torus is indicated by the pink line and an example spar is indicated by the orange line. The radial strap is the green line along the bottom of the model, extending around the $6^{th}$ torus.**

the torus shape. The cords run along the inner major circumference at ±60° from the horizontal. In the FEA model cross section, the cords are represented as discrete points on the line representing the tori surface cross section. After revolving the cross section, the cords are resolved as lines traveling along the major circumference, as seen in Fig. 40. Cords are modeled with representative material properties. The final component, the radial strap, attaches to the nose cone below $T_1$ and travels parallel to the IAD front surface until it attaches to and wraps around $T_6$, as seen in Fig. 41. The radial strap continues around $T_6$ until the intersection between $T_6$ and $T_7$. While it is tangent to all the tori, the radial strap is only attached to $T_6$, being free to separate from the tangency points of all other tori.

Like the high-fidelity model, the simplified stacked tori model reduces computational expense by exploiting symmetry and simulating a wedge section instead of a full decelerator. Except for the radial strap, all the stacked tori model components are axisymmetric. The radial strap pattern is 12-fold rotationally symmetric, because the static load test article configuration has 12 discrete radial straps, with the 12 wedges defined between adjacent pairs of straps each exhibiting planar symmetry about their centerline. As a result, the simplified stacked tori validation model utilizes a wedge

section of 15°. This wedge section, shown in Figs. 39(b) and 39(c), is generated by revolving all components, except for the radial strap, in the aforementioned cross section about the central axis.

#### *3.2.3.2 Simplified Stacked Tori Validation Model: Boundary Conditions*

In free flight, the only constraint on the inflatable decelerator is through contact with the reentry vehicle body. In the static load test program, the radial strap was constrained to the test article nose cone via a pin, as seen in Fig. 42(b). The tori were not directly attached to the nose cone themselves but were firmly secured by pairing loop straps that traveled around the first torus and were attached to the nose cone on both sides, similar to the radial strap. The pairing loop straps forced the torus into its housing on the nose cone, with friction counteracting movement of the torus relative to the nose cone.

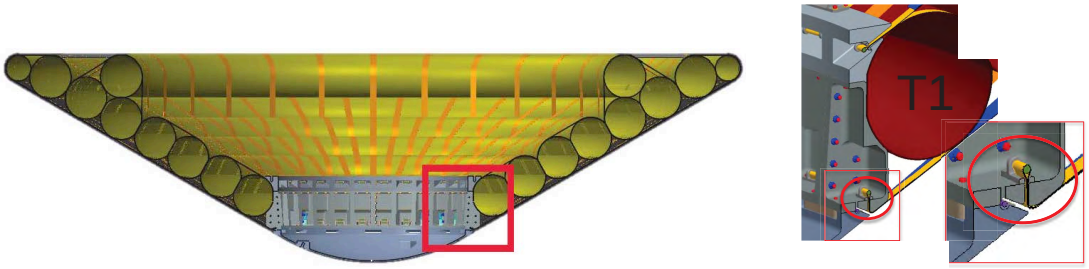


(a) Static load test centerbody attachment region [117]. Note that the configuration shown is the alternate tri-torus design with an additional torus between $T_6$ and $T_7$

(b) Static load test centerbody attachment mechanism [117]

**Figure 42: Static load test centerbody attachment**

The simplified stacked tori validation model uses fixed boundary conditions, with all six degrees of freedom set to zero, to approximate the centerbody attachment of the tori and radial strap. Seen in Figs. 43(c) and 43(d), the fixed boundary conditions are applied to the flat inner surface of the first torus, which simulates the direct contact with the centerbody, and the endpoint of the radial strap. Based on the static load test documentation, it looks possible for the first torus to be in

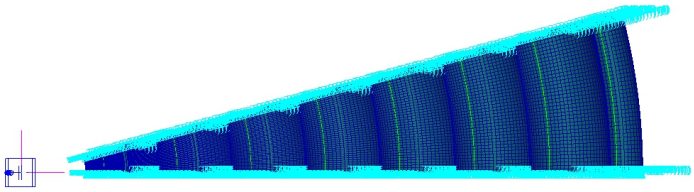

(a) Simplified stacked tori model symmetry boundary conditions

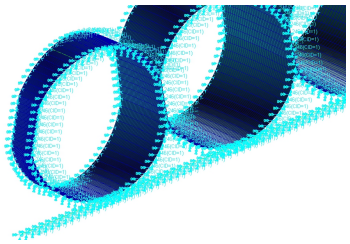

(b) Simplified stacked tori model symmetry boundary conditions close-up

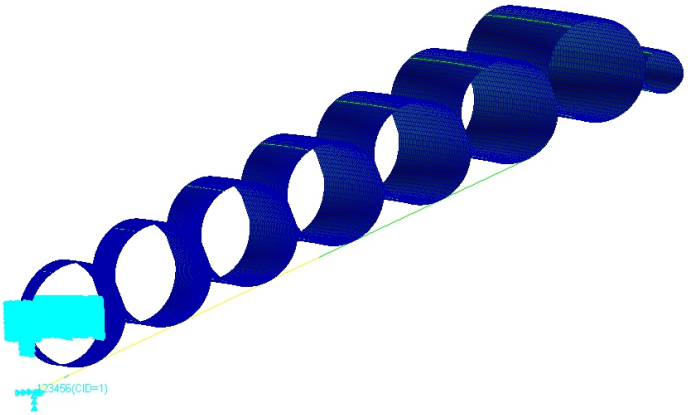


(c) Simplified stacked tori model fixed boundary conditions

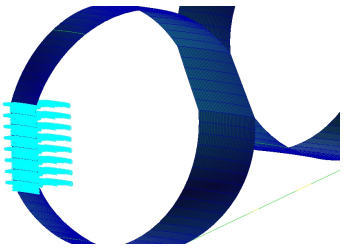

(d) Simplified stacked tori model fixed boundary conditions close-up

**Figure 43: Simplified stacked tori model boundary conditions**

constant contact, or to be able to make contact, with the sidewalls of the nose cone housing throughout the test. However, in order to mirror the boundary conditions implemented by the high-fidelity stacked tori model, these interactions are ignored and, except for the fixed boundary condition surface, the torus is free to deform as necessary. Given the proximity to the imposed boundary conditions, the error due to this assumption is expected to be negligible. The radial strap's translation and rotation are similarly constrained in all directions. Seen in Fig. 39(a), the radial strap is modeled to terminate directly underneath the flat inner surface of the first torus. This termination location approximately corresponds to the region where the strap contacts the nose cone, immediately prior to the bend and attachment to the pin. While the nose cone contact does not fully constrain rotation of the radial strap, any deformation of the strap under load is expected to be in the direction of reducing the decelerator cone angle, in which case the nose cone would locally constrain the strap rotation. Again, due to uncertainty in the nose cone design, the contact distance between the nose cone and radial strap and associated friction is ignored in the simplified model and is instead incorporated into the fixed boundary condition assumption.

The second set of boundary conditions used in the simplified model are symmetry boundary conditions on the 0° and 15° cross sections, seen in Figs. 43(a) and 43(b). The symmetry boundary conditions constrain the nodal translation in the azimuthal direction and rotation in the decelerator axial and radial directions (a cylindrical coordinate system is used for the finite element analysis) and are required when using symmetry to simplify a model.

#### *3.2.3.3 Simplified Stacked Tori Validation Model: Model Simplification*

The simplified model reduces the high-fidelity stacked tori design complexity by eliminating the pairing loop straps, described in Fig. 38, that are used to constrain

adjacent tori. Instead, adjacent tori are bonded together. In the simplified model, the tori interfaces, herein referred to as spars and highlighted in orange in Fig. 41, are geometrically designed into the model as a single piece of material with double thickness. It is important to note that directly bonding tori is also performed in current stacked tori test articles design, which uses a resin to glue adjacent tori as a supplementary measure for securing them together. Eliminating the pairing loop straps from the model drastically reduces the complexity, removing over two thirds of the total individual components. It also decouples the finite element model design from stacked tori test article design and allows the model to generate new stacked tori configurations without having to develop unique strap patterns for each.

Equally as important as the reduction in the total number of modeled components is the reduction in the complexity of the physics simulated by the simplified finite element model. The simplified model eliminates simulated contact between adjacent components, instead bonding all adjacent surfaces together. Contact is expensive to simulate with finite element models, requiring an accurate characterization of each individual surface in addition to the interactions between them. Bonded surfaces remove two of these aspects, requiring only the simulation of a single, conjoined surface. Contact is especially expensive for models involving flexible fabrics, as they can experience significant deformation, potentially interacting with many adjacent components across significant distances. For example, for a wedge model of the static load test model seen in Figs. 36 and 38, a single torus could be in contact with the two adjacent tori contacting its entire major circumference, 4 different pairing loop straps contacting up to half of its cross sectional circumference, 2 chevron straps contacting a quarter of its cross sectional circumference, and 1 radial strap contacting a quarter of its cross sectional circumference. This corresponds to as many as nine unique contact sets active over significant distances for each individual torus. An equally large number of contact sets would also exist between adjacent radial

and pairing loops straps, which overlap. The accounting and simulation of all these potential interactions is prohibitively expensive for models that are intended for design space exploration, with overall complexity growing exponentially with increase in decelerator scale.

To compensate for the removal of the pairing loop straps and the associated loss of stiffness, the simplified model instead increases the thickness of the torus structural fabric. In the finite element model, the tori fabric is modeled with shell elements. Therefore, the thickness is a convenient parameter to control as it does not physically manifest itself in the model and is, instead, a scaling parameter on the mathematical element formulation, influencing the stiffness and other properties.

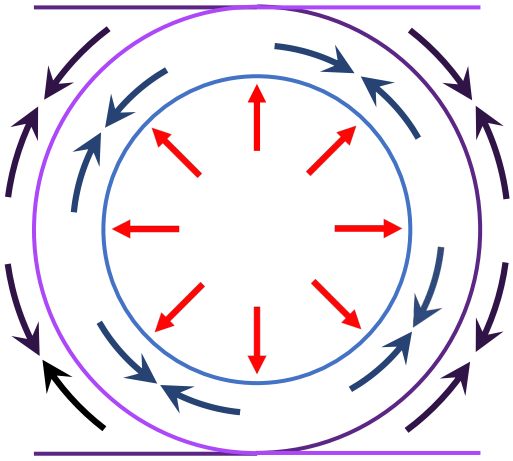

**Figure 44: Diagram of the cross section of a single torus, depicting the torus fabric (blue) and pairing loop straps (purple) along with forces from the inflation gas pressure (red), tori fabric stress (dark blue), and pairing loop strap stress (dark purple). Note that two pairing loop straps interact with a single torus, each over half of its minor circumference.**

Conceptually, this substitution is intuitive. Consider the cross section of a single torus and strap system shown in Fig. 44. Note that a single torus interacts with two pairing loop straps (shown in light and medium purple), each contacting half of the minor circumference of the torus, that combine to restrain the full minor circumference. In this example, the set of pairing loops is considered as a single strap

for simplicity, ignoring the extra length between adjacent tori. During inflation, the final torus shape is the resultant of the interactions between the gas pressure and the pairing loop strap and torus fabric material stiffness. The gas pressure acts to uniformly increase the minor diameter of the torus whereas the stress in the torus fabric and straps acts to counteract the change in minor diameter. Any increase in the torus size results in an increase in length of both the torus fabric and pairing loop straps, generating a corresponding axial stress. The effects of the torus fabric and pairing loop straps can be simplified into a linear system of two parallel springs, one representing each component, with the total load equal to the sum of the loads in each spring. Because the pairing loop straps resist the increase in diameter in the same manner as the torus structural fabric, through an axial stress in the material, the pairing loop straps can be replaced with a corresponding increase in resistance generated by the torus fabric. In the spring example, the two-spring system can be replaced by a single spring of increased stiffness. In the simplified finite element model, the increased stiffness is developed by increasing the thickness of the torus structural fabric.

Analysis of the pairing loop strap replacement in a decelerator model subject to aerodynamic loading is fundamentally the same as the case of inflation loading. However, because the aerodynamic load is external and asymmetric, the discussion requires an evaluation of the entire inflatable surface rather than an isolated torus. Consider the diagram of the inflatable cross section shown in Fig. 45. The diagram separates out components on the windward (green) and leeward (blue) sides but groups components on a single side. Deformation, or bending, of the IAD cross section due to aerodynamic loading results in an elongation of the windward side of the decelerator relative to the leeward. The components on each side can again be simplified into a single linear spring model, similar to the inflation model. Because both the torus fabric and the pairing loop straps resist overall IAD deformation

through an axial stress generated in the material, the stiffness of the pairing loop straps can be replaced by an increased stiffness in the torus structural fabric. In the simplified finite element model, the increased stiffness is developed through an increase in torus fabric thickness.

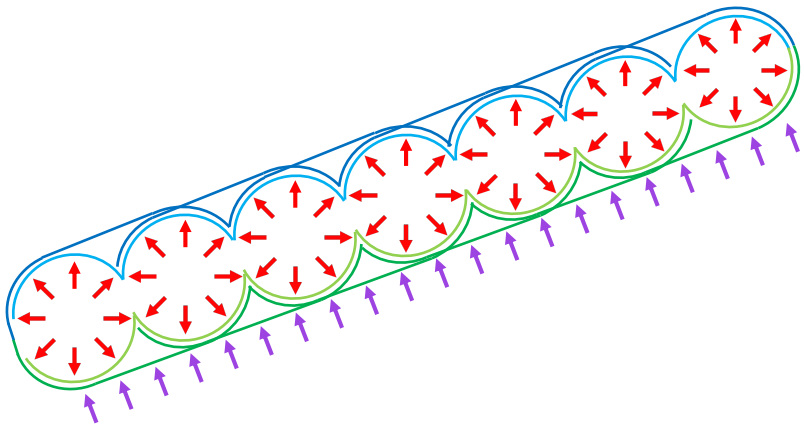

**Figure 45: Diagram of the cross section of the inflatable decelerator, depicting components on the windward (green) and leeward (blue) sides including the torus fabric (light blue/green) and pairing loop straps (dark blue/green) along with forces from the inflation gas pressure (red) and aerodynamic pressure (purple).**

It is assumed in this analysis that the effects of the torus fabric and strap bending stiffness can be ignored. Given that both the components are composed of moderately flexible fabrics, it is reasonable to expect that their bending stiffness is much smaller than their axial stiffness, which scales linearly with thickness. By replacing the stiffness of the discreet pairing loop straps with an increased in the thickness of the axisymmetric torus fabric, the impact of the pairing loop straps is also averaged over the entire torus surface. As a result, the deformation results will be somewhat homogenized across the entire wedge model. However, pairing loop strap patterns are design to approximate a uniform load between adjacent tori and should be dense enough that the homogenization should result in a small error.

The scaling of the torus structural fabric thickness allows the simplified model to reduce complexity and simplify the high-fidelity stacked tori model. The thickness

therefore becomes a tuning parameter used by the model. Each unique stacked tori decelerator configuration contains a different pairing loop strap pattern and, thus, will have a different equivalent torus fabric thickness. As a result, part of the simplified model verification process involves determining the equivalent thickness for each configuration as well as modeling a correlation between the stacked tori decelerator design parameters and the resulting thickness values.

#### *3.2.3.4 Simplified Stacked Tori Validation Model: Loading*

The load cases for the simplified validation model are the same as for the high-fidelity model and mirror both the loading steps of the static load test and an actual flight sequence, which involves tori inflation exoatmospherically under no external load followed by the application of the aerodynamic load. The inflation pressure load is applied to the interior of all tori surfaces, depicted in light blue in Fig. 46(a). No inflation pressure is applied to the spars between tori because all the load cases simulated involve uniform pressure applied to all tori. As such, the pressure load on each side of the spar cancels out. Removing the canceling loads is computationally efficient and improves the model robustness, avoiding uneven loading developing on the spar due to small errors in the direction of the applied pressure loads when the model undergoes large displacements. The inflation load is similarly unnecessary on the $T_1$ surface in contact with the centerbody due to the fixed boundary conditions applied to these nodes.

After application of the inflation load, the aerodynamic load is applied to the external, windward surfaces of the tori, shown in light green in Fig. 46(b). The simplified model implements the aerodynamic load as a pressure with a magnitude determined by the total load on decelerator, as measured by the ram load cell in the static load test, divided by the surface area of all aerodynamic-loaded surfaces. The aerodynamic load is applied on the bottom 20% of the tori surfaces, defined as any

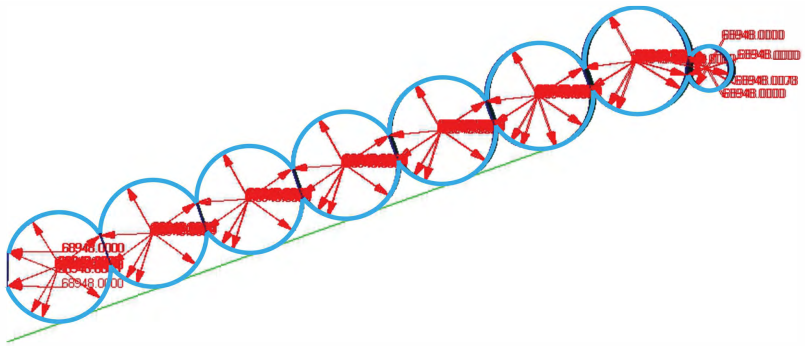

(a) Simplified stacked tori model subject to inflation pressure loading. Inflation load is applied to the interior of the curves highlighted in light blue.

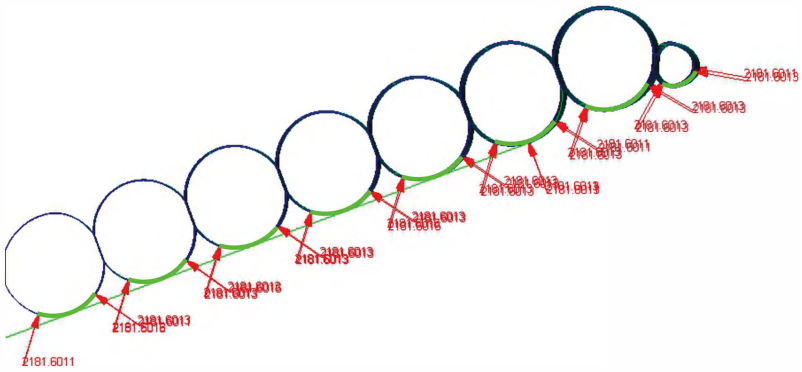

(b) Simplified stacked tori model subject to aerodynamic pressure loading. Aerodynamic load is applied to the exterior of the curves highlighted in light green.

**Figure 46: Simplified stacked tori model loading**

point with a height less than 0.2*$D_{torus}$ from the windward apex of the circular cross-section. The aerodynamic load is not applied to the entire windward surface because stacked tori decelerator flight hardware is typically fitted with an aerodynamic cover and thermal protection system, or vacuum bag in the case of the static load test, that distribute the load over the tori. The actual percentage of the tori that is loaded by the cover is uncertain but is estimated to be around 20% based on the input of subject matter experts. Above 20% is also the region where the tori surface normals increasingly point towards each other and cancel out rather than contribute to overall IAD surface deflection. Nevertheless, exploratory simulations of the simplified model show the overall response of the decelerator to be relatively insensitive to

the percentage of the tori surface subject to aerodynamic loading due to the total aerodynamic load being normalized over the actively loaded surface area. Overall, a total variation in deflection of around 10% is observed across the range of applicable loading regions (0.12*$D_{torus}$ to 0.3*$D_{torus}$).

The stacked tori geometry used to generate the finite element models is based on laser scans of the inflated static load test article. In order to account for the fact that the initial, unloaded geometry of the simplified validation model is defined by the inflation pressure loaded static load test article, an additional load case is included in both the high-fidelity and simplified finite element models between the inflation pressure and aerodynamic pressure load cases to force the IAD back to its original shape following inflation, which is the same as the static load test's inflated shape. It is observed that the inflation pressure tends to cause the stacked tori to deflect outwards (increase in cone angle). Therefore, the additional load case is used to counteract the inflation pressure deflection and bring the IAD surface back to the original location. This is implemented by specifying a thermal expansion coefficient for the tori cords that run along the inside circumference of each torus, shown in Fig. 40, and a reduction in the FEA model temperature to contract the cords and create an inward deflection of equal and opposite magnitude. The temperature drop is adjusted for each validation case such that the HIAD surface returns to the initial geometry following both the inflation and temperature loading steps. The last load case, the aerodynamic pressure loading, is applied to the simplified model after the temperature loading step.

During model validation, the implementation of the additional temperature stress step is evaluated to understand whether it artificially influences the final deflection results. Residual errors in the simplified model surface between the initial geometry and temperature loading steps are observed to be negligible, being greater than two orders of magnitude smaller than the final, aerodynamic loaded deflections. The fact

that the temperature loading is only applied to the cords, such that they support the majority of the load restraining the tori expansion, or cone angle increase, also conforms to real-life physics and design intent, where the torus cords are designed to resist in-plane expansion from the inflation pressure and the torus structural fabric is intended to resist increases in the torus cross sectional dimensions.

### 3.2.4 Simplified Stacked Tori Model Validation Results

Validation of simplified models is necessary to gain confidence in the model's ability to simulate the relevant physics and in the assumption made during model development. A number of assumptions and simplifications are made in the development of the simplified stacked tori validation model: most notably the removal of the pairing loop straps and modulation of the tori structural fabric thickness but also the elimination of contact modeling, the introduction of a temperature loading step, and the specific application of the aerodynamic loading. Therefore, validation of the model serves to demonstrate that the model assumptions do not introduce unacceptable error and to understand the model tuning parameters, such as the tori structural thickness.

#### *3.2.4.1 Simplified Stacked Tori Validation Model: Validation Metrics*

IADs are composed of thin, flexible fabrics stiffened by an inflation pressure and are typically characterized by large deflections compared to rigid structures. Nevertheless, IADs are expected to maintain their shape when subject to the large aerodynamic forces during entry. Therefore, the primary metric for structural performance considered in this thesis is the IAD surface deflection under load, as it has large implications on decelerator selection during conceptual design.

The static load test, the most relevant and complete data set available, utilized a convenient test sensor for measuring the IAD deflection under load. This test incorporated a string pot mounted to the aft apex of $T_7$ to measure displacement of the torus with high accuracy, seen in Fig. 47. The string pot measurement is particularly

convenient because it provides a single metric from which to validate against, which allows for the targeting of a single value when adjusting the simplified model tuning parameters. However, validating based on a single point on the IAD surface incorporates the inherent assumption that displacement at this point is characteristic of the entire surface deflection.

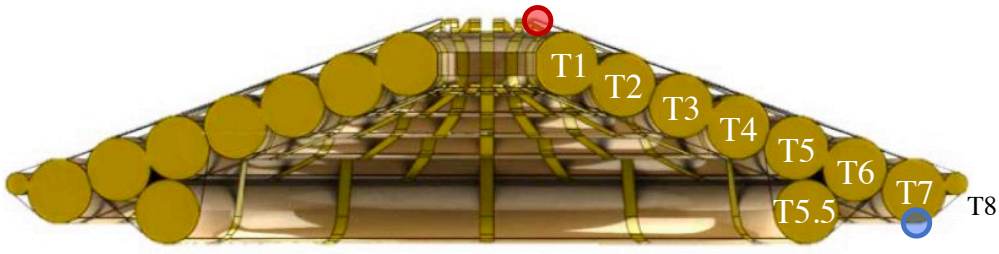


**Figure 47: Instrumentation locations for static load test. Blue circle is location of string pot displacement sensor and red circle is location of load pin radial strap force sensor. Note, this figure is a repeat of Fig. 37 and is duplicated here for convenience. [118]**

The static load test string pot measures deflection of the $T_7$ apex in the Z-direction, or up and down with respect to Fig. 47. All deflections are defined relative to the inflated state, which mirrors decelerators in actual flight. To best simulate the string pot measurements, the simplified validation model tracks the deflection of the node closest to the apex of the $T_7$ torus on the 0° radial (radial containing the radial strap). Motion of the selected node is decomposed into the Z-direction and deflection is defined as the Z-position of the node during the aerodynamic loading case minus the Z-position of the node during the temperature loading case. Because the temperature loading case brings the structure back to its initial geometry, which is defined to be the static load test post-inflation geometry, the calculated deflection from the FEA model is equivalent to the static load test and flight definitions.

The exclusive use of a single point as a validation metric for the global IAD deflection also assumes that the simplified model can accurately simulate the interactions between the tori and other structural members along the entire IAD surface. Given

the removal of important structural components such as the pairing loop straps and the bonding of tori surfaces, this assumption is not guaranteed to be correct. As a result, it is necessary to validate the global deformed shape of the simplified stacked tori model against the actual surface deflection arising in a physical test article. The NFAC wind tunnel test, discussed in Section 2.4, provides a useful data set for validating global deflections because the photogrammetry instrumentation used in the test is specifically tailored to resolving the global surface deflection with high spatial resolution. While the NFAC test article geometry is not an exact copy of the static load test, being a previous-generation 6 m, 60° design, the overall structural configuration is identical and can be simulated with the simplified validation model with minimal modifications. The high-fidelity finite element model is another way to obtain global deformation data without any modification of the simplified model.

Given that the photogrammetry measurements are generated from photographic imaging of the test article, the data set only contains information on the location of points on the IAD windward surface. This also means that components located on the interior of the decelerator are shadowed by components on top of them and do not show up in the data. In regions with dense strap patterns, therefore, the underlying tori can be difficult to resolve, requiring judicious selection of validation data points to obtain a representative data set. This does, however, allow for the simultaneous correlation of many different components with a single image. Shape validation based on the high-fidelity FEA model does not suffer from similar restrictions, allowing for the isolation of any feature of interest to be used in the comparison.

Although IAD deflection is the primary metric of interest, structural deformation is always inherently coupled to the internal stresses generated within the decelerator. The static load test was, therefore, also instrumented to measured internal forces. The most relevant of these measurements calculates the force generated in the radial strap via a load pin, located in the nose cone at the attachment to the radial strap,

seen in Fig. 47. The radial strap loads are included in this validation study as an additional metric to assess the load response estimation capabilities of the simplified model.

While the strap loads cannot be directly measured from the FEA model, they can be calculated from the stresses reported for the strap elements. The strap load is calculated by isolating the first strap element, closest to the decelerator nose, to best approximate the location of the strap load sensor in the static load test. Stress values are available for four integration points on the beam element, representing the top and bottom surfaces of the beam on either end. The stresses along the top and bottom surfaces represent the combined axial and bending stresses generated on the element, with the average of the two values calculating the stress along the mid-plane. The mid-plane stress (average) is most representative of the static load measurement because it eliminates the effects of bending and simulates the measurements of the pin sensor. The conversion from strap load to strap stress is shown in Eq. 6, where $F$ is the strap load, $\sigma$ is the strap stress, $t$ is the strap thickness, and $w$ is the modeled strap width. The factor of 2 accounts for the fact that the strap is modeled at half the width due to the symmetry simplification.

$$F_{strap} = 2 * \sigma_{mid-plane} * t_{strap} * w_{strap} \tag{6}$$

To confirm the calculations, the strap load is also determined by calculating the magnitude of the reaction loads at the fixed boundary condition at the end of the radial strap, multiplying by two due to the use of symmetry. (Given the flexible strap and the small HIAD deflections, the contributions due to the reaction moments are negligible). Both methods predict the same strap load, which confirms the calculation.

#### *3.2.4.2 Simplified Stacked Tori Validation Model: Validation Approach*

The simplified stacked tori validation model has a single tuning parameter, the torus structural thickness, that needs to be optimized during the validation process. The

simplified model, however, needs to match the static load test $T_7$ deflection and radial strap loads across all load conditions as well as the HIAD NFAC test global surface deflections, resulting in many more metrics to match than tunable parameters. Therefore, a general validation strategy is to select a single static load test configuration, inflation pressure, and applied load value (typically selected in the middle of the applicable range) on which to perform the optimization. The torus fabric thickness is optimized to the static load test deflection value measured by the string pot. The temperature value for the temperature load case is simultaneously optimized to drive the combined inflation and temperature load deflection value back to 0. The thickness and temperature optimization processes are coupled, as any increase in thickness reduces the expansion due to the inflation load in addition to the aerodynamic deflection. After a satisfactory combination of temperature and thickness is found that matches the static load test deflection value with a temperature load case deflection approximately equal to zero, the simplified model is solved, using these parameters, for the entire range of applied external load values. For each load value, the $T_7$ deflection and radial strap load are calculated for comparison with the static load test data and the global deflected surface is computed for comparison against the photogrammetry data or high-fidelity FEA solution, depending on the configuration.

#### *3.2.4.3 Simplified Stacked Tori Validation Model: Deflection Response Validation*

Static load test deflection information is available for the 3.7m, 70° configuration subject to 10 psi and 12 psi inflation pressures. Data for the 15 psi inflation pressure case is unavailable but the high-fidelity FEA model has been solved for this inflation pressure and can be used as a surrogate data set. The high-fidelity FEA model has also been extrapolated to 6.0 m, 70° and 12.0 m, 70° configurations, with deflection curves as a function of applied load being similarly available.

The 3.7 m, 70°, 10 psi inflation pressure validation results are shown in Fig. 48,

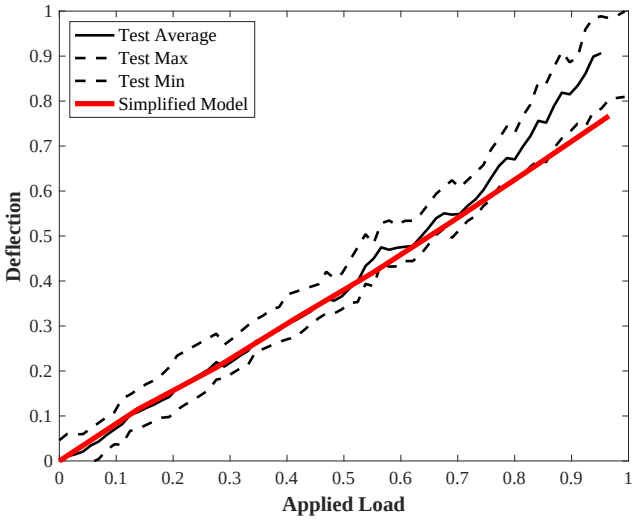


**Figure 48: Deflection vs applied load for the 3.7 m, 70° configuration with 10 psi inflation pressure**

plotting the simplified validation model results against the min and max bounds of the test data (all loads and deflections normalized to the range of 0 to 1). Tuning of the thickness model results in a thickness ratio estimate of 4.52 ($t_{ReducedOrderModel}/t_{Original}$). It is evident from the graphs that the simplified model correlates very well with the test data, tracking the average line throughout the majority of the applied load range and is within, or near, the min and max bounds of the test data for all simulated cases. The main discrepancy observed between the simplified model and test data is that the test data maximum bound exhibits an increase in slope above 70% maximum applied load, which is not observed in the simplified results. Nevertheless, the fact that the simplified model is able to stay within the bounds of the test uncertainty for almost all external load cases lends significant credibility to its ability to accurately simulate stacked tori IAD performance.

The 3.7 m, 70°, 12 psi inflation pressure validation results are shown in Fig. 49. Tuning of the thickness model results in a thickness ratio estimate of 4.33. The simplified model predictions for this test case match the static load test results even better than the 10 psi inflation pressure case, tracking the test average line through

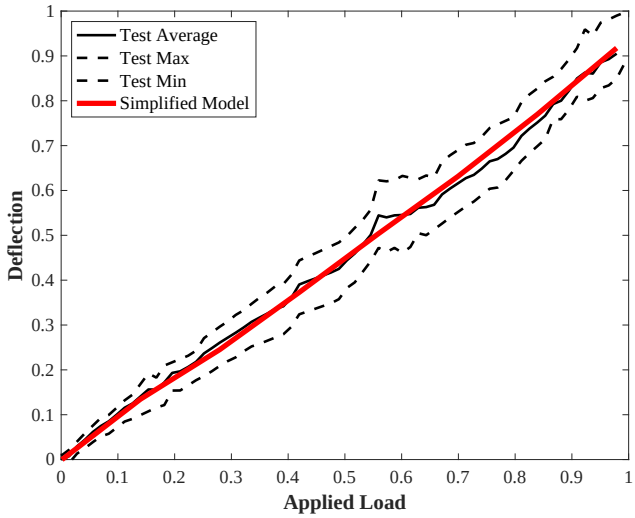


**Figure 49: Deflection vs applied load for the 3.7 m, 70° configuration with 12 psi inflation pressure**

the entire range of applied load and staying far away from the min and max bounds. It is interesting to note that the test results of the 12 psi inflation pressure test case do no exhibit an increase in slope at higher applied loads as is seen for the 10 psi inflation pressure test case. This behavior mirrors the linear nature of the simplified model and results in a uniformly improved correlation, with practically no discernible difference between the simplified estimates and the averaged test results.

The 3.7 m, 70°, 15 psi inflation pressure validation results with respect to the high-fidelity FEA model are shown in Fig. 50. The high-fidelity FEA model, like the simplified model, is validated against the 3.7 m static load test results. However, unlike the validation test data, because the high-fidelity FEA model is deterministic, it provides a single data curve for comparison rather than a distribution of validation results. Tuning of the thickness model results in a thickness ratio estimate of 5.51. The simplified model and high-fidelity models track each other nearly identically through most of the applied loading range. The slope of the high-fidelity FEA deflection curve increases above 70% maximum applied load, like what was observed with the 3.7 m, 10 psi inflation pressure test data maximum bound. While this behavior

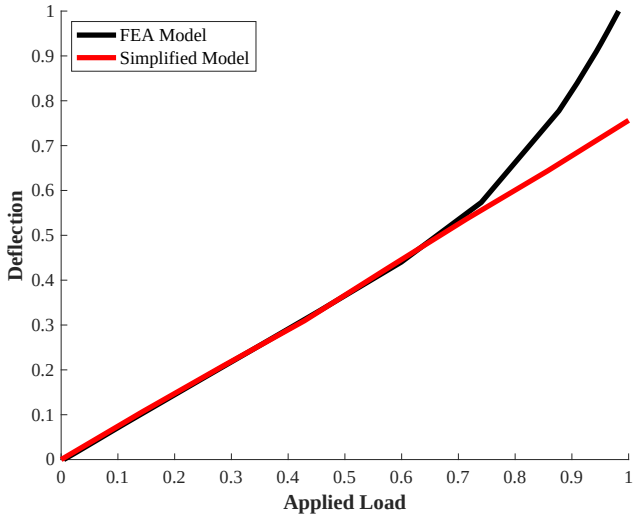


**Figure 50: Deflection vs applied load for the 3.7 m, 70° configuration with 15 psi inflation pressure. Comparison between the simplified model and high-fidelity FEA model.**

is not mirrored in the simplified model results, it is unclear which trend is the most characteristic of the stacked tori structural response, as the slope change is observed in the 10 psi test data but not the 12 psi data. Nevertheless, these results clearly support the assertion that the simplified model accurately predicts the response of the 3.7 m configuration for the majority of the range of applied loads and captures the behavior of the 12 psi inflation pressure stacked tori configuration, with the caveat of conflicting behavior being observed between different static load test conditions.

A comparison of the deflection curves for the 3.7 m, 70° stacked tori decelerator for all three inflation pressures is shown in Fig. 51. All curves display monotonic increases in deflection with increasing applied load. The deflection at a given load is reduced with increased inflation pressure, which supports the idea that the inflation pressure helps stiffen the decelerator. However, the variation in deflection is not linear with inflation pressure, with a significantly greater reduction being observed between 12 psi and 15 psi over 10 psi and 12 psi, even when taking into account the uneven sampling of inflation pressure.

The deflection comparisons between the 6.0 m, 70° and 12.0 m, 70° simplified

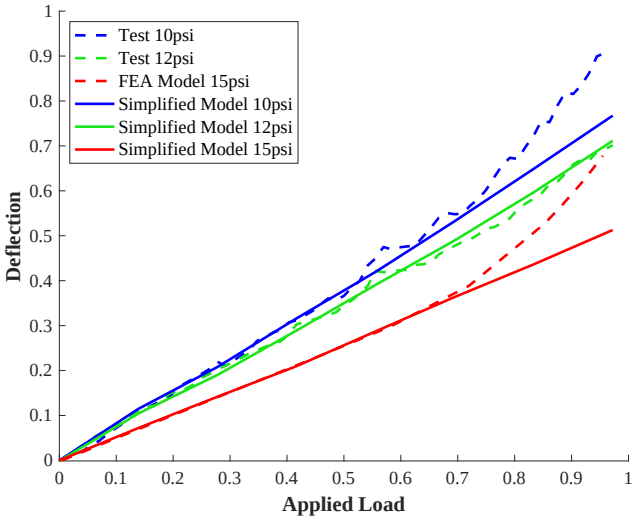


**Figure 51: Comparison of deflection vs. applied load for all 3.7 m, 70° configurations**

model and high-fidelity FEA models are shown in Fig. 52. Note that these large-scale FEA models are extrapolations of the high-fidelity 3.7 m model. Tuning of the thickness model results in a thickness ratio estimate of 10.83 for the 6.0 m configuration and a thickness ratio estimate of 12.88 for the 12.0 m configuration. The deflection curve for the 6.0 m, 70° configurations match through the entire range of applied load. The one minor exception is at small applied loads, where the high-fidelity model has a slightly elevated deflection response compared to its overall linear trend. The 12.0 m, 70° deflection curves show more deviation, with the simplified model exhibiting a slight concave shape. Greater deviation between the models is to be expected, however, as they are further extrapolated from their supporting validation test data. Nevertheless, despite these small differences, the overall character of the deflection response is similar among both models and lends credibility to the simplified model. Further evaluation of the degree of correlation can be achieved with supporting test data to provide an estimate of reasonable uncertainty bounds.

Overall, the deflection response of the simplified stacked tori validation model shows a high degree of correlation to the available validation data sets across a wide

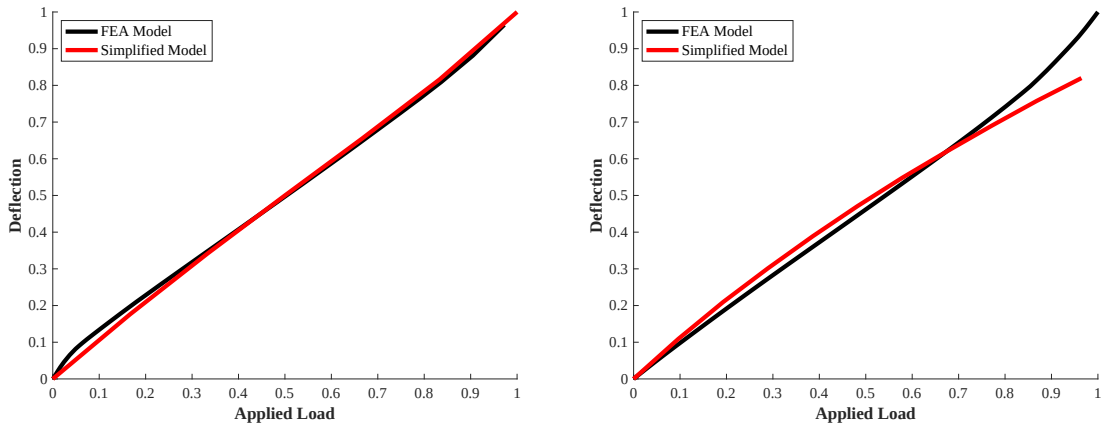


(a) Deflection vs. applied load for the 6.0 m, 70°, 15 psi configuration

(b) Deflection vs. applied load for the 12.0 m, 70°, 20 psi configuration

**Figure 52: Deflection vs applied load comparisons against the high-fidelity FEA 6.0 m, 70° and 12.0 m, 70° configurations**

range of configurational parameters and loading states. Therefore, the simplified model demonstrates that it can capture the relevant structural response with a much simpler and faster model. It is important to note that each version of the simplified model is individually tuned to the validation data set by adjusting the torus structural thickness, which is used to compensate for the removal of the pairing loop straps. However, this confirms that the simplified model is able to accurately simulate the overall deflection response across all loading cases to within an internal scaling parameter. Further evaluation of the thickness scaling is welcomed upon the availability of new test data sets.

#### *3.2.4.4 Simplified Stacked Tori Validation Model: Radial Strap Load Validation*

The radial strap load data is available from all three static load test conditions of the 3.7 m, 70° stacked tori decelerator, at 10 psi, 12 psi, and 15 psi inflation pressures. Like the deflection data, radial strap load data is obtained from the load pins of multiple radial straps during static load testing and enables an evaluation of the ability of the simplified model to accurately simulate the structural response.

The 3.7 m, 70°, 10 psi inflation pressure radial strap load validation results are

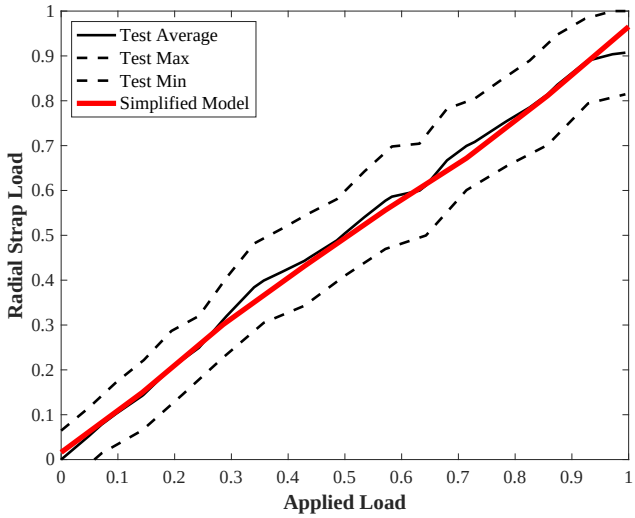


**Figure 53: Radial strap load vs applied load for the 3.7 m, 70° configuration with 10 psi inflation pressure**

shown in Fig. 53, plotting the simplified validation model results against the min and max bounds of the test data (all loads normalized to the range of 0 to 1). As evidenced by the figure, the simplified model correlates very well with the test data, tracking the average test data curve over the entire range of external loading, staying well within the bounds of the data, and even exhibiting the slight curvature trend seen in the test data. Note that the leveling off of the radial load response of the test data at the largest applied loads is not necessarily representative of the actual decelerator response at this load due to the completion of the test run and the noisy signal, indicating other interacting factors.

The 3.7 m, 70°, 12 psi inflation pressure radial strap load validation results are shown in Fig. 54. The correlation of the simplified model for the 12 psi configuration is also very good, if not quite as exact as for 10 psi inflation pressure. The simplified predicted response tracks the test data average at lower values of applied external load but drops below the average for the remainder of the simulated external load values. Nevertheless, the predicted response is well within the bounds of the test data.

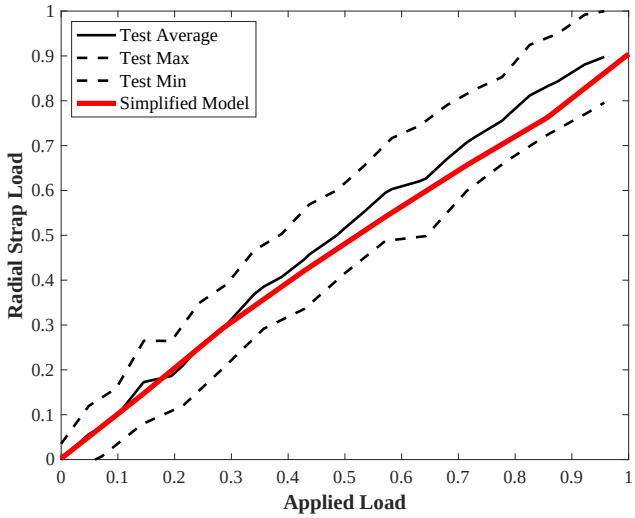


**Figure 54: Radial strap load vs applied load for the 3.7 m, 70° configuration with 12 psi inflation pressure**

The 3.7 m, 70°, 15 psi inflation pressure radial strap load validation results are shown in Fig. 55. The predicted radial strap load response of the simplified model for the 15 psi configuration, like the 10 psi and 12 psi configurations, shows a high degree of correlation to the static load test data. The simplified model response is close to the average line across all values of applied external load and exhibits the curvature seen in the test data, albeit with a slightly shallower slope. However, this is potentially due to the lack of available test data for the 3.7 m, 15 psi inflation pressure deflection response and the simplified model torus thickness, instead, being tuned to the high-fidelity FEA model.

A comparison of the radial strap load curves of the 3.7 m, 70° stacked tori decelerator for all three inflation pressures is shown in Fig. 56. All curves are remarkably similar, overlapping over the entire range of external applied load and showing no trend in radial strap load as a function of inflation pressure. This demonstrates that the radial strap load is insensitive to inflation pressure.

Overall, it is clear that the simplified validation model is able to predict the stacked tori radial strap load response across a range of decelerator configurations

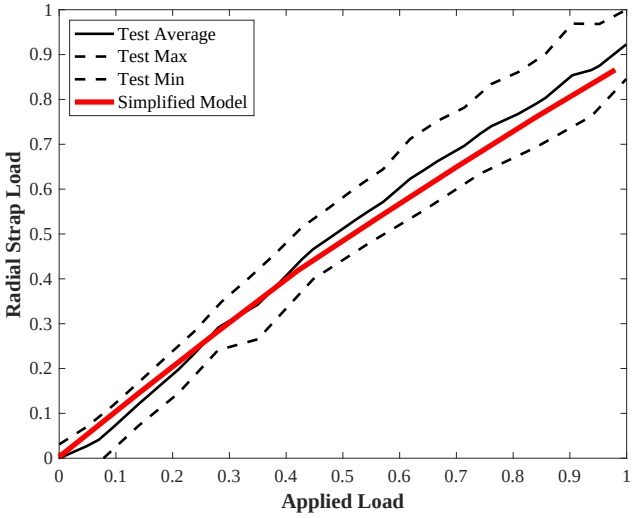


**Figure 55: Radial strap load vs applied load for the 3.7 m, 70° configuration with 15 psi inflation pressure**

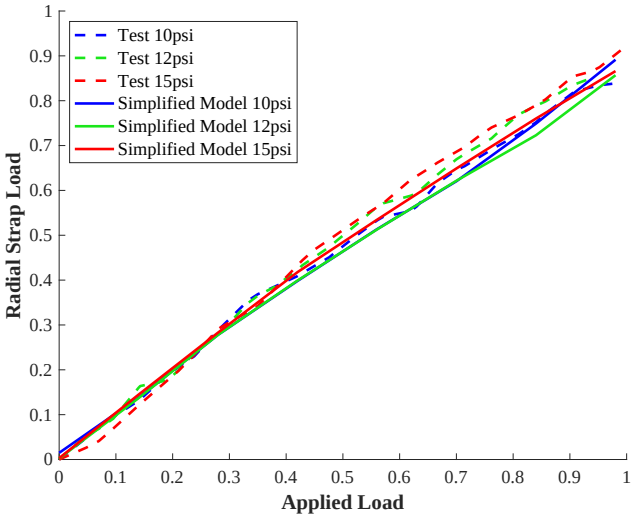


**Figure 56: Comparison of radial strap load vs. applied load for all 3.7 m, 70° configurations**

and external loading. The simplified model response is well within the bounds of the test data uncertainty for all 3.7 m configurations, often matching the average radial load strap response and displaying the same curvature trends. As a result, based on the radial strap load validation study, it is evident that the lack of pairing loop straps and contact modeling does not detrimentally impact the simplified model structural response predictions. Even more significant is that the tuning parameter of the simplified model, the torus structural thickness, is optimized solely based on the $T_7$ deflection data, without input from the radial strap load response. The fact that the simplified model can resolve both the deflection and radial strap load response while adjusting a single parameter significantly improves confidence in the model and its ability to predict the overall stacked tori structural response.

#### *3.2.4.5 Simplified Stacked Tori Validation Model: Deflected Shape Validation*

Deflected shape data is available from both the high-fidelity FEA model and the NFAC wind tunnel test, encompassing the 3.7 m, 70° and 6.0 m, 70° stacked tori decelerators along with a similar 6.0 m, 60° configuration. Data from the high-fidelity FEA model allows for comparisons of the entire deflected IAD geometry including components on the interior of the decelerator. However, this validation is against another computational model that was, itself, validated against the same static load test deflection data and, in the case of the 6.0 m, 70° configuration, later extrapolated outside of the validation data set. Data from the wind tunnel test represents the response of the decelerator under a real, representative loading environment. However, because the photogrammetry instrumentation was only set up to image one side of the decelerator, the structural response of the entire decelerator must be inferred from the shape of the windward surface.

The 3.7 m, 70°, 15 psi inflation pressure deflected shape results are shown in Fig. 57, displaying the deflection of the simplified validation model cross-section compared

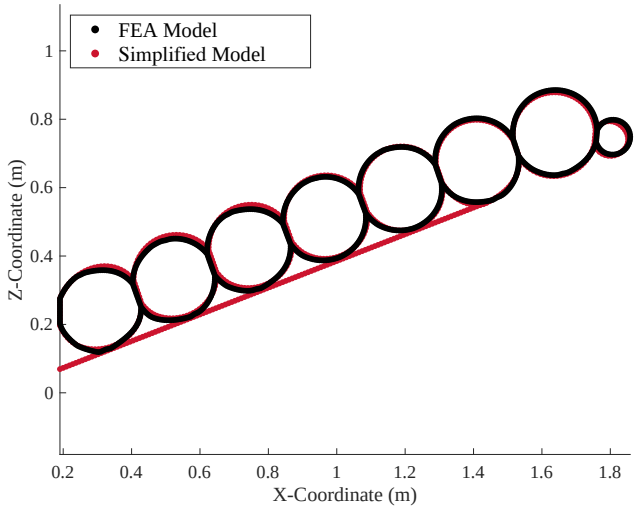


**Figure 57: Deflected shape comparison between simplified stacked tori validation model and high-fidelity FEA model for the 3.7 m, 70° configuration with 15 psi inflation pressure**

with the high-fidelity FEA model. As evidenced by the figure, the structural responses of the simplified validation model and the high-fidelity FEA model correlate very well. The tori shapes and sizes are nearly identical. There is a slight discrepancy between the simplified and high-fidelity models at $T_1$, where the simplified model deflects slightly more than the high-fidelity model. A bump is seen on the windward side of the high-fidelity $T_1$, causing it to align more with the simplified radial strap than the first torus in that local region. This is evidence of the pairing loop straps in the high-fidelity model, which attach to the centerbody in the same location as the radial strap. Because the pairing loop straps are removed in the simplified model, a similar deformation is not captured. Nevertheless, the absence of the pairing loop straps is not visible anywhere else in the simplified model, which otherwise has almost no difference compared to the high-fidelity model. This result improves confidence in the validity of the simplified model and the removal of the pairing loop straps. Small differences are observed in the local region around the nose due to the absence of a pairing loop strap connected to $T_1$, but these differences do not substantially propagate throughout the model and have minimal impact on the overall decelerator

deformation.

The 6.0 m, 70°, 15 psi inflation pressure deflected shape results are shown in Fig. 58, displaying the deflection comparison between the simplified validation model and the 6.0 m high-fidelity FEA model. The relative deflections between the simplified and high-fidelity FEA models are similar to the 3.7 m results, but with a slightly larger difference towards the outer tori in the 6.0 m case. Even so, the models converge at $T_5$, from the intersection of the radial strap. The slight bump on the high-fidelity model $T_1$ due to the pairing loop straps is also apparent in the 6.0 m model. Despite the differences between the two models appearing larger than in the 3.7 m comparison, when compared with the relative aerodynamic deflection between the two diameter vehicles, the differences are approximately proportional to the overall deflection. This shows that the simplified model behaves well across different scales.

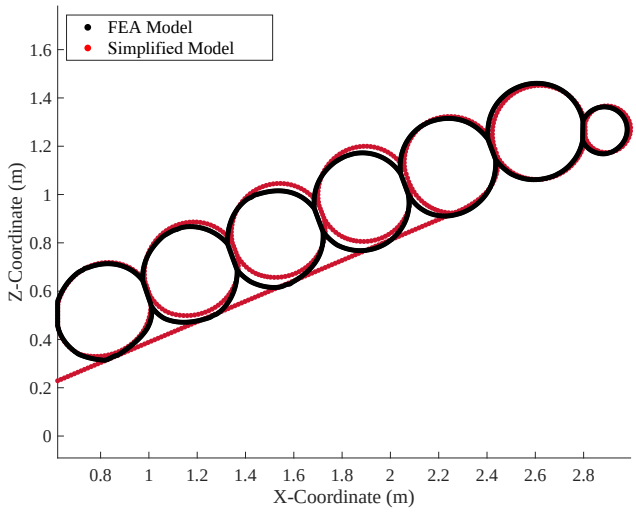


**Figure 58: Deflected shape comparison between simplified stacked tori validation model and high-fidelity FEA model for the 6.0 m, 70° configuration with 15 psi inflation pressure**

The NFAC wind tunnel test provides a valuable validation data set because it allows for a comparison of the simplified model structural response to actual test data. However, there are a few differences between the NFAC configuration and the simplified model that need to be accounted for. The NFAC test article is a 6.0 m, 60°

decelerator and is composed of older-generation, less-performant materials. These differences are directly incorporated into the definition of the simplified model. What is difficult to capture, however, is that the photogrammetry system images the entire surface during testing. Due to the nature of flight testing and the dynamic content of the IAD motion, at very few moments is the deflection of the test article uniform around its entire circumference. Therefore, the deflection measured along a single radial direction, or even wedge section, can vary significantly across the decelerator. For this reason, the NFAC wind tunnel validation data is not used to calculate the simplified model thickness ratio, as it can result in a wide range of possible values depending on the data used to correlate the model. Instead, a nominal thickness ratio is assumed for the simplified model and a group of photogrammetry data points are selected that have a similar overall deflection. The NFAC wind tunnel data does, however, provide a realistic comparison of the full-fidelity decelerator deflected shape, which is not assessed with the static load test point-wise deflection validation and which is more credible than the validation against a similar finite element analysis model.

The NFAC deflected shape validation results are shown in Fig. 59, with Fig. 59(b) depicting the entire HIAD deflected surface, the black region denoting the points selected for the cross sectional deflected surface comparison, and with Fig. 59(a) showing the simplified model deflected shape in red along with the photogrammetry surface profile in black. The black region to the upper left of the decelerator in Fig. 59(b) is selected for the comparison because its overall deflection is similar to the simplified model, with the wedge section slightly wider than the simplified model wedge degree in order to capture sufficient data to resolve the radial strap and tori contours. Seen in Fig. 59(a), the photogrammetry data only captures the shape of the windward surface of the decelerator. Nevertheless, the correlation between the two data sets is very good, with the simplified model matching the overall deflected

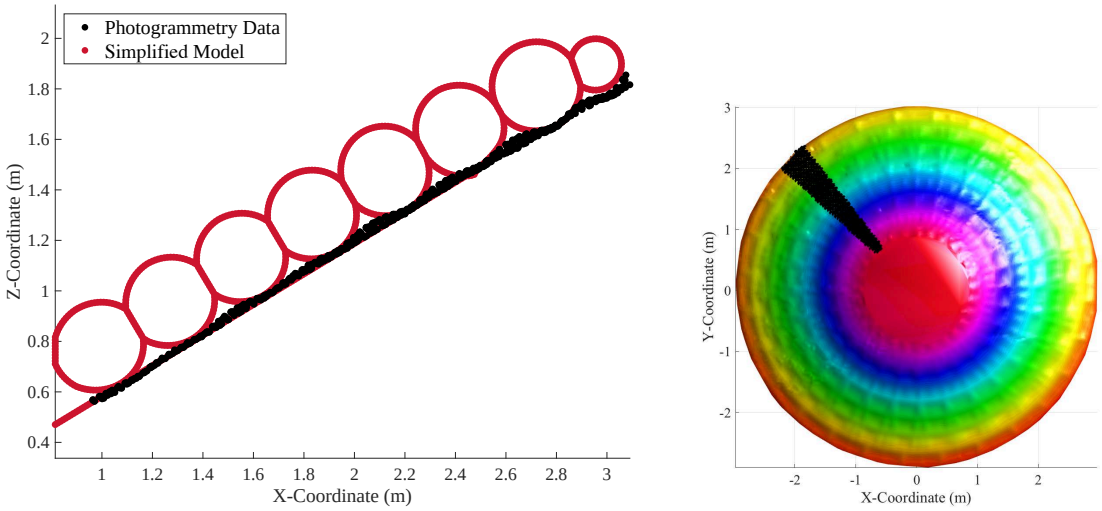


(a) Deflected shape comparison between the simplified stacked tori validation model and the NFAC wind tunnel photogrammetry data

(b) Selected points used in the deflected shape comparison

**Figure 59: Deflected shape comparison between simplified stacked tori validation model and the NFAC wind tunnel photogrammetry data for the 6.0 m, 60° configuration**

shape of the IAD surface across the entire cross-section.

The photogrammetry data in Fig. 59(a) is somewhat fuzzy, confounding the response of the tori with the radial straps that are laid on top. Therefore, a thinner wedge of photogrammetry data points is selected away from the radial straps, shown in Fig. 60(b), to isolate the features of the tori. The resulting deflected surfaces of the simplified validation model and the NFAC wind tunnel test article seen in Fig. 60(a) are nearly identical. The peaks of the NFAC IAD tori correspond exactly with the peaks of the simplified validation model tori and the regions in between the tori, imaging the overlaid aerocover on the wind tunnel test article, contour around the simplified model tori. The only major exception is with the shoulder torus, where the deflected shoulder torus locations in each model do not perfectly match. However, information on the shoulder torus geometry and location was not available when developing the simplified model and was, instead, estimated based on the static load test configuration. As a result, this discrepancy is not concerning, as the initial

geometry of the shoulder torus is likely different and because it contributes little to the overall structural performance of the decelerator.

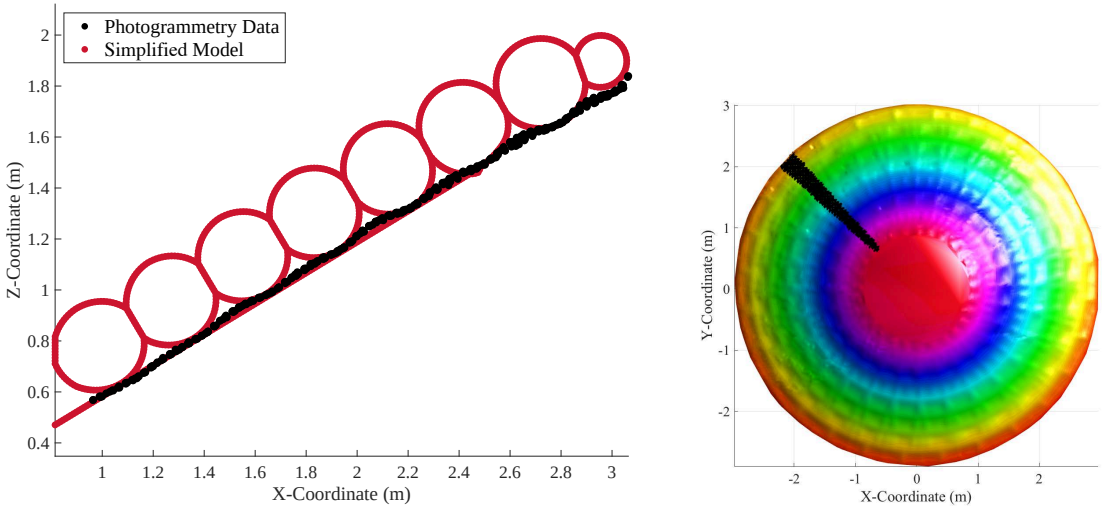


(a) Deflected shape comparison between the simplified stacked tori validation model and the NFAC wind tunnel photogrammetry data, isolating the tori

(b) Selected points used to isolate the tori in the deflected shape comparison

**Figure 60: Deflected shape comparison of the tori between simplified stacked tori validation model and the NFAC wind tunnel photogrammetry data for the 6.0 m, 60° configuration**

The fact that the simplified model compares so well against test data alleviates any concern about the small, but noticeable discrepancies observed between the simplified model and the high-fidelity FEA model. While the high-fidelity deflection data is valuable and enables an evaluation of the simplified model performance across a wide range of configurations and environments, it too is a numerical approximation of the realistic physics and is tuned to static load test response data. Therefore, exact correlation with the test data is much preferred over the high-fidelity FEA model.

The same methodology is applied to the initial set of data to isolate the deflected shape of the radial strap, seen in Fig. 61(b). The deflected cross-section in Fig. 61(a) shows that the photogrammetry radial strap locations overlay the radial strap of the simplified model. There is a small deviation near the nose that can be attributed to the interaction of the centerbody, radial strap, tori, and pairing loops in this region.

In addition, due to the lack of radial straps between $T_7$ and the shoulder torus, the isolated data resolves the torus contours.

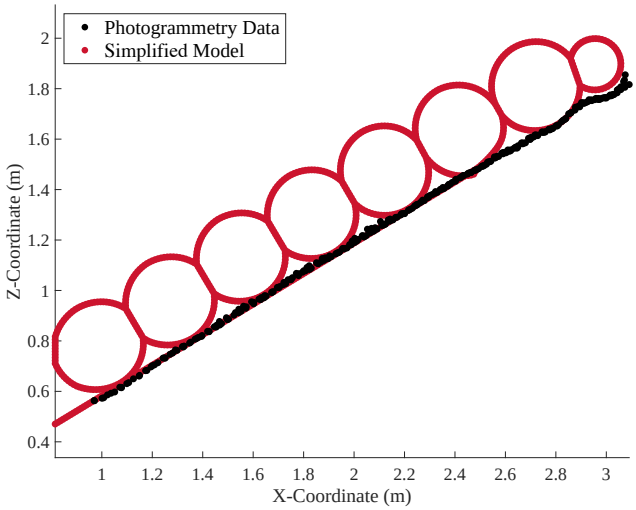


(a) Deflected shape comparison between the simplified stacked tori validation model and the NFAC wind tunnel photogrammetry data, isolating the radial strap

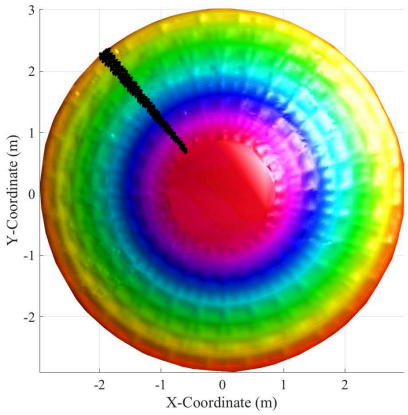


(b) Selected points used to isolate the radial strap in the deflected shape comparison

**Figure 61: Deflected shape comparison of the radial strap between simplified stacked tori validation model and the NFAC wind tunnel photogrammetry data for the 6.0 m, 60° configuration**

The overall correlation between the simplified model deflected shape and the NFAC wind tunnel photogrammetry data is very good and lends significant credibility to the validity of the simplified model. The model is able to resolve detailed features observed in the photogrammetry data set, including the exact location of the tori peaks and the contours of their deflected surface. The radial strap response is similarly predicted with a high degree of accuracy. The combined deflected surface validation effort, showing the degree of correlation to both the high-fidelity FEA model and the wind tunnel test data, along with the point-wise deflection validation, constructs a cohesive argument of the simplified validation model's ability to accurately simulate the stacked tori decelerator's structural response at a number of different scales.

This validation study also shows the power of photogrammetry instrumentation

in the validation of computational models. While photogrammetry is not particularly suited to obtaining point-wise measurements used in tuning simplified model parameters, it enables global measurements across an entire decelerator body, which is difficult to obtain with other instrumentation devices. This global information allows for quick, qualitative comparisons between data sets to identify discrepancies in features or trends that would be missed with point-wise measurements. The discrepancies in global phenomena can be used to identify fundamental errors in the decelerator modeling and avoid validation against point-wise measurements that do not represent the overall decelerator response. Therefore, when used in conjunction with a full suite of validation data sets, including point-wise deflection measurements, photogrammetry and measurements of the global decelerator response enable increased confidence in the predictive capabilities of numerical models.

#### *3.2.4.6 Simplified Stacked Tori Validation Model: Mesh Convergence*

A mesh convergence study is conducted on the simplified model to understand the impact of the mesh size on the predicted results. For the study, multiple models are solved, each with different uniform element sizes between 0.2 m and 0.011 m. For the 6.0 m, 70° configuration, these element sizes correspond to a range of 16 to 291 elements per side, respectively, with the side length being defined as the shortest distance from the IAD theoretical nose to the outer edge of the shoulder torus as described in Eq. 7. For reference, the side length of the 3.7 m, 70° configuration is 2.0 m, the side length of the 6.0 m, 70° configuration is 3.2 m, and the side length of the 12.0 m, 70° configuration is 6.4 m.

$$L_{Side} = \frac{R_{Maj}}{\cos(90 - \theta_{Half-Cone})} \tag{7}$$

The mesh convergence results are displayed in Fig. 62. Note that the x-axis, the mesh size, is plotted on a log-axis to enhance the plot detail. The convergence

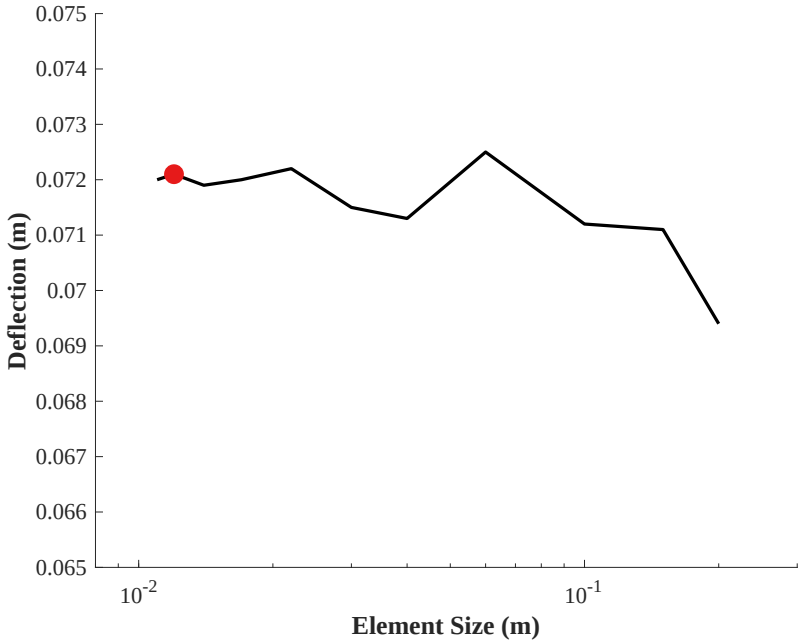


**Figure 62: Mesh convergence results showing deflection at the aft apex of $T_7$ as a function of element size (plotted on a log scale). Red circle denotes the selected element size for the 6.0 m, 70° configuration.**

behaves like a decaying oscillation about a log-type function, with the results starting to converge around element sizes of 0.1 to 0.06 m, or 32 to 53 elements per side, where the error compared to the converged deflection is approximately 1% or less. The element size chosen for the 6.0 m, 70° configuration is 0.012 m, or 267 elements per side, well within the converged limit, and is chosen to allow margin when applied to the other configurations.

A 0.012 m element size is similarly used for the 3.7 m, 70° configuration. It is assumed that all features of the finite element model scale with the overall decelerator size and, as a result, that the accuracy of the mesh scales with the ratio of the element size to the overall decelerator size. The resulting mesh density, 167 elements per side, is lower than that of the more conservative 6.0 m, 70° design but is still well within the 32 to 53 element per side convergence limit. The element size is increased for the 12.0 m, 70° configuration, up to 0.025 m, to reduce computational expense when solving the larger model. The corresponding mesh density of 256 elements per side is

similar to that of the 6.0 m, 70° configuration and is, therefore, conservatively dense.

### 3.2.5 Simplified Stacked Tori Validation Model Conclusions

Simplified computational models that can rapidly explore the configurational and flight environment design spaces can enable structural information to be introduced into the conceptual design phase. However, based on approximating certain features and physics of high-fidelity models, simplified models require thorough validation efforts to ensure they properly estimate actual vehicle performance.

This thesis develops a simplified stacked tori finite element model based on a high-fidelity finite element model and the most recent static load test HIAD geometry. In order to improve the model efficiency, several computationally expensive features are approximated. The pairing loop straps that join adjacent tori are removed, with their contribution to the decelerator stiffness being approximated by an increase in the torus structural fabric. Similarly, contact is not simulated in the model, with adjacent features instead approximated as being glued together.

These simplifications, in particular the tuning of the torus thickness, have the potential to alter the structural performance of the decelerator. As a result, a comprehensive validation study is conducted, validating the simplified model's point-wise deflection, radial strap load, and full surface deformation. The model correlates well with the static load test deflection and radial strap load data, matching the test data profiles and even staying within the uncertainty of the test data throughout the entire range simulated. The model deflected surface also matches both high-fidelity FEA models and the NFAC wind tunnel photogrammetry data set. The comparison with high-fidelity simulations shows the simplified model to accurately predict the structural response of the decelerator and the wind tunnel test data comparison reaffirmed this assertion, with the simplified model matching the test article deflection nearly exactly. The combination of the three validation metrics and comparisons against

three separate data sets lends significantly credibly to the simplified model's ability to simulate inflatable decelerator structural response.

The simplified model uses the torus thickness as a tuning parameter to replace the stiffness loss due to the removal of the pairing loop straps. While the tuning parameter does allow the simplified model to better match the validation deflection data, the use of a tuning parameter does not reduce the significance of correlation observed during the validation efforts. For each decelerator design (3.7 m/70°/10 psi, 6.0 m/70°/15 psi, etc.) the simplified model torus thickness is adjusted to match the deflection of one external load case. Based on this one value, the simplified model is observed to match the deflection test data across the entire range of external loads, keeping within the test data uncertainty. More so, the simplified model is also able to simultaneously match the radial strap load results to within the test data uncertainty across all external loads and match the deformed surface deflection. Therefore, by tuning the thickness based on a single metric and a single load case, the simplified model is able to match three different metrics for three different data sets subject to a wide range of external loads. The fact that the model can match all these conditions, in addition to the global deflected shape, proves that the simplified model is able to capture the relevant structural response of the stacked tori decelerator.

## *3.3 Generalized Simplified Stacked Tori Decelerator Model*

The simplified stacked tori validation model is useful for comparing against the available validation test data and demonstrating the capabilities of simplified computational models. This model, however, is inflexible for modeling general stacked tori decelerators, with the geometry of each model being defined by the equivalent static load test article design. As a result, it is necessary to develop a generalized simplified model that is not tied to the static load test geometry definition and that can be used to describe any possible configuration for use in design space exploration.

### 3.3.1 Generalized Simplified Stacked Tori Decelerator Model: Design

The generalized simplified model standardizes the stacked tori design and reduces the number of geometric variables. The simplified validation model, based on the geometry of the static load test vehicle and seen in Fig. 63, is defined by the torus center locations, centerbody diameter, and the torus and shoulder torus cross sectional diameters. This corresponds to 19 independent geometric variables per configuration. The generalized model, seen in Fig. 64, splits the geometric definition into sets of independent variables and fixed variables. The independent variables, the major diameter, centerbody diameter, number of tori, and cone angle, are based on unique features defining different stacked tori configurations. The fixed parameters define general characteristics common across all stacked tori decelerators or parameters defining the model implementation and include the centerbody overlap ratio ($a$), the tori overlap ratios ($b$), and the ratio of the torus and shoulder torus radii. Thus, the design space necessary to define a unique configuration is reduced from 19 variables down to 4, with these variables more naturally relating to characteristic features of the stacked tori design.

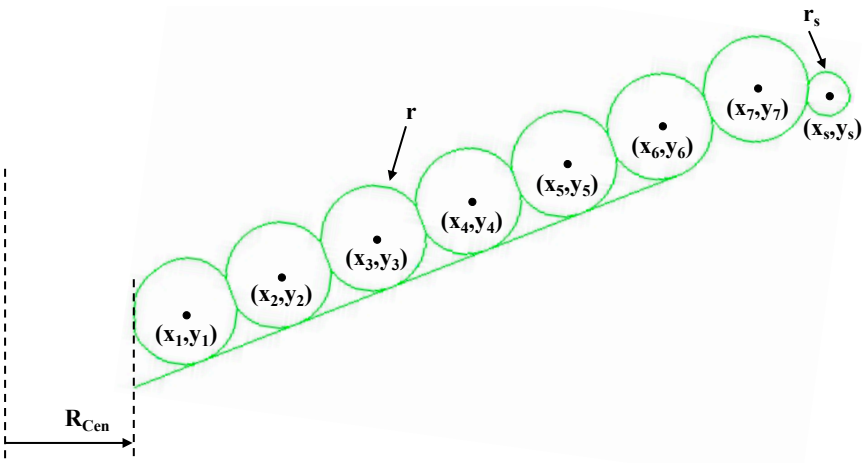


**Figure 63: Geometric parameters used to define the simplified stacked tori validation model**

The definitions of the fixed design variables are based on the corresponding values

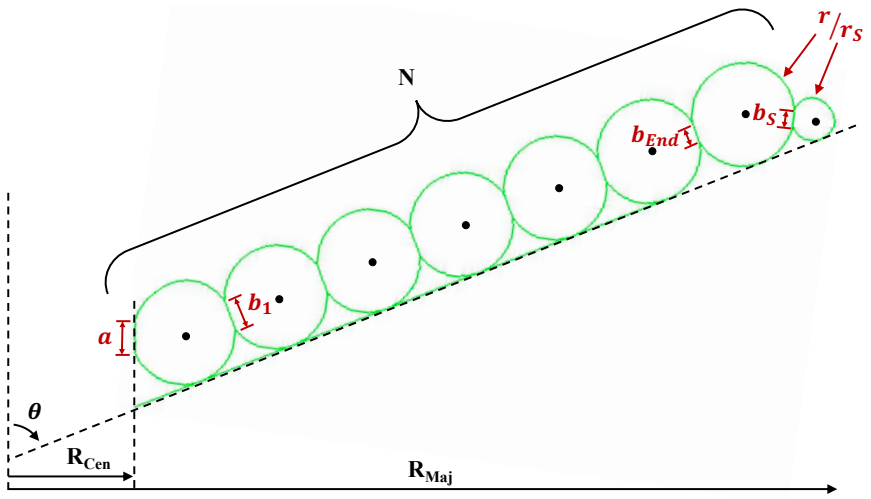


**Figure 64: Geometric parameters used to define the generalized simplified stacked tori model. Independent variables are shown in black and fixed variables are shown in red.**

observed in the validation models. For example, the ratio of the torus and shoulder torus radii in the generalized model is an approximation of the values calculated in each of the validation models, which tend to fall within a similar range. In addition, all parameters are normalized based on the torus cross-sectional radius so that the length parameters scale with the decelerator size. These changes allow for consistency across all generated stacked tori designs to eliminate sources of variability when performing the design space exploration.

### 3.3.2 Generalized Simplified Stacked Tori Decelerator Model: Geometric Definition

The use of the major diameter and the number of tori as independent geometric parameters results in the torus cross-sectional diameter being a dependent parameter. This was decided because, while the torus cross-sectional diameter is an important parameter and is used to scale all the fixed parameters, it does not define fundamentally different stacked tori configurations. Instead, the torus cross-sectional radius, herein simply referred to as $r$ or the torus radius, is calculated from the set of independent geometric parameters. The algorithm is based on relating the side length

and base diameter of the decelerator, $L$ and $L'$, shown in Fig. 65.

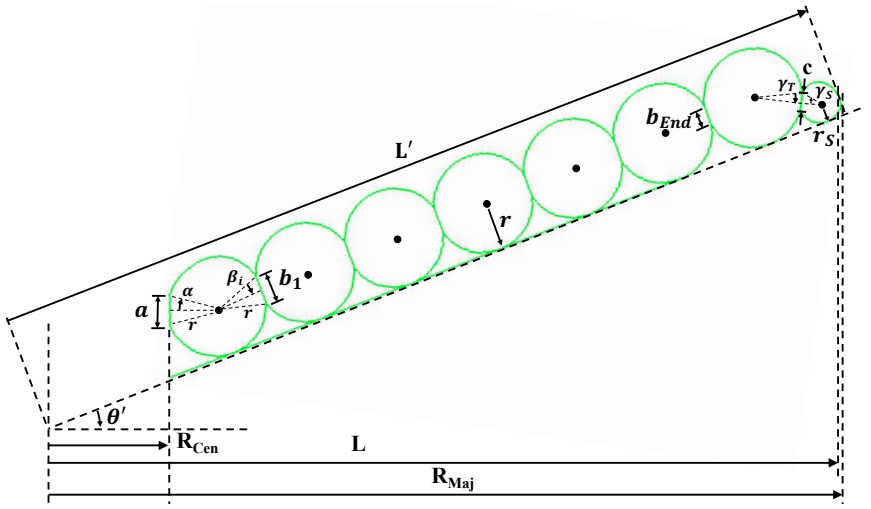


**Figure 65: Definition of parameters used in stacked tori geometry calculation**

Both $L$ and $L'$ are functions of the torus radius, $r$, and are related based on Eq. 8. However, because they are complicated functions, the torus radius cannot be isolated and solved for analytically. Instead, Newton's method, described in Eq. 9, is used to numerically find the root of Eq. 8, or the value of the torus radius that drives Eq. 8 to zero. Starting from a guess of the torus radius, $r_k$, Newton's method uses a first order Taylor approximation to estimate an updated value of the torus radius, $r_{k+1}$. This process is iteratively repeated to converge upon the value or $r$ satisfying $f(r) = 0$.

$$f(r) = L' - \frac{L}{\cos(\theta')} = 0 \tag{8}$$

$$r_{k+1} = r_k - \frac{f(r_k)}{f'(r_k)} \tag{9}$$

Newton's method requires full expressions of the function being optimized, $f(r)$, and its derivative, $f'(r)$, expressed in terms of the torus radius, $r$. $L$ can be expressed in terms of the major radius, $R_{Maj}$, as described in Eq. 10. While not explicitly

shown in this equation, $L$ is a function of the torus radius through the shoulder torus radius, $r_s$, which is defined to be proportional to the torus radius via the constant $\epsilon$, as described in Eq. 11. Note also that the variable $\theta'$ is the complementary angle of the half-cone angle, $\theta$.

$$L = R_{Maj} - r_s\big(1 - \cos(\theta')\big) \tag{10}$$

$$r_s = \epsilon r \tag{11}$$

The side length, $L'$, is calculated by summing the length of each individual component along the decelerator surface, as shown in Eq. 12. The definition of $L'$ therefore includes contributions from the nosecone radius, the torus/nosecone overlap, each torus' cross-sectional diameter, the tori overlap, and shoulder torus diameter and overlap.

$$L' = (r - r_s)\tan(\theta') + \frac{R_{Cen}}{\cos(\theta')} + \frac{2r\sin(\alpha)}{2\cos(\theta')\tan(\theta')} + \sum_{i=1}^{N-1} 2r\cos(\beta_i) + \sqrt{\big(r\cos(\gamma_T) + r_s\cos(\gamma_S)\big)^2 - (r - r_s)^2} + r_s \tag{12}$$

The derivative of Eq. 8 is also computed for use in Newton's method, shown in Eq. 13. Following the completion of the Newton's method algorithm to calculate the torus radius, the numerical model cross-section geometry is then defined based on the torus center locations and radii in a similar manner to the simplified validation model.

$$f'(r) = \frac{\partial\left(L' - \frac{L}{\cos(\theta')}\right)}{\partial r} =$$
$$(1-\epsilon)\tan(\theta') + \frac{\cos(\alpha)}{\cos(\theta')} + \sum_{i=1}^{N-1} 2\cos(\beta_i)$$
$$+ \frac{1}{2}\Big[\big(r\cos(\gamma_T) + r_s\cos(\gamma_S)\big)^2 - (r-r_s)^2\Big]^{-\frac{1}{2}}$$
$$* \Big[2\big(r\cos(\gamma_T) + r_s\cos(\gamma_S)\big)\big(\cos(\gamma_T) + \epsilon\cos(\gamma_S)\big) - 2(r-r_s)(1-\epsilon)\Big]$$
$$+ \frac{\epsilon}{\cos(\theta')} \quad (13)$$

### 3.3.3 Generalized Simplified Stacked Tori Decelerator Model: Loading

The loading conditions used in the high-fidelity and simplified validation models are established to mirror static load testing rather than actual flight conditions. In particular, the aerodynamic loading is based on a total applied force, which is later distributed among the whetted surfaces, and an additional temperature loading step is employed to resolve the discrepancies between the pre and post-inflation loaded geometric definitions. The generalized stacked tori model eliminates the dependency on the static load test data by redefining the load conditions to reflect the loading seen in flight.

The aerodynamic loading is redefined based on a pressure applied to all whetted surfaces rather than an applied load. The loading is, therefore, independent of model geometry and instead approximates the forcing due to an external dynamic pressure, with the caveat that a constant pressure is applied in the simplified model rather than a spatially varying dynamic pressure load. The magnitude of the external aerodynamic pressure, along with the constant torus inflation pressure, constitute the two remaining independent variables of the generalized FEA model, representing the inflation state and flight environment.

The generalized simplified stacked tori model also removes the artificial temperature loading step. Because the generalized model is no longer trying to match the geometry of the static load test decelerator, the initial, pre-inflation loaded geometry is assumed to be the as-designed geometry defined by the independent design parameters. Subsequent inflation loading stresses the torus fabric and cords and resists the applied aerodynamic loading. The removal of the temperature loading eliminates the temperature tuning variable and better approximates the fabrication of actual stacked tori decelerators, who's geometry would be based on an as-designed configuration rather than an initial design generated to target a given inflated shape. This change also allows for the unbiased comparisons of trends with respect to individual design variables.

### 3.3.4 Generalized Simplified Stacked Tori Decelerator Model: Meshing

The meshing of the generalized simplified stacked tori model is adjusted slightly from the simplified validation model, which utilizes a fixed element size per configuration. Mesh sizing of the simplified validation models is roughly based on the ratio of element length to the decelerator side length, being a metric for the overall size of the decelerator. However, while this method does adapt the mesh size with that of the FEA model, the mesh size is also required to be sufficiently small to resolve the small-scale features of the model. In the case of the stacked tori, these smaller features are the structural tori. The 3.7 m, 6.0 m, and 12.0 m, static load test-based models all have between 6 and 7 structural tori, so the size of the tori in each model is approximately proportional to the side length. However, the number of tori of designs generated by the generalized model can vary widely, from 5 up to 12 tori. As a result, the mesh sizing of the generalized simplified model is adapted based on the number of elements per torus cross-sectional circumference, rather than the decelerator side length or a fixed element length, in order to better scale the mesh according to the features of

each unique model and enable a consistent mesh convergence across the entire range of simulated configurations.

The mesh convergence study in Section 3.2.4.6 provides the data necessary to evaluate this change. As seen in the mesh convergence results for the 6.0 m decelerator, the deflection values converge starting with element sizes of 0.1 m to 0.06 m, corresponding to approximately 12 and 20 elements per torus, respectively. The final element sizes chosen for the simplified validation models are 0.012 m for the 3.7 m and 6.0 m models and 0.025 for the 12.0 m model, correspond to 64 (3.7 m), 102 (6.0 m), and 76 (12.0 m) elements per torus. All mesh densities are well within the limits of convergence. Based on these results, a global mesh density of 75 elements per torus is chosen for the generalized simplified model. The 75 elements per torus is conservative with respect to the 12 to 20 elements per torus convergence limit with sufficient margin and either equals or exceeds the element densities of the 3.7 m and 12.0 m validation models. The 6.0 m validation model mesh is denser than 75 elements per torus, but the 6.0 m model's 0.012 m element length was initially sized to retain margin when using the same element size for smaller-scale models. In addition, as observed in Fig. 62, densities above the selected 75 elements/torus, or 0.016 m for the 6.0 m model shown in the figure, do not significantly impact the deflection results.

### 3.3.5 Generalized Simplified Stacked Tori Decelerator Model: Torus Thickness Model

The generalized simplified model, like the validation model, requires the torus thickness to be adjusted to compensate for the removal of the pairing loop straps. However, unlike the validation model, the generalized stacked tori model is used to simulate a wide number of potential configurations, often deviating significantly from the static load test validation designs. Therefore, a surrogate model of the equivalent torus thickness, informed by the thicknesses used in the stacked tori FEA validation model,

must be developed to ensure the accurate simulation of decelerator deflections across the full range of possible configurations.

Torus thickness data is available for the 70°, 3.7 m comparisons against the static load test and the 6.0 m and 12.0 m comparisons against the high-fidelity FEA model. While the 6.0 m, 60° configuration is compared against the NFAC wind tunnel test data, a thickness value is not estimated during the comparison because the NFAC test article is composed of older-generation materials that do not accurately reflect the current capabilities of the IAD fabrics and because the NFAC test article deflections are not radially symmetric, often varying significantly due to the dynamic content of motion, which is not captured in the finite element model.

The thickness ratio results, or the simplified validation model thickness divided by the actual torus thickness, are shown in Fig. 66, plotted against the major diameter and inflation pressure, and in Table 2. Determination of the thickness variation with respect to the other design parameters is difficult because all available models have the same cone angle, only one configuration is available with a varying number of tori, and their minor diameters scale with the major diameter. Based on the conceptual model in Section 3.2.3.3, both the torus fabric and pairing loop straps contribute to the overall stiffness of the decelerator, resisting the torus inflation and aerodynamic loading, and are interchangeable. Therefore, it is expected that the torus thickness ratios will best correlate with the decelerator major diameter, the design parameter that most influences the pairing loops strap pattern and density. This is confirmed in Fig. 66(a), with a clear, monotonic trend being observed between the thickness ratio and the major diameter. While the other geometric parameters also influence the strap pattern design to some degree, they are expected to be second-order effects, and so are less important to characterize given the limited number of validation data points.

It is also evident in Fig. 66(b) that the torus thickness ratios are insensitive to

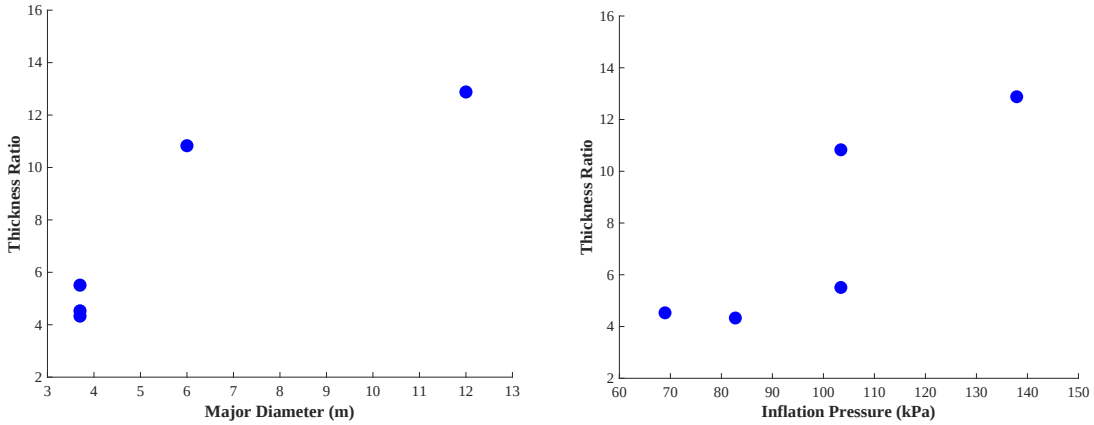


(a) Thickness values as a function of major diameter

(b) Thickness values as a function of inflation pressure

**Figure 66: Thickness values of all configurations determined during the simplified model validation study**

inflation pressure. This fact is somewhat obscured by the inflation pressure increasing with major diameter but is supported by multiple features in the graph. The first of which is the large jump between both configurations with a 15 psi (103 kPa) inflation pressure. This jump accounts for over 50% of the entire thickness variability with no change in inflation pressure and indicates that other parameters are driving the thickness ratio values. The other indication is with the three 3.7 m configurations at 10, 12, and 15 psi inflation pressures (69, 83, and 103 kPa, respectively). Comprising 50% of the full range of inflation pressure, these three configurations account for only 15% of the total thickness ratio variability. In addition, the thickness ratio values are not even monotonic with inflation pressure. The combination of all these observations leads to the conclusion that thickness ratio and inflation pressure are likely not correlated.

The thickness ratio values being independent of the inflation pressure is also supported by the conceptual model. Whereas the torus fabric and pairing loop straps are interchangeable, the inflation pressure instead provides the counteracting force during inflation and is treated as being infinitely stiff during aerodynamic loading.

Under these simplified assumptions it has no impact on the stiffness scaling between the torus fabric and pairing loop straps.

Inspection of Fig. 66(a) shows the thickness ratio to increase with increasing major diameter, displaying a log-like trend of decreasing slope. Multiple basis functions are considered for the regression of an analytic, surrogate thickness model. Of these candidate functions, log functions are determined to have insufficient curvature. Functions of the form $\frac{1}{x^n}$ are able to achieve higher curvatures and are, therefore chosen for the surrogate model. A model of the form $c_1 + \frac{c_2}{x}$ is ultimately chosen, seen in Fig. 67 and Eq. 14. While this model has slightly less curvature than the underlying training data, fitting both constant coefficients and the exponent of $x$ would require the training data at all three major diameters. The use of all data points to train a model removes any flexibility and results in a model that is overly sensitive to uncertainty in the underlying training data. Therefore, the $\frac{1}{x}$ model is desirable from a robustness perspective. The surrogate thickness model also has a fixed maximum bound, similar to what is inferred from the training data, so the model will not blow up when extrapolated to large diameter vehicles. The thickness model is not, however, bounded for small diameter vehicles, predicting a negative thickness ratio for vehicles with a 2 m major diameter and smaller. Therefore, care should be taken when estimating the thickness of vehicles smaller than the 3.7 m static load test articles. It should be noted, however, that IADs, such as the configurations considered in this thesis, are targeted at high-mass, large diameter vehicles, so this constraint on small diameter decelerators is not expected to limit the applicability of the surrogate model.

$$\frac{t}{t_0} = 17.31 - \frac{45.74}{D_{Maj}} \tag{14}$$

The surrogate model predicted thickness ratio values are shown in Table 2 along with the thickness ratios obtained from the finite element model validation study.

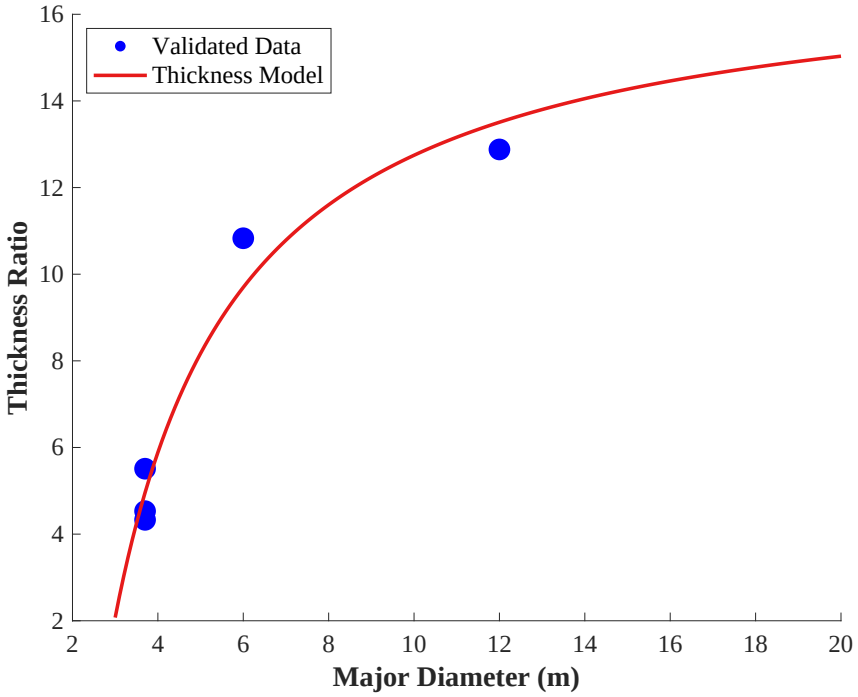


**Figure 67: Thickness values as a function of major diameter, plotted again the surrogate thickness model predicted results**

Because the analytic model varies only with the major diameter, the variation due to inflation pressure in the 3.7 m models is ignored, predicting an average value among all three points. The % difference values between the model and training data are generally around 10%. The largest exception is with the 3.7 m, 12 psi configuration. Because the analytic model averages all the 3.7 m results, this large difference is unavoidable, due to the underlying uncertainty in the training data and this particular configuration predicting the thickness ratio farthest away from that average.

The surrogate thickness model is incorporated into the generalized simplified stacked tori model definition, calculating the required torus thickness prior to generating the model geometry. It is important to note that, while errors in the thickness model could distort the data, they are not expected to significantly influence the overall conclusions made. Uncertainty in the thickness model will not influence comparisons between decelerators with the same major diameter and, due to the surrogate

**Table 2: Thickness ratio results for each configuration along with the thickness model predicted results and % differences**

| Configuration | Thickness Ratio | Model Predicted Ratio | % Difference |
|---|---|---|---|
| 3.7 m, 70°, 10 psi | 4.53 | 4.96 | 9.5 |
| 3.7 m, 70°, 12 psi | 4.33 | 4.96 | 14.5 |
| 3.7 m, 70°, 15 psi | 5.51 | 4.96 | -10.0 |
| 6.0 m, 70°, 15 psi | 10.83 | 9.70 | -10.5 |
| 12.0 m, 70°, 20 psi | 12.88 | 13.51 | 4.9 |

thickness model being monotonic in major diameter just like the training data, all trends with respect to major diameter should be preserved, albeit with a possible distortion in the slope of said trends.

### 3.3.6 Generalized Simplified Stacked Tori Decelerator Model: Wedge Degree Model

The variations in strap pattern used on different stacked tori configurations changes the number of radial straps and decelerator rotational symmetry. Like the torus thickness discussion in Section 3.3.5, the change in the strap pattern therefore results in a different wedge degree for the stacked tori finite element model, described in Fig. 68. Because the generalized finite element model will be used to explore new decelerator configurations, a wedge degree model must be established to account for the new configuration strap pattern and the associated radial symmetry.

All stacked tori decelerator configurations used in the validation study have a similar strap configuration, composed of radial, chevron, and pairing loop straps. Therefore, all models provide supporting data from which to construct the surrogate wedge degree model. The only caveat is that all 3.7 m configurations (with varying inflation pressure) used the same decelerator and strap pattern design and, therefore, contribute one data point.

The wedge degree angle used in the simplified finite element model is a derived parameter based on the number of radial straps in the corresponding stacked tori configuration. As a result, the surrogate model is fit to the number of radial strap

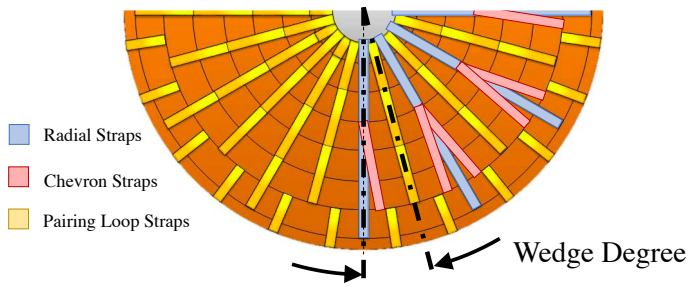


(a) Definition of the wedge degree based on the decelerator strap pattern

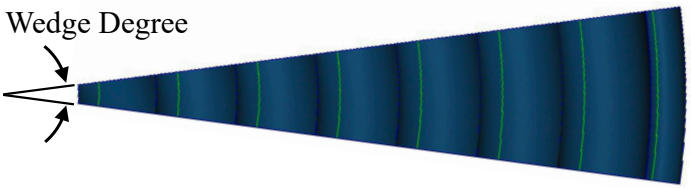


(b) Visualization of the simplified model wedge degree

**Figure 68: Definition of the simplified model wedge degree**

data rather than the wedge degree. The resulting wedge degree is then calculated from surrogate strap model using the same analytic conversion equation used for the finite element validation models, shown in Eq. 15.

$$\theta_{Wedge} = \frac{180}{N_{Straps}} \tag{15}$$

It is evident from the plot shown in Fig. 69(a) that the major diameter dominates variation in the number of radial straps. The variation due to the cone angle is represented by the two 6.0 m data points, with one configuration featuring a 60° cone angle and the other 70°. The small difference in the number of straps between these two configurations compared to the overall variability demonstrates that number of straps is not sensitive to the decelerator cone angle. This is intuitive, as the strap pattern is sized based on the expected load in the IAD, which is most influenced by the major diameter.

As a result, the surrogate radial strap model is fit using only basis function comprised of the major diameter. Like the torus thickness model, the number of radial

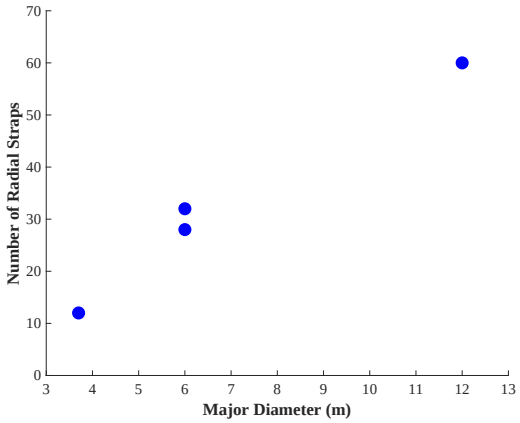


(a) Number of radial straps as a function of major diameter

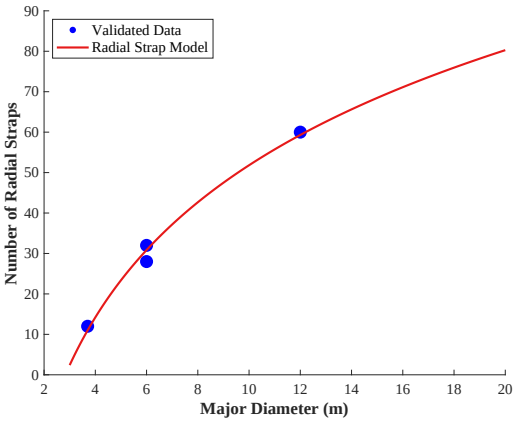


(b) Surrogate radial strap model predicted results along with training data

**Figure 69: Radial strap model and supporting data**

straps increases with respect to major diameter, with a decaying slope. Given the shallower curvature of the radial strap data, a logarithmic function is observed to fit the data well and enables a robust model that is relatively insensitive to uncertainty in the limited number of fitting data points. The resulting radial strap model is seen in Eq. 16.

$$N_{RadialStraps} = -42.71 + 41.05 \ln (D_{Maj}) \tag{16}$$

The surrogate wedge degree model can be analytically derived from the radial strap model, resulting in Eq. 17. As evidenced by Fig. 70, the model correlates well with the supporting test data, producing the same exponential decay-like function with respect to major diameter. The surrogate model is bounded for large diameter vehicles, avoiding potential problems due to extrapolation. However, like the thickness model, the wedge degree model is similarly unbounded for small diameter decelerators. While it is not anticipated to be used for decelerators smaller than those tested in the static load test series, care should be taken when applying the model to IADs with diameters less than the 3.7 m.

$$\theta_{Wedge} = \frac{180}{-42.71 + 41.05 \ln\left(D_{Maj}\right)} \tag{17}$$

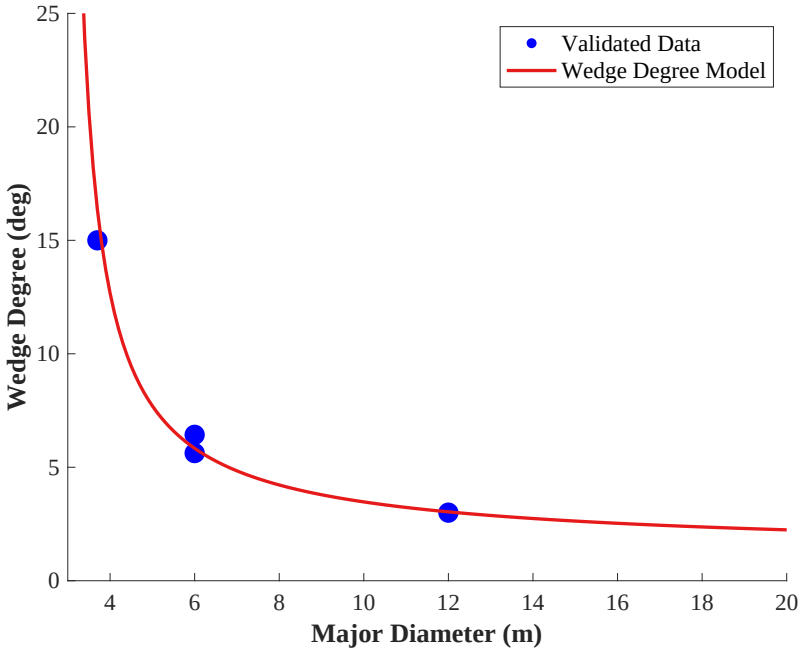


**Figure 70: Surrogate wedge degree model predicted results along with supporting data**

The surrogate model performance results for the radial strap and wedge degree models are shown in Tables 3 and 4. The % difference results for both models are at or below 10% for all configurations, with the largest error observed for the 6.0 m, 60° configuration. This is the only configuration with a 60° cone angle and, as a result, is the most likely to deviate from the overall trend of the other 70° configurations.

**Table 3: Number of radial straps for each configuration along with the strap model predicted results and % differences**

| Configuration | # Radial Straps | Model Prediction | % Difference |
|---|---|---|---|
| 3.7 m, 70° | 12 | 11.0 | -8.3 |
| 6.0 m, 60° | 28 | 30.8 | 10.2 |
| 6.0 m, 70° | 32 | 30.8 | -3.6 |
| 12.0 m, 70° | 60 | 59.3 | -1.2 |

The wedge degree model is incorporated into the finite element model prior to

**Table 4: Wedge degree angle for each configuration along with the wedge degree model predicted results and % differences**

| Configuration | Wedge Angle (deg) | Model Prediction (deg) | % Difference |
|---|---|---|---|
| 3.7 m, 70° | 15.00 | 16.4 | 9.1 |
| 6.0 m, 60° | 6.43 | 5.84 | -9.3 |
| 6.0 m, 70° | 5.63 | 5.84 | 3.7 |
| 12.0 m, 70° | 3.00 | 3.04 | 1.2 |

generating the stacked tori geometry. Use of the model is not anticipated to significantly skew any conclusions determined during design space exploration. Large configurations are predicted to use dense strap patterns with many radial straps. As such, the variation in wedge degree between two large-diameter design is likely not a significant factor in their overall deflection response.

### 3.3.7 Generalized Simplified Stacked Tori Decelerator Model: Mass Model

The second metric used to evaluate the decelerator performance, along with the surface deflection, is the IAD total mass. The surface deflection determines the decelerator rigidity and the total mass determines the penalty to the ballistic coefficient, described in Eq. 1, associated with the IAD. Optimal IADs designs are ones that minimize both of these metrics, when compared with IADs of similar scale and drag coefficient.

Stacked tori decelerators are composed of a series of inflatable tori held together with straps. Therefore, their mass can be determined from summing the mass of the straps, torus fabric, and inflation gas. It is assumed in this analysis that the structural components can be aggregated into a single area-based fabric density parameter. A constant area-based fabric density is used in this thesis for all configurations with the understanding that the fabric densities of larger-scale decelerators would likely be higher due to the denser strap patterns. Nevertheless, the fabric density uncertainty is not expected to impact comparisons between decelerators of similar scale and will impact the relative fabric mass slope, but not the ordering, between decelerators of

different scales. There is likewise no adjustment to the fabric density estimate based on the surrogate thickness model. Even though the simplified FEA model is simulated with an increased torus thickness, the thickness increase is strictly implemented to approximate the stiffness loss due to the removal of the pairing loop straps. In reality, this configuration would still have the same strap pattern and, therefore, the same fabric mass.

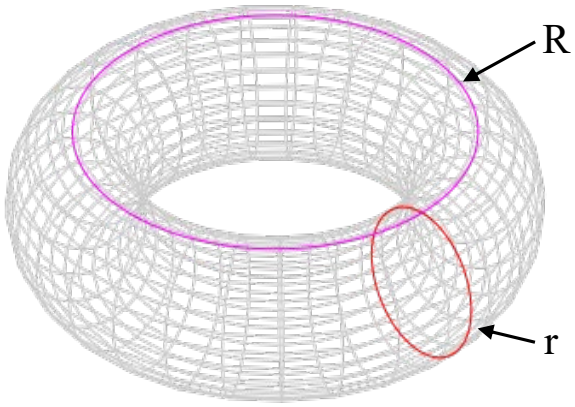


**Figure 71: Diagram of a torus describing the major and minor (cross-sectional) radii**

Ignoring the straps, which are combined into the fabric density equation, the stacked tori surface area and total fabric mass can, therefore, be calculated by summing the surface areas of each torus, described in Eq. 18. In the equation, $R$ is the torus major radius and $r$ is the cross-sectional radius, shown in Fig. 71. The total decelerator surface area is shown in Eq. 19, with the subscript $i$ referring to properties of the $N$ structural tori and the subscript $s$ referring to properties of the shoulder torus. It should be noted that the spars between tori are captured in this methodology because the spars are modeled with double thickness and result from the interactions between adjacent tori.

$$SA_{Torus} = 4\pi^2 Rr \tag{18}$$

$$SA_{Total} = 4\pi^2(r\sum_{N} R_i + r_s R_s) \tag{19}$$

The gas density is calculated from rearranging the ideal gas law, described in Eq. 20. In the equation, $P$ is the inflation pressure, $\mathcal{R}_{Gas}$ is the universal gas constant, $\mathcal{M}$ is the gas molar mass, and $T$ is the gas temperature. It is assumed that all inflation gas is pure nitrogen, which has historically been used in stacked tori decelerators. The temperature of the inflation gas during descent varies and is a complex function of the radiative and conductive heat transfer to the decelerator surface, as well conduction throughout the vehicle. Calculation of the temperature is impossible to assess without detailed knowledge of the entry profile and full decelerator material properties. Therefore, the inflation pressure is assumed to be determined at room temperature, around 22 °C for all vehicles in order to provide a consistent comparison.

$$P = \rho_{Gas}\frac{\mathcal{R}_{Gas}}{\mathcal{M}}T \tag{20}$$

The volume of a torus is shown in Eq. 21 and is summed over all tori to generate the expression for the total gas volume in Eq. 22. The summation does ignore the overlap between tori, assuming all tori cross-sections are perfectly circular with a radius $r$, which is accepted as error in the simplified model. However, this error is expected to be small compared to the overall gas volume.

$$V_{Torus} = 2\pi^2 R r^2 \tag{21}$$

$$V_{Total} = 2\pi^2(r^2\sum_{N} R_i + {r_s}^2 R_s) \tag{22}$$

The total mass of the decelerator is the sum of the gas and fabric masses, the product of the fabric density and total surface area and the product of the gas density

and the total volume, respectively. The expression for the total mass is seen in Eq. 23.

$$m_{Total} = \rho_{Fabric} SA_{Total} + \rho_{Gas} V_{Total} \tag{23}$$

### 3.3.8 Generalized Simplified Stacked Tori Decelerator Model: Angular Deflection Calculations

The simplified stacked tori validation model deflection results are all formulated in terms of the axial deflection of the aft-most point on torus $T_7$ in order to mirror the instrumentation from the static load testing. While this definition of deflection is convenient for validation purposes, it is not a good metric for characterizing the IAD surface deflection. The point chosen, on the outermost structural torus, is outside of the radial strap and subject to edge-effects that don't reflect the general surface deflection of the decelerator. In addition, the point is on the aft surface of the decelerator and, as a result, is not directly impacted by the aerodynamic pressure. Most importantly, however, is that the deflection is reported in terms of the axial deformation. Therefore, the same axial deflection on a 3 m model and a 12 m model would appear equally significant.

A much more appropriate metric for the decelerator deflection is the angular deformation of the surface under load. The angular deflection better relates to the design parameters describing the IAD shape and is insensitive to decelerator scale. Rotation is taken about the IAD attachment point to the centerbody and is measured at the interface of the radial strap and $T_{N-1}$, as seen in Fig. 72.

Being at the intersection of two structural members, this deflection point is less sensitive to local deformations and is a robust metric to track the decelerator global deflection. Nodes on torus $T_{N-1}$ are useful because they are far from the boundary conditions along the centerbody and any resulting local deformation effects and are also away from the decelerator edge and the associated edge effects. Also, tracking

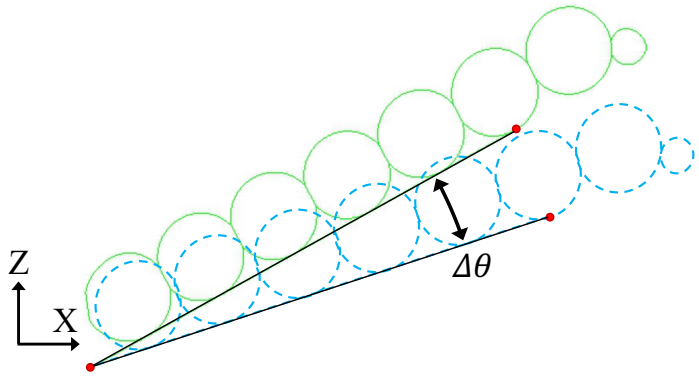


**Figure 72: Diagram of angular deflection calculation**

a node on the windward side of the decelerator allows for a direct assessment of the aerodynamic pressure effects rather than inferring them from the aft of the torus.

The Patran and Nastran FEA packages generate two files that are used to calculate the IAD angular deformation. The first of which, the BDF output from Patran, contains a detailed list of the nodes, elements, and loading information. The angular deflection routine first isolates all the node data and determines the center of rotation point (the radial strap attachment to the centerbody) by selecting the node with the smallest Z-coordinate. The deflection point is determined by selecting the node associated with both radial strap and torus elements that has the smallest Z-coordinate (note that the radial strap attaches to the tangency point and wraps around $T_{N-1}$).

Once the center of rotation and deflection nodes are determined, the PCH output from Nastran is used to identify the inflation and aerodynamic-loading deformation data for both nodes. The initial IAD half cone angle is calculated based on the deformed locations of the two nodes subject to inflation pressure loading and the final angle is calculated based on the aerodynamically-loaded deformed locations, with the angular deflection being the difference between the two. The angles are calculated between a line extended from the center of rotation parallel to the Z-axis and a line from the center of rotation through the deflection point.

The deflected angle is assessed between the inflation and aerodynamic-loaded

states because this mirrors actual planetary entry, where the IAD is inflated exoatmospherically and is deflected based on the aerodynamic loading during descent. However, because the decelerator geometries in this study are defined prior to applying the inflation pressure, this means that the deflected angle will be with respect to the inflated half-cone angle, which may be slightly larger than the cone angle design variable, depending on the decelerator scale and inflation pressure.

### 3.3.9 Generalized Simplified Stacked Tori Decelerator Model: Model Verification

Verification of the generalized simplified stacked tori model is necessary to ensure that the changes made to the simplified validation model do not adversely affect the performance predictions. This involves inspection of the finite element model session file to ensure it is coded properly as well as comparisons against known results.

The first verification study that is performed to assess the generalized model is a comparison against the 3.7 m simplified validation model. For this study, the generalized model parameters are adjusted to best match those of the baseline validation model, within the constraints of the generalized model definition. The geometric definition of the generalized model, synthesized based on the validation model characteristics, is able to match nearly exactly. The loading conditions, however, are different. The generalized model removes the temperature loading step used in the validation model to eliminate reliance on the static load test. Therefore, this difference must be accepted as a source of error. While the temperature loading does not directly impact the deflection, it does preload the components and likely contributes to a slight reduction in aerodynamic deflection. The other differences, the use of the thickness and wedge degree models, introduce some error as they are tuned to, but are not identical, to the baseline 3.7 m validation model.

The verification results are shown in Tables 5 and 6 for runs conducted at two different applied surface pressures. It is evident from the tables that the two runs

**Table 5: Deflection comparison between the 3.7 m, 70°, 12 psi simplified verification and generalized models at lower aerodynamic loading**

| | X-Def (m) | Y-Def (m) | Z-Def (m) | Abs-Def (m) |
|---|---|---|---|---|
| Validation Model | -1.77E-03 | 0.00 | 4.19E-02 | 4.02E-02 |
| Generalized Model | -1.47E-03 | -1.85E-05 | 4.23E-02 | 4.23E-02 |
| % Difference | -17.17% | N/A | 0.96% | 5.29% |

**Table 6: Deflection comparison between the 3.7 m, 70°, 12 psi simplified verification and generalized models at higher aerodynamic loading**

| | X-Def (m) | Y-Def (m) | Z-Def (m) | Abs-Def (m) |
|---|---|---|---|---|
| Validation Model | -2.62E-03 | 0.00 | 7.63E-02 | 7.46E-02 |
| Generalized Model | -1.88E-03 | -1.60E-05 | 7.93E-02 | 7.93E-02 |
| % Difference | -28.41% | N/A | 3.89% | 6.29% |

correlate very well. The Z-deflection results, the primary metric of interest that is used for the initial validation against the static load test data, are within 5%. This demonstrates that the generalized simplified stacked tori model is able to accurately simulate the IAD deflections. The Y-deflection predictions are similarly small, only off by an order of $10^{-}5$ m. The X-deflection results are the most different and are likely a result of the temperature loading step, which contracts the cords running along the interior of the tori major circumferences to counteract the slight cone angle increase due to inflation. The deviation in X-deflection isn't a direct result of the temperature loading, because the total deflection is taken with respect to the post-temperature loaded state, but likely contributes to a small different in the pre-aerodynamically-loaded surface angle and cord tension, which influence the results. Nevertheless, these results demonstrate that the simplifications and assumptions made in the development of the generalized model, such as the temperature loading and thickness and wedge models, do not drastically impact the surface deflection.

A single FEA session file can simulate a wide range of topologically equivalent designs, accommodating variations in major diameter, minor diameter, and cone angle. However, a unique session file must be created for each design with a unique number

of tori because they are not topologically equivalent. A direct comparison is possible between the stacked tori validation model and the generalized model with 7 tori but is not possible for generalized model configurations with other numbers of tori due to the lack of equivalent test articles with the same geometry. Therefore, each unique session file must be verified to demonstrate that it is coded properly and is able to simulate the relevant IAD response.

Like the 7-tori general model, each session file is verified through inspection of the code for each aspect of the FEA model, ensuring its definition is equivalent to that used in the 7-torus model with the additional modifications necessary for the greater or fewer number of tori. In addition, the design space is evaluated by performing a sweep in the number of tori to ensure continuity of results and the preservation of trends. While parameter sweeps do not prove the accuracy of a model, they are often able to indicate potential errors and are a valuable tool in the absence of any other supporting data.

3.7 m, 70°, 12 psi models, like the one discussed in the above validation, are generated for the parameter sweep to relate the topological variants to the validated 3.7 m static load test model. Results are simulated for the full range of number of tori, simulating vehicles from 5 to 12 structural tori at two different applied aerodynamic pressures. The Z-deflection of the node on the leeward apex is tracked for each configuration and is plotted in Fig. 73. As observed in the figure, the curves with respect to number of tori are continuous and do not display any obvious outliers. A gradual increase in deflection is observed with increasing number of tori, which is to be expected as the tori cross-sections get smaller and provide less resistance to deformation.

The combination of code inspection and observation of trends among topological variants is used to determine that the generalized simplified model is developed

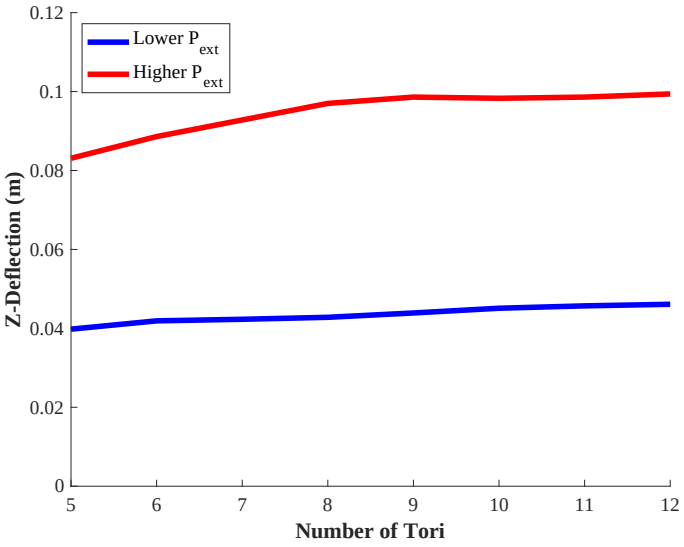


**Figure 73: Results of the generalized simplified model parameter sweep in number of tori**

properly. The generalized model predicts similar results to the simplified model validated in Section 3.2.4 and topological variants are shown to preserve expected trends in the data. The primary uncertainty that cannot be verified is the impact on the models from design parameters that do not have sufficient supporting evidence to evaluate, such as the number of tori and cone angle. These uncertainties are accepted in this analysis as possible sources of error that are expected to impact the slopes of observed trends, but not necessarily relative ordering of design performance. When further supporting data becomes available, the models can be adjusted to accommodate the new experimental evidence and will be able to provide more accurate performance predictions.

## *3.4 Simplified Tension Cone Model Development*

Like the stacked tori configuration, exploration of the tension cone design space requires a validated simplified model to rapidly simulate many solutions. Validation efforts for the stacked tori configuration demonstrate that simplified models can accurately capture the deformation of complex multi-torus vehicles. While less complex

than stacked tori decelerators, tension cone configurations employ a large tension skirt that behaves significantly differently than the inflation pressure supported structural tori. Therefore, tension cone validation efforts must show that simplified models can also accurately simulate the flexible tension skirt. If so, it can be assumed that tension cone decelerators can be reliably modeled, having demonstrated the accurate simulation of both the tension cone tension skirt and structural torus.

### 3.4.1 Simplified Tension Cone Model: Tension Skirt Validation

Despite models of entire tension cone decelerators being less prevalent in the literature, analytical descriptions of the tension cone tension skirt are available. One particular formulation by Anderson et. al. uses linear membrane theory to analytically calculate the geometry and stress state developed in a tension skirt when subject to an applied axisymmetric load [36]. This analytical description is, therefore, a valuable data set from which to evaluate the ability of finite element analysis to simulate the deformed tension skirt and, by extension, the full tension cone response. The analytical model is also particularly useful because the geometry and symmetry assumptions mirror those used in the simplified finite element models.

Figure 74 shows a diagram of the Anderson tension cone model, depicting the stress directions and geometric variables. Note that the variable $\sigma$ is used in this thesis to replace $N$ from the original literature paper in order to avoid ambiguity with the number of tori variable used elsewhere in this thesis.

#### *3.4.1.1 Tension Skirt Validation: Analytical Model*

The analytical model assumes that the tension skirt is in a tensile stress state and that the ratio of the circumferential stress ($\sigma_\theta$) to the meridional stress ($\sigma_\phi$) is a constant, described in Eq. 24. These assumptions give rise to two design variables, the stress ratio ($\lambda$) and the shape factor ($B^2$), which define the decelerator shape and stress distribution. For a uniform applied pressure distribution ($P$), the tension skirt

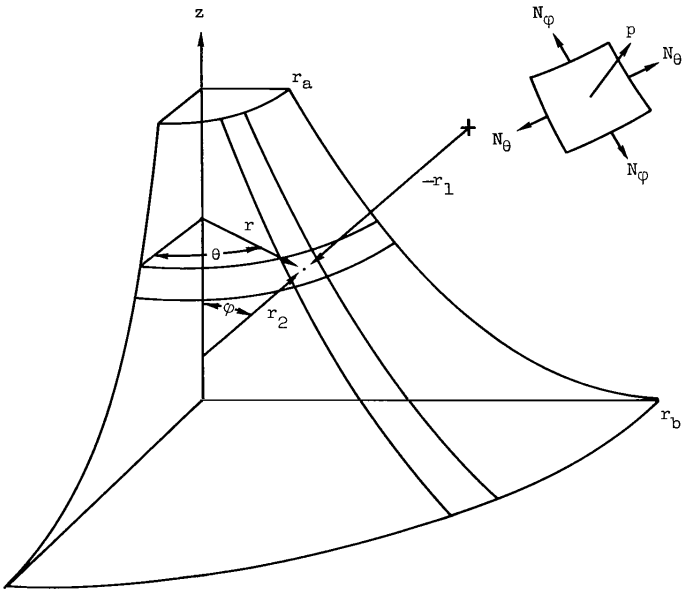


**Figure 74: analytical tension skirt model and parameters [36]**

geometry can be calculated via Eqs. 25 and 26. Axial and radial coordinates of the tension skirt for the shape parameters $\lambda = 0.3$ and $B^2 = 0.5$ (used throughout this validation study) are listed in Table 7 [36].

$$\lambda = \frac{\sigma_\theta}{\sigma_\phi} = constant \tag{24}$$

$$sin(\phi) = B^2\Big[\Big(\frac{r_b}{r}\Big)^\lambda - \Big(\frac{r}{r_b}\Big)^{(2-\lambda)}\Big] \tag{25}$$

$$\frac{\partial z}{\partial r} = -tan(\phi) \tag{26}$$

The shape parameters also determine the stress state generated in the tension skirt. Equation 27 describes how the meridional stress varies based on radial location. In the equation, $r$ is the radial location, $\sigma_{\phi,0}$ is the meridional stress calculated at the base (interface of the tension skirt and structural torus), $\lambda$ is the specified stress ratio, and $r_b$ is the radius at the tension skirt interface to the torus. The meridional stress at the tension skirt base can be calculated based on the pressure distribution and

**Table 7: Axial and radial coordinates of the tension skirt for $\lambda = 0.3$ and $B^2 = 0.5$ [36]**

| Radial Coordinates | Axial Coordinates |
|---|---|
| 0.20 | 0.3618 |
| 0.25 | 0.3061 |
| 0.30 | 0.2595 |
| 0.35 | 0.2193 |
| 0.40 | 0.1840 |
| 0.45 | 0.1527 |
| 0.50 | 0.1251 |
| 0.55 | 0.1006 |
| 0.60 | 0.0791 |
| 0.65 | 0.0603 |
| 0.70 | 0.0442 |
| 0.75 | 0.0307 |
| 0.80 | 0.0197 |
| 0.85 | 0.0111 |
| 0.90 | 0.0049 |
| 0.95 | 0.0012 |
| 1.00 | 0.0000 |

shape factor. Therefore, both the meridional and circumferential stresses throughout the article can be calculated for a chosen pressure distribution and shape factor, as shown in Eqs. 28 and 29. In the equations, $t$ is the tension skirt thickness. These equations assume a constant base radius during deformation and, as such, do not allow the tension skirt to move radially inward or outward at the base. As a result, the analytical description of the tension skirt approximates the structural torus as being rigid. This implies that the circumferential strain at the nose and base are equal to zero, which can be shown to be equivalent to Eq. 24 when $\lambda$ is the Poisson's ratio, $\nu$.

$$r^{1-\lambda}\sigma_\phi = \sigma_{\phi,0} {r_b}^{1-\lambda} \tag{27}$$

$$\sigma_\phi = \frac{P r_b}{2B^2 t}\left(\frac{r_b}{r}\right)^{1-\lambda} \tag{28}$$

$$\sigma_\theta = \lambda \sigma_\phi \tag{29}$$

#### *3.4.1.2 Tension Skirt Validation: Finite Element Model*

A finite element model of the tension skirt is developed in Patran/Nastran and is used for validation against the analytical formulation. To mimic the analytical assumptions using FEA, the validation model simulates the tension skirt and includes the effects of the rigid nosecone and structural torus through boundary conditions, fully constraining the nodes along the interface to the aeroshell and allowing axial displacement only for the nodes along the interface to the torus. The design variables used to construct the tension cone are listed in Table 8. Note that, while the model is constructed with metric parameters, the applied pressure is presented in imperial units to reflect the original literature results. Isotropic material properties are assumed for the flexible tension skirt, with values listed in Table 9 [106]. A picture of the final meshed FEA model is shown in Fig. 75, composed of 15,386 four-node shell elements.

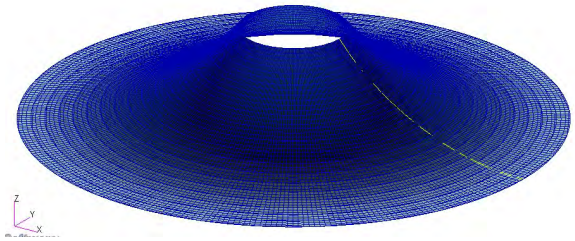

**Figure 75: Meshed FEA model of the tension skirt**

**Table 8: Design variables used to create the FEA validation model [106]**

| Property | Symbol | Units | Value |
|---|---|---|---|
| Stress ratio | $\lambda$ | | 0.3 |
| Shape factor | $B^2$ | | 0.5 |
| Uniform pressure | $P$ | psi | 0.1, 1.0 |

**Table 9: Isotropic material properties used in the tension cone FEA model [106]**

| Property | Symbol | Units | Value |
|---|---|---|---|
| Density | $\rho$ | kg/m$^3$ | 1125.88 |
| Thickness | $h$ | m | 0.00033401 |
| Young's modulus | $E$ | Pa | 2.66E+9 |
| Poisson's ratio | $\nu$ | | 0.3 |
| Shear modulus | $G$ | Pa | 1.023E+9 |

#### *3.4.1.3 Tension Skirt Validation: Results*

Results of the tension skirt model validation study are shown in Figs. 76 and 77 for applied external pressures of 0.1 psi and 1.0 psi, respectively. The graphs depict both the meridional and circumferential stresses calculated from the FEA model against the theoretical values predicted from linear membrane theory. Overall, the finite element results correlate well with the analytical model. Maximum percent differences between the FEA and analytical meridional stress predictions are 3.0% for the 0.1 psi external pressure case and 2.8% for the 1.0 psi case. Maximum percent differences for the circumferential stress predictions are 27.2% for 0.1 psi external pressure and 29.9% for 1.0 psi external pressure.

It can be observed from these results that the FEA and analytical meridional stress predictions are almost identical, with small deviations arising near the tension skirt base. The circumferential stress predictions agree in the center of the tension skirt, but do not maintain the same degree of correlation throughout. Other studies in the literature have observed the circumferential stresses to be sensitive to small shape variations near the base of the tension skirt, reproducing similar deviations in the circumferential stress predictions between FEA and analytical models as those presented here [106]. Deviation in circumferential stress predictions near the nose are likely due to the adjacent boundary conditions in the FEA model and the local geometry in this region. The nose of the theoretical tension cone shape becomes

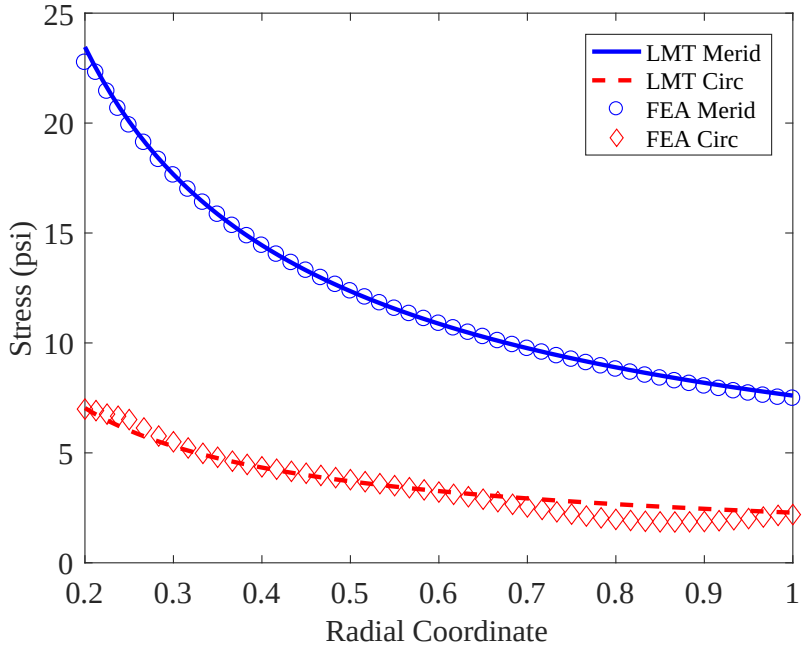


**Figure 76: Meridional and circumferential stress results predicted by the analytical linear membrane theory model (LMT) and FEA models for a 0.1 psi applied external pressure**

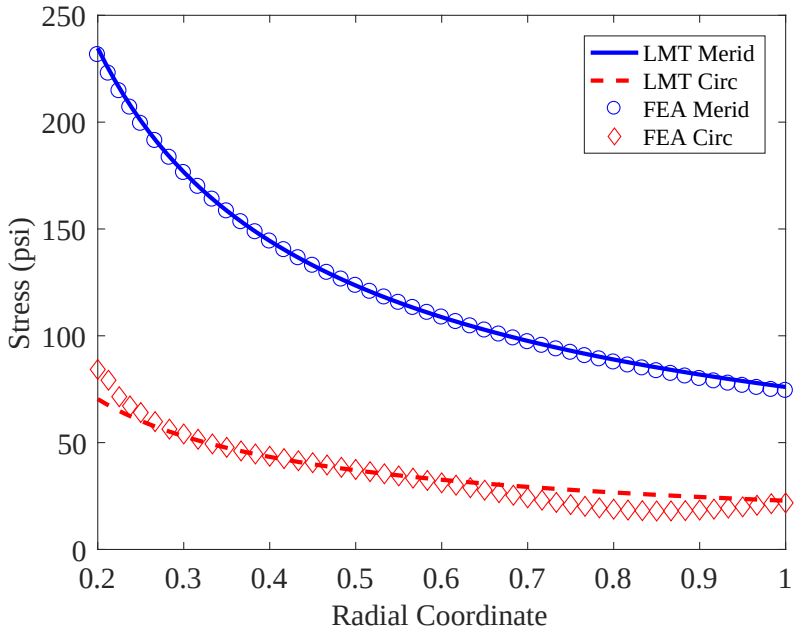


**Figure 77: Meridional and circumferential stress results predicted by the analytical linear membrane theory model (LMT) and FEA models for a 1.0 psi applied external pressure**

very slender, with contours approaching parallel to the axis of revolution. In this region, the applied pressure, acting normal to the tension skirt surface, is directed nearly radially inwards. This loading is primarily resolved in the circumferential stress direction and likely contributes to the increased offset.

These results show that the finite element predictions are in good agreement with analytical tension skirt models, exhibiting similar trends and stress magnitudes throughout the tension skirt. Results correlate particularly well in the middle of the decelerator, away from the imposed boundary conditions, with goodness of agreement also maintained at different loading conditions. The tension skirt validation results demonstrate that the simplified finite element tension cone models can accurately resolve the deformation of a tension skirt under load. When considered in conjunction with the previous stacked tori validation results, which show the simplified models able to capture the deformation of structural tori, these validation studies support the assertion that simplified finite element modeling can sufficiently simulate the deformation of a full tension cone decelerator.

### 3.4.2 Simplified Tension Cone Model: Geometry

The simplified tension cone model geometry, shown in Fig. 78, is composed of a tension skirt extending from the centerbody to a single structural torus and shoulder torus. Unlike the linear membrane theory analytical model, the tension skirt is implemented as a straight conical frustum. This is done to simplify the modeling and to eliminate the dependence on the two additional variables, $\lambda$ and $B^2$, thus reducing the model dimensionality. While this approximation is expected to influence the stress distribution arising in the tension skirt, it is anticipated that such deviations would be small compared to the other approximations made in the simplified modeling.

The tension skirt is modeled as being attached to the centerbody and extends

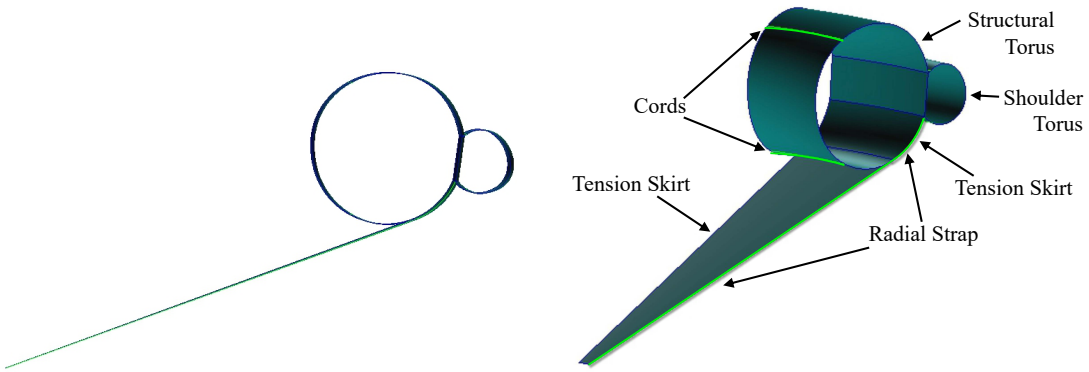


(a) Cross section view of the tension cone model

(b) Tension cone wedge view showing modeled components

**Figure 78: Geometry of simplified tension cone model**

tangent to the structural torus, wrapping around until it terminates at the intersection to the shoulder torus. The radial strap is attached to the centerbody like the tension skirt and likewise extends tangent to the first torus, wrapping around until the shoulder torus intersection. The radial strap is modeled as being attached to the tension skirt along its entire length, which is equivalent to being stitched or bonded in a test article. No other straps are modeled.

Two sets of boundary conditions are used to constrain the model. The first simulates the centerbody attachment and fixes all nodes along the nose of the tension skirt (radial distance of $R_{Cen}$ away from the axis of symmetry). The second enforces symmetry along the front and back cross-sectional faces of the wedge model by constraining the azimuthal translation along with the radial and axial rotation, just like the stacked tori model. The inflation and aerodynamic loading conditions are identical to the stacked tori model, but with the aerodynamic pressure also applied normal to the tension skirt face along with the tori.

### 3.4.3 Simplified Tension Cone Model: Model Development

The simplified tension cone model is based on the generalized simplified stacked tori model, removing all but the last structural torus and shoulder torus. Instead of

the remaining tori, the tension skirt is added, extending from the nose cone to the single structural torus. The radial strap is attached to the tension skirt along its entire length, from the nose cone to around the structural torus. The removal of the multiple tori eliminates the need for the number of tori parameter, $N$, and replaces it with the tension skirt radius parameter, $R_{TS}$, which defines the radial extent of the tension skirt. The rest of the design variables apply to both models and are retained. Likewise, all applicable fixed variables, such as the ratio of the shoulder torus radius to the structural torus radius and the shoulder torus overlap ratio, are identical between the stacked tori and tension cone decelerators. The remaining fixed variables, including the centerbody overlap ratio and structural torus overlap ratios, are not needed.

The tension skirt is modeled to have the same material properties as the structural tori. Given that the structural torus fabrics have been developed to withstand large tensile loads during hypersonic entry, these materials are assumed to be extensible to use in the tension skirt. In addition, the torus thickness model, developed to account for the removal of the pairing loop straps by scaling the modeled torus thickness, is also applied to the tension skirt. Despite the tension skirt not utilizing pairing loops, some additional strap pattern will likely be incorporated into the tension skirt to help transmit aerodynamic loads from the decelerator to the centerbody. With no existing applications of tension cone decelerators to hypersonic entry, it is assumed without supporting data that the structural impact of this strap pattern would be similar to that of the pairing loop straps between structural tori and, as such, the thickness models would be similar. The wedge degree model, representing the radial strap pattern density, is also applied to the tension cone model without modification.

The use of the thickness and wedge degree models allows for an unbiased comparison between the stacked tori and tension cone configurations, agnostic of the modeling implementation. This is equivalent to comparing the overall impact of each

configuration instead of a comparison of the strap pattern modeling, which is more useful for the high-level trades performed during conceptual design.

### 3.4.4 Simplified Tension Cone Model: Geometry Calculation

Like the stacked tori configuration, the tension cone model calculates the torus radius, $r$, from the specified design variables by relating the decelerator side length and base radius, $L'$ and $L$, shown in Fig. 79. The parameters $L$ and $L'$ can be calculated from the design variables and fixed variables via Eqs. 30 and 31. In the equations, $\theta'$ is the complement to the half cone angle, $\theta$, and $R_{TS}$ is the radial coordinate of the tension skirt tangency point to the structural torus.

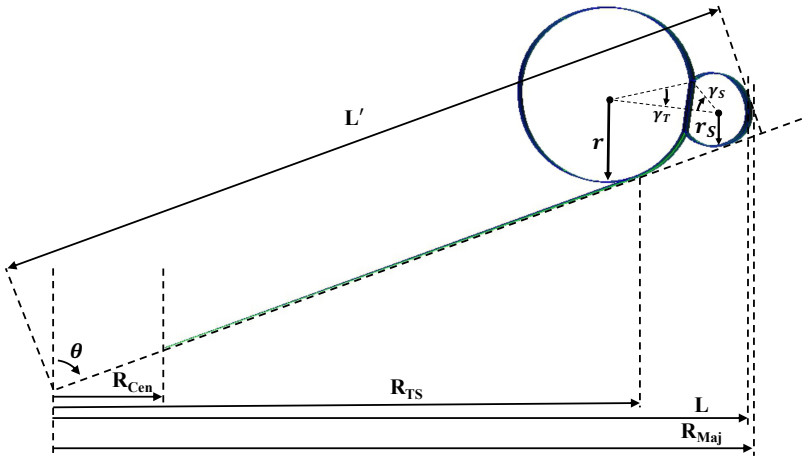


**Figure 79: Geometry definition of the simplified tension cone model**

$$L = R_{Maj} - r_s\big(1 - \cos(\theta')\big) \tag{30}$$

$$L' = \frac{R_{TS}}{\cos(\theta')} + \sqrt{\big(r\cos(\gamma_T) + r_s\cos(\gamma_S)\big)^2 - (r - r_s)^2} + r_s \tag{31}$$

Newton's method is used to converge on the value of the torus radius, $r$, that satisfies Eq. 32 by iteratively driving the expression to zero. Based on a reformulation of the $1^{st}$ order Taylor approximation of the function $f(r)$, Newton's method requires the expression for the first derivative of the function, shown in Eq. 33.

$$f(r) = L' - \frac{L}{\cos(\theta')} = 0 \tag{32}$$

$$f'(r) = \frac{\partial\left(L' - \frac{L}{\cos(\theta')}\right)}{\partial r} = \\ + \frac{1}{2}\Big[\big(r\cos(\gamma_T) + r_s\cos(\gamma_S)\big)^2 - (r - r_s)^2\Big]^{-\frac{1}{2}} \\ * \Big[2\big(r\cos(\gamma_T) + r_s\cos(\gamma_S)\big)\big(\cos(\gamma_T) + \epsilon\cos(\gamma_S)\big) - 2(r - r_s)(1 - \epsilon)\Big] \\ + \frac{\epsilon}{\cos(\theta')} \tag{33}$$

Determining the value of the torus radius fully defines the tension cone geometry. However, unlike the stacked tori configuration, due to the introduction of the tension skirt, certain combinations of design variables can lead to invalid geometries. The tension cone model assumes there is no contact between the structural torus and the centerbody. For small values of $R_{TS}$ relative to the major radius, $R_{Maj}$, the resulting structural torus radius can be large enough such that the torus inner surface interferes with the theoretical boundary of the centerbody. Therefore, an additional constraint is added to the tension cone geometry definition to ensure the torus and centerbody do not overlap, expressed in Eq. 34. Due to the functional dependence on the torus radius, $r$, this constraint can only be evaluated after the geometry definition is solved, with a negative result indicating an invalid geometric definition and the termination of the analysis routine.

$$R_{TS} \geq R_{Cen} + r\big(1 + \sin(\theta')\big) \tag{34}$$

### 3.4.5 Simplified Tension Cone Model: Mass Model

The primary addition in the tension cone mass model is the tension skirt mass term. Because the tension skirt does not utilize a supporting inflation gas, it only contributes to the fabric mass term based on its surface area. The region of the tension

skirt between the centerbody attachment point and the torus tangency point is the geometry of a conical frustum, or a cone with a flat truncated nose. The surface area of a conical frustum is defined in Eq. 35, where $S_{ConFrust}$ is the side length of the skirt, defined in Eq. 36.

$$SA_{ConFrust} = \pi(R_{TS} + R_{Cen})S_{ConFrust} \tag{35}$$

$$S_{ConFrust} = \frac{R_{TS} - R_{Cen}}{\sin(\theta)} \tag{36}$$

In the simplified model, the tension skirt also wraps around the first torus, terminating at the spar. This is implemented to approximate the anticipated integration of a tension skirt into a test or flight article, where the tension skirt will likely be stitched into the torus fabric near the outside circumference of the torus. Shown in Fig. 80, the surface area of the tension skirt wrap around section is defined by sweeping a line segment from the tangency point with the torus through an angle of 90° and revolving that line about the IAD axis of symmetry, represented by the double integral in Eq. 37. This expression can be solved to produce Eq. 38. The 90° sweep is chosen to approximate the location of the spar overlap region between the two tori. As seen in Fig. 80, the sweep tends to slightly over-predict the total extent of the tension skirt. However, it produces a calculation that is independent of each decelerator's specific geometry or implementation of the tension skirt. As a result, the consistent sweep angle enables an unbiased comparison across all designs. The 90° sweep is also slightly different than how the tension skirt is implemented in the finite element model, where the tension skirt terminates at the spar. However, it is anticipated that this slight increase in the stiffness within the overlap of the two adjacent tori is negligible.

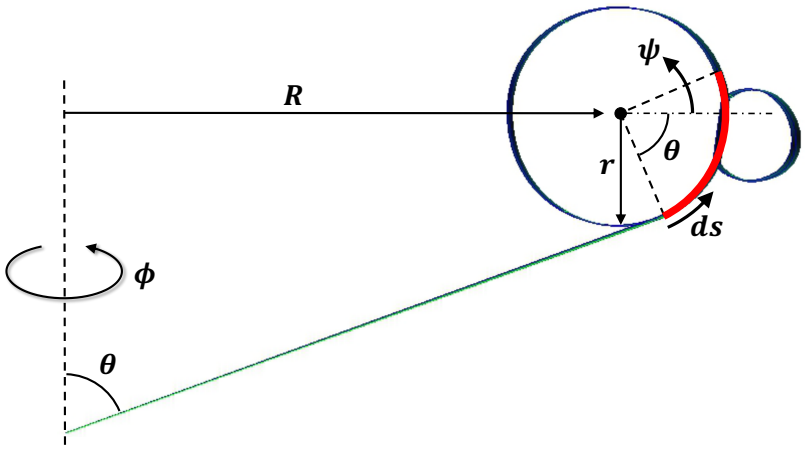


**Figure 80: Depiction of the tension skirt wrap around region used in the surface area calculations**

$$SA_{WrapAround} = \int_{0}^{2\pi} \int_{-\theta}^{\frac{\pi}{2}-\theta} \Big(R + r\cos(\psi)\Big) r d\psi d\phi \tag{37}$$

$$SA_{WrapAround} = \pi^2 Rr + 2\pi r^2 \Big(\cos(\theta) + \sin(\theta)\Big) \tag{38}$$

The resulting total surface area is expressed in Eq. 39 and includes the contributions of the structural torus, shoulder torus, and tension skirt. The total surface area is multiplied by the aggregate fabric density, like the stacked tori configuration, to determine the total fabric mass. This methodology therefore assumes that the tension skirt has the same averaged fabric density as the structural tori. As mentioned in the previous section, the tension skirt is assumed to have a strap pattern and employ the same materials as the structural tori. Thus, in the absence of supporting data, it is assumed that the aggregate density of the tension skirt region is the same as that of the structural tori.

$$SA_{Total} = 4\pi^2(rR + r_s R_s) + \frac{\pi(R_{TS}^2 - R_{Cen}^2)}{\sin(\theta)} + \pi^2 Rr + 2\pi r^2 \Big(\cos(\theta) + \sin(\theta)\Big) \tag{39}$$

Because the tension skirt does not contribute to the total inflated volume, the expression for the tension cone gas volume is the same as that for the stacked tori

evaluated at $N = 1$, seen in Eq. 40. The total mass of the decelerator is likewise the same as the stacked tori configuration, summing the product of the fabric surface area and aggregate fabric density and the product of the inflated volume and inflation gas density.

$$V_{Total} = 2\pi^2(r^2R + r_s^2R_s) \tag{40}$$

## *3.5 Stacked Tori Design Space Exploration Case Study*

The computationally efficient simplified models enable the simulation of many different IAD configurations. This is necessary for the initial trade studies performed during conceptual design that simulate many candidate configurations in order to identify areas of the design space with favorable system performance. Furthermore, design space exploration studies can be used to develop response surface models that interpolate the performance results and enable rapid performance predictions of new decelerator geometries.

A case study is presented here, which investigates the stacked tori decelerator design space. Parameter sweeps are performed for all the design variables to identify their relative influence on the decelerator structural and mass performance. These results are also used to generate response surface equations analytically approximating the design space results.

### 3.5.1 Stacked Tori Design Space Exploration Case Study: Design Space

The stacked tori design space is constructed to allow for a full exploration of the relevant design parameters and their interactions. Sweeps are performed on each of the independent design variables and a full factorial design of experiments is conducted, solving for each possible combination of design parameter values. Despite its expense, the full factorial design space is invaluable, as it provides a sufficient number of candidate design solutions to use in training and validating the response surface

model. The full factorial design of experiments is enabled by the efficient simplified stacked tori model, providing a full solution on the order of minutes and allowing for solutions to the entire design space to be obtained in a few days.

The design space parameters and their possible values are shown in Table 10. A total of 5 configurational parameters are studied, discretized into 3 to 4 possible values. For the full factorial design of experiments, this corresponds to a total of 576 possible unique designs, with 468 valid configurations after applying the design constraints.

**Table 10: Design variable values used in the stacked tori design space exploration case study**

| Parameter | Variable | Units | Values |
|---|---|---|---|
| Major Diameter | $D$ | m | 3.7, 6.0, 12.0, 20.0 |
| Centerbody Diameter | $D_{Cen}$ | m | 0.25, 1.00, 3.00, 6.00 |
| Half-Cone Angle | $\theta$ | ° | 50, 60, 70 |
| Number of Tori | $N$ | N/A | 5, 7, 9, 12 |
| Inflation Pressure | $P_{Inf}$ | kPa | 50, 70, 100 |
| Aerodynamic Pressure | $P_{Aero}$ | Pa | 1000 |

The design space domains are all informed by heritage studies and test programs to determine realistic ranges for each of the design parameters. The major diameter takes values between 3.7 m and 20.0 m, with the 3.7 m, 6.0 m, and 12.0 m options based on the static load test, NFAC wind tunnel test, and high fidelity FEA model configurations [117, 118, 16]. The smaller diameters are applicable to ground test or small flight test vehicles such as IRVE and IRVE-III whereas the larger, 12.0 m diameter has applications to vehicle recovery efforts such as the HULA launch vehicle booster recovery mission [17, 42, 119, 120, 121]. The 20.0 m upper bound is a projected estimate for the diameter of a potential human-class mission (10+ MT payload mass) such as those discussed in the EDL:SA study, which considered HIAD decelerators between 20 m and 80 m diameter [76].

The centerbody diameter values span the range of 0.25 m to 6 m and are similarly

influenced by heritage designs. The lower bound of 0.25 m is based on the 3.7 m static load test article, which has a centerbody 0.4 m in diameter. The upper bound of possible centerbody diameters is limited to below 10 m based on the largest anticipated payload shrouds of future launch vehicles [76]. However, a constraint is enforced on the design space such that the centerbody diameter is no more than half the major diameter for valid designs. Therefore, the maximum centerbody diameter considered in the design space study is 6 m to allow for valid geometries with both the 12.0 m and 20.0 m major diameter configurations. The two intermediate values of 1 m and 3 m are similar to the centerbody diameters of the 6.0 m and 12.0 m validation models, with diameters of 1.2-1.8 m and 4.0 m, respectively, while staying within the $\frac{1}{2}D_{Maj}$ constraint of the configuration with the next smallest major diameter.

The half-cone angle values chosen for the design space are taken directly from heritage test vehicles. Early HIAD test vehicles, such as IRVE-III and IRVE-II, employed a 60° half-cone angle, based on its demonstrated stability characteristics for reentry missions. More recent configurations, such as the static load test article, transitioned to a 70° half-cone angle in order to increase the vehicle drag area. Stability concerns arise for vehicles with half-cone angles increasing above 70° so a third value of 50° is chosen for the design space study to increase the half-cone angle domain and better identify the sensitivity of the performance results.

There is significantly less heritage data to form a basis for the reasonable domain of the number of tori. Both the 3.7 m and 6.0 m, 60° configurations utilize 7 structural tori whereas the 6.0 m, 70° configuration uses 6. It is assumed that larger diameter vehicles, such as the proposed 20+ m diameter human-class decelerators, will require more tori to span the larger side length. Therefore, 12 tori is chosen as the upper limit for the design space. An additional constraint is enforced on all designs resulting from any combinations of parameters such that the tori cross sectional diameters are greater than 0.2 m or smaller than 2.0 m, the lower bound being a practical limit

for structural members and the upper bound being a reasonable manufacturing limit. For reference, a 20.0 m, 50° configuration with a 0.25 m diameter centerbody and 12 structural tori would have tori cross section diameters of approximately 1 m.

The inflation pressure values considered in the design space are taken directly from the NFAC wind tunnel test program. The 8, 10, and 15 psi inflation pressures used in the NFAC test correspond to 55, 69, and 103 kPa, respectively. These values are rounded and used in the design space. While the NFAC wind tunnel test sometimes specified different inflation pressures for different tori, this study considers only uniform inflation pressures to aid in establishing trends and sensitivities to the design variables.

The aerodynamic pressure, despite being specified for each run of the design space, is not a design variable and is instead a function of the vehicle characteristics, atmosphere, and the resulting trajectory. A single aerodynamic pressure is chosen to enable comparisons between different stacked tori configurations. Performance variation with respect to aerodynamic pressure is not evaluated because the range is so dependent on the vehicle architecture and mission, which is outside the scope of this study. The aerodynamic pressure value chosen is based on the results of the EDL systems analysis study, which simulated descent trajectories for several candidate architectures to land humans on Mars [76]. Of the 8 architectures considered, 5 of them utilized HIADs for hypersonic deceleration. The upper bound of peak dynamic pressure observed over all configurations was 10 kPa, occurring in an architecture utilizing a mid-L/D rigid aeroshell instead of a HIAD for hypersonic deceleration. Dynamic pressures for architectures employing HIADs ranged from 600 Pa, with 68-82 m lifting HIADs, to 4.2 kPa, with 23 m lifting HIADs. Note that the use of lifting HIADs is expected to reduce the peak dynamic pressure compared to a ballistic HIADs such as those considered in this study. With a desire to enable a uniform comparison between HIAD configurations across a wide range of scales and mission

classes, a moderate value of 1000 Pa is chosen for the design space simulations to induce sufficient deformation while avoiding non-linear deflections that would result from extreme loading.

### 3.5.2 Stacked Tori Design Space Exploration Case Study: Results

The results of the full stacked tori design space study are shown in Fig. 81. The graph plots the angular deflection of the HIAD surface along the x-axis against the total mass (sum of the fabric and gas mass) along the y-axis. Preferable designs are ones that result in both low deflection and low mass relative to other configurations of similar scale (configurations with the same drag area).

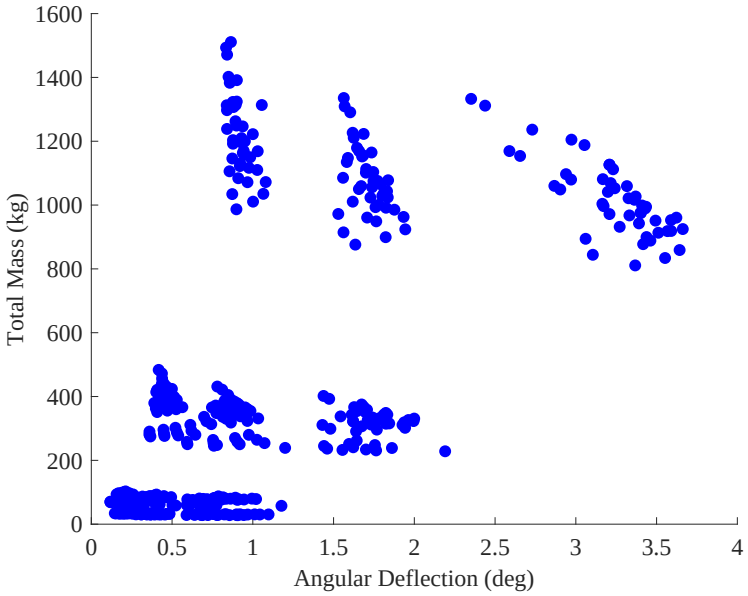


**Figure 81: Stacked tori design space results**

The design space graph exhibits a distinct clumping of the results, with several solutions producing similar mass and deflection values. This clumping typically indicates that a subset of the design parameters dominates the variability in the response. Each variable's impact on the design space can be determined by recoloring Fig. 81 based on unique values of the design parameters. The grouping of colors can help to visually determine the sensitivity of the response to that individual parameter, with

dominant variables defining the structure of the isolated groups and non-dominant variables having similar parameter values dispersed throughout the design space.

Figure 82 shows the design space results sorted by major diameter. Unique values of the major diameter clearly separate the data into different horizontal bands. Adjacent bands exhibit a large jump in mass and a shift in the range of deflection, with both the mass and angular deflection increasing with increasing major diameter. It is clear from the figure that the major diameter dominates the variability in the design space response. Configurations with unique values of major diameter are distinct from each other and span the entire range of both total mass and angular deflection, with minimal to no overlap between distinct groups.

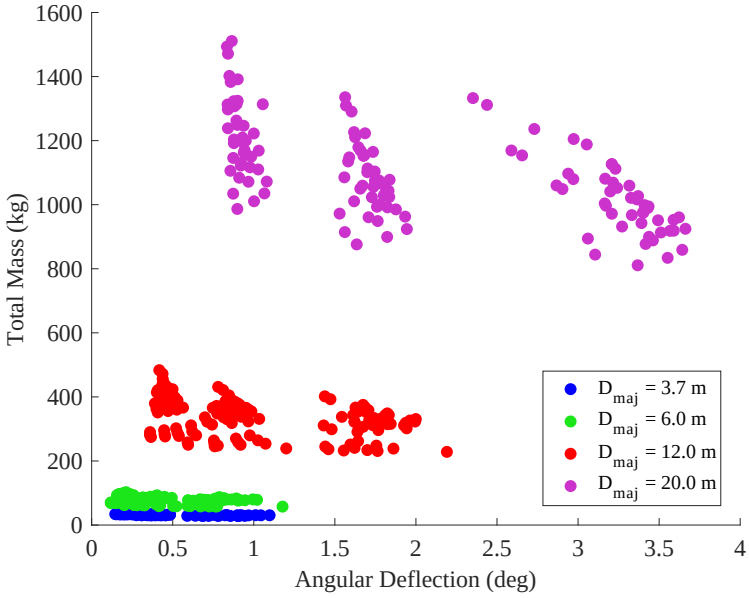


**Figure 82: Design space results organized based on values of major diameter**

Figure 83 shows the design space results sorted by half-cone angle. Like the major diameter, unique values of the half-cone angle also separate the design space results into separate groups. Except for the $D_{Maj} = 3.7$ m and 6.0 m results, there is minimal overlap between distinct groups. Nevertheless, the spacing between groupings isolated by the half-cone angle is smaller than between different values of $D_{Maj}$, indicating

that it is a less-dominant parameter. The results also show that the cone angle has a large effect on the surface deflection, with increasing cone angle values being able to scale from the smallest to largest deflection values. The total mass is, conversely, relatively insensitive to the half-cone angle, with a minimal reduction in the range of mass values between groupings with increasing cone angle.

Figure 84 shows the design space results sorted by the number of tori. It is evident from the significant scattering of these results that the number of tori is not a major contributor to the variability of the results. Instead, this parameter starts to segment individual groups of results into definable sub-structures. In general, increasing number of tori corresponds to a decrease in the range of angular deflection, with minimal overlap between adjacent groups. The total mass results show a much subtler impact, varying across the design space dependent on the values of other parameters.

Figures 85(a) and 85(b) show the design space results sorted by the values of the centerbody diameter and inflation pressure, respectively. Like the number of

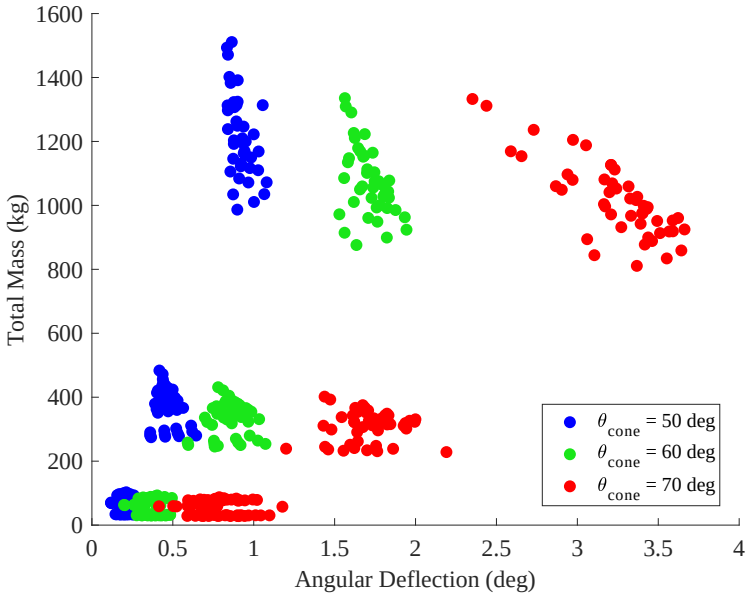


**Figure 83: Design space results organized based on values of half-cone angle**

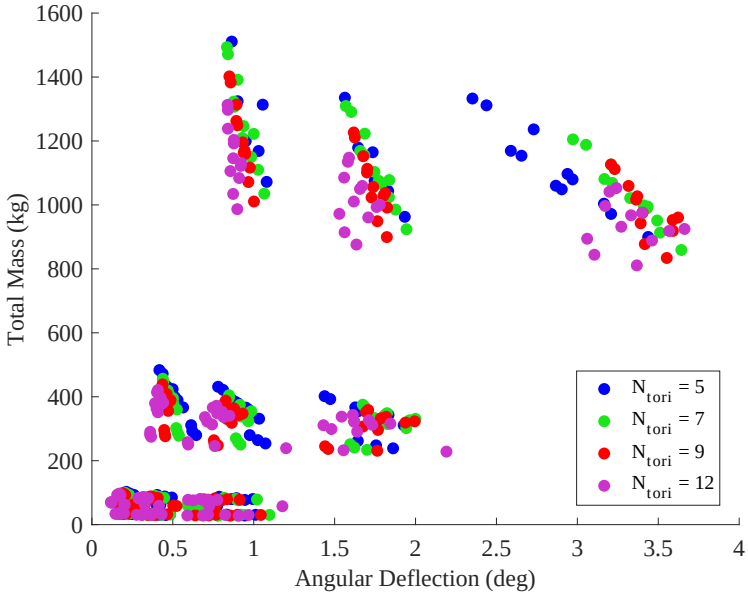


**Figure 84: Design space results organized based on number of tori**

tori results, the designs spaces exhibit a scattering of results, distributed within the individual data groups. This indicates that both parameters do not contribute significantly to the overall result variation.

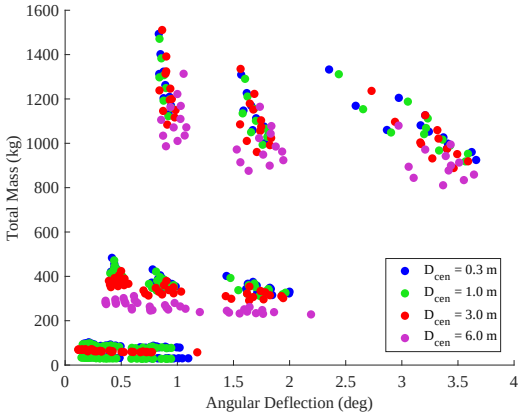


(a) Design space results organized based on values of centerbody diameter

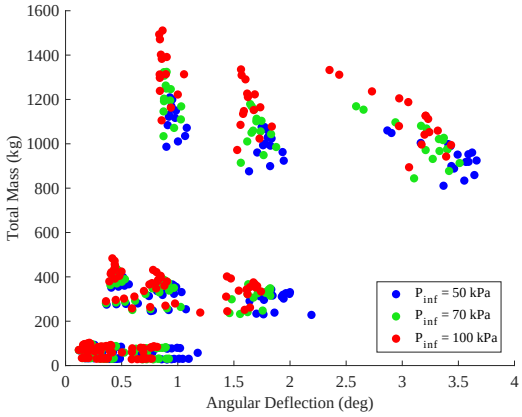


(b) Design space results organized based on values of inflation pressure

**Figure 85: Design space results sorted based on centerbody diameter and inflation pressure**

Sorting the entire design space based on unique values of each parameter enables a characterization of the overall results topology with respect to the primary variables

that drive the response. However, as is observed with the centerbody diameter and inflation pressure results, the impact of less sensitive variables can be confounded by the other parameters and be difficult to determine. The relative impact of each variable is better determined by isolating individual values of more sensitive parameters to reduce the design space and magnify the impacts of the lower order variables. This process is performed sequentially in order to rank the impact of each parameter and determine how it might be adjusted to optimize the response.

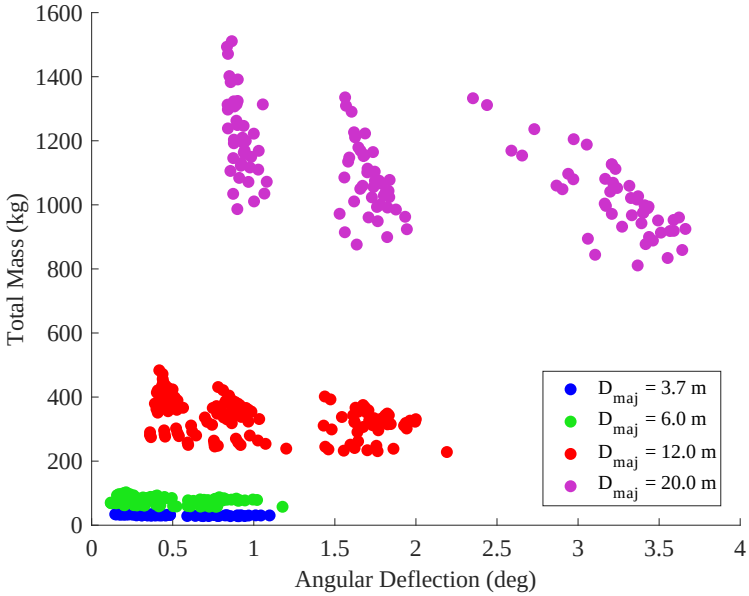


**Figure 86: Design space results organized based on values of the major diameter**

As discussed when referencing Fig. 82 (reproduced here in Fig. 86 for convenience), the major diameter is the primary factor governing the overall mass and deflection response. While it is obvious from Fig. 86 that both the mass and deflection can be minimized by reducing the major diameter, because it is a primary contributor to the vehicle ballistic coefficient, the major diameter is typically fixed for a desired mission and is therefore not an optimizable parameter. Instead, picking a desired mission class will typically correlate to an appropriate value of major diameter, which will dictate the possible ranges of mass and deflection for stacked tori

decelerators. Isolation of the major diameter results therefore aids conceptual design by providing a rapid high-level check to determine if the possible ranges of mass and deflection are valid for the vehicle being considered.

Figure 87 isolates all of solutions for configurations with a major diameter of 12 m in order to focus the design space and determine the impact of the remaining design variables. Design solutions are organized based on values of the half-cone angle, which clearly resolves the major groupings observed in the results. It can be seen that larger cone angles correspond to a significant increase in angular deflection, due to the IAD surface being oriented more normal to the oncoming flow, as well as a slight reduction in the range of total mass. However, like the major diameter, the half-cone angle is typically fixed for a given mission class based on the stability and aerodynamic drag requirements for the vehicle and, therefore, is typically not optimizable.

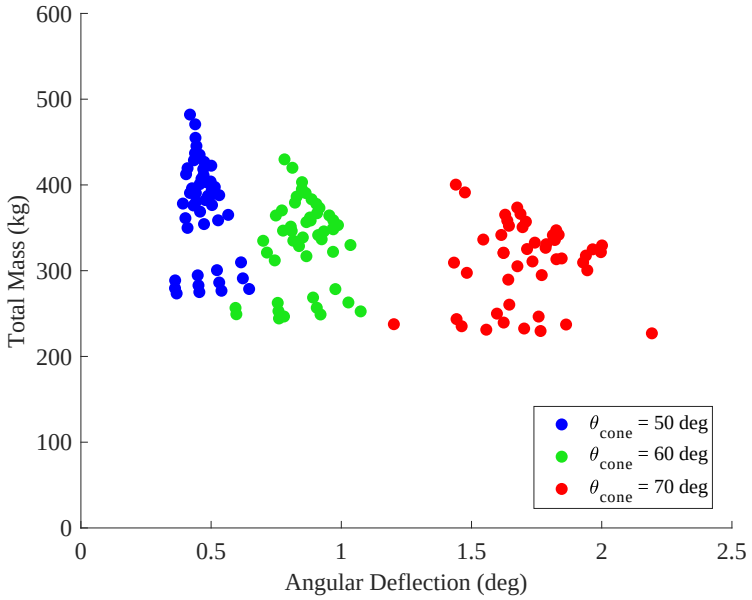


**Figure 87: Design space results isolating solutions for $D_{Maj} = 12$ m organized based on values of the half-cone angle**

Figure 88 isolates all the solutions for configurations with $D_{Maj} = 12$ m and $\theta_{Cone} = 50°$, organizing data points based on the number of tori. While there is no distinct separation between groups based on different number of tori, as is seen

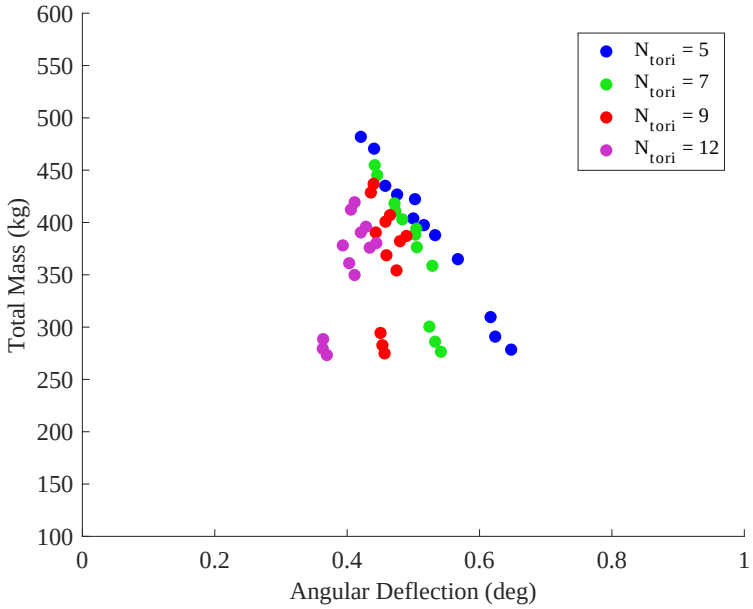


**Figure 88: Design space results isolating solutions for $D_{Maj} = 12$ m and $\theta_{Cone} = 50°$ organized based on number of tori**

with the major diameter and cone angle variables, the number of tori parameter does highlight line-like sub-structures in the data. The correlation between the number of tori and these major sub-structures indicates that it is the third-most dominant design parameter. Unlike the major diameter and cone angle, however, the number of tori parameter is optimizable for a given mission. As seen in Fig. 88, an increase in the number of tori correlates with a reduction in the angular deflection and a slight decrease in the possible range of total mass, due to the reduction in gas mass. The non-intuitive relationship between the number of tori and angular deflection is discussed later in Section 3.5.2.1.

Figure 89 isolates all of the solutions for configurations with $D_{Maj} = 12$ m, $\theta_{Cone} = 50°$, and $N_{Tori} = 9$, organizing data points based on the value of the centerbody diameter. The centerbody diameter is observed to partition the line-like structure isolated by a single value of $N_{Tori}$ into distinct groups of three data points. The further partitioning of the data grouping into definable substructures indicates that the centerbody diameter is the fourth-most dominant design parameter. Like the

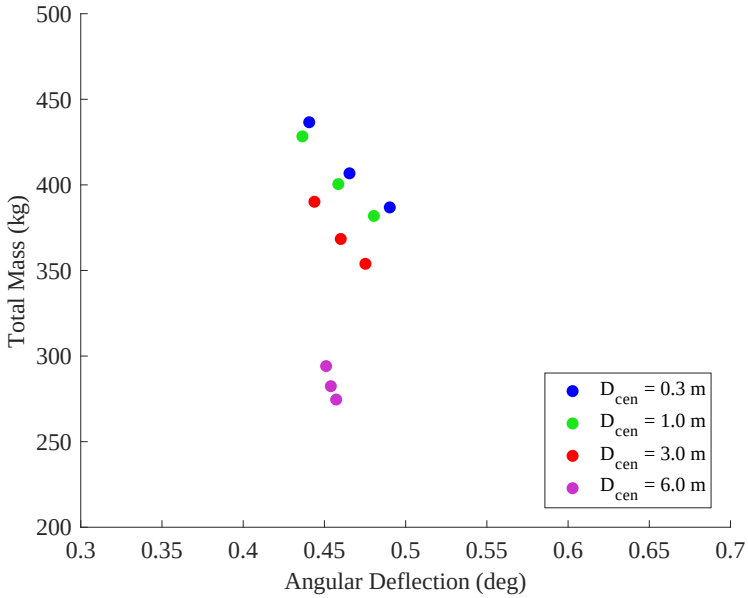


**Figure 89: Design space results isolating solutions for $D_{Maj} = 12$ m, $\theta_{Cone} = 50°$, and $N_{Tori} = 9$ organized based on values of the centerbody diameter**

major diameter, the centerbody diameter is fixed in most cases based on the mission payload and launch vehicle payload shroud diameter. Nevertheless, it can be seen that larger centerbody diameters, typically corresponding to larger, more massive payloads, result in a lower IAD mass and a shrinking of the total range of angular deflection about a common midpoint. Note that, while the IAD mass decreases, the total mass of the entry vehicle likely increases due to the increase in payload mass.

Figure 90 shows the same isolated solutions for configurations with $D_{Maj} = 12$ m, $\theta_{Cone} = 50°$, and $N_{Tori} = 9$, but organized based on the inflation pressure. For each grouping of points defined by a single value of the centerbody diameter, the inflation pressure determines the arrangement of the three points. Because the inflation pressure scales solutions along the line defined by the centerbody diameter and all other higher order parameters, it can be determined to be the fifth, or least, dominating parameter. The inflation pressure is an optimizable parameter for each mission, with an upper bound determined by the torus fabric strength. Increases in inflation pressure are seen to increase total mass through an increase in gas mass and

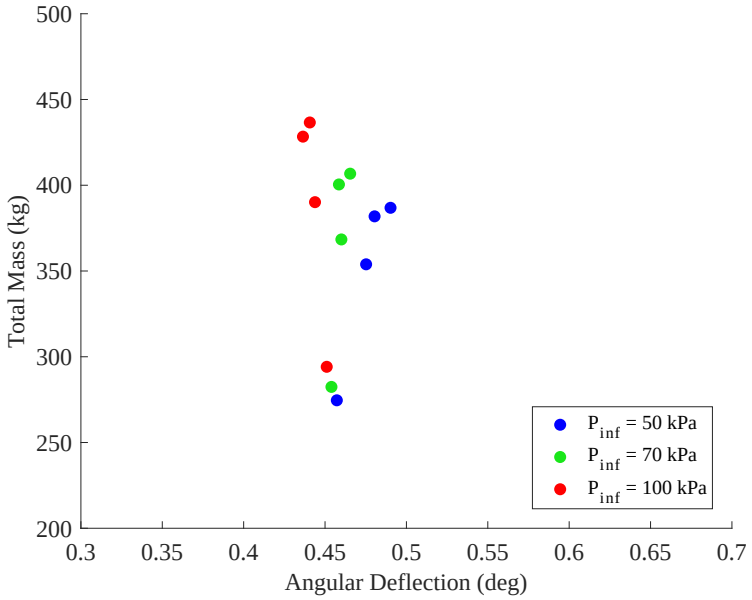


**Figure 90: Design space results isolating solutions for $D_{Maj} = 12$ m, $\theta_{Cone} = 50°$, and $N_{Tori} = 9$ organized based on values of inflation pressure**

decrease angular deflection due to increase in structural torus stiffness. Based on the particular objective function of each mission, the inflation pressure can therefore be scaled to optimize towards either result metric.

#### *3.5.2.1 Stacked Tori Design Space Exploration Case Study: Angular Deflection Versus Number of Tori Discussion*

The inverse relationship between the number of tori and the angular deflection observed during the parameter impact study in Section 3.5.2 is not intuitive. It is expected that the increase in the number of tori and the corresponding reduction in the tori radius would result in tori that are less stiff and, therefore, prone to higher deflection values. Instead, the more numerous, smaller tori are seen to result in smaller deflections under aerodynamic load. Figure 91 shows the deflected cross sections of two decelerators with the same configurational parameters except their number of tori, with one configuration composed of 5 structural tori and the other 12. In the figure, open circles are used to represent the post-inflation state and solid circles are used to represent the post-aerodynamically loaded state. Figure 91(a)

shows that deflection of the IAD surface is approximately linear and that the smaller deflection measurement of the 12-torus decelerator is not due to non-linear effects. Figure 91(b) shows a zoomed-in view of the region around the radial strap interface to the structural tori. It is important to note that the deflection value is defined as the difference between the inflated and aerodynamically-loaded state. Therefore, even though the 12-torus IAD post-aerodynamically loaded surface (solid circles) is aft of the 5-torus surface, it has a lower deflection because the difference between the aerodynamically-loaded and inflation loaded (open circles) surfaces is smaller.

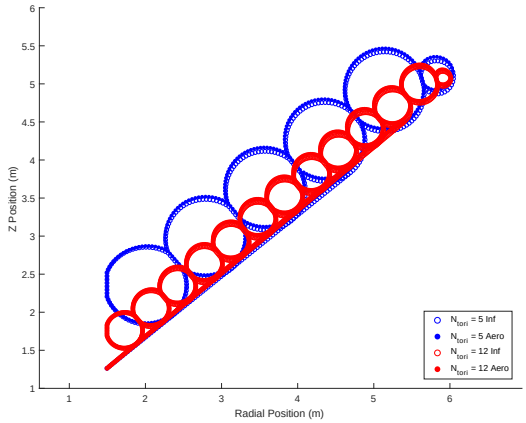


(a) Comparison of deflection results between a 12-torus stacked tori and 5-torus stacked tori decelerator

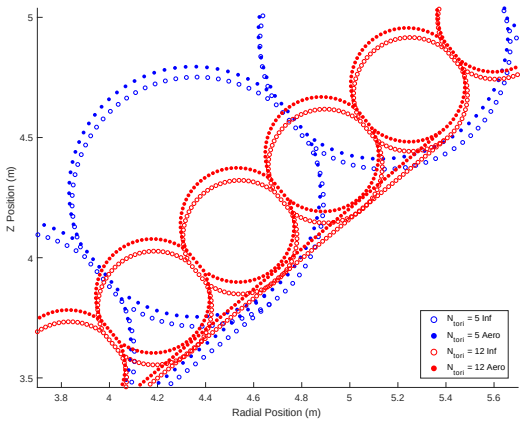


(b) Comparison of deflection results between a 12-torus stacked tori and 5-torus stacked tori decelerator, zooming in on intersection of the radial strap with the structural tori

**Figure 91: Comparison of deflection results between stacked tori decelerators with different number of tori. "Inf" legend entries refer to the deflected state after inflation loading and "aero" legend entries refer to the deflected state after inflation and aerodynamic loading.**

There are two noticeable differences between the two configurations. The first is that the radial strap interface location is radially farther out for the 12-torus configuration due to it attaching to $T_{N-1}$ with smaller tori. The second is that the inflated surface of the 5-torus configuration is deflected more windward than the 12-torus inflated surface. Given that both surfaces are approximately linear, the differing radial strap attachment point is not expected to significantly alter the deflection values.

However, the cone angle comparison results show that the cone angle has a significant impact on the surface deflection. Therefore, it is anticipated that the greater amount of inflation gas in the 5-torus configuration contributes to an increase in the instantaneous cone angle over that of the 12-torus configuration's post-inflation surface. The 5-torus inflated surface is therefore oriented more-normal to the freestream flow, resulting in an increase in aerodynamic deflection.

### 3.5.3 Stacked Tori Design Space Exploration Case Study: Response Surface Development

The 456 configurations generated in the design space exploration study are also used to construct response surface equations to estimate the mass and surface deflection of the stacked tori decelerators. These response surface equations enable approximations of the mass and deflection response of candidate decelerator designs in the conceptual design phase and can be used in conjunction with the design space study results to better understand the impacts of different design trades. These equations are particularly valuable in early conceptual design because, while they are informed by computational modeling results, the response surfaces themselves can be evaluated without numerical simulation or software.

The response surface equations in this study are composed of second-order polynomials of the design variables, including pair-wise interaction terms, that approximate the decelerator mass and deflection responses. The response surface equations are generated by performing a regression of the mass or deflection response with respect to the assumed basis functions to determine their polynomial coefficients. The regression equations are evaluated at a subset of the design study data points, with 274 of the 456 configurations (60%) being used to generate the response surface model and the remaining 183 configurations (40%) being used to validate the equation's ability to accurately predict the response.

The full response surface equations are shown in Eqs. 41 and 42. In the equations, $m_{Tot}$ denotes the decelerator total mass (sum of fabric mass and gas mass) in kilograms, $\Delta\theta_{Cone}$ denotes the decelerator surface angular deflection in degrees, $D_{Maj}$ denotes the decelerator major diameter in meters, $\theta_{Cone}$ denotes the decelerator half-cone angle in degrees, $N_{Tori}$ denotes the total number of tori, $D_{Cen}$ denotes the decelerator centerbody diameter in meters, and $P_{Inf}$ denotes the inflation pressure in kilopascals.

$$\begin{aligned} m_{Tot,ST} = {} & 171.8186 + 23.8515D_{Maj} - 8.4914\theta_{Cone} - 0.8305N_{Tori} \\ & - 6.4810D_{Cen} + 0.6011P_{Inf} + 3.5807D_{Maj} * D_{Maj} - 0.7360D_{Maj} * \theta_{Cone} \\ & + 0.1104\theta_{Cone} * \theta_{Cone} - 1.7003D_{Maj} * N_{Tori} + 0.0113\theta_{Cone} * N_{Tori} \\ & + 1.0742N_{Tori} * N_{Tori} - 1.2100D_{Maj} * D_{Cen} + 0.3400\theta_{Cone} * D_{Cen} \\ & + 1.1990N_{Tori} * D_{Cen} - 2.8018D_{Cen} * D_{Cen} + 0.2746D_{Maj} * P_{Inf} \\ & - 0.0185\theta_{Cone} * P_{Inf} - 0.1289N_{Tori} * P_{Inf} - 0.1754D_{Cen} * P_{Inf} \\ & + 0.0004P_{Inf} * P_{Inf} \end{aligned} \quad (41)$$

$$\begin{aligned} \Delta\theta_{Cone,ST} = {} & -8.361805 + 0.347093D_{Maj} + 0.272088\theta_{Cone} - 0.003677N_{Tori} \\ & - 0.069268D_{Cen} - 0.004110P_{Inf} - 0.002470D_{Maj} * D_{Maj} - 0.006042D_{Maj} * \theta_{Cone} \\ & - 0.002336\theta_{Cone} * \theta_{Cone} - 0.003350D_{Maj} * N_{Tori} - 0.000796\theta_{Cone} * N_{Tori} \\ & + 0.005146N_{Tori} * N_{Tori} - 0.004247D_{Maj} * D_{Cen} + 0.001671\theta_{Cone} * D_{Cen} \\ & + 0.010562N_{Tori} * D_{Cen} - 0.004171D_{Cen} * D_{Cen} + 0.000153D_{Maj} * P_{Inf} \\ & + 0.000226\theta_{Cone} * P_{Inf} - 0.000170N_{Tori} * P_{Inf} - 0.000401D_{Cen} * P_{Inf} \\ & - 0.000041P_{Inf} * P_{Inf} \end{aligned} \quad (42)$$

It is important to note that the cone angle deflection is expressed as a negative quantity in the response surface equation, as well as in the figures in this section,

rather than a positive quantity as was used in design space exploration figures. The negative convention is intentionally used for the response surface to clearly indicate that surface deflections result in a reduction in cone angle. The opposite convention is used in the design space exploration figures, however, because it is easier to conceptualize the absolute magnitude of the cone angle deflection when relating larger or smaller deflections. It is also important to note that these equations are typically only valid over the domain in which they were generated and validated, that being the domain of the stacked tori design space exploration study. Because response surface equations simply approximate the shape of the input computational simulation results, they can be subject to significant errors when used for extrapolation. Likewise, care also needs to be taken with construction of the input parameters to ensure that reasonable configurations, such as ones with centerbody diameters smaller than their major diameter, are estimated.

The response surface's goodness of fit can be evaluated in several different ways. The simplest method is using the equation's coefficients of determination, or the $R^2$ and adjusted $R^2$ metrics. The $R^2$ value conveys the proportion of the variability in the mass and deflection results that can be attributed to the independent basis functions. The adjusted $R^2$ metric is similar but also takes into account the number of basis functions used in the response surface equation and the degree to which each additional basis function improves the model prediction of the mass and deflection responses.

**Table 11: $R^2$ and adjusted $R^2$ values for the stacked tori mass and deflection response surface equations**

| | Mass RSM | Deflection RSM |
|---|---|---|
| $R^2$ | 0.9981 | 0.9836 |
| Adjusted $R^2$ | 0.9980 | 0.9823 |

The coefficients of determination for both models are shown in Table 11. Both the $R^2$ and adjusted $R^2$ metrics are seen to be very good. The mass equation, in

particular, has a very high $R^2$ value, which is to be somewhat expected. Despite the decelerator mass being a function of the torus cross-sectional radius, which is determined by a linear solver routine, the equations for the fabric and gas mass are analytical expressions composed of linear and quadratic functions of the design variables. Therefore, the mass term is expected to be well characterized by the polynomial response surface equations. The angular deflection $R^2$ value, while not as good as the mass value, still demonstrates that the response surface basis functions explain a significant portion of the deflection's variability. Despite the deflection being determined from computational numerical simulations, which are expected to be more difficult to characterize with simple linear and quadratic basis functions, the response surface still performs well. In addition, both adjusted $R^2$ values are similar to the $R^2$ values, which demonstrates that the vast majority of basis functions are significant and positively contribute to the model.

Another way to assess the response surface model and identify deficiencies is through the actual by predicted plot, which displays the actual simulated mass and deflection values plotted against the results predicted by the response surface equation. A perfect fit would show on the plot as a straight, diagonal line, indicating that the response surface predictions exactly match the actual value of the desired objective at every point. Any outliers or trends in the data, therefore, indicate a non-ideal fit and that the response surface is not exactly capturing the contours of the actual data.

Actual by predicted plots of the stacked tori decelerator mass and deflection responses are shown in Fig. 92. The figures show the data points used to evaluate the fit (in black) distributed about the diagonal perfect fit line (in red), along with the mean of the response (horizontal blue line). The additional two red lines, which bound the perfect fit line, represent the 95% confidence intervals of the data. The mass model shown in Fig. 92(a), in particular, looks very good and displays a tight

grouping of data around the perfect fit line. The data is segmented into distinct groups, which reflect the dispersion of results based on the major diameter. While an even sampling of mass data points would be preferable, the fact that all the groups lie on the perfect fit line is encouraging. Small trends do emerge for the lower mass decelerators, indicating that the response surface has a worse fit in these regions, but the overall graph corroborates the response surface's good fit of the mass data.

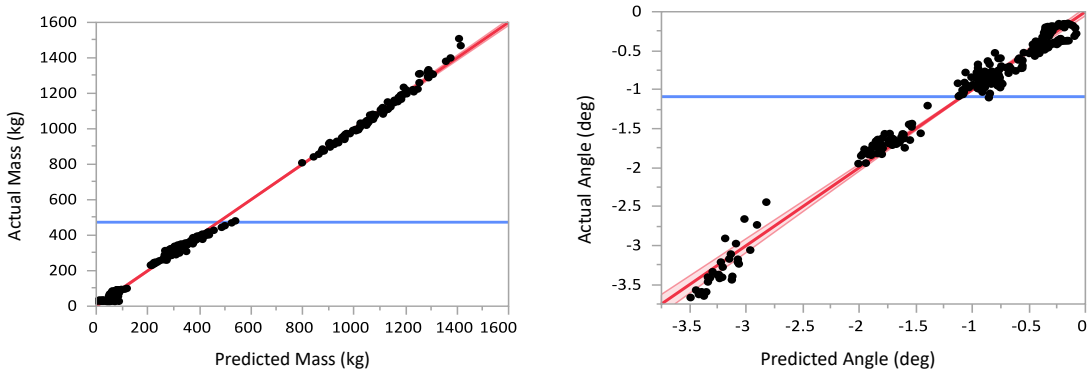


(a) Actual by predicted plot of the stacked tori mass response surface equation

(b) Actual by predicted plot of the stacked tori deflection response surface equation

**Figure 92: Response surface goodness of fit assessments showing actual stacked tori mass and deflection values versus response surface predicted values**

The actual by predicted plot of the deflection, displayed in Fig. 92(b), also shows the data to be distributed about the perfect fit line, but with more dispersion than in the mass response plot. This dispersion reflects the slightly lower $R^2$ value of the deflection objective, demonstrating that the response surface equation cannot capture the entire variability of the deflection response. The widening of the 95% confidence curves also reflects this, showing a slight reduction in the confidence of the model predictions. Nevertheless, the lack of obvious trends or outliers in the data indicate an overall good fit.

The response surface models can also be assessed using a residual by predicted plot that instead graphs the residual value of the response (the difference between the actual value and response surface predicted value) versus the response surface

predicted value. A good response surface fit would have small residuals resulting from randomly distributed errors and, therefore, would display a random cloud of data points normally distributed about the horizontal line of 0 residual. This plot is useful because it focuses on the differences between the model and actual response and therefore can highlight trends or grouping in the data that indicate a less than perfect fit.

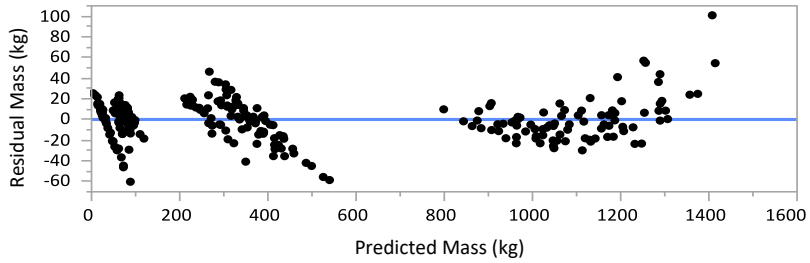


(a) Residual by predicted plot of the stacked tori mass response surface equation

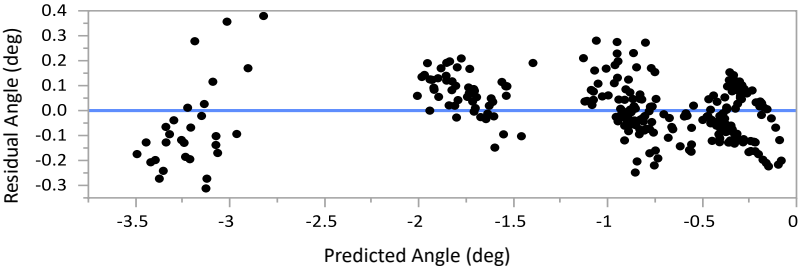


(b) Residual by predicted plot of the stacked tori deflection response surface equation

**Figure 93: Response surface goodness of fit assessments showing residual stacked tori mass and deflection values versus response surface predicted values**

Residual by predicted plots of the stacked tori decelerator mass and deflection responses are shown in Fig. 93. The figures show the data points used to evaluate the fit (in black) distributed about the horizontal perfect fit line (in blue). The mass response residual vs predicted plot shown in Fig. 93(a) shows residuals that are generally distributed around 0 but also with obvious trends arising in the data. Data points corresponding to the lower mass configurations have a negative sloping trend whereas residuals for the higher mass configurations behave almost quadratically.

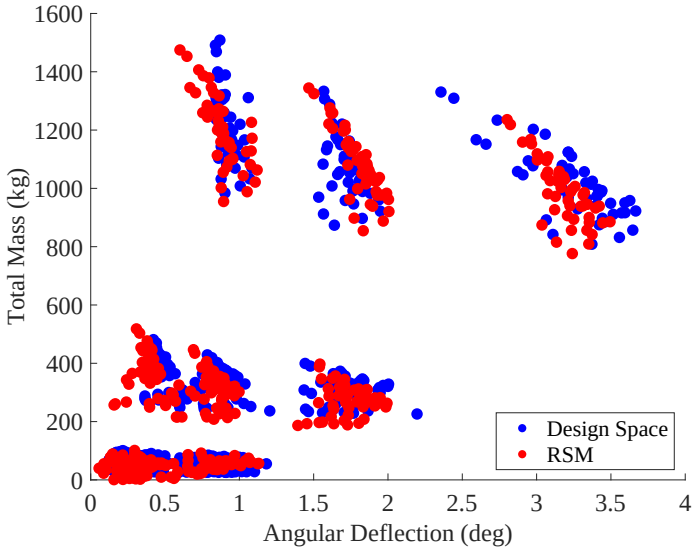


**Figure 94: Comparison of stacked tori response surface mass and deflection predictions to actual simulated values**

These local trends indicate the higher order basis functions or transformations of individual bases functions could improve the model predictions.

The residual by predicted plot of the deflection, displayed in Fig. 93(b), shows the data points to be approximately scattered around the line of 0 residuals. The configurations with largest deflection (absolute value) exhibit a positive slope of the residuals and configurations with deflections closer to zero display a non-linear pattern, especially towards small absolute-value deflection responses. Like the plot of the mass response, these results indicate that other response surface terms could improve the predictions of the models.

An overall qualitative evaluate of the response surface models is also available by plotting the response surface equation predictions overlaid on the stacked tori design space. As evidenced by the comparison in Fig. 94, the mass and deflection response surfaces perform very well. In particular, the response surface equations are able to capture all relevant major grouping of the data. The general shape and size of the individual groups are captured but offsets exist between the model predicted and actual results. Nevertheless, the response surface equations predict the general size

and shape of the data groups and can even reasonably approximate where in the group a particular solution will be located. Therefore, these results show that the response surface equations are perfectly suited for use in conceptual design and will provide a reasonable estimate of the mass and deflection response of a wide range of stacked tori configurations. It is important to note however, that these equations are only valid for designs within the bounds of the fitted data and could vary significantly from actual mass and deflection values if extrapolated to configurations outside of the case study design space.

## *3.6 Tension Cone Design Space Exploration Case Study*

A case study analyzing the effects of the design parameters on the tension cone design space is also developed. Parameter sweeps are performed for all the tension cone design variables to identify their relative influence on the decelerator structural and mass performance. These results are also used to generate response surface equations that approximate the design space results with analytical equations.

### 3.6.1 Tension Cone Design Space Exploration Case Study: Design Space

The tension cone design space is constructed similar to that of the stacked tori, performing simultaneous parameter sweeps of each parameter in a full-factorial design. The tension cone design space mirrors the stacked tori design space, with the tension skirt radius parameter substituted for the number of tori to reflect the differences in the configuration geometries. The design space parameters and their possible values are shown in Table 12. A total of 5 configurational parameters are studied. For the full factorial design of experiments, this corresponds to a total of 972 possible unique designs, with 828 valid configurations after applying the design constraints.

Except for the major and centerbody diameter values, all the tension cone parameters are the same as in the stacked tori design space study to assist with ease of comparison. The use of similar parameter values also reflects the fact that both

**Table 12: Design variable values used in the tension cone design space exploration case study**

| Parameter | Variable | Units | Values |
|---|---|---|---|
| Major Diameter | $D$ | m | 3.7, 6.0, 12.0 |
| Centerbody Diameter | $D_{Cen}$ | m | 0.25, 0.50, 1.00, 3.00, 6.00 |
| Half-Cone Angle | $\theta$ | ° | 50, 60, 70 |
| Tension Skirt Radius | $R_{TS}$ | m | (-1.0, -0.9, ... -0.2)+$\frac{D_{Maj}}{2}$ |
| Inflation Pressure | $P_{Inf}$ | kPa | 50, 70, 100 |
| Aerodynamic Pressure | $P_{Aero}$ | Pa | 1000 |

configurations are being considered for the same application: hypersonic deceleration of large payloads. The tension cone design space eliminates decelerators with major diameters of 20.0 m, the largest stacked tori design simulated, because a single torus is unable to supporting the aerodynamic loading at such a large scale. This observation reflects the fundamental differences between tension cone and stacked tori decelerators, that the tension cone design is thought to reduce the mass of inflatable decelerators relative to stacked tori configurations at the expense of the IAD structural rigidity. This also reflects the fact that tension cone decelerators have traditionally been considered for less severe supersonic deceleration applications. To compensate for the removal of the $D_{Maj} = 20.0$ m parameter value, an additional centerbody diameter value of 0.5 m is added to improve the resolution of the design space for smaller vehicles constrained by the $D_{Cen} < \frac{1}{2}D_{Maj}$ limit.

The tension skirt radius parameter is defined in terms of the major diameter to generate the maximum number of valid geometries, avoiding cases where the tension skirt is larger or much smaller than the major diameter. The set of $R_{TS}$ values are defined as the major radius added to the set of lengths between -1 m and -0.2 m in increments of 0.1 m. The tension skirt radius parameter is defined in this way to produce torus diameters in the approximate range of 0.25 m to 1.5 m, falling within both the upper and lower constraints on the torus size. The coupling of the tension skirt radius to the major diameter means that an even comparison cannot be made

between the tension skirt radii of configurations of different sizes. Instead, an implicit comparison can be made between each design's torus cross-sectional diameter, which is a more appropriate comparison because the cross-sectional diameter is the main contributor to the IAD structural rigidity.

An additional constraint is enforced on the tension skirt configurations, along with the maximum and minimum tori diameters and the centerbody diameter to major diameter ratio. Tension cones are assumed to attach to the centerbody only at the interface to the tension skirt. For certain geometries with a large centerbody diameter and small tension skirt radius, the structural torus can extend radially inward of the centerbody diameter, interfering with the assumed payload. These cases are rejected in the design space study due to being considered unfeasible, which establishes the minimum possible value of $R_{TS}$ for a given set of design parameters.

### 3.6.2 Tension Cone Design Space Exploration Case Study: Results

The results of the full tension cone design space study are shown in Fig. 95(a). The graph shows some separation between discrete groups of data points, although not to the extent that was seen in the stacked tori design space. Therefore, it appears that the mass and deflection responses are still more sensitive to a subset of the design parameters but that the full range of parameter sensitivities is smaller than that of the stacked tori design space. The data groupings arising in the tension cone design space are also observed to take on a different shape than was previously seen. Instead of more linear and triangular structures, the tension cone design space exhibits groups that are more curved. These curved sections evolve in shape and direction throughout the design space, indicating that the parameter interactions terms are important factors in the decelerator response.

Figure 95(b) overlays the tension cone design space over that of the stacked tori. Note that the $D_{Maj} = 20.0$ m configurations are removed from the stacked tori data

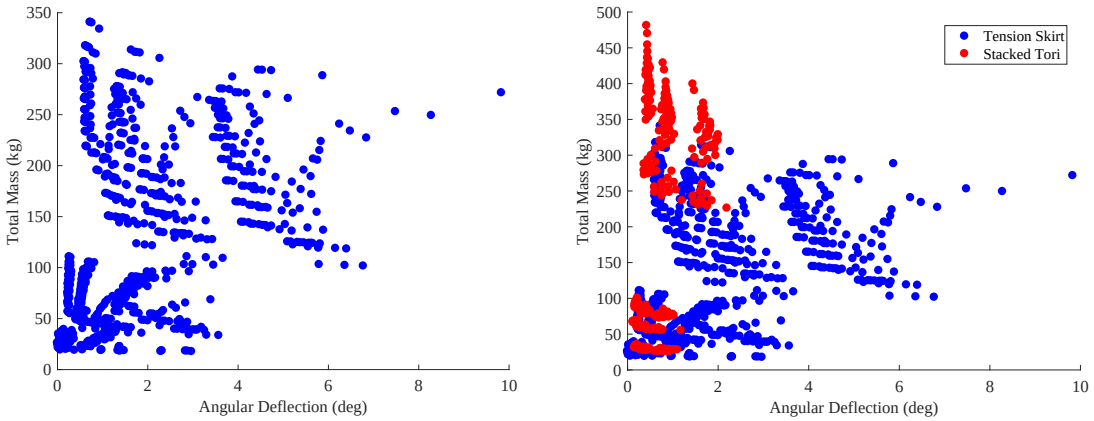


(a) Tension cone design space results

(b) Comparison of tension cone (blue) and stacked tori (red) design space results

**Figure 95: Tension cone and stacked tori design space results**

set in this graph to reflect their removal from the tension cone design space. The results confirm the general assertion that stacked tori decelerators tend to produce higher-mass, lower-deflection solutions whereas tension cone decelerators tend to produce lower-mass, higher-deflection solutions. Mass results vary between 20 kg and 500 kg for stacked tori configurations up to 12.0 m diameter and between 20 kg and 350 kg for similar tension cone decelerators. Conversely, stacked tori decelerators deflect between 0 to 2 degrees whereas tension cone decelerators deflect between 0 and 10 degrees. Therefore, it can be seen that variations in the IAD configuration can be used along with the design parameters to optimize the inflatable decelerator structural and mass performance.

The tension cone designs space is partitioned based on each parameter to understand the sensitivity of the structural and mass performance to the design variables. Figure 96 organizes the tension cone design space based on unique values of the major diameter. The figure shows that the major diameter separates the data points into horizontal bands, clearly separating the design space into its primary grouping and indicating that the major diameter is a primary driver of the result variability. Adjacent bands are observed to have separate, non-overlapping ranges of total mass

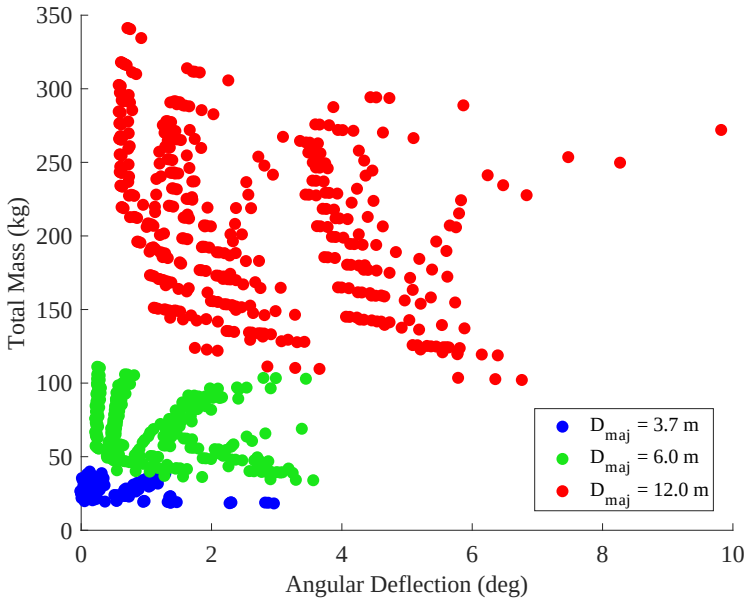


**Figure 96: Tension cone design space results organized based on values of major diameter**

along with overlapping ranges of angular deflection, exhibiting a small increase in the deflection lower bound and a large jump in the deflection upper bound with increasing major diameter.

Figure 97 organizes the design space based on values of the half-cone angle. The half-cone angle is observed to separate the data into definable groups with moderate spacing in between, indicating that it, too, is a dominant design parameter. Groups with adjacent values of the half-cone angle have a slight reduction in the overall mass but exhibit large jumps in angular deflection. Overall, it is also seen that the shape characteristics of the different groups are retained with only slight distortion across the range of half-cone angle.

Variations of the design space results with respect to the centerbody diameter are displayed in Fig. 98. Instead of defining separate groups of data, the centerbody diameter is observed to segment individual groups into definable substructures, resolving the curved line structures seen throughout the design space. The centerbody diameter primarily impacts the IAD surface deflection and typically has minimal

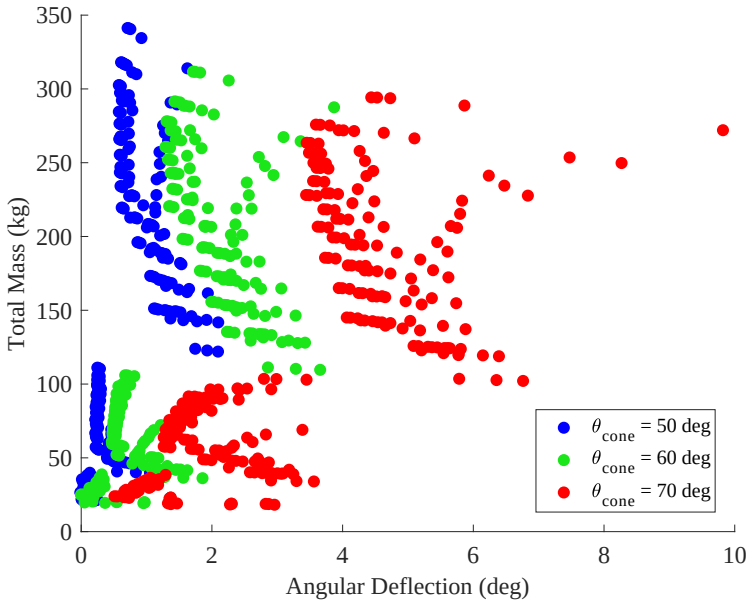


**Figure 97: Tension cone design space results organized based on values of the half-cone angle**

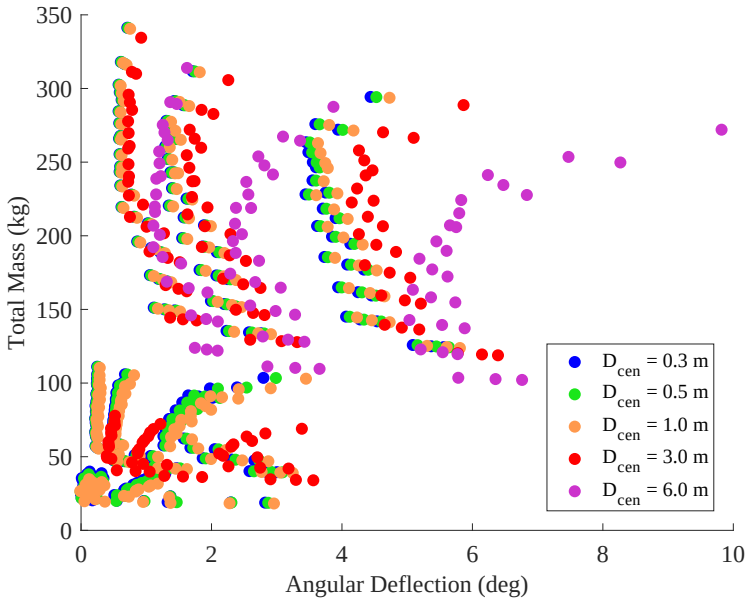


**Figure 98: Tension cone design space results organized based on values of the centerbody diameter**

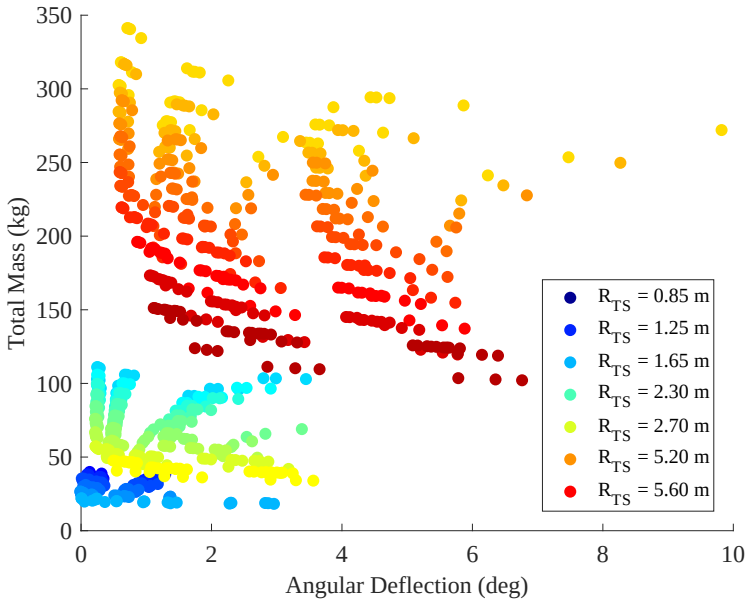


**Figure 99: Tension cone design space results organized based on values of the tension skirt radius**

impact on the range of total mass.

Figure 99 partitions the design space based on the values of the tension skirt radius. While the tension skirt radius is not observed to give rise to repeatable structures within the data, it is important to note that the range of tension skirt radius values are defined based on the given value of the major diameter. Therefore, instead of evaluating between like values of the tension skirt radius, comparisons should be made between large and small values of the tension skirt radius based on the applicable range defined by that configuration's major diameter. The tension skirt is observed to be a strong driver of the results variability, able to traverse the entire range of total mass for each grouping of major diameter. At first glance, it appears that the tension skirt radius does not correspond to any definitive substructure within the data. However, this is more a function of the high sampling resolution of the parameter, resulting in a more continuous variation of the results across the applicable range of the tension skirt radius. When looking closely at the $D_{Maj} = 12.0$ m results, it can instead be observed that unique values of the tension skirt radius resolve diagonal

lines across the data group.

The distribution of the design space based on the inflation pressure is seen in Fig. 100. As observed in the figure, designs with similar inflation pressure values are distributed almost uniformly about the design space. This indicates that the mass and deflection results have a low sensitivity to the inflation pressure.

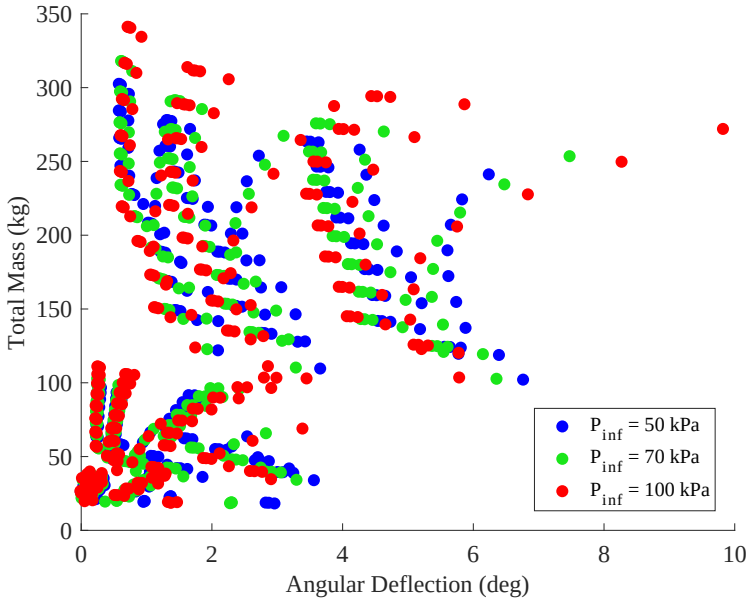


**Figure 100: Tension cone design space results organized based on values of the inflation pressure**

As was performed with the stacked tori case study, the tension cone design space is also iteratively focused by isolating individual values of the most dominant design variables, the remaining results organized by the lower order factors. In this way, parameter sensitivities of the lower order variables can be better visualized to aid in developing an intuitive understanding of the design response.

As seen in Fig. 96, provided here in Fig. 101 for convenience, the major diameter is clearly the most dominant parameter. The major diameter heavily contributes to the variability in the results, being able to span the entire range of angular deflection and total mass. Like the stacked tori configurations, the major diameter is fixed for a given mission based on the ballistic coefficient requirements and, therefore, is not an

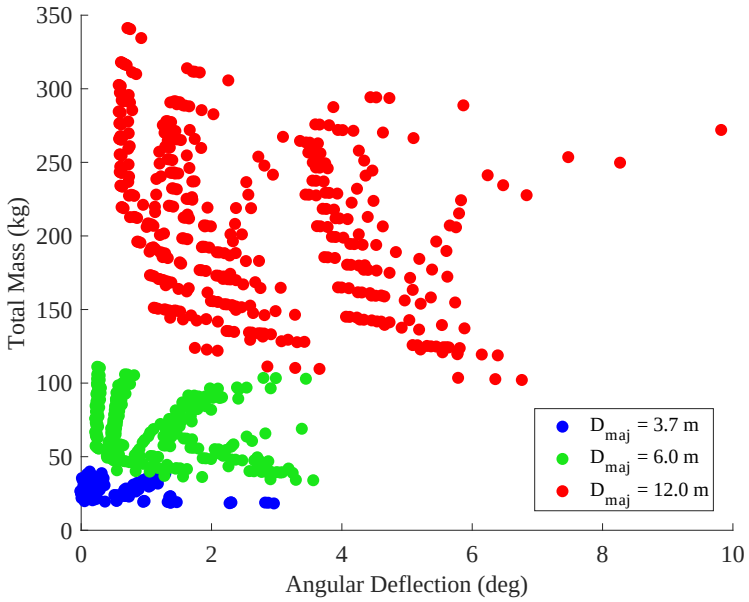


**Figure 101: Tension cone design space results organized based on values of major diameter**

optimizable parameter. Instead, the value of major diameter dictated by the mission requirements will drive the general range of mass and deflection values expected from the tension cone decelerator implementation.

Figure 102 isolates all configurations with a major diameter of 12 m to highlight the variability of the design space results with respect to the lower order parameters. The cone angle resolves the largest structures of the isolated data points, the y-shaped groups, demonstrating that it is the second most sensitive design variable. Like the major diameter, the cone angle is also typically set for a given mission based on stability and ballistic coefficient constraints. Therefore, the prescribed cone angle value will further refine the possible range of expected mass and deflection values rather than be optimized to a desired result. Nevertheless, larger values of the cone angle, corresponding to lower ballistic coefficient vehicles, will typically result in higher deflection values, due to the sides of the decelerator being oriented more normal to the oncoming flow, and a slight reduction in the total mass.

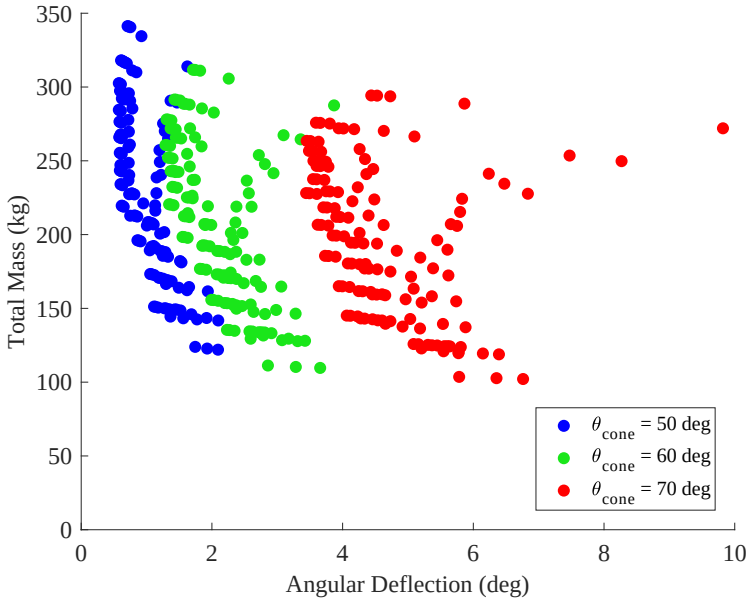


**Figure 102: Tension cone design space results isolating solutions for $D_{Maj} = 12$ m organized based on values of the half-cone angle**

Figure 103 isolates all configurations with a major diameter of 12 m and half-cone angle of 60°. The centerbody diameter parameter resolves curved lines that compose the y-like shapes seen in Fig. 102 and indicate that it is the third-most dominant design variable. The centerbody diameter is also generally determined by the mission class and launch vehicle and is not optimizable. Increases in the centerbody diameter result in a slight reduction in the decelerator mass (that is counteracted by an increase in the payload and vehicle structural mass) and a larger increase in the surface angular deflection. The non-intuitive relationship between the centerbody diameter and angular deflection is discussed later in Section 3.6.2.1.

Figure 104 isolates all configurations with a major diameter of 12 m, half-cone angle of 60°, and centerbody diameter of 3 m. Sorting the remaining data points based on the tension skirt radius resolves a series of parallel lines for large and small values of the tension skirt radius, with an intermediate region in between that transitions between the two differing slopes. The tension skirt radius is an optimizable parameter that can be adjusted to meet a certain mass or deflection constraint. Increases in $R_{TS}$

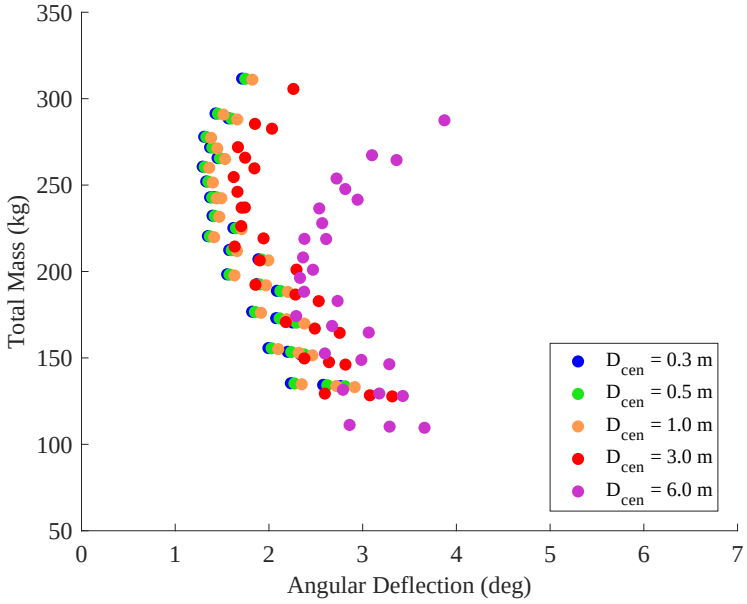


**Figure 103: Tension cone design space results isolating solutions for $D_{Maj} = 12$ m and $\theta_{Cone} = 60°$ organized based on values of the centerbody diameter**

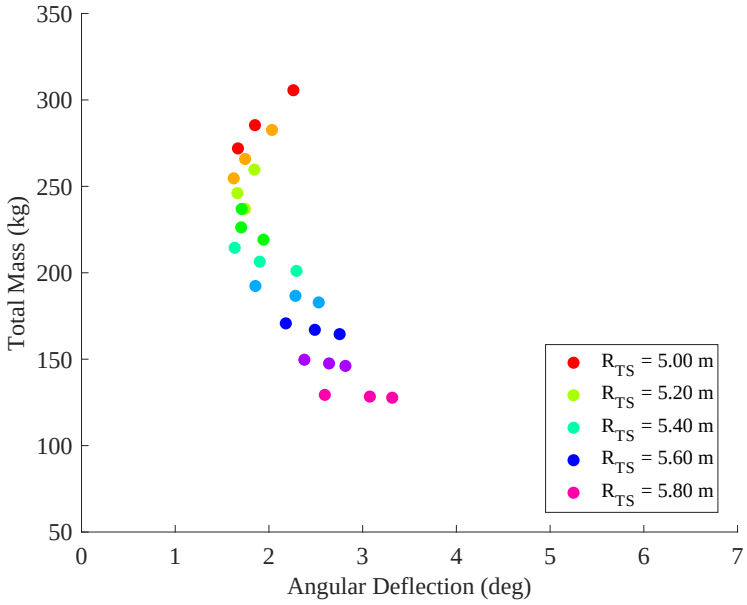


**Figure 104: Tension cone design space results isolating solutions for $D_{Maj} = 12.0$ m, $\theta_{Cone} = 60°$, and $D_{Cen} = 3$ m organized based on values of the tension skirt radius**

are observed to strictly decrease the decelerator mass due to the reduction in torus radius but can either decrease or increase the angular deflection based on the current set of design variables.

Figure 105 also isolates configurations with a major diameter of 12 m, half-cone angle of 60°, and centerbody diameter of 3 m but organizes the results based on the inflation pressure. The inflation pressure resolves finer line structures composing the data set defined by a single centerbody diameter value. The three lines are mutually parallel for small and large values of the tension skirt radius but change slope in the middle and, thus, reverse the trend of angular deflection with respect to inflation pressure.

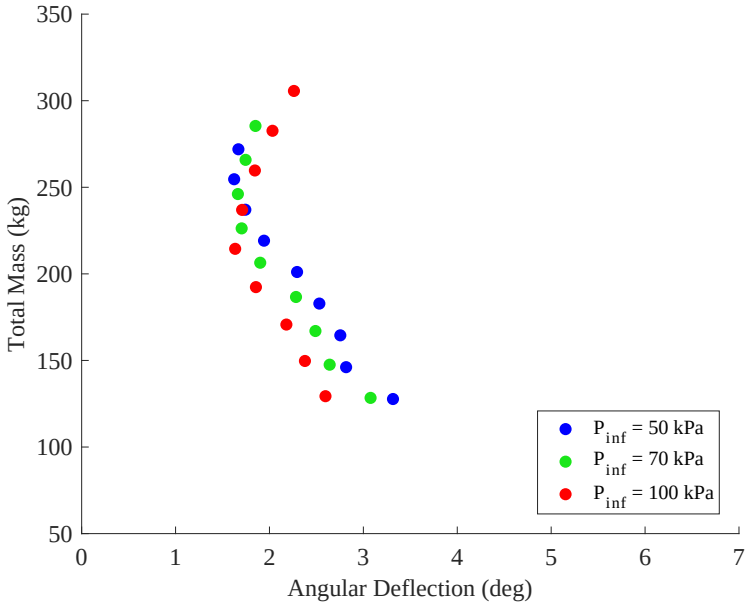


**Figure 105: Tension cone design space results isolating solutions for $D_{Maj} = 12.0$ m, $\theta_{Cone} = 60°$, and $D_{Cen} = 3$ m organized based on values of the inflation pressure**

Like the tension skirt radius, the inflation pressure is an optimizable parameter and can be tuned to achieve a desired performance. Increases in the inflation pressure always result in an increase in total decelerator mass due to the increase in gas mass. However, based on the region of the graph, the inflation pressure can be observed to

both increase and decrease the angular deflection. For larger values of the tension skirt radius (lower portions of the curve in Fig. 105), increasing the inflation pressure corresponds with a stiffening of the structural tori and a reduction in the angular deflection, which is intuitive. However, for smaller tension skirt radii (seen in the upper portions of the curve in Fig. 105), increases in the inflation pressure counter-intuitively result in increased angular deflection. This phenomenon is because smaller tension skirt radii result in larger torus radii. Coupled with the increased inflation pressure, the larger torus radii deflect the IAD surface forward under inflation loading, resulting in the surface being more normal to the oncoming flow and a subsequently larger deflection during aerodynamic loading. The transition point between an increase and decrease in angular deflection depends on the both the inflation pressure and tension skirt radius, balancing the increased inflation pressure projecting the IAD surface forward during inflation loading with the increased pressure stiffening preventing the IAD surface from deflecting backward during aerodynamic loading.

#### *3.6.2.1 Tension Cone Design Space Exploration Case Study: Angular Deflection Versus Centerbody Diameter Discussion*

The trend of increasing angular deflection with increasing centerbody diameter observed in Fig. 103 seems counter-intuitive. Larger centerbody diameters, which correspond to shorter side lengths, would generally be expected to produce smaller deflections. Figure 106 shows the cross-section profiles of two tension cone decelerators with centerbody diameters of 3 m and 6 m. Seen in the figure, the post-inflation and post-aerodynamically loaded torus locations are nearly identical. Therefore, the increased angular deflection of the $D_{Cen} = 6$ m IAD stems from the fact that its surface is rotating about a smaller radius circle, similar to the relationship between inscribed and central angles of a circle. In addition, upon further inspection, the identical torus locations of both configurations does make intuitive sense. Given that the tension cone stiffness is dominated by the structural performance of the single

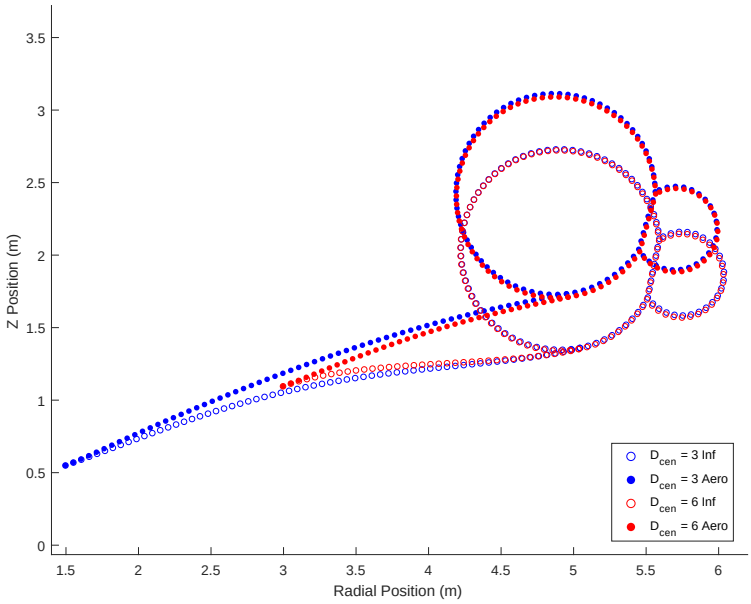


**Figure 106: Comparison of deflection results between tension cone configurations with 3 m and 6 m centerbody diameters. "Inf" legend entries refer to the deflected state after inflation loading and "aero" legend entries refer to the deflected state after inflation and aerodynamic loading.**

torus, because both configurations have an identical torus, they should deflect the same amount under inflation and aerodynamic loading.

### 3.6.3 Tension Cone Design Space Exploration Case Study: Response Surface Development

The 828 configurations generated in the design space exploration study are used to construct response surface equations to estimate the mass and surface deflection of new tension cone decelerator configurations for use in conceptual design. The tension cone response surface model is again composed of second-order polynomial basis functions of the design variables, including their pair-wise interactions. The mass and deflection responses are regressed against the basis functions to determine the polynomial coefficients, evaluating the responses at a subset of the data points, with 497 of the 828 solutions (60%) being use to generate the response surface model and the remaining 331 configurations (40%) being used to validate the model.

The full response surface equations are shown in Eqs. 43 and 44, with the variable

$R_{TS}$ denoting the tension skirt radius in meters. It is important to note that the deflection response surface is again formulated to produce a negative value to indicate a reduction in cone angle when subjected to aerodynamic loading.

$$\begin{aligned} m_{Tot,TC} = {} & 62.8560 - 15.0853D_{Maj} - 2.0215\theta_{Cone} + 45.1421R_{TS} \\ & - 2.0802D_{Cen} - 0.2005P_{Inf} + 8.1539D_{Maj} * D_{Maj} - 0.4648D_{Maj} * \theta_{Cone} \\ & + 0.0253\theta_{Cone} * \theta_{Cone} - 8.7537D_{Maj} * R_{TS} + 0.5642\theta_{Cone} * R_{TS} \\ & - 12.2238R_{TS} * R_{TS} + 0.1792D_{Maj} * D_{Cen} + 0.0300\theta_{Cone} * D_{Cen} \\ & - 0.3874R_{TS} * D_{Cen} - 0.6983D_{Cen} * D_{Cen} + 0.3068D_{Maj} * P_{Inf} \\ & - 0.0021\theta_{Cone} * P_{Inf} - 0.5696R_{TS} * P_{Inf} + 0.0049D_{Cen} * P_{Inf} \\ & + 0.0001P_{Inf} * P_{Inf} \end{aligned} \quad (43)$$

$$\begin{aligned} \Delta\theta_{Cone,TC} = {} & -21.748840 + 2.827661D_{Maj} + 0.674170\theta_{Cone} - 4.574110R_{TS} \\ & + 0.504490D_{Cen} + 0.029595P_{Inf} - 0.827652D_{Maj} * D_{Maj} - 0.004248D_{Maj} * \theta_{Cone} \\ & - 0.005721\theta_{Cone} * \theta_{Cone} + 3.489062D_{Maj} * R_{TS} - 0.018864\theta_{Cone} * R_{TS} \\ & - 3.682184R_{TS} * R_{TS} - 0.083813D_{Maj} * D_{Cen} - 0.009583\theta_{Cone} * D_{Cen} \\ & + 0.175830R_{TS} * D_{Cen} - 0.009771D_{Cen} * D_{Cen} - 0.014547D_{Maj} * P_{Inf} \\ & + 0.000055\theta_{Cone} * P_{Inf} + 0.029478R_{TS} * P_{Inf} - 0.000182D_{Cen} * P_{Inf} \\ & - 0.000097P_{Inf} * P_{Inf} \end{aligned} \quad (44)$$

The response surface's goodness of fit is evaluated based on the coefficients of determination, $R^2$ and adjusted $R^2$. The $R^2$ performance of both models is shown in Table 13. The mass response surface $R^2$ value is very good and the adjusted $R^2$ value is practically identical, showing that the basis functions can account for nearly the entire variability of the mass response, with the vast majority of basis functions being significant. This makes sense given that the tension cone decelerator is composed of a single torus and tension skirt, with both the fabric and gas mass

**Table 13: $R^2$ and adjusted $R^2$ values for the tension cone mass and deflection response surface equations**

| | Mass RSM | Deflection RSM |
|---|---|---|
| $R^2$ | 0.9992 | 0.9718 |
| Adjusted $R^2$ | 0.9992 | 0.9706 |

terms being summations of quadratic or lower order functions of the design variables. The deflection response $R^2$ value is notably less than that of the mass response and is also less than that of the stacked tori deflection response. This is likely due to the tension cone producing significantly larger deflections along with the non-linear behavior of the tension skirt deflection, which is therefore harder to capture with low-order basis functions.

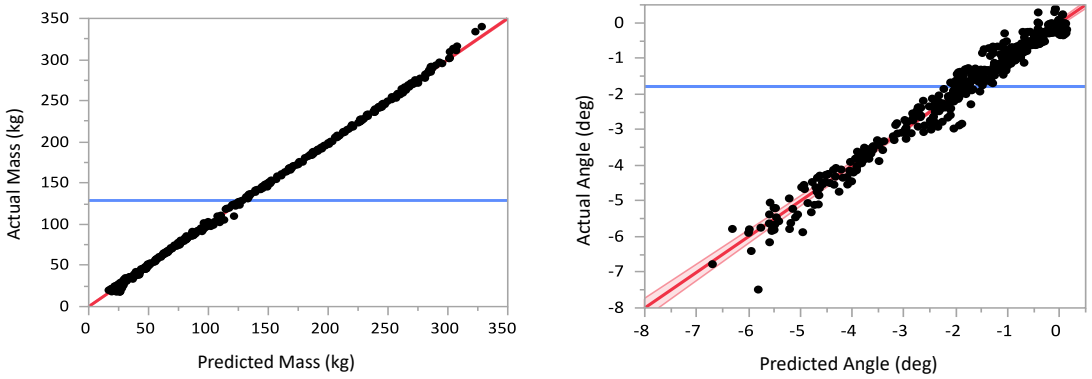


(a) Actual by predicted plot of the tension cone mass response surface equation

(b) Actual by predicted plot of the tension cone deflection response surface equation

**Figure 107: Response surface goodness of fit assessments showing actual tension cone mass and deflection values versus response surface predicted values**

Likewise, the tension cone response surface's goodness of fit is assessed via actual by predicted plots, shown in Fig. 107. The mass response actual by predicted plot, seen in Fig. 107(a), shows a nearly perfect correlation. Data points are tightly distributed about the perfect fit line and are evenly spaced with no obvious outliers, clumping, or trends. The deflection response graph in Fig. 107(b) still shows the data points to be approximately evenly distributed about the range of total deflection with

no obvious clumping or trends, but with a much larger dispersion of the data about the perfect fit line. This indicates that the response surface model is capturing the overall shape of the data and is not missing any fundamental characteristics but could benefit from more variability with an increased number of fitting terms.

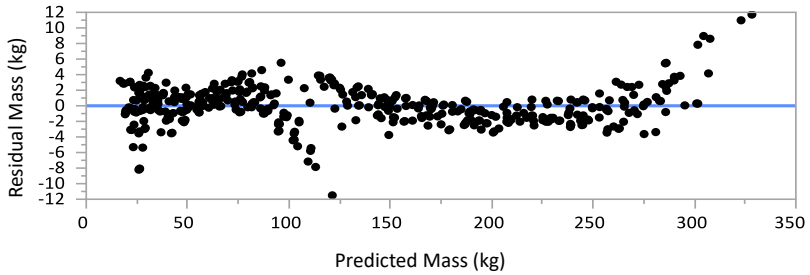


(a) Residual by predicted plot of the tension cone mass response surface equation

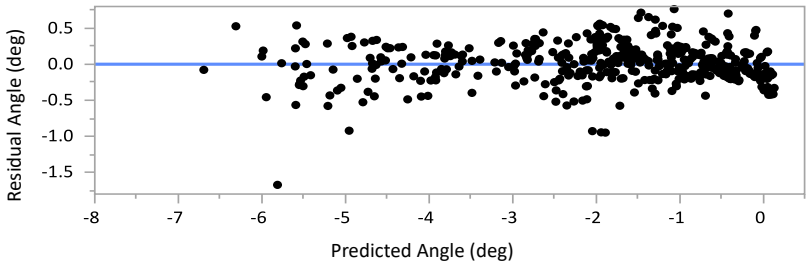


(b) Residual by predicted plot of the tension cone deflection response surface equation

**Figure 108: Response surface goodness of fit assessments showing residual tension cone mass and deflection values versus response surface predicted values**

The tension cone response surface models are also assessed via residual by predicted plots to better highlight trends within the residuals. Seen in Fig. 108(a), the residuals of the mass response do show a non-linear trend with respect to their predicted values. This indicates that higher order terms could be beneficial to further reduce the model residuals. However, aside from the general non-linear trend, the residuals appear to be approximately normally distributed about their centerline with minimal evidence of clumping. The deflection response residual by predicted plot, shown in Fig. 108(b), looks even better than that of the mass response. Data

points are grouped around the zero-residual line with no obvious overall trends. The distribution is mostly random with only one major outlier.

The comparison of the actual by predicted (in Fig. 107) and residual by predicted plots (in Fig. 108) also highlights the benefit of using both assessments to understand the response surface goodness of fit. For the tension cone design space study, the deflection residual by predicted plot in Fig. 108(b) looks better than the plot of the mass residuals in Fig. 108(a), displaying minimal evidence of clumping or overall trends in the data. However, when observing the actual by predicted graphs, the response surface mass model in Fig. 107(a) is obviously better, with model predictions that closely trace the actual response. As evidenced by this example, both curves provide unique information and contribute to a holistic assessment of the models, with the residual by predicted plot highlighting characteristic trends or groupings in the residuals and the actual by predicted plot providing an overall context of the magnitude of these residuals.

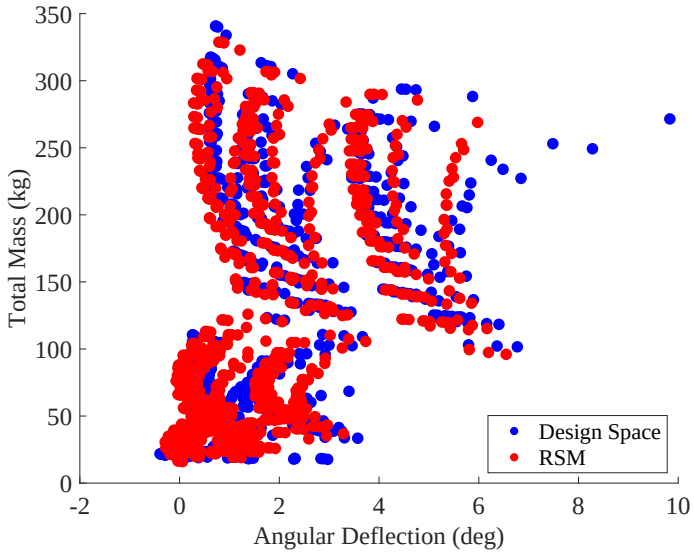


**Figure 109: Comparison of tension cone response surface mass and deflection predictions to actual simulated values**

The overall accuracy of the response surface models is lastly evaluated by overlaying the response surface equation predicted results with the simulated design space

results. As evidenced by Fig. 109, the response surfaces predict the mass and deflection results to a relatively high degree of accuracy. Major groupings of data points are retained in addition to the overall shape of the clusters. The correlation is observed to be better for large diameter configurations, likely due to the greater spacing of results. As such, exact spacing and trends of the smaller diameter vehicles are somewhat distorted, with the response surfaces predicting the general location of the mass and deflection responses, but with trends that more reflect the curvature of the larger diameter vehicles. Nevertheless, overall correlation of the response surfaces is very good, predicting the general locations of the stacked tori configuration's mass and deflection responses and even preserving the near-exact trends of the larger diameter vehicle responses. Therefore, these results demonstrate that the response surface equations can provide a reasonable estimate of the mass and deflection response of a wide range of stacked tori configurations during conceptual design.

## *3.7 Summary and Implications*

This study develops and validates simplified stacked tori and tension cone models to better understand the implications of decelerator design on their structural performance. These models are able to rapidly approximate the mass and deflection of candidate decelerator configurations and enable IAD structural performance to be assessed earlier in the design process such as during the conceptual design phase.

In particular, a simplified stacked tori model is developed, mirroring the geometry of a traditional stacked torus design used in static load testing for the NASA HIAD program and high-fidelity FEA modeling. This simplified model incorporates several modifications to improve modeling efficiency, most notably by eliminating expensive contact modeling and removing the pairing loop straps from the model definition. The resulting finite element model is validated against three different ground test and high-fidelity modeling data sets, assessing its predictions of the local and global

deformations and localized stresses. The model is observed to correlate very well with all validation data sets, often staying within the uncertainty of testing data across a range of geometries and loading conditions. The high degree of correlation with the validation data, along with the dramatic reduction in simulation cost, demonstrates that simplified modeling is a viable method for enabling structural performance estimation early in the design cycle.

To improve the applicability of the simplified stacked tori model, a generalized simplified model is developed, which abstracts the stacked tori geometry definition into a set of design parameters that can be used directly in conceptual design studies. An additional simplified model is also created for a tension cone decelerator that removes the stacked tori's inner tori and replaces them with a flexible tension skirt. Validation of the tension skirt simulation against analytic predictions displays a high a degree of correlation, again showing that simplified tension cone models are applicable for assessing structural performance during conceptual design.

In order to demonstrate the utility of the simplified models for use in early phase design activities, case studies are conducted to simulate the mass and deflection of many stacked tori and tension cone configurations. The case studies involve discretizing the ranges of each design variable to construct a full factorial design space and then simulating each resulting configuration to assess its structural and mass performance. The surface deflection and mass results are analyzed to understand their sensitivity to each design parameter and to isolate the relative impact of each of the design variables. These results are valuable for informing future mission designers on the possible ranges of IAD decelerator mass and deflection along with the general impacts of IAD configuration decisions. In addition, response surface models are generated to approximate the mass and deflection responses of the stacked tori and tension cone decelerators. These response surfaces decouple the IAD structural and mass predictions from the computational simulations and allow mission designers to

perform faster estimations of the IAD performance, even enabling integration of the IAD structural and mass performance into high-level architecture optimization and trade studies.

# CHAPTER IV

# FORMULATION AND EVALUATION OF A HYBRID INFLATABLE DECELERATOR CONFIGURATION

## *4.1 The Hybrid Decelerator Configuration Concept*

The tension cone and stacked tori configurations represent two of the most prolific IAD designs that have been developed. Both implementing some form of conical structure supported by inflatable tori, each design can reduce an entry vehicle's ballistic coefficient through an increase in the decelerator drag area with minimal increase in mass. However, both designs go about achieving this goal differently. Stacked tori configurations, utilizing several structural tori, are developed for extreme loading environments such as the hypersonic deceleration regime but are relatively heavy due to the large number of components used in their construction. Tension cone configurations, utilizing a single structural torus and tension skirt, are developed for moderate loading environments such as the supersonic deceleration regime and are much lighter, due to their thin fabric skirt. These generalized characteristics are reflected in the stacked tori and tension cone mass and deflection performance in Fig. 95(b), where stacked tori designs typically produce higher mass, lower deflection solutions and tension cone designs typically produce lower mass, higher deflection solutions.

The general idea behind the hybrid decelerator concept is to incorporate elements from both the stacked tori and tension cone designs in order to improve both the decelerator mass and stiffness performance. Seen in Fig. 110, the hybrid configuration adopts the tension skirt from the tension cone design and multiple tori from the stacked tori design. In this way, the hybrid configuration can improve inflatable decelerator performance by leveraging the high stiffness of multiple tori with the

lower mass of the tension skirt. This modification can be thought of as a stiffening of the tension cone's single structural torus in order to enable tension cone designs to reduce their surface deflection and withstand the higher loading environments during hypersonic descent. Equivalently, the modification can also be interpreted as a reduction in mass of the stacked tori configuration by removing the inner tori, which experience less compressive loading, and replacing them with a more mass efficient tension skirt that can support the high tensile stresses in this region. In addition, both the number of tori and tension skirt radius parameters can be independently varied to optimize the decelerator performance characteristics based on the requirements of a specific mission.

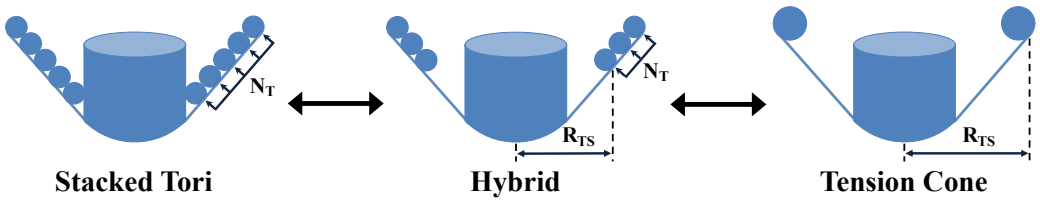


**Figure 110: Diagram of the hybrid inflatable decelerator configuration in relation to the reference stacked tori and tension cone designs**

## *4.2 Hybrid Configuration Model Development*

The hybrid configuration finite element model is shown in Fig. 111, with the cross-section view in Fig. 111(a) and a description of the modeled components in Fig. 111(b). As seen in the figures, the FEA model combines elements of the stacked tori and tension skirt models into a single configuration. Because the hybrid model includes multiple tori along with a tension skirt, both the $N_{Tori}$ and $R_{TS}$ design variables are used in the geometry definition.

### 4.2.1 Hybrid Configuration Finite Element Model Implementation

The finite element model attaches the tension skirt between the centerbody and the first torus, mimicking the implementation of the tension cone model. Similarly, the

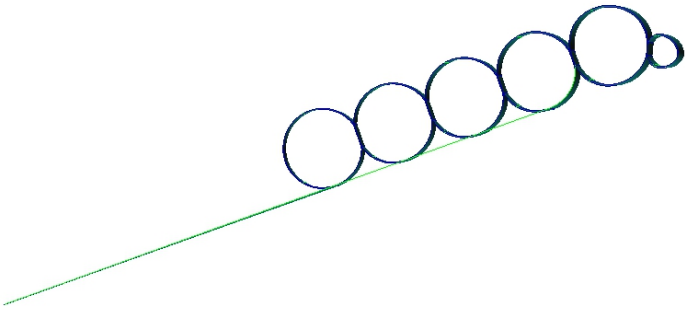

(a) Cross section view of the hybrid configuration

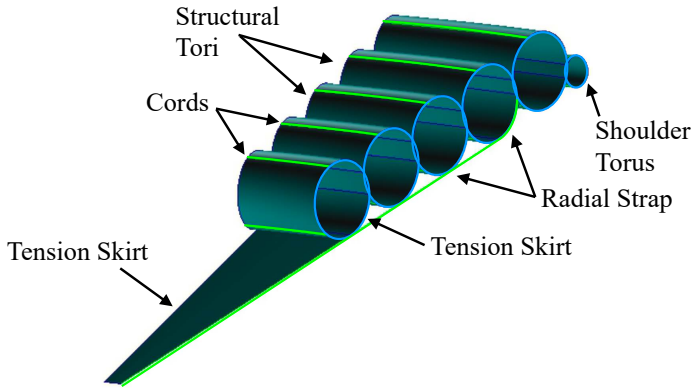


(b) Hybrid configuration FEA wedge model showing simulated components

**Figure 111: Geometry of the hybrid configuration**

additional tori copy the implementation of the stacked tori model, including the same tori overlap and other fixed parameters. The radial strap takes characteristics from both the stacked tori and tension cone models, attaching to the tension skirt from the centerbody to $T_1$, similar to the tension cone model, but then continuing on without the tension skirt between $T_1$ and $T_{N-1}$ like the stacked tori model. Two special cases arise for models with two or fewer tori. For configurations with $N = 2$, the radial strap attaches between the centerbody and $T_1$. Because $T_1$ is $T_{N-1}$ in this case, the radial strap does not continue on in order enforce a consistent termination at $T_{N-1}$ as was used for the stacked tori configurations. For the case of $N = 1$, the radial strap attaches to $T_1$ because it is the only structural torus. As a result, both designs with $N = 1$ or 2 behave similarly to tension cone decelerators, attaching the radial strap to the first torus.

Boundary conditions of the hybrid model are the same as those of the tension cone model, fixing nodes along the nose cone and enforcing symmetry among all nodes on the front and back cross sections. Because the hybrid configuration is intended for hypersonic entry and descent applications, the HIAD fabric and strap material properties are used in the model. The thickness and wedge degree models are also implemented to account for an associated strap pattern.

### 4.2.2 Hybrid Configuration Geometry Definition

The hybrid decelerator geometry definition is a combination of both the stacked tori and tension cone equations. Like the other methods, the hybrid algorithm constructs equations for the side length and base radius and equates their expressions to solve for the torus radius. As evidenced by Fig. 112, which shows the relevant parameter definitions for the hybrid configuration, the hybrid geometric definition can either be formed by adding the multi-torus terms to the tension cone decelerator geometric expression or by replacing the centerbody overlap term of the stacked tori geometric expression with that of the tension skirt. The resulting expression for the decelerator

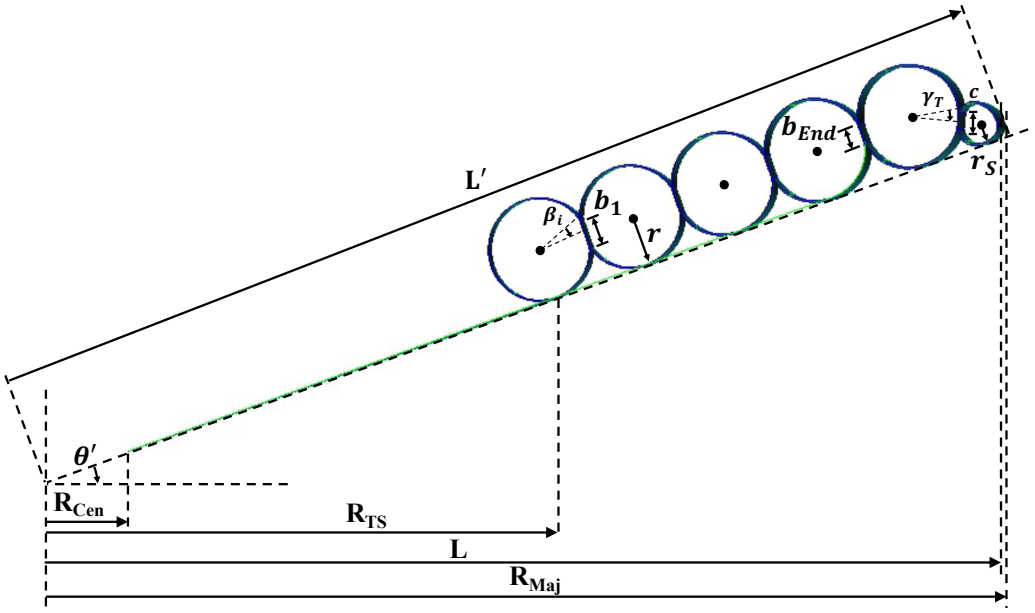


**Figure 112: Geometry definition of the hybrid decelerator model**

side length, $L'$, is shown in Eq. 45. Like the previous methods, the adjusted base radius, $L$, is calculated based on the major radius as in Eq. 46.

$$L' = \frac{R_{TS}}{\cos(\theta')} + \sum_{i=1}^{N-1} 2r\cos(\beta_i) + \sqrt{\big(r\cos(\gamma_T) + r_s\cos(\gamma_S)\big)^2 - (r - r_s)^2} + r_s \tag{45}$$

$$L = R_{Maj} - r_s\big(1 - \cos(\theta')\big) \tag{46}$$

Newton's method is used to iterate on the value of the torus radius, $r$ that satisfies Eq. 47. The function's derivative with respect to the torus radius, used in the Newton's method algorithm, is expressed in Eq. 48. The hybrid configuration also has the same constraint on the tension skirt radius as the tension cone configuration, such that the tension skirt is sized large enough so that the first torus does not intersect with the theoretical centerbody. This constraint is expressed in Eq. 49.

$$f(r) = L' - \frac{L}{\cos(\theta')} = 0 \tag{47}$$

$$\begin{aligned} f'(r) = \frac{\partial\left(L' - \frac{L}{\cos(\theta')}\right)}{\partial r} = \\ \sum_{i=1}^{N-1} 2\cos(\beta_i) + \frac{1}{2}\Big[\big(r\cos(\gamma_T) + r_s\cos(\gamma_S)\big)^2 - (r - r_s)^2\Big]^{-\frac{1}{2}} \\ * \big[2\big(r\cos(\gamma_T) + r_s\cos(\gamma_S)\big)\big(\cos(\gamma_T) + \epsilon\cos(\gamma_S)\big) - 2(r - r_s)(1 - \epsilon)\big] \\ + \frac{\epsilon}{\cos(\theta')} \end{aligned} \tag{48}$$

$$R_{TS} \geq R_{Cen} + r\big(1 + \sin(\theta')\big) \tag{49}$$

### 4.2.3 Hybrid Configuration Mass Model

The hybrid configuration mass model is similarly a combination of the stacked tori and tension cone mass terms. Like the two baseline configurations, the total mass

is determined from the sum of the fabric and gas mass components, the fabric mass being the product of the fabric surface area and density and the gas mass being the product of the inflatable volume and the gas density. The hybrid decelerator does not add any inflatable components in addition to that of the stacked tori configuration and, therefore, has the same expression for the total volume, shown in Eq. 50. The expression for the hybrid configuration surface area accounts for the multiple tori, shoulder torus, the conical frustum portion of the tension skirt, and the wrap around portion of the tension skirt and is shown in Eq. 51.

$$V_{Total} = 2\pi^2(r^2 \sum_{N} R_i + {r_s}^2 R_s) \tag{50}$$

$$SA_{Total} = 4\pi^2(r \sum_{N} R_i + r_s R_s) + \frac{\pi(R_{TS}^2 - R_{Cen}^2)}{\sin(\theta)} + \pi^2 Rr + 2\pi r^2\Big(\cos(\theta) + \sin(\theta)\Big) \tag{51}$$

## *4.3 Hybrid Model Verification*

There are no existing data sets against which to validate the hybrid decelerator configuration performance. Although, specific features, such as the tension skirt and multiple tori, have been individually validated in the tension cone and stacked tori validation studies. Therefore, verification of the hybrid model involves inspection of the code to ensure proper modeling and comparisons of the relevant features against the validated stacked tori and tension cone session files.

The hybrid model predictions can also be compared against the baseline tension cone and stacked tori configurations to validate their results. The tension cone design can be recovered exactly by setting the hybrid configuration number of tori parameter to one. Results are compared directly for this case. The stacked tori geometry can also be approximated by setting the tension skirt radius parameter to its minimum value, resulting in the first torus being located adjacent to the centerbody, like the

stacked tori design. While not resolving an identical geometry, this pseudo-stacked tori model allows for a comparison against the validated stacked tori results.

The hybrid configuration comparison against the validated generalized simplified stacked tori model is accomplished by tuning the hybrid model to replicate all design parameters of the stacked tori model, matching the major diameter, centerbody diameter, cone angle, number of tori, and inflation pressure. The tension skirt is sized to the minimum tension skirt radius constraint to best approximate the stacked tori torus locations. It is important to note that, despite the similar tori locations, there are still fundamental differences between the tuned hybrid configuration and the stacked tori model. Because the hybrid model does not allow for a centerbody overlap, the tori locations and radii are close but not match exactly. More importantly, however, are the differences in boundary conditions, which cannot be replicated. Along with fixing the radial strap to the centerbody, the stacked tori model also constrains the inner surface of the first torus to the centerbody structure to mimic the contact in this region. Given that the tori are not allowed to contact the centerbody in the hybrid model, there is no boundary condition enforced on the first torus, which allows for additional degrees of freedom. Nevertheless, despite these differences, the pseudo-stacked tori comparison results are still the closest available way to verify the hybrid decelerator model against test data.

Results of the comparison, showing the deflected cross sections of both the hybrid and stacked tori models, are shown in Fig. 113. As seen in the figure, the deflected responses are very close, with the inflation response of the two models (depicted with hollow markers), being practically identical. The overall angular deflection of the hybrid model, measured at the intersection of the radial strap and structural tori, is also nearly an exact match to the stacked tori decelerator. The main difference between the two models is that tori one through five of the stacked tori model are deflected aft further than those of the hybrid model. This is due to the impact of the

differing boundary conditions. $T_1$ of the stacked tori model is attached to both the centerbody and $T_2$, which results in it becoming significantly distorted under load. Conversely, $T_1$ of the hybrid model is attached on the windward side to the tension skirt and to $T_2$, with the asymmetrical boundary conditions resulting in a more circular cross section and reduced deflection. This difference is seen to propagate throughout the subsequent tori but decay before $T_6$ and the radial strap attachment point. Without the difference in boundary conditions, the deflection of $T_7$ and the shoulder torus are observed to be nearly identical.

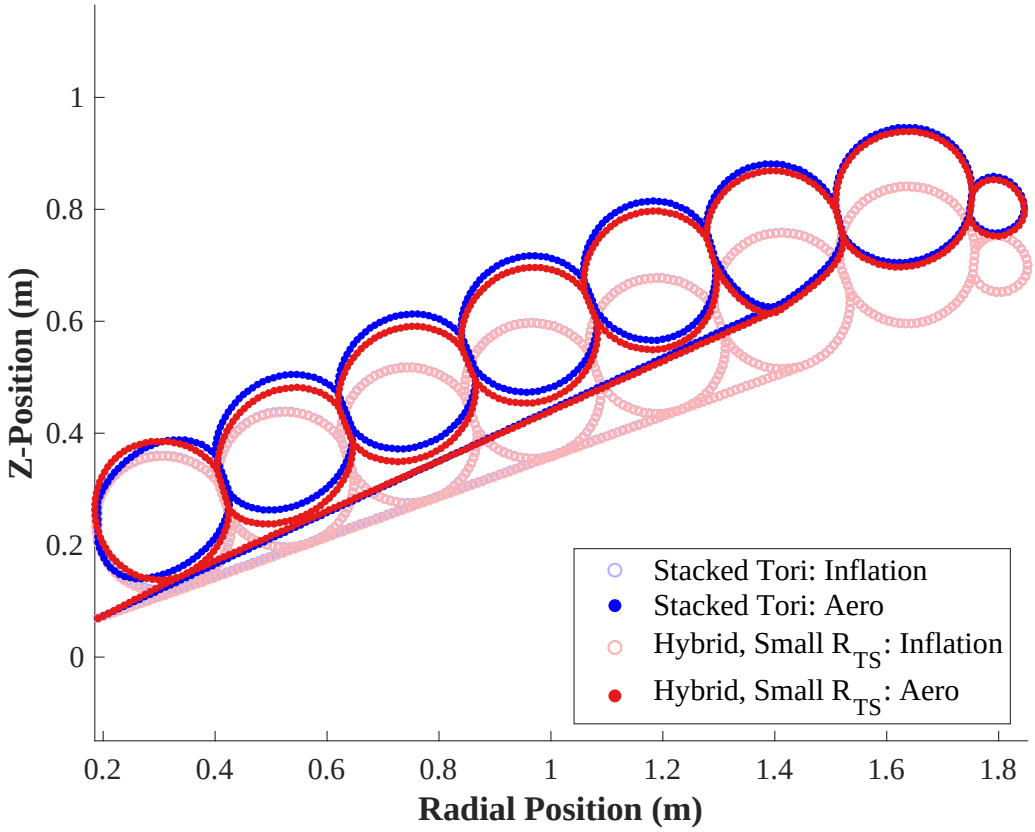


**Figure 113: Verification of the hybrid configuration model against the validated generalized simplified stacked tori model**

Overall, given the large differences in boundary conditions and features near the centerbody, the two deflected surfaces match surprisingly well. The overall deflection response is captured by the hybrid configuration with the primary discrepancies being the deformation of the first torus and the slightly increased curvature of the

stacked tori surface interior to $T_6$. These results, therefore, lend confidence to the hybrid configuration FEA model and its ability to simulate the deflections of inflatable decelerators.

## *4.4 Hybrid Model Parameter Impact Studies*

The hybrid decelerator configuration is a new design that has not previously been studied. As such, it is difficult to predict the resulting deformed surface under load. In order to better understand the hybrid design and interpret the future design space study results, parameter sweeps are performed with respect to the number of tori and tension skirt radius design parameters. These sweeps are used to better understand the impact of both parameters on the resulting deformation and to conceptualize the deformed shape relative to the baseline stacked tori and tension skirt configurations.

### 4.4.1 Hybrid Model Parameter Study: Addition of Tension Skirt

The tension skirt addition study is performed to understand how the hybrid tension skirt impacts the deformed shape of the stacked tori decelerator. The investigation is performed on the verified stacked tori model and the pseudo-stacked tori hybrid model, discussed in Section 4.3, but with an increase in the size of the tension skirt for the hybrid design.

Seen in Fig. 114, despite the larger tension skirt and smaller resulting tori, the hybrid configuration has a smaller angular deflection at the radial strap attachment point to the structural tori. In fact, an interesting phenomenon arises, where the hybrid radial strap attachment point to $T_1$ is located aft of the stacked tori radial strap but the hybrid radial strap attachment point to $T_6$ is located on the windward side. Thus, the structural tori of the hybrid configuration are observed to rotate, causing the smaller angular deflection measurement. The reason for this rotation is due to the removal of the inner structural tori, reducing the compressive stiffness towards the center of the decelerator and instead moving the centroid of the structural

elements radially outward. As a result, the flexible tension skirt allows for radial compression of the inner section of the hybrid decelerator, deforming much like a tension cone, with the tori radially inward of the centroid being compressed and the tori radially outward of the centroid exhibiting less deformation in order to maintain continuity of the surface slope.

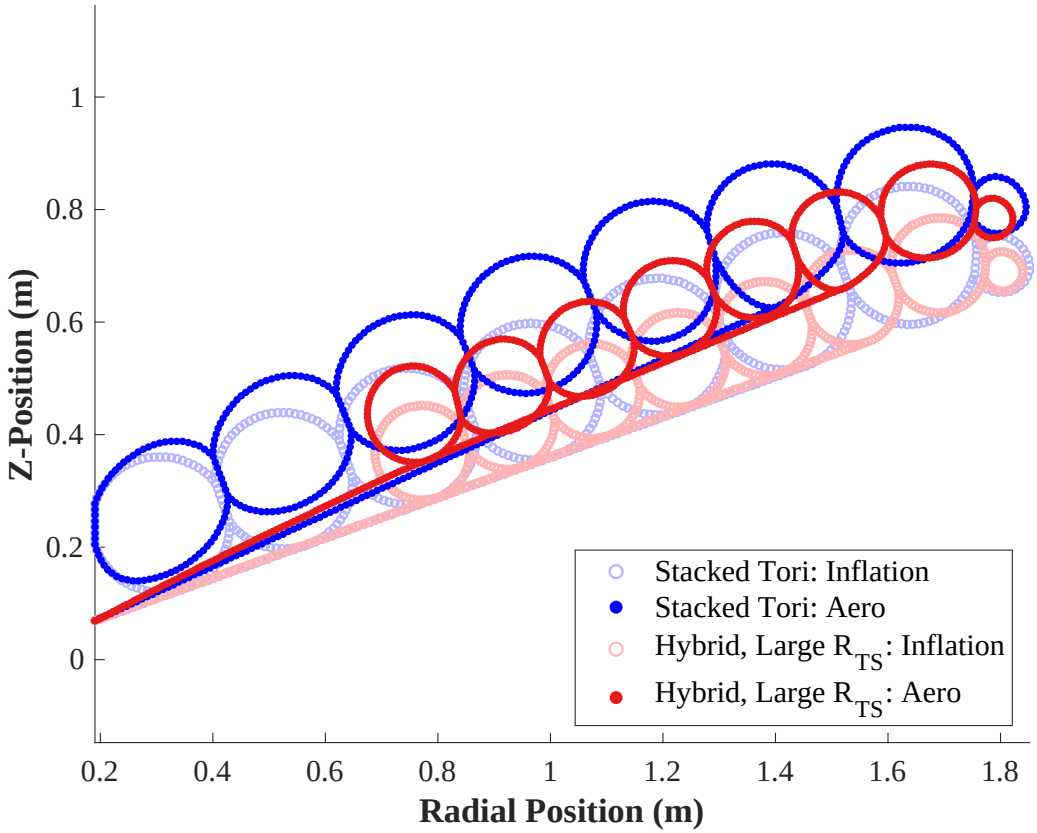


**Figure 114: Comparison of a hybrid configuration model with large tension skirt against the stacked tori model**

Inspection of the figure also provides other features of note. In particular, the stacked tori surface exhibits more curvature than the hybrid surface, despite the hybrid configuration having smaller tori and the flexible tension skirt allowing for rotation. This is likely due to the additional radial strap attachment point to $T_1$ in the hybrid configuration and the fact that it is shifted radially outward due to the smaller tori. The extra attachment point provides an additional boundary constraint on the structural tori mid-way along the side of the decelerator that reduces the length

over which the tori are unsupported. This shorter unsupported span is observed to reduce the overall flexure in the surface and results in a reduction in the curvature of the tori stack. Note, however, that this degree of surface deflection is atypical for the stacked tori configuration and is due somewhat to the large aerodynamic loading applied.

As seen before in the pseudo-stacked tori hybrid discussion in Section 4.3, the hybrid design shown in Fig. 114 also exhibits significantly less distortion of the first torus than the stacked tori design. Thus, it can be concluded that the use of the asymmetric boundary conditions on the first torus, constraining it between the tension skirt and $T_2$, contributes to a more circular torus cross section. It is also interesting to note that the inflation profiles of both decelerators are nearly identical, indicating that the presence of the tension skirt does not significantly impact the angular deflection under inflation loading.

Overall, it is evident that the deflected hybrid surface has features in common with the two baseline designs but that they combine to create a unique deformed state. The replacement of the inner structural tori with the tension skirt reduces the IAD's compressive stiffness in this region, resulting in an increased deflection of the tension skirt and inner tori like that of the tension cone. The stack of multiple tori behaves like the single structural member of the tension cone design but extends the tension skirt attachment location radially inward, changing the inflection point of the surface. Using multiple tori to support the tension skirt also is observed to induce a rotational effect of the IAD surface, pushing the outer tori in the windward direction to maintain continuity of the tori stack. This rotation of the tori stack about its approximate centroid appears to be characteristic of the hybrid configuration deformation and results in a reduction of the angular deflection measurement under load. Therefore, it is evident that the hybrid configuration shows the potential to reduce the mass deflection, or at least allow for an optimization of either result metric, relative to the

baseline stacked tori and tension cone decelerators.

### 4.4.2 Hybrid Model Parameter Study: Tension Skirt Parameter Sweep

The effects of the tension skirt are further investigated by performing parameter sweeps across a wide range of values. For consistency, all cases are run on the 3.7 m, 70° model discussed in Sections 4.3 and 4.4.1 with inflation and external pressures of 83,000 Pa and 2,500 Pa, respectively. Two sweeps in $R_{TS}$ are run for both 4-torus and 7-torus configurations to understand how the trends evolve across the design space.

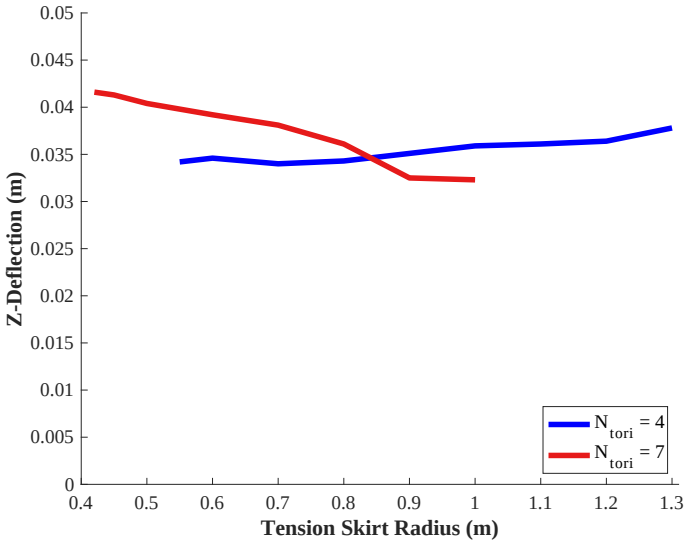


**Figure 115: Deflection results across the parameter sweep in tension skirt radius**

The results of the two parameter sweeps are shown in Fig. 115, displaying the deflection (calculated as the difference in the axial position between the aerodynamic and inflation loaded states) of the aft peak of the final torus, $T_N$. This original definition of deflection is chosen to allow for referencing to the earlier stacked tori validation and parameter studies and, due to the single value of centerbody and major diameters used for the configurations, generally produces equivalent trends as the angular deflection measurement. Figure 115 displays two approximately linear curves with opposite trends. For the 7-torus configuration, deflection is observed to decrease

(improve) with increasing tension skirt radius. For the 4-torus configuration, it is observed to increase (get worse). The conflicting trends indicate that there are multiple competing phenomena with varying effects at different scales and that interactions between the various design parameters are significant. This also demonstrates that the value of the tension skirt radius producing the smallest deflection varies across the design space and is not easily optimized to a minimum or maximum value. It is important to note that, like in the tension cone design space study, the ranges of tension skirt radius are different for each configuration based on the varying constraints on torus size. Therefore, assessments with respect to relative values of tension skirt radius are more appropriate than directly comparing identical values. Note also that minor deviations from the overall trend for isolated runs can be attributed to several factors, such as slightly different discretization of the torus mesh and selected nodes or slight variations in the nonlinear solver.

The deflected shapes of the two extreme 7-torus configurations, the designs with tension skirt radii of 0.42 m and 1.00 m, are plotted in Fig. 116 to investigate the decreasing trend in deflection. It can first e observed that the inflated states of the two decelerators, which are nearly identical, do not contribute to the differences in deflection. Under aerodynamic loading, the smaller, $R_{TS} = 0.42$ m configuration approximates a stacked tori design, with inflatable structural members distributed evenly along the decelerator. The resulting deformed surface is observed to be relatively straight, with a linearly increasing deflection with increasing radial position. The larger, $R_{TS} = 1.00$ m configuration concentrates the structural members towards the outer radius of the decelerator and produces an approximately bilinear deflected surface. This bilinear deflected surface results from the large deflection of the tension skirt, a pivot point at the tension skirt attachment to the structural tori, and a shallow sloped tori stack. This uneven loading about the structural tori centroid causes a rotation of the tori, similar to what was observed in the stacked tori comparison

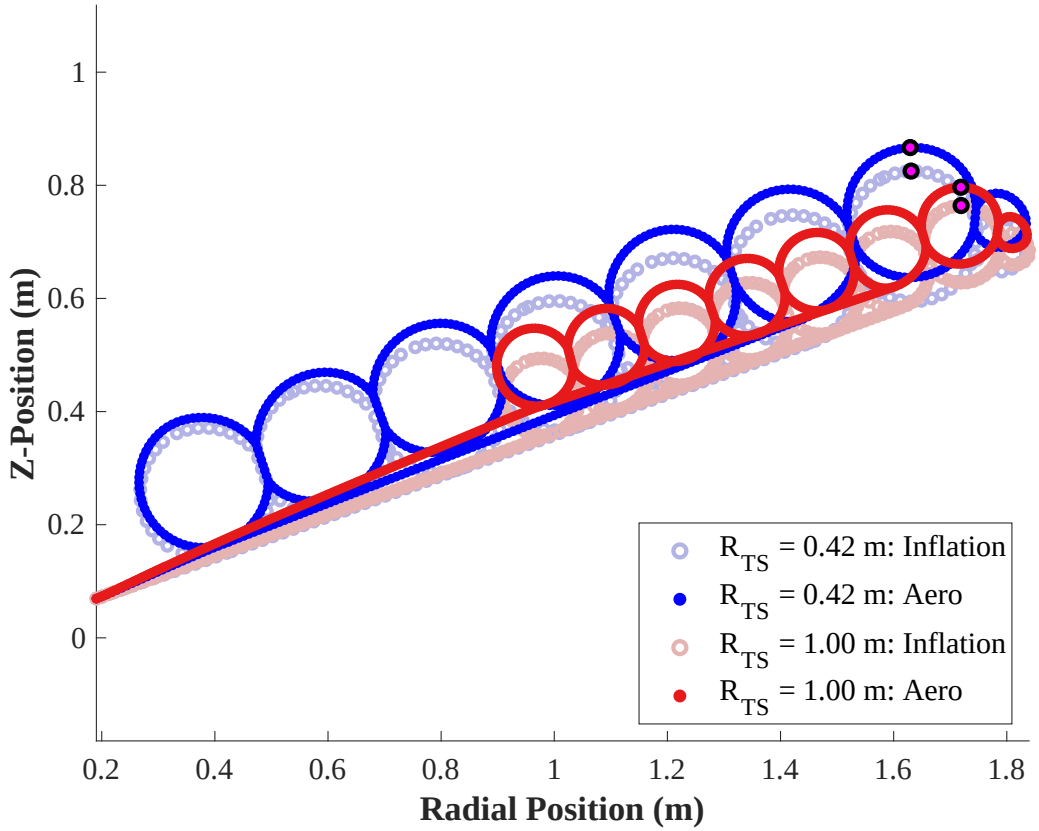


**Figure 116: Comparison of the deflected cross sections of two 7-torus hybrid configurations with different values of tension skirt radius**

study, and deflects the outer tori towards the freestream flow. At the same time, the smaller tori of the large tension skirt radius design are experiencing an overall larger compression compared to the small $R_{TS}$ design. However, for the 7-torus configuration, the rotational effects deflecting the outer tori forward are seen to overcome the general increase in deflection of all tori and result in the smaller axial deflection. Note that this reduced deflection comes at the expense of an increased surface slope towards the center of the decelerator.

The deflected shapes of the two extreme 4-torus configurations, the designs with tension skirt radii of 0.55 m and 1.30 m, are plotted in Fig. 117. For these configurations, the larger tension skirt radius instead corresponds to a larger deflection. Once again, like the 7-tori decelerators, the inflation states are similar between the two configurations and do not appear to significantly influence the difference in deflection

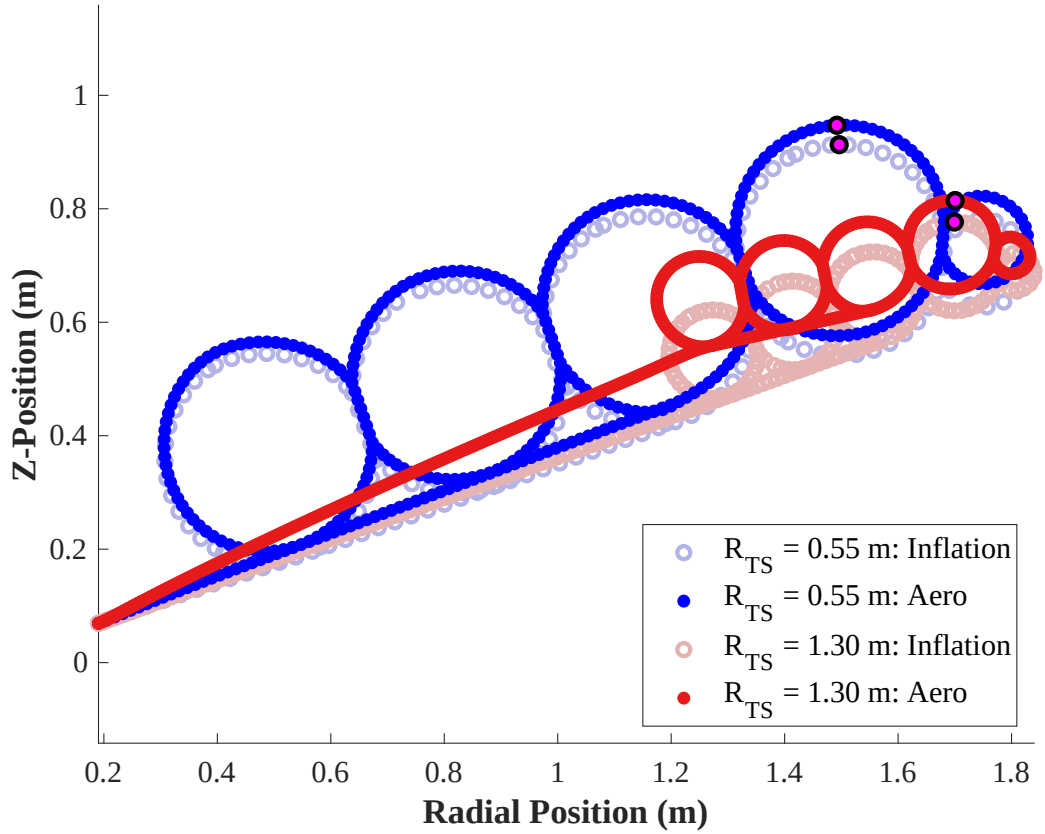


**Figure 117: Comparison of the deflected cross sections of two 4-torus hybrid configurations with different values of tension skirt radius**

values. The two designs are also observed to deflect in the same general manner as their 7-tori counterparts, with the small $R_{TS}$ configuration deflecting linearly with respect to radial position and the large $R_{TS}$ configuration exhibiting a large deflection of the tension skirt that pushes the outer tori forward to maintain continuity of the multi-torus stack. However, unlike the 7-torus case, the 4 tori in the large $R_{TS}$ design are small enough that the overall compression of the structural tori from aerodynamic loading is enough to overcome the deflection gains due to the rotation of the torus stack and produces a larger axial deflection. As a result, the increase in tension skirt radius and the corresponding reduction in the torus cross section diameter is seen to dominate the overall deflection response in this regime.

The tension skirt radius parameter sweep study illuminates several phenomena

that influence the decelerator deflection. Larger tension skirt radii reduce the cross-sectional diameter of the structural tori, generally decreasing their resistance to compression from external aerodynamic loading. However, larger tension skirts also push the structural members further towards the periphery of the decelerator and allow for a rotation of the multi-torus stack due to the differential stiffness in the inner and outer regions of the decelerator. This rotational effect is observed to decrease the local deflection of outer tori and, in some cases, contribute to an overall reduction in surface deformation. As seen in comparisons to the stacked tori decelerators, the additional attachment point between the tension skirt and first torus also can reduce distortion of the tori cross sections and reduce the total span over which the tori stack can deform.

### 4.4.3 Hybrid Model Parameter Study: Number of Tori Parameter Sweep

The impact of differing numbers of tori is studied by performing parameter sweeps across a wide range of values at two different tension skirt radii. All cases are again run on the 3.7 m, 70° model with inflation and external pressures of 83,000 Pa and 2,500 Pa, respectively. Two sweeps of $N_{Tori}$ are conducted at both $R_{TS} = 1.15$ m and $R_{TS} = 0.80$ m, allowing a comparison of the trends across the design space.

The results of the parameter sweeps are shown in Fig. 118, displaying the axial-deflection of the final torus, $T_N$, as a function of the number of tori. One significant feature that stands out is that there is a discontinuity in the results for $N = 2$ and $N = 1$. This change in behavior is due to the difference in the hybrid configuration radial strap design for 1- and 2-torus decelerators, discussed in Section 4.2.1. Due to the radial strap terminating at $T_{N-1}$, both the 1- and 2-torus configurations are variations of a tension cone decelerator with the tension skirt and radial strap connecting to and ending at the first torus. As a result, these configurations do not behave the same as the traditional hybrid decelerators. The 2-torus design does not benefit as much from

rotations of the cohesive multi-torus stack connected by the radial strap and the 1-torus tension cone design exhibits a significant rotation about the torus cross section center point, which rotates the aft apex forward and reduces the axial-deflection measurement, but would also rotate the radial strap intersection aft and increase the angular deflection measurement. In the absence of the single and double-torus configurations, the results behave smoothly across the entire design space.

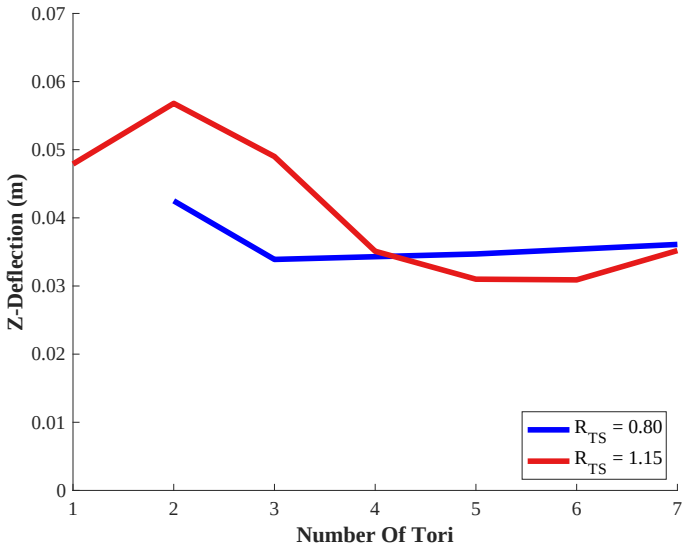


**Figure 118: Deflection results across the parameter sweep in number of tori**

Unlike the tension skirt radius study, the number of tori parameter sweep at $R_{TS} = 1.15$ m is non-linear and both curves in Fig. 118 exhibit significantly different behaviors. Ignoring the data points at $N = 1$ and 2, the curve of deflection versus number of tori for $R_{TS} = 1.15$ m decelerators appears quadratic, with an easily definable minimum, whereas the curve is practically linear for $R_{TS} = 0.80$ m decelerators. Therefore, these results confirm the observations of tension skirt radius parameter sweep, that the hybrid configuration deflection is characterized by multiple competing phenomena that may or may not allow for optimization in any single parameter.

The deflected shapes of the 2-torus, 5-torus, and 7-torus configurations with $R_{TS} =$

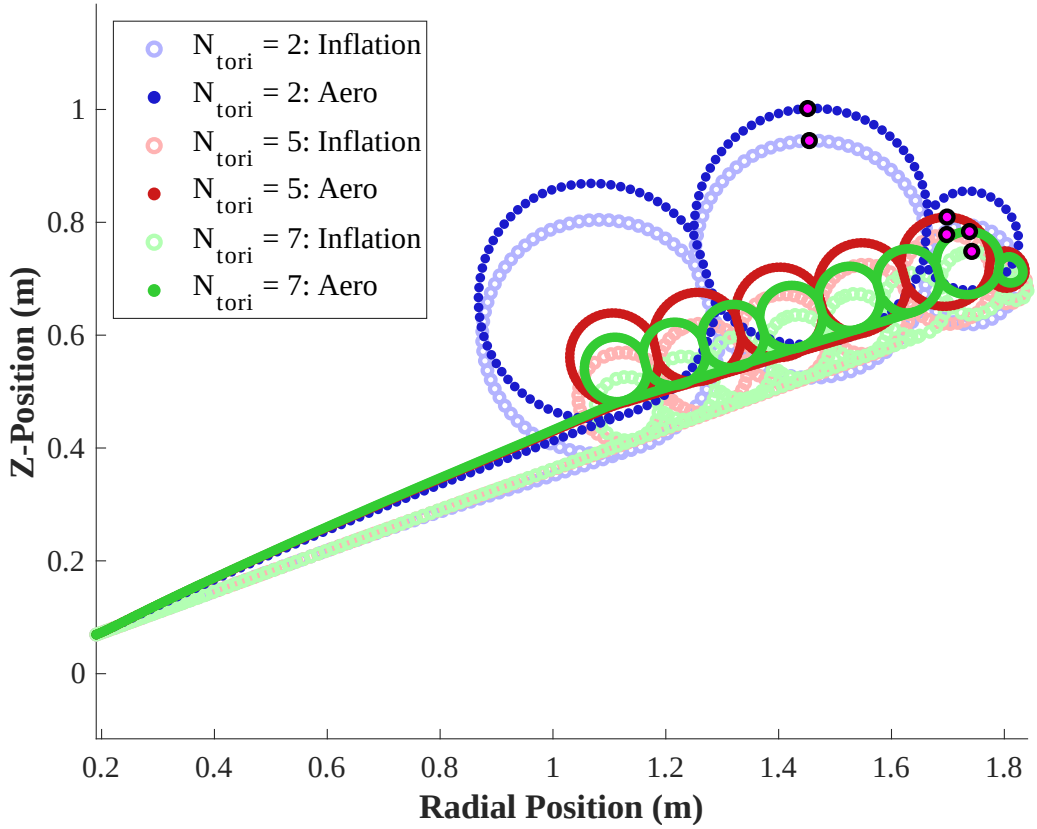


**Figure 119: Comparison of the deflected cross sections of three hybrid configurations with a tension skirt radius of 1.15 m and different number of tori**

1.15 m are plotted in Fig. 119 to investigate the quadratic trend with respect to the number of tori. As observed in the figure, because all the configurations are composed of a tension skirt and multiple tori, they all exhibit a rotation of the multi-tori stack to some degree. The 2-torus configuration with the largest tori is observed to have the least deformation at the tension skirt interface to $T_1$. However, multiple factors contribute to a small rotation of the two-torus stack that ultimately results in it having the largest overall axial deflection of the three configurations. The fewer tori of the $N = 2$ design means that the outer tori are located closer to the center of rotation and, coupled with the lack of a radial strap attaching $T_1$ to $T_2$, contributes to diminished rotational effects due to having a shorter, less rigid moment arm. Along with the smaller deflection at the tension skirt interface to $T_1$, the 2-torus

configuration therefore behaves closer to the linear stacked tori deflection than the other hybrid designs.

The 5-torus and 7-torus configurations have much more similarly sized tori and, as a result, deflect in a similar manner. Both designs benefit from significant rotation of the multi-torus stack, which contributes to their overall reduction in deflection compared to the 2-torus design. The 7-torus decelerator, with the smaller tori, is seen to deflect more at the tension skirt interface to $T_1$, as would be expected. However, the 7-torus configuration torus stack is also seen to rotate less than that of the 5-torus IAD due to the increased global compression on the tori. The larger overall compression is able to dominate the 7-torus decelerator's deflection characteristics and result in a larger axial deflection at the final torus. Given that the 5-torus and 6-torus vehicles are located at the minimum of the deflection curve in Fig. 118, it is evident that $N = 5, 6$ is the transition point where the compression of the overall smaller tori overcomes the impacts of the torus stack rotation.

The deflected cross sections of the 2-torus, 3-torus, and 7-torus configurations with $R_{TS} = 0.80$ m are plotted in Fig. 120. Inspection of the figure shows that rotational effects due to the tension skirt and torus stack interactions are less significant than in the $R_{TS} = 1.15$ m case, with the windward deflected surfaces generally appearing more linear for the configurations with small tension skirts. The reduction in the torus stack rotational effect is likely due to two reasons: that the shorter tension skirt provides less distance for deflection prior to the $T_1$ intersection point and that the shorter tension skirt results in larger tori, which resist the increase in deflection of the inner tori. As a result, small tension skirt hybrid decelerator configurations appear to behave more similarly to stacked tori designs, with deflection increasing with greater numbers of tori due to the reduced overall stiffness of the structural tori and their corresponding increase in global deflection.

As discussed in the tension skirt radius parameter study, the hybrid decelerator

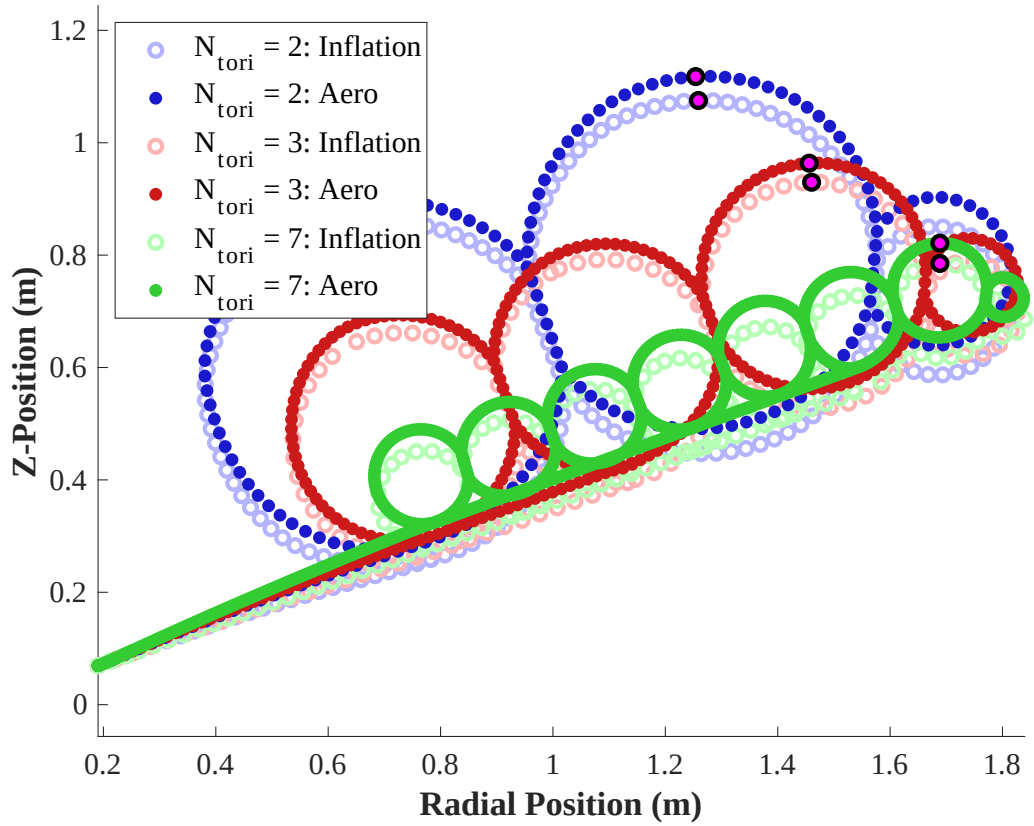


**Figure 120: Comparison of the deflected cross sections of three hybrid configurations with a tension skirt radius of 0.80 m and different number of tori**

deflection is a balance of both the overall compression of the structural tori and the rotation of the tori stack due to the differential deflection of the inner and outer tori. The impact of these two phenomena varies across the design space, with the configuration that results in the minimum deflection best leveraging the deflection reduction of the tori stack rotation while minimizing deflection due to torus compression. In general, both phenomena tend to increase with decreasing torus radii, either due to having a large tension skirt or many tori. Because configurations with a smaller tension skirt reduce the magnitude of the torus stack rotation and the impact of its corresponding reduction in deflection, the minimum deflection configurations with $R_{TS} = 0.80$ m are therefore observed to shift towards designs with fewer tori

that are better able to mitigate the torus compression. This explains why the minimum deflection configuration with $R_{TS} = 0.80$ m has 3 tori whereas the minimum deflection configuration with $R_{TS} = 1.15$ m has 5 to 6 tori.

The reason why the 2-torus configuration does not continue the trend of decreasing deflection with decreasing number of tori is not due to the balance of the tori stack compression and rotation but is instead because of differences in its design, behaving more so like a tension cone decelerator compared to the other configurations. Given that $T_1$ is the same as $T_{N-1}$ for the 2-torus configuration, the radial strap does not continue on to attach to the subsequent tori and reduces continuity of the entire tori stack. The greater independence between adjacent tori therefore allows the final torus to deflect more and is the reason for the discontinuous behavior of the $R_{TS} = 0.80$ m curve in Fig. 118. The other two configurations, the 3-torus and 7-torus designs, do show evidence of small rotations of the torus stack. However, despite its larger surface rotation, the overall compression of the structural tori in the 7-torus decelerator result in a larger total axial deflection.

The number of tori parameter sweep provides further insight into the deflection of the hybrid decelerator configuration and the impacts of the torus stack rotational effects first observed in the $R_{TS}$ parameter sweep. The non-linear relationship between deflection and number of tori shows the competing relationship between the multi-torus stack rotation and the uniform tori compression. Both phenomena are seen to vary across the design space and have varying sensitivity to both the number of tori and tension skirt radius parameters depending on the values of the other design variables. As a result, the minimum deflection configuration varies throughout the design space and cannot be easily optimized across any single variable. The number of tori parameter sweep also highlights the differences between the 1 and 2-torus, tension cone-like configurations and the standard hybrid configurations with a radial strap constraining the multi-torus stack. The small N configurations are observed to

introduce discontinuities in the deflection trends and disrupt the tori stack rotation phenomenon observed in the other hybrid designs.

## *4.5 Hybrid Decelerator Design Space Exploration Study*

The hybrid model performance is evaluated by simulating several candidate configurations across multiple mission classes. Like both the stacked tori and tension cone case studies, a design space study is developed by performing parameter sweeps across the design variables to understand their impact on the decelerator structural and mass performance. Comparisons are made between the hybrid decelerator and the two baseline configurations to understand the applicability of each design across a range of decelerator scales and Pareto-optimal solutions are found for each. These data points are also used to generate response surface equations that analytically approximate the design space results.

### 4.5.1 Hybrid Decelerator Design Space Setup

The hybrid decelerator design space study is established to understand the hybrid decelerator structural and mass performance in the context of the stacked tori and tension cone performance across a wide range of mission classes, ranging from large robotic missions (1 -2 MT) up to human class missions (10 - 40 MT). In this way, each configuration can be evaluated across the different scales to understand their relative benefits and deficits. Due to the wide range of mission classes and the large number of design variables, adding variation of both the number of tori and tension skirt radius parameters, the design space is split up into three independent sub-spaces: a human-class scale mission, a large-robotic scale mission, and an intermediate scale mission. The human class mission (10 - 40 MT) represents the upper bound of decelerator sizing and evaluates the IAD design best suited to land large payloads on Mars. The large-robotic mission (1 - 2 MT) corresponds to the lower bound of inflatale decelerator aplicability and evaluates the HIAD design best suited to land smaller,

MSL-class payloads on Mars. This mission class also represents the upper bound in performance of traditional rigid aeroshell, parachute solutions. The intermediate scale represents a mission in between the aforementioned mission classes and is intended to provide an additional data point to better evaluate moderately sized HIADs and to understand the trends in performance with respect to scale. This intermediate class would be applicable to ISS down-mass or launch vehicle asset recovery missions similar in size to the proposed Vulcan engine recovery mission [121, 120].

As discussed in the stacked tori and tension skirt design space studies in Sections 3.5 and 3.6, a number of design variables are fixed based on high-level mission requirements, such as the major diameter and cone angle being set based on mission deceleration and stability targets. Therefore, the hybrid decelerator design space study also fixes certain parameters to ensure relevant designs are considered for each mission class. These constant parameters reduce the number of simulated geometries and allow for a greater variation of the variables that can be optimized to improve the decelerator performance. It is important to note that small deviations between the fixed parameter values used in this study and those used in previous literature studies or experiments are not concerning because all values are approximated in order to enable relevant comparisons between the design parameters that are varied in the design space.

The human-class design space study parameters are shown in Table 14. The major diameter is fixed at 20.0 m based on the EDL:SA human-Mars study, which analyzed three different architectures involving 23 m HIAD decelerators [76]. Similarly, the centerbody diameter is set to 9.0 m based on the payload shroud diameter assumed for the EDL:SA study. The 70° half-cone angle is larger than the 60° vehicles considered in the EDL:SA investigation based on more recent studies indicating that a 70° half-cone angle does not induce undesirable stability characteristics. Lastly, the

aerodynamic pressure is informed by the human-Mars EDL:SA study, which calculated a peak dynamic pressure of 4,200 Pa for the 23 m lifting HIAD decelerators. This study increases the 4,200 Pa to 5,000 Pa to try and compensate for difference between the two architectures, including the fact that this thesis simulates ballistic, rather than lifting, HIAD vehicles, which experience higher dynamic pressures during atmospheric descent.

**Table 14: Design variable values used in the hybrid decelerator human-class (10 - 40 MT) design space study**

| Parameter | Variable | Units | Values |
|---|---|---|---|
| **Fixed Parameters** | | | |
| Major Diameter | $D$ | m | 20.0 |
| Centerbody Diameter | $D_{Cen}$ | m | 9.0 |
| Half-Cone Angle | $\theta$ | $^\circ$ | 70 |
| Aerodynamic Pressure | $P_{Aero}$ | Pa | 5000 |
| **Variable Parameters** | | | |
| Number of Tori | $N$ | N/A | 1 through 12 |
| Tension Skirt Radius | $R_{TS}$ | m | 4.5, 4.75, 5.00... 9.75 |
| Inflation Pressure | $P_{Inf}$ | kPa | 50, 70, 100, 150, 200 |
| **Constraints** | | | |
| $2 \geq D_{Tori} \geq .01 * D_{Maj}$ | | | |
| $N \geq 5$ if $R_{TS} = 0$ | | | |
| $N \leq 7$ if $R_{TS} > 0$ | | | |

The variable parameters of the hybrid design study are the number of tori, the tension skirt radius, and the inflation pressure. The number of tori can vary from 1 torus (or a tension cone decelerator) up to 12, with the caveat that purely hybrid designs (or design with $R_{TS} > 0$) are restricted to 7 and fewer tori. This restriction is due to the increased complexity and the small tori that arise from vehicles with a tension skirt and large number of tori. Vehicles with $N > 7$ are restricted to only stacked tori configurations, which are included in the design space study along with tension cone decelerators as a comparison to existing heritage designs. Like the stacked tori design space study, stacked tori geometries are also considered down to a lower bound of 5 structural tori. Independent of the number of tori domain

restriction, the tori diameters are additionally constrained to between 1% of the decelerator major diameter and 2 m to ensure that tori are not too small or too large such that they are not manufacturable. The tension skirt radius is sized to encompass the full range of possible locations between the centerbody and major diameters in increments of 0.25 m with the expectation that a number of design will be unfeasible due to insufficient tension skirt length or tori that exceed the torus diameter constraints. The inflation pressure values mirror the stacked tori and tension cone design space studies and are based on the inflation pressures considered for the NFAC wind tunnel testing of Section 2.4. Due to the large scale of the human-class HIADs and the associated loading, two additional inflation pressures of 150 and 200 kPa are also considered to understand the inflation pressure's impact on the decelerator stiffness. The higher inflation pressure values are based on experiments demonstrating that the tori can support inflation pressures up to 30 psi (300 kPa) without failure of the torus structural fabric [120].

The large robotic-class design space parameters are shown in Table 15. The major diameter value is based on a follow-on EDL:SA study that designed a next-generation architecture to land MSL-class (1 - 2 MT) payloads on Mars [77]. The centerbody diameter is similar in size to the MSL entry vehicle, which has a maximum diameter of 4.5 m, and is sized to be the same as a Delta IV (MSL launch vehicle) payload shroud to accommodate larger 2 MT vehicles. A 70° half-cone angle is used for the large robotic-class design space, like the human-class design space, due to the anticipated drag benefits, and is slightly larger than the exploration feed-forward architecture value, which increased from 60° to 65° compared to the original EDL:SA study. However, unlike the original EDL:SA study, the follow-on exploration feed-forward study did not publish simulated trajectory profiles and, therefore, the anticipated peak dynamic pressures are unknown. It is expected that the lower mass payloads will significantly reduce the trajectory's peak dynamic pressure due to their lower ballistic

coefficient. Therefore, a value of 1000 Pa is chosen for this study.

**Table 15: Design variable values used in the hybrid decelerator large robotic-class (1 - 2 MT) design space study**

| Parameter | Variable | Units | Values |
|---|---|---|---|
| **Fixed Parameters** | | | |
| Major Diameter | $D$ | m | 8.0 |
| Centerbody Diameter | $D_{Cen}$ | m | 4.7 |
| Half-Cone Angle | $\theta$ | ° | 70 |
| Aerodynamic Pressure | $P_{Aero}$ | Pa | 1000 |
| **Variable Parameters** | | | |
| Number of Tori | $N$ | N/A | 1 through 12 |
| Tension Skirt Radius | $R_{TS}$ | m | 2.35, 2.45, 2.55... 3.85 |
| Inflation Pressure | $P_{Inf}$ | kPa | 50, 70, 100 |
| **Constraints** | | | |
| $2 \geq D_{Tori} \geq .01 * D_{Maj}$ | | | |
| $N \geq 5$ if $R_{TS} = 0$ | | | |
| $N \leq 7$ if $R_{TS} > 0$ | | | |

Like the human-class mission, the large robotic design space simulates vehicles composed of 1-12 tori, including pure hybrid configurations with 7 or fewer tori (including 1-torus tension cone designs) and stacked tori configurations with 5 or greater tori. The tension skirt radius is sized to span the entire possible range between the centerbody and major diameters, with the expectation that some configurations will be invalid due to violating tension skirt or torus sizing constraints. The tension skirt radius is sampled at 0.10 m due to its smaller overall range and the desire to maintain approximately the same sampling density as the human-class mission space. The inflation pressures again mirror the HIAD wind tunnel testing values of 50, 70, and 100 kPa, but without the higher 150 and 200 kPa values because they are not as relevant to this smaller, lower-deflection mission space.

The intermediate design space parameters, shown in Table 16, are sized to be halfway in between the large robotic and human-class design spaces. Both the major and minor diameter values are the approximate medians of the larger and smaller mission classes and the aerodynamic pressure is also chosen as the midpoint. Given

that both the large robotic and human-class vehicles employ a 70° half-cone angle, this value is used directly for the intermediate design space. The number of tori and inflation pressure values are identical to the large robotic design space and the tension skirt radius values are scaled based on the intermediate design space major and centerbody diameters, with a sampling spacing of 0.25 m. While vehicle sizing trends are not necessarily linear, the midpoint values provide a convenient reference point and allow for a vehicle design distinct of both the larger and smaller mission classes. It is important to again note that, because the fixed values are used for all configurations in this mission class, minor discrepancies between the geometric or loading relations are not expected to significantly influence the comparison results.

**Table 16: Design variable values used in the hybrid decelerator intermediate-class design space study**

| Parameter | Variable | Units | Values |
|---|---|---|---|
| **Fixed Parameters** | | | |
| Major Diameter | $D$ | m | 14.0 |
| Centerbody Diameter | $D_{Cen}$ | m | 7.0 |
| Half-Cone Angle | $\theta$ | ° | 70 |
| Aerodynamic Pressure | $P_{Aero}$ | Pa | 3000 |
| **Variable Parameters** | | | |
| Number of Tori | $N$ | N/A | 1 through 12 |
| Tension Skirt Radius | $R_{TS}$ | m | 3.50, 3.75, 4.00... 6.75 |
| Inflation Pressure | $P_{Inf}$ | kPa | 50, 70, 100 |
| **Constraints** | | | |
| $2 \geq D_{Tori} \geq .01 * D_{Maj}$ | | | |
| $N \geq 5$ if $R_{TS} = 0$ | | | |
| $N \leq 7$ if $R_{TS} > 0$ | | | |

### 4.5.2 Hybrid Decelerator Design Space Exploration Results

The results of the hybrid decelerator design space study are shown in Fig. 121 for all three mission classes. As observed in the figure, the design space results are distributed in curved arcs that enforce a compromise between low mass and low deflection solutions. For the most part, the curved arcs and trends in the data appear to

be preserved across all mission classes, with the mass and deflection results roughly proportional to decelerator scale. Major grouping is clearly evident from the separation of data between different mission classes but substructures within the groups are more difficult to observe compared to the stacked tori and tension cone configurations due to the combining of many factors into a single mission class. The importance of IAD structural and mass optimization is also evident from these results, with certain configurations resulting in deflections up to 30° and others resulting in inflatable decelerator masses up to 1.4 MT.

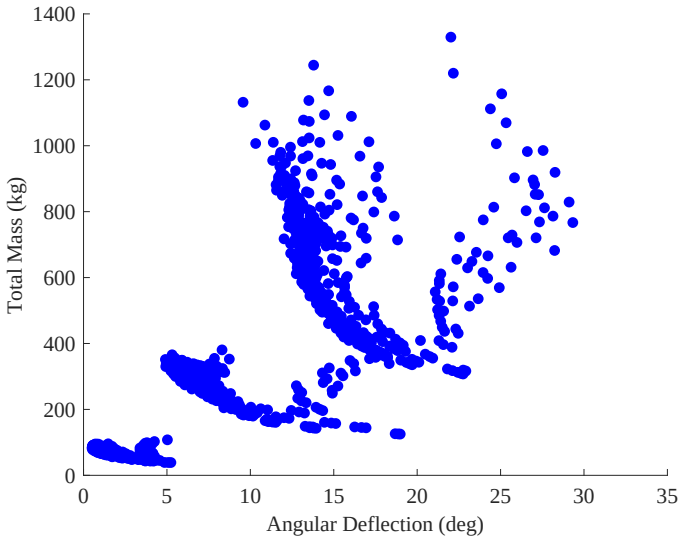


**Figure 121: Hybrid decelerator design space results for all three mission classes**

#### *4.5.2.1 Hybrid Design Space Study: Stacked Tori and Tension Skirt Comparison*

Figure 122 decomposes the design space into the three different mission classes, isolating the hybrid, stacked tori, and tension cone decelerator solutions. While there are a few exceptions, on average the stacked tori solutions tend to encompass the lower deflection, higher mass regions of the design space, whereas the tension cone solutions encompass the lower mass, higher deflection regions, with the hybrid solutions spanning between the two heritage designs. The figures confirm the original

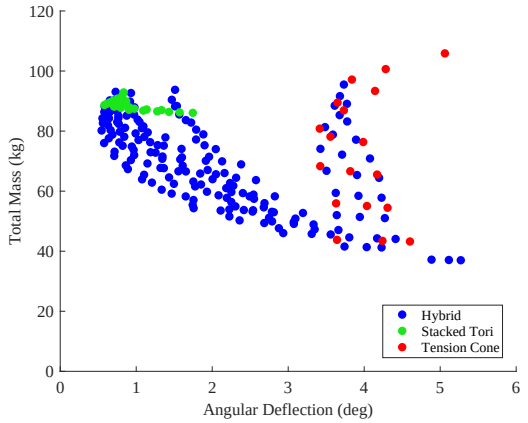


(a) Hybrid decelerator, stacked tori, and tension cone design space comparison for the large robotic mission class

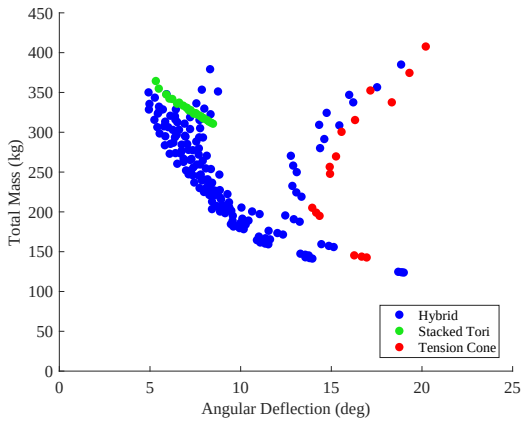


(b) Hybrid decelerator, stacked tori, and tension cone design space comparison for the intermediate mission class

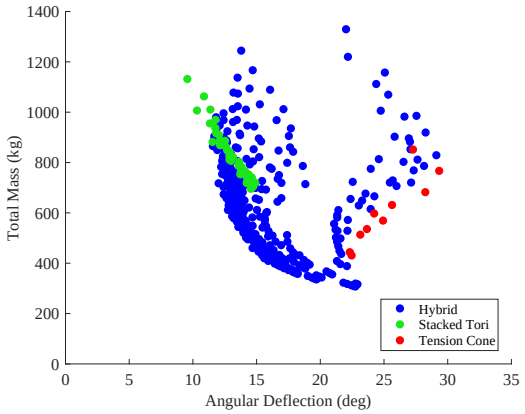


(c) Hybrid decelerator, stacked tori, and tension cone design space comparison for the human-scale mission class

**Figure 122: Mission class design space results isolating the stacked tori (green), tension cone (red), and hybrid decelerator (blue) configurations**

intent of the hybrid configuration development, that the hybrid decelerator enables a way to bridge between the two disparate design spaces and provide a wider range of intermediate mass and deflection solutions. It is also interesting to note that all three decelerator types exhibit different trends in the distribution of their mass and deflection results. The stacked tori results tend to lie on a straight line that enforces a compromise between low deflection and low mass designs whereas the tension cone results are generally oriented perpendicular to the stacked tori solutions and tend to

have an optimal design or set of designs. The hybrid decelerator results transition between the two solutions and lie along the curved arcs that define the overall results distribution. As a result, the hybrid configuration allows for solutions with more moderate total mass and deflection and allows for optimization of the design based on the objective function of each particular mission.

#### *4.5.2.2 Hybrid Design Space Study: Parameter Impact*

Figure 123 shows all hybrid design space results partitioned by mission class, isolating data points with a common major diameter, centerbody diameter, and aerodynamic pressure. As to be expected, different mission classes partition the design space into the primary grouping of data, with almost no overlap between adjacent groups. Varying the mission class, here equivalent to varying the major and centerbody diameters and the aerodynamic pressure, produces significant variation in both the mass and deflection performance, with an increase in mission-scale resulting in large increases in the range of both total mass and deflection.

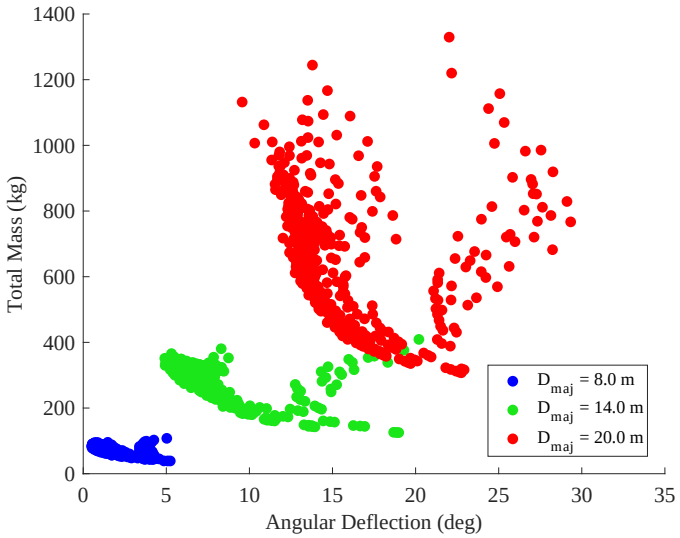


**Figure 123: Hybrid decelerator design space results grouped based on mission class**

Figure 124 sorts the hybrid design space by number of tori. This partitioning

clearly shows the number of tori parameter to further refine the large curved sections into finer lines. The distribution of the different colors shows that the primary impact of increasing number of tori is a general increase in deflection. Except for the $N = 1$ and $N = 2$ configurations however, there is significant overlap between adjacent groups. The configurational differences between the 1 and 2-torus designs discussed in the parameter sensitivity studies of Section 4.4.3 are also evident in Fig. 124. The large gap between the $N \leq 2$ and $N \geq 3$ data sets, resulting from the significantly greater deflection of the 1 and 2-torus configurations, demonstrates that the differences in the radial strap attachment have a significant impact on the decelerator performance.

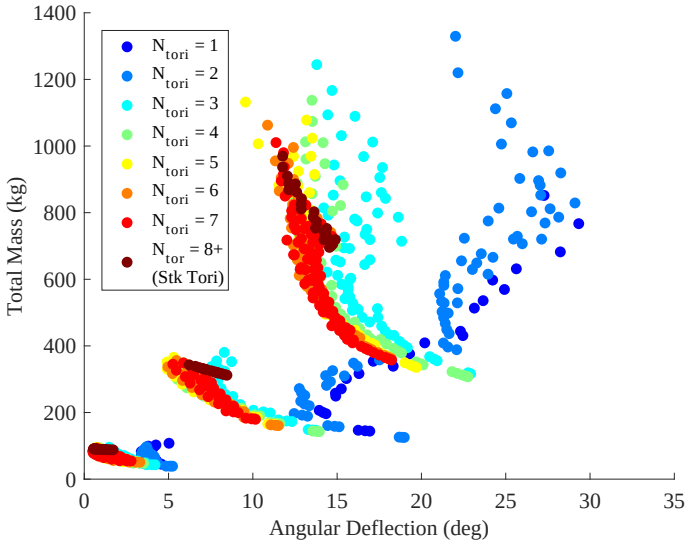


**Figure 124: Hybrid decelerator design space results grouped based on number of tori**

Figure 125 shows the hybrid configuration design space sorted by tension skirt radius. The distribution of colors, showing a gradual transition across the results for each mission space, demonstrates that the tension skirt radius significantly drives variability of the results, with the primary variation with respect to total mass. However, the tension skirt radius also impacts the decelerator deflection due to the curvature of the design space results. It is important to note that the reason the tension skirt

radius partitioning is more gradual and does not highlight distinct groups in the data is because of the high sampling density of the tension skirt radius parameter. In addition, because the range of tension skirt radius is defined based on the major and centerbody diameters of a given configuration, comparisons across mission classes should not be made with respect to identical values of $R_{TS}$ but rather between small and large $R_{TS}$ values relative to that mission class.

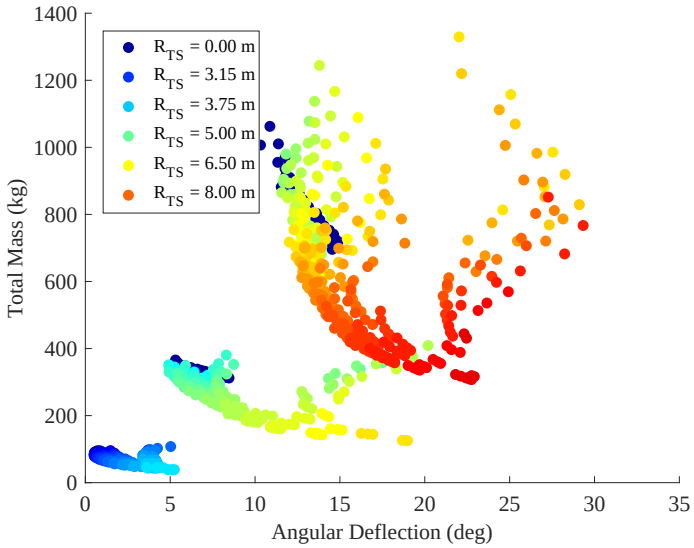


**Figure 125: Hybrid decelerator design space results grouped based on tension skirt radius**

Figure 126 segments the design space based on the final variable parameter, the inflation pressure. As seen in the graph, data points sorted by inflation pressure exhibit a larger scattering of the results, with like-valued designs being found on opposite sides of the design space. Nevertheless, patterns still emerge in the data based on the different colors. Like the number of tori, the inflation pressure is seen to resolve even finer curved sub-structures in the data groups, with changes in inflation pressure impacting both total mass and deflection.

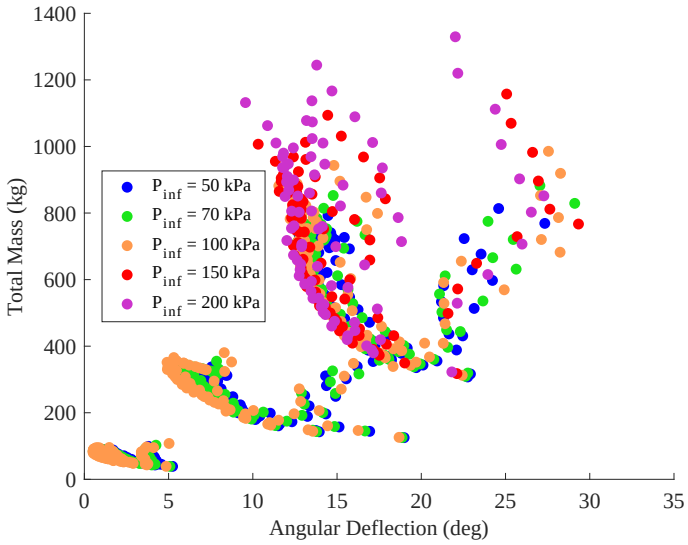


**Figure 126: Hybrid decelerator design space results grouped based on inflation pressure**

#### *4.5.2.3 Hybrid Design Space Study: Dominating Parameters*

While sorting the design space based on each parameter is useful to understand the impact of dominating parameters and the global trends, the sensitivity to the lower-order variables can often be masked in the process. Therefore, as was performed with the stacked tori and tension cone design space exploration studies, the hybrid design

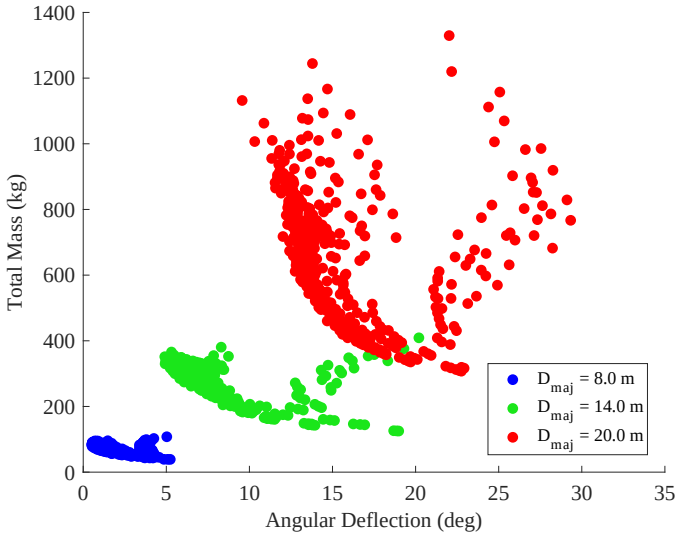


**Figure 127: Hybrid decelerator design space results grouped based on mission class (duplicate of Fig. 123)**

space is iteratively focused by isolating individual values of higher-order parameters to evaluate the sensitivity to each design variable. Figure 123 (duplicated here in Fig. 127 for convenience) shows the entire design space parameterized based on mission class, the overall dominating parameter. Variations in mission class contribute to a wide variability of the mass and deflection results. Despite the mission class variables being fixed based on the overall vehicle architecture and, therefore, not controllable by the mission designer, they can be used to define the possible range of mass and deflection performance for any inflatable decelerator solution.

Figure 128 isolates the human-scale mission class results from Fig. 127, sorting them by the number of tori. The number of tori grouping isolates the only definable substructure in the data, the separation between designs with 2 tori and 3 tori. This gap, and the corresponding reduction in deflection with the increase in number of tori, arises from the difference in boundary conditions between the two cases. In the $N = 3$ case, the radial strap attaches to $T_1$ and continues on to terminate at $T_2 = T_{N-1}$. For the $N = 2$ case, the radial strap attaches to and terminates at $T_1 = T_{N-1}$. Therefore,

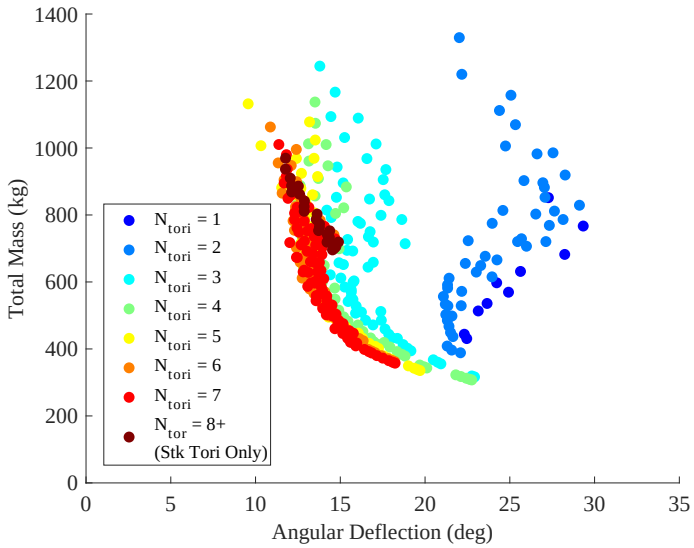


**Figure 128: Hybrid decelerator design space results isolating the human-scale mission class, grouped based on number of tori**

configurations with 3 or more tori benefit from increased continuity of the multi-torus stack and the rotational phenomena seen in pure hybrid configurations. These benefits are observed for isolated parameter sweeps in Section 4.4.3 and are confirmed here to be applicable to all sets of design parameters. In fact, this design space study shows that the method of the radial strap attachment is so important that it is the single most dominating driver of the deflection performance other than mission class. Aside from the large separation between the $N = 2$ and $N = 3$ data sets, adjacent groups of number of tori are otherwise seen to be overlapping.

The $N_{Tori}$ parameter is not automatically set based on the mission class and is, therefore, optimizable. Figure 128 shows that an increase in the value of $N_{Tori}$ corresponded to a slight reduction in the range of total mass, with a shrinking of both the high and low extremes of the range, along with a substantial reduction in deflection. The reduced deflection, however, is more prominent for smaller number of tori configurations and becomes indistinguishable for higher number of tori decelerators, as the adjacent groups begin to significantly overlap. The dark brown 8+ tori configurations represent stacked tori only solutions and are grouped in a line because they

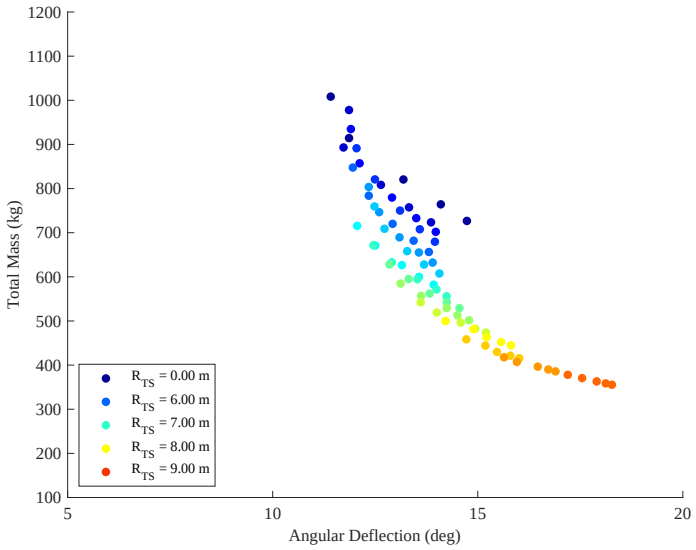


**Figure 129: Hybrid decelerator design space results isolating human-scale decelerators with 7 tori, grouped based on tension skirt radius**

do not allow for any variation of the tension skirt radius. As a result, the stacked tori solutions are all located near the smallest tension skirt radius solutions of the hybrid configurations, which best approximate their deflection and mass behavior.

Figure 129 isolates configurations with 7 tori from Fig. 128 and sorts the results based on values of the tension skirt radius. As observed in Fig. 125, the tension skirt radius scales the results along the grouping defined by a single value of $N_{Tori}$ and can contribute to significant variability in total mass and deflection. Like the number of tori, the tension skirt radius is not fixed based on mission requirements and is, therefore, optimizable. Increases in $R_{TS}$ are seen to decrease total mass and increase angular deflection, with a larger impact to total mass for small values of $R_{TS}$ and a larger impact to deflection for large values of $R_{TS}$. Note that $R_{TS} = 0$ is the special case of the stacked tori decelerator, shown in dark blue, and corresponds, on average, to the set of solutions with the highest mass and lowest deflection.

Figure 130 further isolates configurations with a tension skirt radius of 7.25 m from Fig. 129, sorting the remaining data points based on the value of inflation

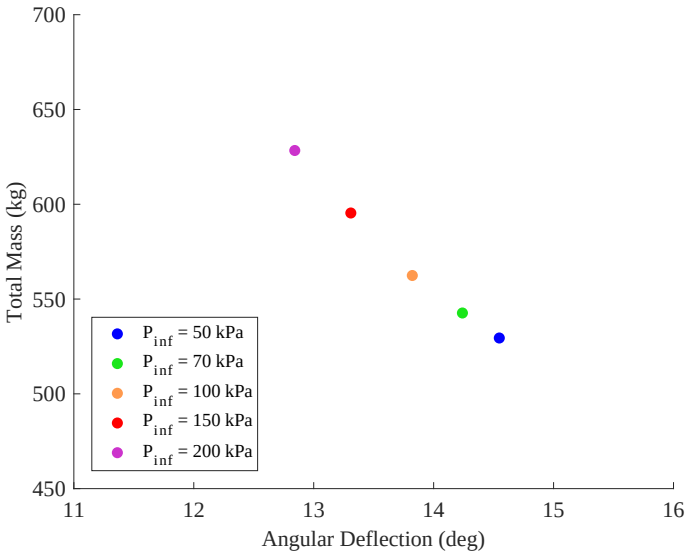


**Figure 130: Hybrid decelerator design space results isolating human-scale decelerators with 7 tori and a 7.25 m tension skirt radius, grouped based on inflation pressure**

pressure. The inflation pressure, like the tension skirt radius, is observed to scale the results along the define group but acts on a smaller range compare to the tension skirt radius. The inflation pressure is seen to impact both the decelerator mass and deflection, with increases in inflation pressure corresponding to an increase in mass and a decrease in deflection, both of which are to be expected.

#### *4.5.2.4 Hybrid Design Space Study: Pareto Frontier*

Optimal IAD configurations, as defined in this study, are ones that minimize both total mass and angular deflection. Given the two competing objectives, it is impossible to define a single, optimal solution that simultaneously minimizes both mass and deflection because you can always improve one objective by worsening the other. Instead, a set of solutions can be extracted, known as Pareto optimal solutions, which define an optimal boundary of the design space, where any one Pareto optimal solution cannot be improved upon in both mass and deflection by any other single solution. The set of Pareto optimal solutions defines all possible multi-objective optimal solutions, from which the best solution can be selected based on the specific weighting of the two performance metrics defined by the given mission.

For this study, the Pareto frontier, or the set of Pareto optimal solutions, lies along the bottom left boundary of the design space, closest to the point of zero mass and zero deflection. Pareto optimal solutions for each mission class are visualized by isolating the Pareto frontier and highlighting those solutions based on their configuration type (stacked tori, tension cone, or hybrid). In this way, the performance and applicability of each decelerator type to the different mission classes can be determined, abstracting away lower-level detailed design considerations.

The Pareto frontier of the large robotic-class mission is shown in Fig. 131, with Pareto optimal solutions identified by yellow markers organized based on IAD type.

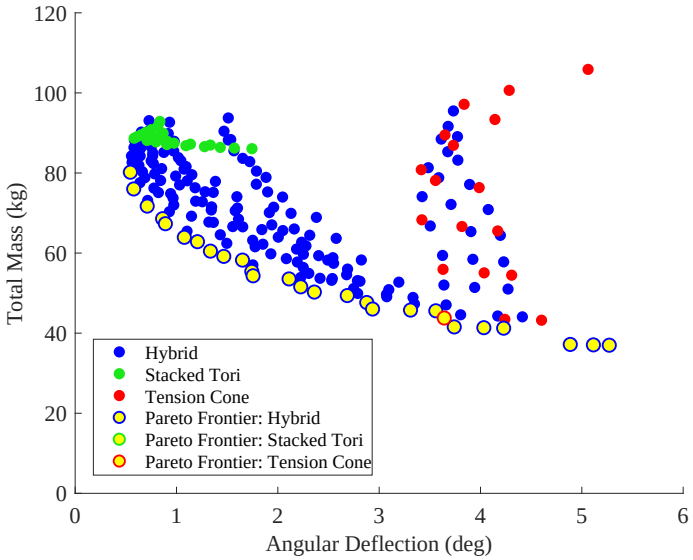


**Figure 131: Pareto frontier of the large robotic-class design space highlighted by yellow markers, identifying contributions from stacked tori (green boundary), tension cone (red), and hybrid (blue) decelerators**

As observed in the figure, the Pareto frontier does not contain any stacked tori configurations, with all solutions having a hybrid configuration that can improve upon both their mass and deflection performance. This indicates that there is no structural or mass-related reason to use a stacked tori decelerator for a large robotic-class mission, a conclusion that makes sense given the fact that stacked tori decelerators are tailored to higher loading, higher mass missions. Conversely, a single tension cone decelerator design is found on the Pareto frontier, located toward the low mass, high deflection region of the design space. This demonstrates that the tension cone design has some applicability to this mission-space, although hybrid solutions exist that can drastically improve the tension cone deflection performance with minimal increase in mass. The remaining Pareto optimal solutions, composing 26 of the 27 configurations on the Pareto frontier, are hybrid decelerator configurations. This is in part due to the hybrid decelerator's ability to bridge between the stacked tori and tension cone design spaces but also due to its favorable performance in regions near both the tension cone and stacked tori decelerator solutions. As a result, the hybrid decelerator

IAD design shows significant promise for applicability to large robotic-class missions.

The Pareto frontier for the intermediate-class mission is shown in Fig. 132. As seen in the picture, all solutions on the Pareto frontier correspond to hybrid designs. This demonstrates that, as the scale of the vehicle increases, the multiple structural tori of the hybrid configuration are better able to resist deflection with negligible increase in total mass such that the hybrid design performs uniformly better than the tension cone decelerator. At this scale, the hybrid decelerator design is also able to reduce surface deflections of the outer tori over that of the stacked tori with the same or reduced mass. Although, the stacked tori solutions are seen be to closer to the Pareto frontier for intermediate-class missions than for large robotic-class missions. Therefore, these results show that hybrid decelerators have significant applicability to intermediate-class missions and show promise over both stacked tori and tension cone decelerators.

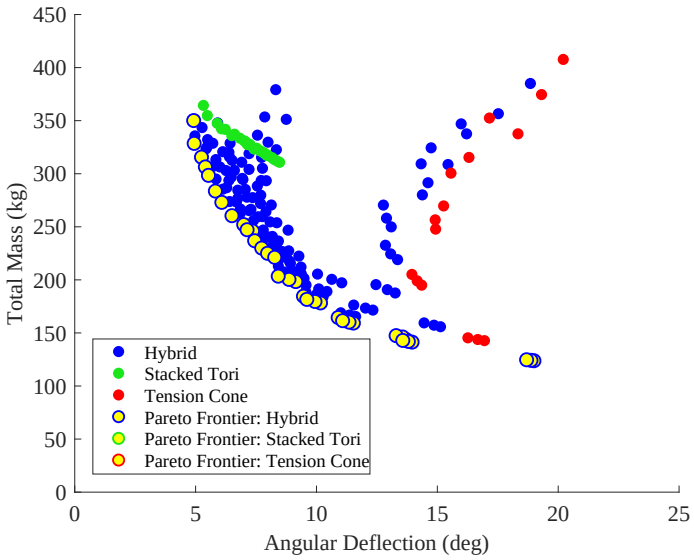


**Figure 132: Pareto frontier of the intermediate-class design space highlighted by yellow markers, identifying contributions from stacked tori (green boundary), tension cone (red), and hybrid (blue) decelerators**

The Pareto frontier results for the human-class mission are shown in Fig. 133. It can be seen from the figure that, as the decelerator size increases, the tension

cone solutions move further away from the Pareto frontier, which demonstrates why they are not considered for large-scale, high loading applications. However, 4 stacked tori configurations do appear on the Pareto frontier, these stacked tori designs all being characterized by their small deflection and large mass. Thus, the stacked tori decelerator is seen to become a viable decelerator option at this large scale due to the higher proportion of structural members, representing the Pareto optimal designs with the smallest deflections. Nevertheless, the stacked tori design also represent the highest mass configurations along the Pareto frontier. Even at this large of a scale, hybrid decelerator designs still compose nearly all of the Pareto frontier and compose all moderate solutions that balance low deflection and low mass. Therefore, Fig. 133 again shows that hybrid solutions are applicable to large human-class missions and, as a result, are applicable across the entire range of mission classes.

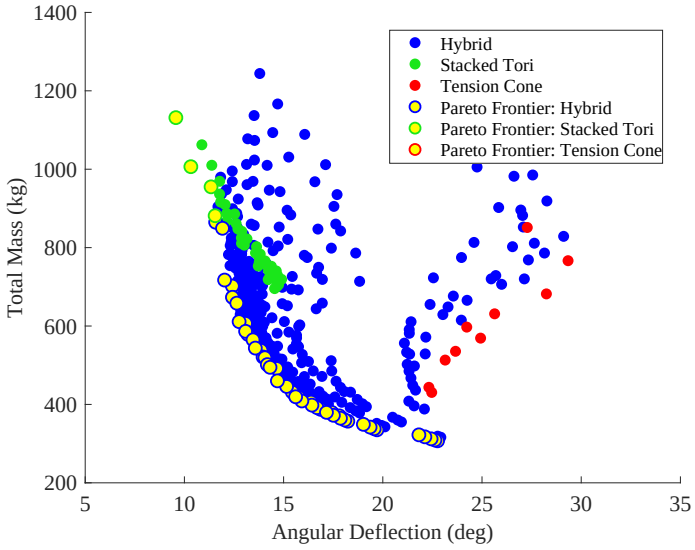


**Figure 133: Pareto frontier of the human-scale design space highlighted by yellow markers, identifying contributions from stacked tori (green boundary), tension cone (red), and hybrid (blue) decelerators**

#### *4.5.2.5 Hybrid Design Space Study: Optimal Solutions*

By defining an objective weighting function of the multiple response metrics, it is possible to refine the set of Pareto optimal results to a single optimum solution. This

objective weighting function rates the importance of each response, with the optimal solution minimizing the sum of all response metrics, scaled by their weight factor (in the case of a min/min problem such as the one considered here).

The objective function developed for this study is shown in Eq. 52. In the equation, $m_{tot}$ refers to the configuration total mass metric and $\Delta\theta$ refers to its deflection. Both objective terms normalize each configuration's mass and deflection values (subscript $i$) based on the minimum value of each metric obtained from any configuration (subscript $min$). This normalization of each metric accounts for the differing scales of the mass (on the order of 100 - 1000 kg) and deflection (on the order of 1 - 15 degrees) and ensures that the metric with the larger magnitude does not dominate the objective weighting process. Normalization can be performed with respect to the minimum value, maximum value, or a median value. The minimum value (or best value) is chosen in this study to express each design's performance relative to the ideal solution and is also chosen because the minimum value is observed to be less prone to errors from outlying points.

$$Obj = \frac{m_{tot,i}}{m_{tot,min}} + 1.5\frac{\Delta\theta_i}{\Delta\theta_{min}} \tag{52}$$

The additional factor of 1.5 in Eq. 52 is added to the deflection term to increase its weight and slightly preference optimal configurations towards low-deflection solutions as this is expected to be a larger impact on the overall decelerator performance. In addition, the objective functions across each mission class are normalized to 1 based on the highest (worst) objective value to simplify graphing and interpretation of the results (overall normalization to 1 is not captured in Eq. 52).

The design space results for the large robotic mission class, sorted by objective function value, are show in Fig. 134. The objective function values for this mission class are particularly influenced by deflection due to the shape of the design space, with a 10-to-1 ratio between the maximum and minimum deflection values compared

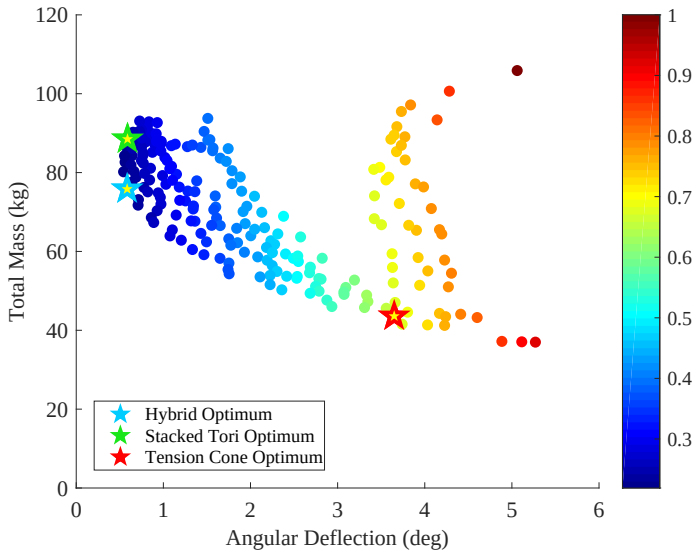


**Figure 134: Large robotic design space sorted by value of objective function, identifying the optimal solutions of the stacked tori (green star), tension cone (red), and hybrid (blue) decelerators**

to a 3-to-1 ratio between the maximum and minimum mass values. As a result, the iso-objective curves, or sets of point with the same objective function values, are more aligned with the deflection axis and drive optimal configurations to lower deflection solutions.

Optimal solutions for each configuration are indicated in the graph by a colored star. The optimal stacked tori configuration, indicated by the green star, is the smallest deflection solution among all stacked tori configurations, due to them all having similar mass. The optimal tension cone configuration, the red star, is the solution lying on the Pareto frontier. While this configuration is not a strict optimum in mass or deflection among tension cone designs, because of its balancing of the two objectives it would likely be the optimum tension cone design regardless of objective function. The hybrid solution, or blue star, also lies along the Pareto frontier and is the Pareto optimal solution with the second lowest deflection value. The optimal hybrid solution is universally better than the stacked tori solution, having a slightly smaller deflection and moderately smaller total mass. Despite the optimal hybrid

solution having approximately twice the mass of the optimal tension cone solution, it is also able to drastically reduce the surface deflection by a factor of 6.

The objective function value results for the intermediate design space are shown in Fig. 135. The design space results are well distributed across both objectives for this mission class due to them both having a 4-to-1 ratio of the maximum to minimum objective values. Therefore, the iso-objective function curves are oriented nearly diagonally across the space, with the slight difference being due to the 1.5 weight applied to the deflection objective.

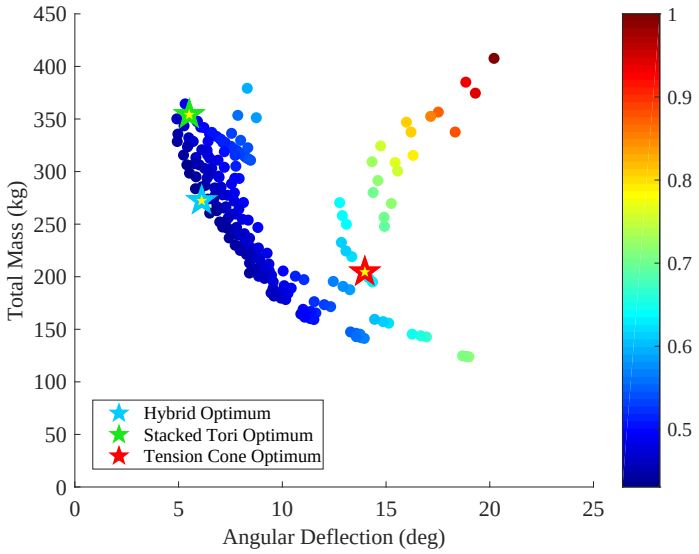


**Figure 135: Intermediate design space sorted by value of objective function, identifying the optimal solutions of the stacked tori (green star), tension cone (red), and hybrid (blue) decelerators**

The optimum stacked tori configuration in Fig. 135 is the solution with the second lowest deflection and second highest mass among stacked tori designs and is the closest solution to the intermediate mission-class Pareto frontier. The tension cone optimum, similarly, is the solution with the smallest deflection. The hybrid optimal solution lies on the Pareto frontier but is located more toward the center of the design space, balancing both objectives. The hybrid optimum is not universally better than the stacked tori optimum but trades a 10% increase in deflection for a

30% reduction in total mass. Compared to the tension skirt optimum, the optimum hybrid solution achieves a factor of two reduction in deflection at the cost of a 30% increase in total mass. In addition, as observed in Fig. 132, because the intermediate mission-class Pareto frontier is composed entirely of hybrid decelerator solutions, any optimal stacked tori and tension cone solution can be individually improved upon by hybrid configuration solutions.

The design space results sorted by objective function are shown in Fig. 136 for the human-class mission. The results for this mission class are more spread out across total mass, with a 4.5-to-1 ratio of the maximum and minimum total mass values compared to a 3-to-1 ratio for deflection. As a result, due to the 1.5 times scaling on the deflection contribution to the objective function, iso-contours of objective function values line up almost exactly orthogonal to the design space result contours.

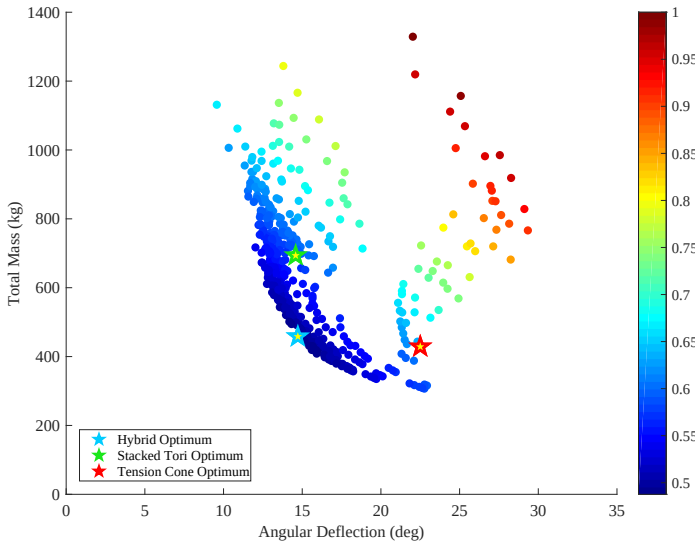


**Figure 136: Human-class design space sorted by value of objective function, identifying the optimal solutions of the stacked tori (green star), tension cone (red), and hybrid (blue) decelerators**

Despite contributing 4 solutions to the Pareto frontier (characterized by high mass, low deflection), the optimal stacked tori configuration is the solution farthest away from these points, with the lowest mass and nearly highest deflection. This is because the stacked tori solutions are distributed over a wide range of mass values

compared to a relatively small range of deflections, allowing for a greater reduction of total mass. The tension cone optimum is the solution with the smallest mass and second smallest deflection, with the distribution of tension cone designs producing a choice between two similarly located solutions. The optimum hybrid configuration is located in the middle of the Pareto frontier and balances both deflection and mass. The hybrid optimum is observed to provide significant benefit over both the stacked tori and tension cone optima, with a 1.5 time reduction in mass compared to the stacked tori and a 1.5 time reduction in deflection compared to the tension cone, with similar values for the other objective of each. Nevertheless, even with significant benefits over the stacked tori and tension cone decelerators, the hybrid decelerator surface still deflects by 15°, which is much too large for an aerodynamic decelerator and would likely require further investigation.

Overall, it is again observed that optimal stacked tori configurations lie in the high mass, low deflection regions of the design space whereas optimal tension cone configurations can approach the low mass, high deflection regions. Hybrid configurations are better able to balance both deflection and mass, providing more intermediate solutions between the stacked tori and tension cone designs. The hybrid optimum is shown to be favorable over the stacked tori and tension cone optima for all three mission classes and is also observed to be just as relevant, if not more relevant, at large scales, strictly improving upon both the stacked tori and tension cone optima for the human-scale mission class.

#### *4.5.2.6 Hybrid Design Space Study: Optimal Configurations*

Figures 134 through 136 are useful for highlighting the optimal solutions with respect to each other and the full design space. However, these graphs do so by abstracting away the supporting details of each configuration. Table 17, therefore, provides the design parameters of the optimal solutions for each decelerator design and mission

**Table 17: Summary of optimal stacked tori, tension cone, and hybrid configuration design parameters**

| Type | $N_{Tori}$ | $R_{TS}$ (m) | $P_{Inf}$ (kPa) |
|---|---|---|---|
| **Large Robotic-Class** | | | |
| Stacked Tori | 11 | N/A | 100 |
| Tension Cone | N/A | 3.9 | 100 |
| Hybrid | 7 | 3.0 | 100 |
| **Intermediate-Class** | | | |
| Stacked Tori | 6 | N/A | 100 |
| Tension Cone | N/A | 6.5 | 100 |
| Hybrid | 4 | 5.3 | 100 |
| **Human-Class** | | | |
| Stacked Tori | 12 | N/A | 50 |
| Tension Cone | N/A | 9.3 | 50 |
| Hybrid | 7 | 8.3 | 200 |

class. Interestingly, optimal parameter sets are not observed to be monotonic with respect to decelerator scale. The number of tori parameter, for example, is seen to decrease between the large robotic and intermediate mission classes but subsequently increases for the human-class mission, with both the stacked tori and hybrid decelerators follow the same non-linear trend. The tension skirt radius is seen to increase with decelerator scale, but this is to be expected due to the range of $R_{TS}$ values being based on the decelerator major diameter. As a fraction of the major diameter, tension cone tension skirt radii are observed to decrease whereas hybrid tension skirt radii instead increase. This opposite trend is also seen with the inflation pressure parameter. The stacked tori and tension cone designs both optimize to the maximum pressure for the large robotic and intermediate-class missions before changing to the minimum pressure for the human-class mission. Optimum hybrid decelerators, conversely, optimize to the highest possible inflation pressure for all mission classes, even after its increase to 200 kPa for the human-class mission. These results elucidate the interdependent, non-linear factors that influence the decelerator structural and mass performance and, as a result, the difficulty of optimizing inflatable decelerator

configurations especially during the early, conceptual phases of design.

Table 18 and Fig. 137 relate the mass and deflection results of each optimum solution for the three mission classes, breaking down the mass term into its gas and fabric mass components. The table and figure further highlight the overall trends observed in the objective function graphs, that the hybrid configuration is generally able to achieve the low deflection of the stacked tori configuration with mass values approaching those of the tension cone configuration. However, it is interesting to note that, while the magnitude of the dispersion between the three optima increases as decelerator scale increases, the relative differences (on a % basis) actually decrease. This shows that, despite their differences, all three configurations are still constrained by having toroidal, inflation pressure-stiffened structural members used to support a compressive aerodynamic load.

**Table 18: Summary of optimal stacked tori, tension cone, and hybrid results**

| Type | $\Delta\theta$ (deg) | $M_{Tot}$ (kg) | $M_{Fab}$ (kg) | $M_{Gas}$ (kg) |
|---|---|---|---|---|
| **Large Robotic-Class** | | | | |
| Stacked Tori | 0.6 | 89 | 84 | 5 |
| Tension Cone | 3.6 | 44 | 43 | 1 |
| Hybrid | 0.6 | 76 | 72 | 4 |
| **Intermediate-Class** | | | | |
| Stacked Tori | 5.5 | 354 | 291 | 63 |
| Tension Cone | 14.0 | 204 | 184 | 20 |
| Hybrid | 6.1 | 272 | 238 | 34 |
| **Human-Class** | | | | |
| Stacked Tori | 14.6 | 694 | 636 | 58 |
| Tension Cone | 22.5 | 429 | 396 | 32 |
| Hybrid | 14.7 | 458 | 401 | 57 |

Figure 137 also shows that the total mass is dominated by the fabric mass, with the intermediate-class stacked tori decelerator having the largest gas mass composition at 18%. Based on this observation and the results from Table 17, it appears that increasing the gas pressure could be beneficial in certain configurations to reduce

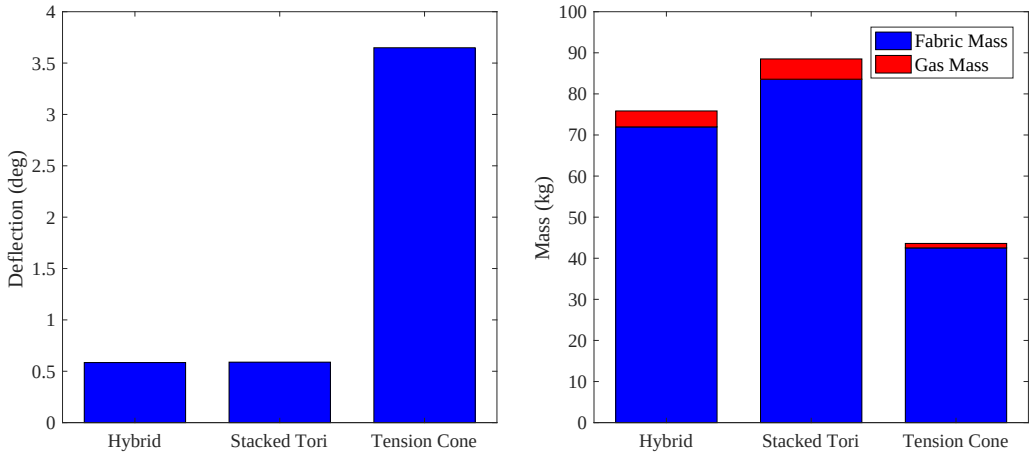


(a) Comparison between optimal hybrid, stacked tori, and tension cone configuration mass and deflection values for the large robotic-class mission

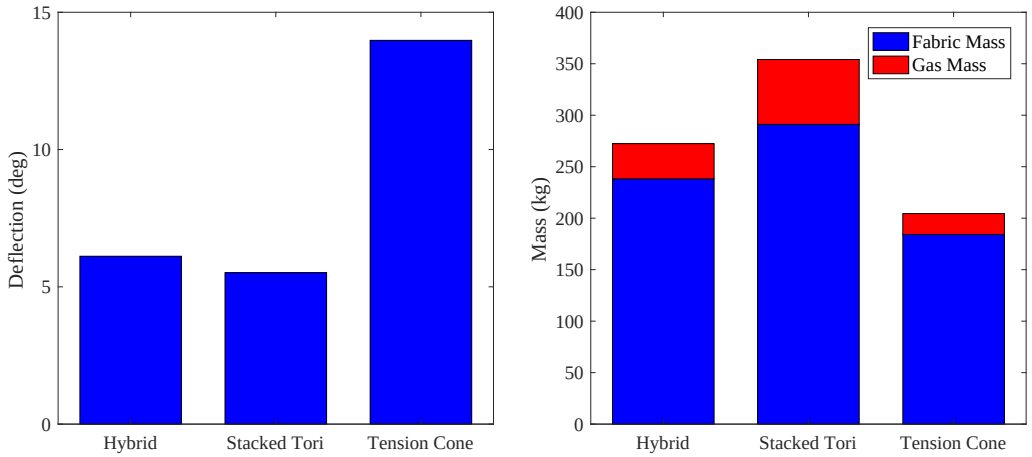


(b) Comparison between optimal hybrid, stacked tori, and tension cone configuration mass and deflection values for the intermediate-class mission

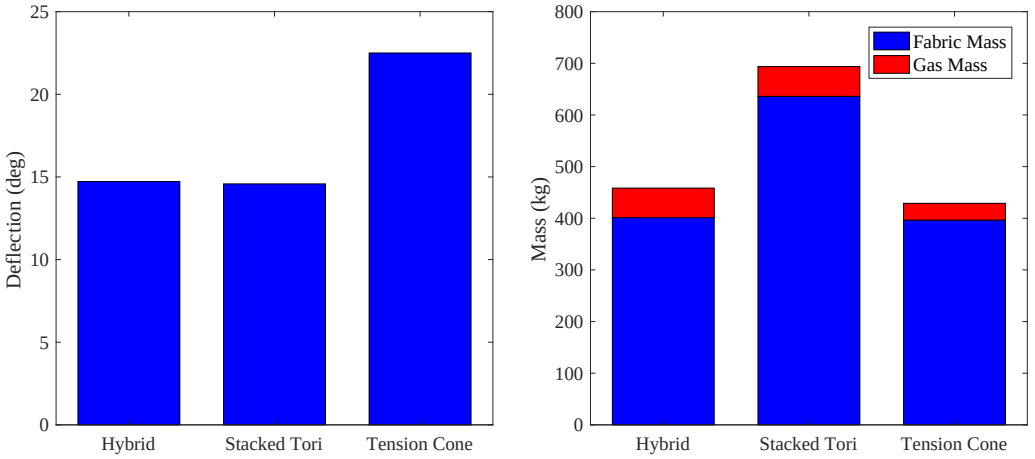


(c) Comparison between optimal hybrid, stacked tori, and tension cone configuration mass and deflection values for the human-class mission

**Figure 137: Comparison between optimal hybrid, stacked tori, and tension cone configuration mass and deflection values**

deflection with minimal relative increase in mass, subject to limits based on the torus fabric strength. This also proves that the simple, aggregate fabric density value determined from the static load test article is likely not sufficient and needs refinement given its significant impact on the decelerator mass results.

#### *4.5.2.7 Hybrid Design Space Study: Optimal Solution Deflected Shape*

The single deflection metric assessed in Figs. 134 through 136 also abstracts away the full deflected surface profile of each optimal configuration. Parameter studies performed in Section 4.4.1 highlight characteristic differences between the behaviors of the stacked tori and hybrid decelerators. Tension cone designs are also observed to behave differently in parameter sweeps conducted in Section 4.4.3. As a result, it is important to also verify the full deflected surface of the optimum designs to understand how their shape influences the performance of the aerodynamic decelerator.

The deformed surface plots of the optimum large robotic-class configurations are shown in Fig. 138, with both the inflated and aerodynamically-loaded states shown in Fig. 138(a) and the aerodynamically-loaded states isolated in Fig. 138(b). Figure 138(a) shows that, on average (ignoring the tension cone design), the optimal solutions do not significantly deflect under load. In addition, all configurations are observed to inflate to the same angle, slightly windward of the undeformed line. Therefore, any relative deflection measurement can be understood based on their aerodynamically-loaded deflections, seen in Fig. 138(b).

The most obvious feature of Fig. 138(b) is that the tension cone decelerator deflects significantly more, and exhibits a significantly higher surface curvature, than the stacked tori and hybrid designs. This figure also displays the rotation of the tension cone torus under load. Without the support of a multi-torus stack, the tension cone has less resistance to rotation and maintains tangency of the tension skirt by rotating about the structural torus' central axis, driving the outer shoulder torus

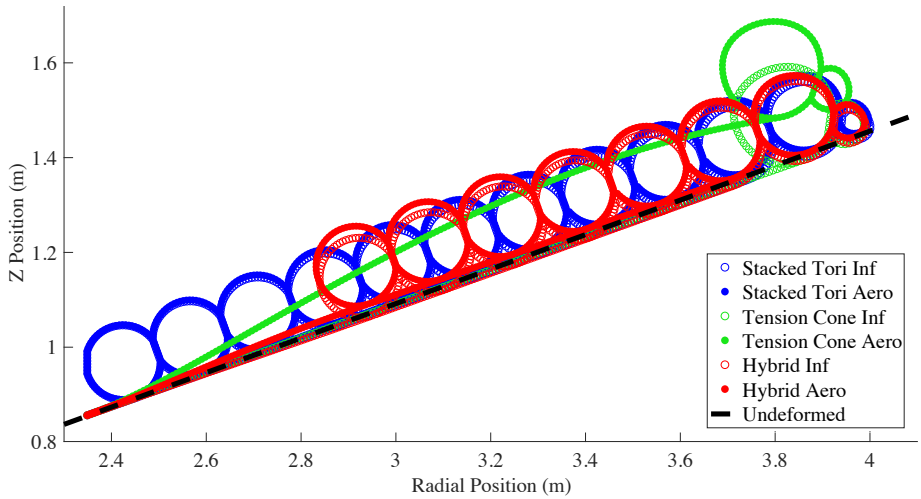


(a) Deflected surface comparison between the optimal large robotic-class stacked tori, tension cone, and hybrid configurations subject to inflation pressure and aerodynamic loading

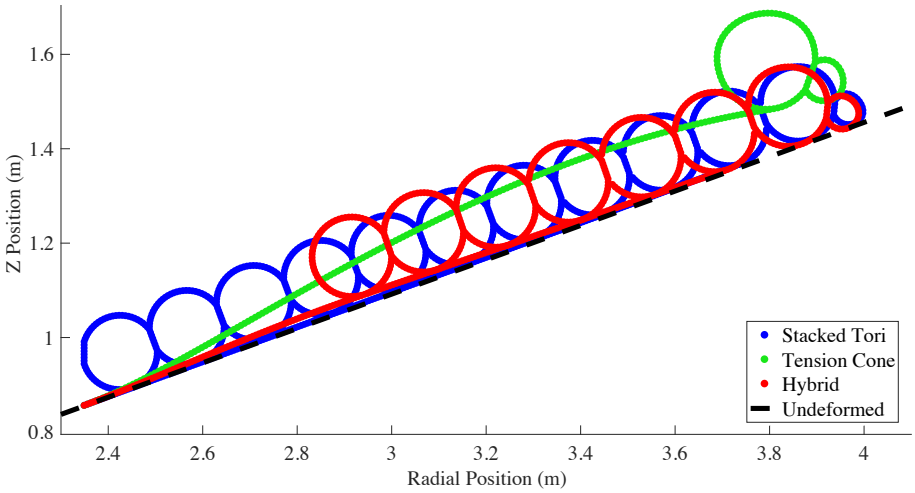


(b) Deflected surface comparison between the optimal large robotic-class stacked tori, tension cone, and hybrid configurations subject to aerodynamic loading

**Figure 138: Deflected surface comparison between optimal large robotic-class hybrid, stacked tori, and tension cone configurations**

towards the freestream flow. Conversely, the stacked tori and hybrid designs are seen to deflect substantially less. At the radial strap to $T_{N-1}$ interface, the cone angle of both designs is nearly identical. However, the hybrid design does deflect slightly more at the interface of the tension skirt to $T_1$ before deflecting back to the undeformed line towards the outer tori whereas the stacked tori surface is straight along its entire length. This results in a slight difference in the local cone angle of each decelerator despite their global deflections being the same. Nevertheless, differences between the two are small and not likely to cause drastic discrepancies in the decelerator drag.

The deformed surface plots of the optimum intermediate-class configurations are shown in Fig. 139, with both the inflated and aerodynamically-loaded states shown in Fig. 139(a) and the aerodynamically-loaded states isolated in Fig. 139(b). Figure 139(a) depicts some variation among the inflated surfaces of the three configurations but the deflections at the radial strap interface to $T_{N-1}$ are similar. Overall, however, the deflections under inflation are much larger (in the windward, or negative, direction) than for the large robotic-class mission. Due to the definition of the cone angle being the as-designed angle and not the as-inflated cone angle, an actual decelerator would enter the atmosphere with a half-cone angle slightly larger than the specified 70° due to this expansion under inflation. While this difference in initial cone angle does impact the resulting aerodynamic deflections, given that all three configurations in Fig. 139(a) are seen to expand approximately the same amount, there is negligible impact to their relative deflections. It is also important to note that overall deflection values are defined as the difference between the inflated and aerodynamic states. Therefore, deflections with respect to the as-designed 70° cone angle are the difference between the reported deflection angle and the initial cone angle change under inflation.

The aerodynamically loaded deformed surfaces of the optimal configurations are

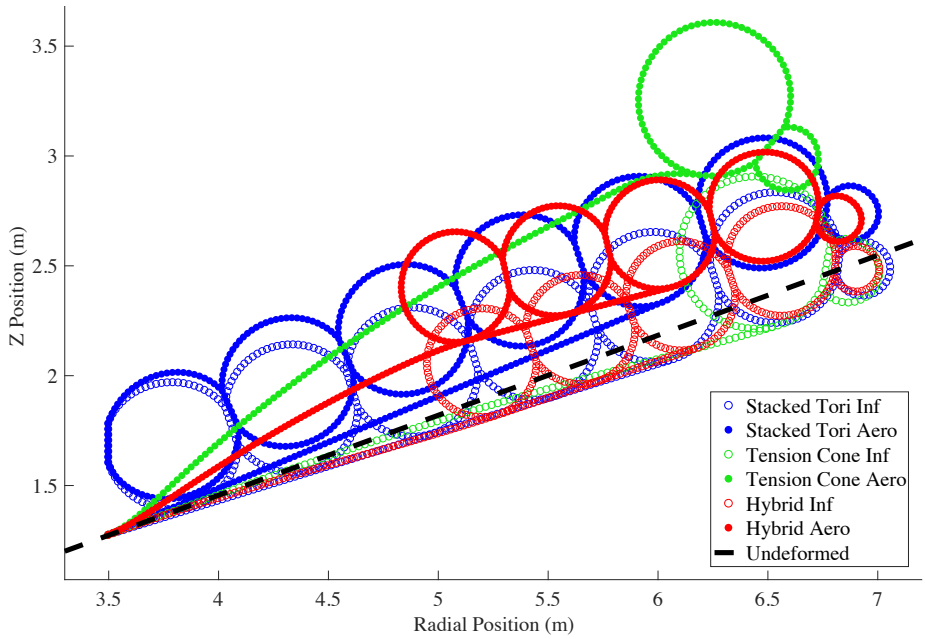


(a) Deflected surface comparison between the optimal intermediate-class stacked tori, tension cone, and hybrid configurations subject to inflation pressure and aerodynamic loading

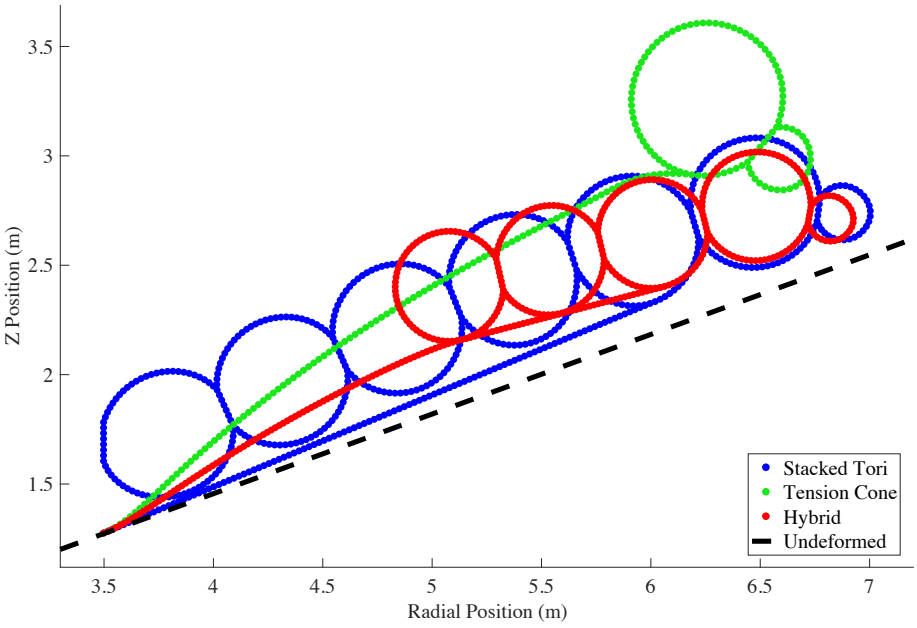


(b) Deflected surface comparison between the optimal intermediate-class stacked tori, tension cone, and hybrid configurations subject to aerodynamic loading

**Figure 139: Deflected surface comparison between optimal intermediate-class hybrid, stacked tori, and tension cone configurations**

isolated in Fig. 139(b). Like the optimal robotic-class mission decelerators, the tension cone design again has a much larger deformation than the stacked tori or hybrid decelerators. The tension cone configuration also exhibits a significant rotation about the structural torus axis, resulting in a large change in the local cone angle at the tension skirt to torus interface and even the shoulder torus being pushed windward of the structural torus. While the effects of the rotation are likely exaggerated compared to an actual implementation due to modeling effects, this example highlight the significant deformation of tension skirt designs at large scales.

The hybrid design is observed to deflect more than the stacked tori configuration throughout the entire tension skirt region, with the rotation of the multi-torus stack driving the radial strap to $T_{N-1}$ interface back in the windward direction to produce an overall deflection measurement only slightly larger than that of the stacked torus. The torus stack rotation continues for the outermost torus, which is seen to be in approximately the same location as the outermost torus of the stacked tori decelerator. Thus, while the global deflection measurements between the two decelerators are similar, their local surface angle can vary significantly. Curvature of the stacked tori surface is also present, though to a lesser degree, and shows that, despite the absence of the flexible tension skirt, the long span of unsupported structural tori still deforms under load.

The deformed surface plots of the optimum human-class configurations are shown in Fig. 140, with both the inflated and aerodynamically-loaded states shown in Fig. 140(a) and the aerodynamically-loaded states isolated in Fig. 140(b). The overall deflection forward of the inflated surfaces is slightly larger than the intermediate mission class configurations but is smaller than would be expected given the increase in scale, which can be attributed to the reduction in inflation pressure of the optimal tension cone and stacked tori designs. Unlike the similar deflection of all three configurations in the large robotic and intermediate-class missions, the hybrid and tension

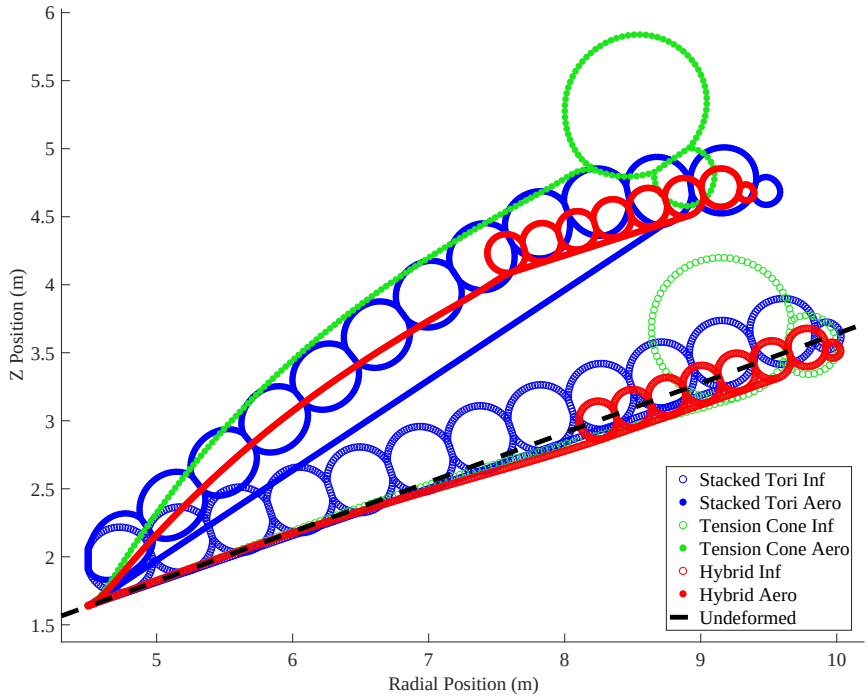


(a) Deflected surface comparison between the optimal human-class stacked tori, tension cone, and hybrid configurations subject to inflation pressure and aerodynamic loading

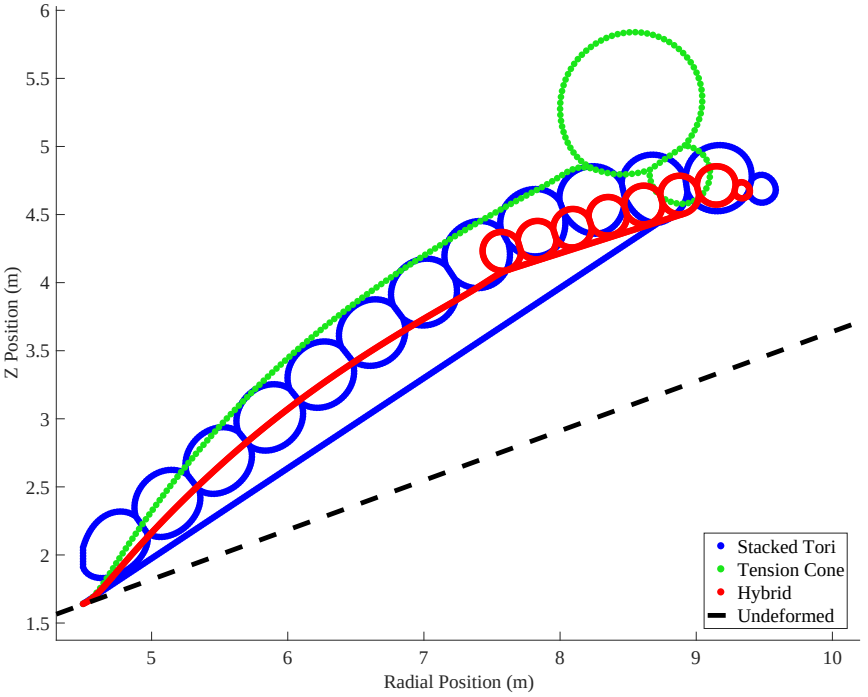


(b) Deflected surface comparison between the optimal human-class stacked tori, tension cone, and hybrid configurations subject to aerodynamic loading

**Figure 140: Deflected surface comparison between optimal human-class hybrid, stacked tori, and tension cone configurations**

cone decelerators deflect forward more than the stacked tori, the hybrid due to its higher inflation pressure and the tension cone due to its concentration of inflation gas towards the very outer diameter of the vehicle. These small differences can account for the variations in the final deflected angle of the hybrid decelerator relative to the stacked tori. Nevertheless, given the small forward deflection of the inflated surfaces, the large cone angle changes under aerodynamic loading can almost directly be interpreted as deflections from the undeformed, as-deigned cone angle.

As seen in Fig. 140(b), the deformed surfaces of the aerodynamically loaded hybrid and stacked tori configurations are substantially similar. Their cone angles at the radial strap interface to $T_{N-1}$ are nearly identical, with the greater deflection measurement of the hybrid decelerator instead being a result of its increased forward deflection under inflation. They both also exhibit significant curvature along their entire surface, with the conjoined tori of the stacked tori deforming in a similar shape to the hybrid decelerator's tension skirt. The curvature of the hybrid decelerator primarily arises from the deformation of the tension skirt and the interface with $T_1$ rather than deformation of the tori themselves whereas the curvature of the stacked tori primarily arises from deformation of $T_1$ and $T_{N-1}$ and the long unsupported span of the structural tori. The surface curvature of the two vehicles results in both of their outer tori being projected forward to produce a larger local cone angle. The stacked tori is also unique in this case. Due to the large span between attachment points of the radial strap and tori as well as the curvature of the multi-torus stack, the radial strap lies far away from the torus stack, rejoining with $T_{N-1}$ at a large angle. In actual implementations, it would be better to include multiple radial straps that attach to intermediate tori to reduce the surface curvature and maintain a more consistent angle between the radial strap and structural tori.

In addition, just like the large robotic and intermediate-class missions, the tension cone decelerator again deforms significantly more than the other two designs under

aerodynamic loading. In this case, while the absolute value of the difference in deflection is greater than the large robotic and intermediate-class missions, the difference as a percentage of the hybrid and stacked tori deflections is less. Therefore, it is evident that, at this scale, all decelerator configurations struggle to resist the severe aerodynamic loading resulting from the high aerodynamic pressure acting over a large surface area. As a result, all configurations produce a fully deformed cone angle that is significantly different from their as-designed 70° angle. These large deformations have many implications on the performance of the decelerator, including a reduction in drag due to the change in cone angle as well as a change in the drag area due to the corresponding reduction of the base diameter. For this magnitude of deformation, other concerns arise such as buckling of the structural tori, which is not simulated in this analysis. It is anticipated that the tension cone and the hybrid decelerators would be better able to resist buckling due to the series of connected tori but, even so, these results indicate that further strengthening of the inflatable structure, with possibly two rows of tori or other stiffening mechanisms, could be beneficial to reduce deflections for these large-scale vehicles. In all cases, any modifications to the inflatable structure should leverage the concepts of the hybrid decelerator configuration highlighted in this study, distributing structural members towards the outer diameters of the vehicle to improve stiffness and reduce excess mass.

### 4.5.3 Hybrid Decelerator Design Space Response Surface Development

The 868 configurations generated in the design space exploration study are used to construct response surface equations to estimate the mass and surface deflection of new hybrid decelerator configurations for use in conceptual design. Like the stacked tori and tension cone decelerators, the hybrid response surface models are composed of second-order polynomial basis functions of the design variables. The mass and

deflection responses are regressed against the basis functions to determine the polynomial coefficients, evaluating the responses at a subset of the data points, with 521 of the 868 solutions (60%) being use to generate the response surface model and the remaining 347 configurations (40%) being used to validate the model.

The full response surface equations are shown in Eqs. 53 and 54. Note that, because of their geometry, the hybrid decelerator response surfaces are a function of both the number of tori and tension skirt radius parameters, and also that the equations are not parameterized based on the half-cone angle and centerbody diameter. This is because the centerbody diameter varies directly with the major diameter among all three mission classes and the half-cone angle is held constant. Thus, these parameters do not provide new information if included in the model. As a result, the major diameter variable in the equations should be interpreted as a surrogate for the vehicle mission class, with a corresponding implied cone-angle and centerbody diameter. It is also important to note that, once again, the deflection response surface is formulated to produce a negative value to indicate a reduction in cone angle when subject to aerodynamic loading.

$$\begin{aligned} m_{Tot,Hb} = &-6.2143 - 13.5196D_{Maj} - 5.8279N_{Tori} + 35.4920R_{TS} + 0.1701P_{Inf} \\ &+ 2.999D_{Maj} * D_{Maj} - 3.8103D_{Maj} * N_{Tori} + 4.7458N_{Tori} * N_{Tori} \\ &+ 2.4074D_{Maj} * R_{TS} + 3.0321N_{Tori} * R_{TS} - 15.5137R_{TS} * R_{TS} \\ &+ 0.2029D_{Maj} * P_{Inf} - 0.2731N_{Tori} * P_{Inf} - 0.2808R_{TS} * P_{Inf} \\ &+ 0.0010P_{Inf} * P_{Inf} \end{aligned} \quad (53)$$

$$\Delta\theta_{Cone,Hb} = 4.573446 - 1.212556D_{Maj} + 1.646093N_{Tori} - 0.923250R_{TS} + 0.016899P_{Inf}$$
$$- 0.021202D_{Maj} * D_{Maj} + 0.084715D_{Maj} * N_{Tori} - 0.216410N_{Tori} * N_{Tori}$$
$$+ 0.146421D_{Maj} * R_{TS} - 0.058438N_{Tori} * R_{TS} - 0.215263R_{TS} * R_{TS}$$
$$- 0.000198D_{Maj} * P_{Inf} + 0.002791N_{Tori} * P_{Inf} - 0.001348R_{TS} * P_{Inf}$$
$$- 0.000051P_{Inf} * P_{Inf} \quad (54)$$

The response surface's goodness of fit is evaluated based on the coefficients of determination, $R^2$ and adjusted $R^2$. The $R^2$ performance of both models is shown in Table 19. The mass response surface $R^2$ value is decent but is the lowest of all three decelerator designs, which is expected given the hybrid decelerator's complicated geometry that incorporates both the tension skirt and multi-torus stack. The deflection response surface $R^2$, likewise, is the lowest of all response surfaces across all three decelerator designs and indicates that a significant portion of the deflection variability cannot be explained by the basis functions. The lower $R^2$ values of the hybrid response surfaces can be explained by several potential factors. In addition to the more complicated geometry, which results in unique phenomena such as the rotational effects of the tension skirt and multi-torus stack, the hybrid decelerator design space is also composed of fewer independent design variable, which allows for less tuning of the response surface equations to the shape of the mass and deflection responses.

**Table 19: $R^2$ and adjusted $R^2$ values for the hybrid decelerator mass and deflection response surface equations**

| | Mass RSM | Deflection RSM |
|---|---|---|
| $R^2$ | 0.9858 | 0.9293 |
| Adjusted $R^2$ | 0.9854 | 0.9274 |

The goodness of fit of the hybrid decelerator response surfaces is also assessed via actual by predicted plots, shown in Fig. 141. The mass response actual by predicted plot, seen in Fig. 141(a), shows the data points to be evenly distributed about the

perfect fit line with no obvious clumping of points, but also with a wide dispersion of data points around the perfect fit line. The subset of points with the highest mass are seen to diverge and generally move farther away from the best-fit line, indicating that higher order terms in the response surface could be beneficial. The deflection response graph in Fig. 141(b) shows poorer correlation, which is reflected in its lower $R^2$ value. Clumping of data points about the perfect fit line is observed, along with divergence of the deflection predictions towards both small and large deflection values. The existence of both the clumping of data points and large deviations of the extreme data points suggests that the deflection response surface could benefit from more basis function to fit the model along with higher order terms to capture more of the deflection variability.

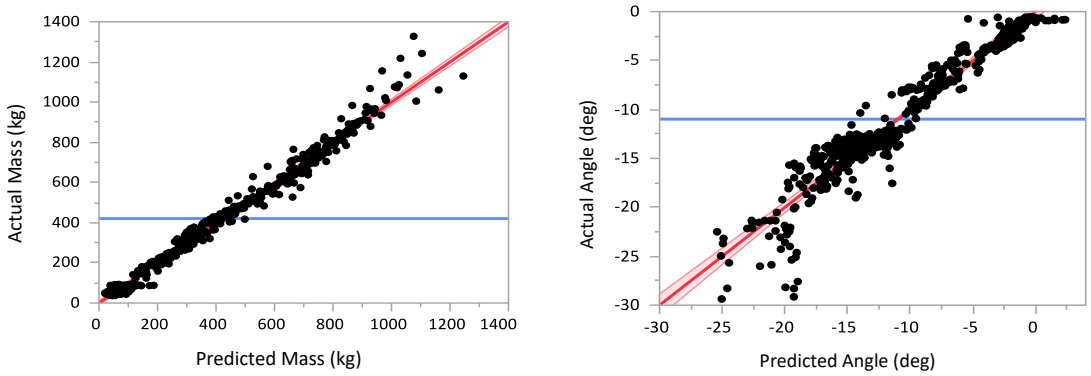


(a) Actual by predicted plot of the hybrid decelerator mass response surface equation

(b) Actual by predicted plot of the hybrid decelerator deflection response surface equation

**Figure 141: Response surface goodness of fit assessments showing actual hybrid decelerator mass and deflection values versus response surface predicted values**

Residual by predicted plots are also used to highlight trends within the residuals to better understand the performance of the hybrid decelerator response surface models. Seen in Fig. 142(a), the residuals of the mass response show a clear non-linear trend with respect to predicted mass, diverging from the 0 residual line toward large mass values as was seen in the actual by predicted plot. Other smaller scale trends are observed in the data such as the negatively sloped group of data points with small

masses and the three outlier data points with large predicted mass and negative residuals. These results indicate the benefit of including higher order terms in the response surface equation in addition to potentially performing a transformation on the mass response to eliminate the global trends in residuals. The deflection response residual by predicted plot, shown in Fig. 142(b), does not show a cohesive global trend of the residuals with respect to predicted deflection but shows significant clumping of results with many different isolated trends. Several global outliers are present and each grouping of data is seen to also have a subset of outliers that to not follow the overall trend of the group. These results again corroborate the suggestions that additional terms and higher order terms could improve the hybrid decelerator response surface predictions.

The overall accuracy of the response surface models is lastly evaluated by overlaying the response surface equation predicted results with the simulated design space

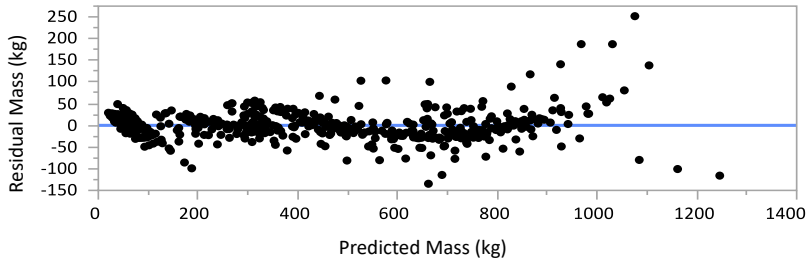


(a) Residual by predicted plot of the hybrid decelerator mass response surface equation

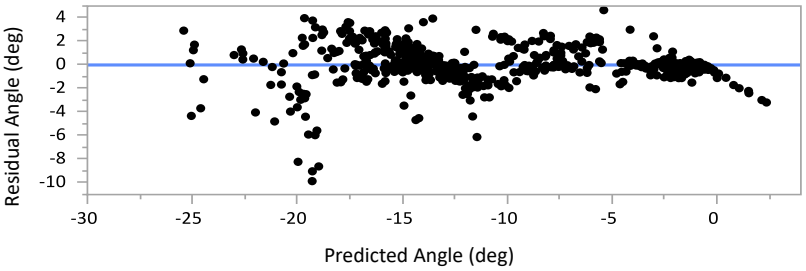


(b) Residual by predicted plot of the hybrid decelerator deflection response surface equation

**Figure 142: Response surface goodness of fit assessments showing residual hybrid decelerator mass and deflection values versus response surface predicted values**

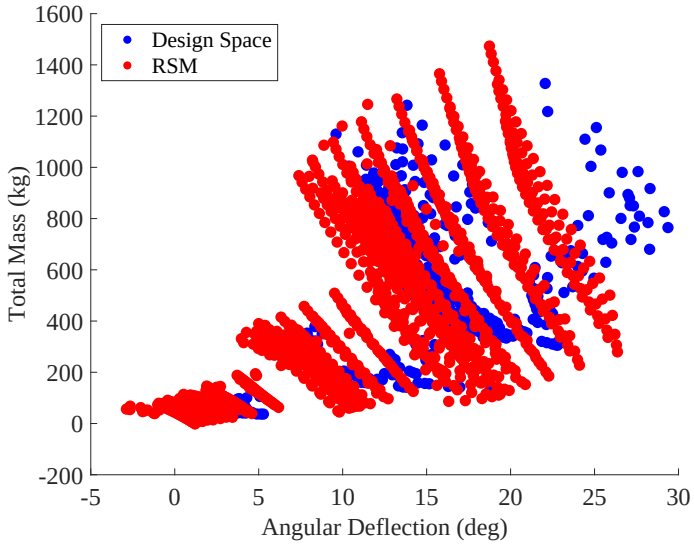


**Figure 143: Comparison of hybrid decelerator response surface mass and deflection predictions to actual simulated values**

results. Seen in Fig. 143, the hybrid response surface models capture the general dispersion of the simulated mass and deflection response but fail to capture any detailed features or trends in the data. The equations correctly predict three isolated groups of data points, with the greatest density of solutions in similar regions as the simulated data. However, the significant curvature of the simulated deflection results is not captured by the response surface models and is approximated as being relatively uniform across the entire design space. This is likely due to the significant nonlinearities present in the underlying training data that evolve across the design space in addition to the relatively fewer basis functions. Nevertheless, the response surface equations are able to predict the approximate mass and deflection performance of the hybrid decelerators and provide a reasonable range for the different mission classes. This fidelity of response surface is sufficient for conceptual design because the approximated results convey an appropriate level of resolution of the mission class performance and variation between configurations, especially for novel hybrid configurations with no underlying validation test data. Any detailed optimization of the decelerator design or higher resolution mass and deflection estimates beyond

those provided by the response surfaces are better suited to higher fidelity analysis methods.

## *4.6 Summary and Implications*

This contribution develops a novel hybrid IAD concept that combines features from both the tension cone and stacked tori decelerators into a single design. The hybrid configuration is motivated by the fact that stacked tori and tension cone decelerators each have unique benefits and deficits, with the stacked tori supporting large external loads at the expense of a large decelerator mass and the tension cone efficiently reducing the decelerator mass with the implementation of a tension skirt at the expense of reduced load-bearing capabilities. By integrating the multi-torus stack of the stacked tori configuration with the tension skirt of the tension cone configuration, the hybrid IAD design can leverage the benefits of both configurations and expand the applicability of the two baseline designs.

The hybrid configuration is designed to concentrate the structural tori towards the outer diameter of the decelerator in order to resist compressive loading and retain the majority of the stacked tori structural stiffness. In addition, the hybrid design replaces the inner tori with a more mass efficient tension skirt, which is designed to take the primarily tensile loading experienced in this region. In this way, the hybrid decelerator can effective mitigating the deficits of the stacked tori and tension cone designs through intentional location of the structural features. The utilization of the tension skirt and multiple tori also introduces more flexibility into the design to enable greater tailoring of the geometry to the specific mission.

Characteristics of the new hybrid design are explored, studying how the introduction of the tension skirt impacts the stacked tori deflection in addition to the impacts of varying the tension skirt length and number of tori. Parameter studies indicate that

the hybrid decelerator deformation also retains aspects of both constituent configurations, with the multiple tori reducing overall deformation and the larger deflections of the tension skirt causing a rotation of the entire multi-torus stack, similar to what would be seen with the tension cone's single torus under load. The rotation of the torus stack is actually observed to decrease deflection of the outer tori in certain instances and can lead to a smaller deflected angle than that of the stacked tori, albeit with a larger curvature of the decelerator windward surface. Deflection of the hybrid decelerator surface, however, is a complicated function of the torus stack rotation along with the overall compression of the tori, with the magnitude of each competing factor evolving across the multi-dimensional design space. These parameter studies demonstrate that the hybrid decelerator's structural performance is highly configuration dependent. While an identification of the conflicting phenomena and a cursory study of the trends has been investigated in this thesis, further study is necessary to better understand the hybrid decelerator design trades. In addition, the impact on the decelerator drag, stability, and heating performance due to the increased curvature and the change in local cone angles across the surface need to be investigated further if hybrid designs are to be considered for future planetary missions.

A full factorial design space study is also conducted for the hybrid decelerator, similar to the stacked tori and tension cone configurations, to understand the performance of the hybrid configuration relative to the two traditional designs. For these studies, the design parameters describing the decelerator's overall size and shape are sized for three different mission classes, large robotic, intermediate, and human-class, in order to reduce the design space and restrict the results to reasonable vehicles. The remaining design variables, describing the details of the structural configuration, are then discretized within appropriate ranges to generate the full set of simulated configurations. The mass and deflection results of the hybrid configuration are compared against those of the stacked tori and tension cone and are sorted by each design

variable to understand their parameter sensitivities.

Overall, stacked tori configurations are confirmed to be located in the high mass, low deflection regions of the design space whereas tension cone decelerators trend towards the low mass, high deflection areas. Hybrid configurations are observed to bridge between the two regions, encompassing both and providing intermediate solutions that often reduce the mass or deflection with minimal impact to the other. A Pareto frontier is constructed to understand the set of optimal solutions. For all three mission classes, hybrid configurations dominate the candidate solutions, with tension cone configurations confirmed to be more applicable to smaller-scale missions and stacked tori configurations more applicable to larger-scale missions. The fact that hybrid configurations represent nearly all Pareto optimal designs shows their versatility and ability to simulate favorable configurations that can balance low deflection with low mass.

Optimization of the design space based on a weighting of the mass and deflection objectives similarly shows hybrid decelerators to generate favorable solutions. For all three mission classes, the hybrid design is able to provide large reductions in mass or deflection relative to the stacked tori and tension cone optima with only a slight degradation in the other objective. Hybrid solutions are also consistently found to be the more moderate solutions, enabling designs that have low mass and deflection and, as a result, better optimize the objective function. Inspection of the deflected surfaces of the optimal configurations shows the optimal hybrid solutions to leverage rotation of the multi-torus stack to reduce deflection but also shows the hybrid solution to have a similar surface profile as the stacked tori for the human-class mission. These results demonstrate that hybrid decelerators have applicability at all three scales, and often offer the most favorable IAD solution. However, the results also show that further design of large scale, human-class decelerators is necessary, with deflections of even optimal solutions approaching 15°.

# CHAPTER V

# SUMMARY AND FUTURE WORK

## *5.1 Research Summary*

This thesis advances the state of the art of inflatable aerodynamic decelerator design and analysis by providing an investigation into the implications of IAD configuration on their structural and mass performance along with establishing photogrammetry as a valid test instrumentation technique for assessing an IAD's global dynamic response. The methodologies and results developed here improve future IAD design efforts by enabling estimates of structural performance information in conceptual design, exploring the configurational impacts of novel decelerator designs, and providing new test methodologies to better evaluate those designs. This research, therefore, starts to explore the next phases in the IAD development process, as inflatable decelerator technology maturation transitions from early-stage concept demonstration to applications on future missions that require expanded capabilities beyond the current configurational design space.

In order to enable evaluations of the IAD's structural performance earlier in the design cycle, computationally efficient models are required that can rapidly simulate many configurations. This thesis therefore develops simplified models of a stacked tori decelerator that remove computational complexity by simplifying the geometry through the strategic use of surrogate modeling. Validation of these models with multiple data sets from ground tests and high-fidelity modeling demonstrate that they can successfully estimate the decelerator structural performance across a wide range of configurations and loading conditions. A simplified model is also developed to estimate the structural performance of tension cone decelerators, with validation of the

model against analytic formulations similarly confirming its predictive capabilities. In order to increase their applicability to conceptual design studies, both models are also parameterized in terms of a universal set of design variables that can uniquely describe a wide range of possible configurations.

In addition, design space exploration studies are conducted for both the stacked tori and tension cone decelerators to demonstrate their usefulness in conceptual design. Mass and deflection results are simulated for a wide range of configurations to determine how the different design parameters impact the decelerator performance as well as the approximate performance ranges of stacked tori and tension cone IADs. These studies highlight the impacts of decelerator design choices and how those effects evolve over the design space. In addition, the performance results are used to generate response surface models, which enable designers to estimate the performance of new configurations without the need for computational simulation capabilities. These response surface equations can be used to facilitate design trades and can also be incorporated in high-level architecture optimization efforts to convey IAD structural performance implications.

As inflatable decelerators mature and develop into a proven technology option for planetary descent, future mission architectures will inevitably impose new restrictions and performance requirements on the decelerator configuration. Therefore, this thesis also introduces a new IAD design that enables greater configurational flexibility and performance by incorporating features from both the stacked tori and tension cone decelerator concepts. The hybrid decelerator design integrates the multi-torus stack of the stacked tori decelerator for increased structural rigidity with the tension skirt of the tension cone decelerator for reduced mass, locating the primary compressive structures towards the outer diameters of the vehicle experiencing higher compressive loading and the primary tensile structures towards the inner regions of the decelerator experiencing higher tensile loading. The inclusion of both features also allows for the

tailoring of the decelerator structural and mass performance to a specific mission through adjusting of both the tension skirt length and number of tori.

The performance of this new hybrid decelerator is explored through parameter studies to understand the impacts of the design variables. These parameter studies highlight the behavior of the hybrid decelerator deflected surface under load and its similarity to both the baseline stacked tori and tension cone deflected surfaces, namely that the hybrid decelerator features both the overall compression of the multi-torus stack as well as the rotation of the tori due to the presence of a tension skirt. These two competing factors vary in magnitude across the design space and interact to influence the overall deflection of the IAD surface.

A design space exploration study is also conducted for the hybrid configuration to help inform future conceptual design efforts. Hybrid design parameters are tailored to large robotic, intermediate, and human-class missions to understand the impacts of the IAD configuration on its structural and mass performance and how those impacts vary across the different mission scales. The overall performance ranges of the hybrid decelerator are compared in relation to the baseline stacked tori and tension cone designs, with hybrid solutions producing more moderate solutions that better balance low deflection with low mass. As a result of their greater configurational flexibility and balance of mass and deflection, hybrid designs are observed to compose nearly all Pareto optimal solutions. Optimization of the three design spaces based on a weighted objective function likewise shows that optimal hybrid solutions are able to simultaneously approach the low mass values of the tension cone designs and the low deflection values of the stacked tori designs across all mission scales. These results demonstrate that hybrid configurations offer potential performance improvements over both the stacked tori and tension cone decelerators and are applicable across all mission scales. Response surfaces are generated that approximate the hybrid performance but, due to the increased complexity of the hybrid decelerator response,

are more suited to assessing general performance ranges and trends rather than more detailed design optimization.

Test diagnostic techniques tailored to photogrammetric data sets are also developed to help assess the structural performance of new inflatable decelerators and to measure their dynamic structural response. The analysis methodologies utilize a time series of photogrammetry frames to analyze motion over the entire IAD surface and are able to extract information that has previously not been available for inflatable decelerators. One of the analysis techniques developed involves determining the positional standard deviation of each data point over all the time series data and uses the single standard deviation value as a metric for the degree of motion at each point. By decomposing the complicated time histories to a single value for each point, the positional standard deviation analysis can rapidly characterize the global dynamic response and clearly present the information visually. Therefore, trends in the data can be easily assessed to provide an intuitive understanding of the decelerator dynamic response.

A second analysis technique transforms the time-history data of select data points into the frequency domain to uncover the frequency content of motion. Because this analysis results in multiple response values for each point, corresponding to the amplitudes at each frequency, trends can be observed by performing sweeps along characteristic dimensions of the decelerators such as along a single radial or about the circumference. This analysis is also able to assess the existence of resonant fluid-structure coupling through inspection of distinct peaks in the frequency spectrum.

Both analyses are applied to photogrammetry data from wind tunnel testing of an inflatable decelerator to demonstrate their capabilities. The positional standard deviation analysis is able to isolate unique characteristics of motion corresponding to deflection, elongation, and twist of the decelerator surface. The analysis also highlights how the features evolve as a function of the design and test parameters. In addition,

mode shapes are isolated for the different characteristic deformations, which enable a better assessment of the decelerator structural performance. The frequency-domain analysis is likewise shown to be valuable for evaluating the decelerator's structural performance. The frequency analysis is able to identify resonant conditions that result in constructive coupling of the fluid-structure interactions for a specific test condition, a phenomenon that has not been previously observed during IAD testing. Trends are also assessed in the radial and circumferential directions and identify how the structural resonance evolves over the entire decelerator. The application of these analyses to existing wind tunnel test data sets proves their utility, providing new information on the decelerator dynamic response and identifying resonance phenomena that have previously been unavailable for inflatable decelerators.

The simplified models and hybrid configuration formulation developed in this thesis provide the foundation for future conceptual design studies and advancement of IAD structural performance assessments. The design space studies and parameter evaluations provide a general assessment of IAD vehicle performance for the stacked tori, tension cone, and hybrid decelerators and enable a first-order assessment of the structural and mass impacts due to IAD configuration design. New test diagnostic techniques are also developed to extract previously unobtainable information regarding the global structural dynamic response. This suite of new analyses and models expands the state-of-the-art of IAD structural performance predictive and assessment capabilities to better inform future IAD design efforts.

## *5.2 Suggestions for Future Work*

Several experimental data sets of stacked tori decelerators were available from which to validate the stacked tori simplified models. This validation data was invaluable for assessing the performance of the simplified model and tuning the thickness model. However, even with access to the three available data sets (two experimental, one

high-fidelity computational), only 4 relevant data points were available to tune the thickness model, those data points only reasonably assessing variation with respect to the major diameter. Therefore, additional validation data is still needed to better tune the surrogate thickness model and to understand its variation with respect to all design variables. This additional data is necessary to reduce the uncertainty in the thickness model estimates and to better understand its performance across a range of conditions. Both of these factors will greatly increase confidence in the thickness model predictions and the overall simplified stacked tori model.

Like the thickness model, a regression model is also used to estimate the finite element model wedge degree angle, which is equivalent to measuring the radial strap pattern density. This model likewise only assesses variation with respect to major diameter based on four data points. The strap pattern density should be designed based on the total load experienced by the decelerator, which is a function of the major diameter, cone angle, minor diameter, and flight environment, among other factors. However, limited data on the strap patterns of existing configurations and limited analysis of the performance of these strap patterns leads to significant uncertainty in the strap pattern density estimates, especially for future novel configurations. Therefore, additional studies to understand the impact of the decelerator strap pattern and to design and evaluate new strap patterns is necessary.

Investigating decelerator strap patterns is particularly necessary for hypersonic applications of tension cone and hybrid decelerator vehicles. It is assumed in this thesis that the strap densities of stacked tori vehicles apply directly to tension cone and hybrid decelerator designs with common cone angles and major diameters based on the assumption that each configuration would therefore experience a similar total applied load. However, the introduction of the tension skirt certainly has an impact on the load distribution throughout the vehicle and influences the requisite strap pattern. Understanding the differences in the stress profiles of the tension cone and

hybrid decelerators and evaluating how those differences impact the resulting strap pattern is also important.

The benefit of more validation test data also extends to the tension cone and hybrid models themselves. The stacked tori decelerator simplified model benefited greatly from the variety of available data and was able to assess its point-wise deflection, point-wise stress, and deflected surface contour. The tension cone decelerator, conversely, was able to assess the surface stress profile, but with the assumption of an attached rigid torus. While other studies and tests are discussed in the literature, detailed test data is often not documented or available and, therefore, the studies are of limited use for simplified modeling efforts. Given that the hybrid configuration is a new design, it is expected that there is no direct supporting test data. However, future efforts to verify the unique deflection characteristics of the hybrid configuration would be invaluable to confirm the trends and overall performance predicted in this thesis.

Results of the design space study estimate that the fabric mass term dominates the inflatable decelerator total mass of optimal configurations across all decelerator designs and mission classes. The fabric mass calculation is based on an aggregate area density determined from a summation of component masses used in stacked tori static load tests. This density value is used in this thesis across all decelerators regardless of configuration or strap pattern and is also assumed to be the density of the tension skirt. Given that the fabric density has such a large impact on the decelerator total mass, a better understand of the component mass breakdown and an assessment of additional mass terms such as the area mass of a representative hypersonic tension skirt will help to better differentiate the mass estimates of vehicles with dissimilar configurations, strap patterns, and other factors.

Inspection of the deflected surfaces of decelerators for the human-class mission also showed all IAD designs to exhibit large deformations, up to tens of degrees.

In addition, significant curvature of the deflected surface resulted in local cone angles that could exceed the overall deflection value. These large deflections are not unexpected, as all previous IAD test articles have been designed for much smaller applications. Given that the simplified models are based on and validated against these smaller heritage test article designs, this thesis confirms that pure extrapolation of the models is likely not appropriate for vehicles with an order of magnitude or greater increase in payload mass. In particular, the assumption of radial straps spanning the entire surface between the first and second to last torus may work well for small-scale decelerators but do not adequately constrain larger decelerators. Among other factors, these large decelerators could benefit from more complicated strap patterns with additional intermediate attachment points or from additional strengthening tori that are placed in parallel, rather than in-line, with the existing multi-torus stack. Further investigation into the most efficient structural reinforcement mechanisms for these large-scale decelerators will be required before IADs can be considered for such large-scale applications.

Further analysis of the effects of the non-linear surface profile on the decelerator aerodynamic and surrounding flowfield response will also help future mission designers understand the impacts of the IAD structural design. While additional reinforcement or strap design efforts would be expected to reduce surface deflection and curvature, it is not logical to anticipate their full elimination over such a large unsupported span. Therefore, future analyses that can correlate the surface deflection and curvature to corresponding impacts on the decelerator drag, stability, and shock response will be useful to better evaluate trade-offs between the mass penalty due to the additional components and the improvement in rigidity.

It is also understood that the elevated temperatures experienced during entry can have significant impacts on the decelerator structural performance. In addition to the variations in gas pressure due to temperature changes, the material properties

of the structural fabrics are also expected to degrade under elevated temperatures. While thermal protection systems used on entry vehicles will significantly reduce heat transfer from the surrounding flowfield into the inflatable structure, temperature increases are still expected to significant impact material properties and the resulting structural response. Future studies that incorporate temperature-dependent material properties into the structural model will be able to assess the sensitivity of the structural response to the thermal environment to assess its impact relative to aerodynamic loading and gain a better understanding of holistic decelerator structural performance.

Lastly, the photogrammetry data reduction methodologies have been developed and were demonstrated to provide valuable insight into the dynamic characteristics of previous inflatable decelerator test articles. However, these findings were obtained with a data set that was not specifically constructed to determine dynamic information. In particular, the temporal resolution of the photogrammetry system was relatively low, restricting the possible frequency range of the data analyzed and potentially introducing aliasing into the calculations. Similarly, differences in camera resolution were shown to influence both the standard deviation and frequency analyses. Future test programs that intend to leverage these photogrammetry analysis techniques should take care when selecting their camera setup to ensure sufficient temporal and spatial resolution of the cameras. In addition, specific test techniques can be established to isolate predicted resonance phenomena, such as by slowly varying a single test parameter to try and isolate the resonant conditions.

# APPENDIX A

# LIST OF PUBLICATIONS

Thesis-relevant publications

- Lin Li, Robert Braun, Julian Rimoli "Photogrammetry Analysis Development to Determine the Dynamic Content of Inflatable Aerodynamic Decelerator Deflection," Journal of Spacecraft and Rockets. (in progress)
- Lin Li, Robert Braun, Julian Rimoli "Simplified Model Development to Understand the Stacked Tori Inflatable Aerodynamic Decelerator Configurational Design Space," Journal of Spacecraft and Rockets. (in progress)
- Lin Li, Robert D. Braun, Alan M. Cassell, "Photogrammetry Analysis of a Hypersonic Inflatable Aerodynamic Decelerator Structural Test Article," AIAA-2014-0353. AIAA SciTech Conference on Jan 13, 2014, National Harbor, Maryland.
- Alan M. Cassell, Gregory T. Swanson, Bill T. Quach, Laura K. Kushner, Jeffrey D. Brown, Lin Li, et. al., "Design and Execution of the Hypersonic Inflatable Aerodynamic Decelerator Large-Article Wind Tunnel Experiment," AIAA 2013-1304, AIAA Aerodynamic Decelerator Systems (ADS) Conference. 25-28 March, 2013, Daytona Beach, Florida.
- Cole D. Kazemba, Alan M. Cassell, Laura K. Kushner, Kevin Tran, Bill T. Quach, Lin Li, et. al., "Determination of the Deformed Structural Shape of HIADs from Photogrammetric Wind Tunnel Data," AIAA 2013-1286, AIAA Aerodynamic Decelerator Systems (ADS) Conference. 25-28 March, 2013, Daytona Beach, Florida.

Non-thesis-relevant publications

- Lin Li, Keir C. Gonyea, and Robert D. Braun, "Finite Element Analysis of the Inflatable Re-Entry Vehicle Experiment," AIAA 2015-0204, 2015 AIAA Science and Technology Forum, Kissimmee, Florida, January 2015.

- Nathaniel Skolnik, Hiromasa Kamezawa, Lin Li, Grant Rossman, Brandon Sforzo, Robert D. Braun, "Design of a Novel Hypersonic Inflatable Aerodynamic Decelerator for Mars Entry, Descent, and Landing," submitted to the AIAA Science and Technology Forum and Exposition 2017.

# REFERENCES


[1] Braun, R. D. and Manning, R. M., "Mars Exploration Entry, Descent, and Landing Challenges," *Journal of Spacecraft and Rockets*, Vol. 44, No. 2, mar 2007, pp. 310–323.

[2] Way, D. W., Powell, R. W., Chen, A., and Steltzner, A. D., "Asymptotic Parachute Performance Sensitivity," IEEEAC Paper 1465, 2005.

[3] "The Global Exploration Roadmap," September 2011.

[4] Major, J., "NASA Mars Rover's Risky Landing Plan: A Step-By-Step Guide," Online, August 2012.

[5] Cruz, J. and Lingard, J., "Aerodynamic Decelerators for Planetary Exploration: Past, Present, and Future," *Guidance, Navigation, and Control and Co-located Conferences*, American Institute of Aeronautics and Astronautics, Aug. 2006, pp. –.

[6] Edquist, K., Dyakonov, A., Wright, M., and Tang, C., "Aerothermodynamic Design of the Mars Science Laboratory Backshell and Parachute Cone," *Fluid Dynamics and Co-located Conferences*, American Institute of Aeronautics and Astronautics, June 2009, pp. –.

[7] Rivellini, T. P., "The Challenges of Landing on Mars," *The Bridge, National Academy of Engineering*, Vol. 34, No. 4, 2004, pp. 13–17.

[8] Manning, R. and Adler, M., "Landing on Mars," *AIAA Space Conference, Long Beach CA*, No. 6742, American Institute of Aeronautics and Astronautics, September 2005.

[9] Malik, T., "NASA Studying 4 Landing Site Options for 2016 Mars Mission," space.com, September 2013.

[10] Samareh, J., "Estimating Mass of Inflatable Aerodynamic Decelerators Using Dimensionless Parameters," 8th International Planetary Probe Workshop, Portsmouth, VA, June 610 2011.

[11] Masciarelli, J. and K., M., "Summary of Ultralightweight Ballute Technology Advances," 2nd International Planetary Probe Workshop, NASA Ames Research Center, Moffett Field, CA, August 2004.

[12] O'Farrell, C., Brandeau, E. J., Tanner, C., Gallon, J. C., Muppidi, S., and Clark, I. G., "Reconstructed Parachute System Performance During the Second LDSD Supersonic Flight Dynamics Test," *AIAA Atmospheric Flight Mechanics Conference, AIAA Aviation*, American Institute of Aeronautics and Astronautics, June 2016, pp. –.

[13] Richardson, E., Munk, M., James, B., and Moon, S., "Review of NASA In-Space Propulsion Technology Program Inflatable Decelerator Investments," *Aerodynamic Decelerator Systems Technology Conferences*, American Institute of Aeronautics and Astronautics, May 2005, pp. –.

[14] Tutt, B. A., Tanner, C. L., Coatta, D. M., and Muppidi, S., "Numerical Modeling of the 8 Meter Attached Isotensoid Supersonic Inflatable Aerodynamic Decelerator," *Aerodynamic Decelerator Systems Technology Conferences*, American Institute of Aeronautics and Astronautics, March 2015, pp. –.

[15] Tanner, C., Cruz, J., and Braun, R., "Structural Verification and Modeling of a Tension Cone Inflatable Aerodynamic Decelerator," *Structures, Structural Dynamics, and Materials and Co-located Conferences*, American Institute of Aeronautics and Astronautics, April 2010, pp. –.

[16] Li, L., Braun, R. D., and Cassell, A., "Photogrammetry Analysis of a Hypersonic Inflatable Aerodynamic Decelerator Structural Test Article," *AIAA SciTech*, American Institute of Aeronautics and Astronautics, Jan. 2014, pp. –.

[17] Lindell, M., Hughes, S., Dixon, M., and Willey, C., "Structural Analysis and Testing of the Inflatable Re-Entry Vehicle Experiment (IRVE)," *Structures, Structural Dynamics, and Materials and Co-located Conferences*, American Institute of Aeronautics and Astronautics, May 2006, pp. –.

[18] Yamada, K., Akita, D., Sato, E., Narumi, R., and Abe, T., "Flare-Type Membrane Aeroshell Flight Test at Free Drop from a Balloon," *Journal of Spacecraft and Rockets*, Vol. 46, No. 3, 2009, pp. 606614.

[19] Clark, I., Cruz, J., Hughes, M., Ware, J., Madlangbayan, A., and Braun, R., "Aerodynamic and Aeroelastic Characteristics of a Tension Cone Inflatable Aerodynamic Decelerator," *Aerodynamic Decelerator Systems Technology Conferences*, American Institute of Aeronautics and Astronautics, May 2009, pp. –.

[20] MacLanahan, D. A, J., "An Investigation of Various Types of Decelerators at Mach Number 2.8," Tech. rep., AEDC-TR-66-136 (AD485279), July, 1966.

[21] Hughes, S., Cheatwood, F., Dillman, R., Calomino, A., Wright, H., DelCorso, J., and Calomino, A., "Hypersonic Inflatable Aerodynamic Decelerator (HIAD)Technology Development Overview," *Aerodynamic Decelerator Systems Technology Conferences*, American Institute of Aeronautics and Astronautics, May 2011, pp. –.

[22] Buck, G., "Testing of Flexible Ballutes in Hypersonic Wind Tunnels for Planetary Aerocapture," *Aerospace Sciences Meetings*, American Institute of Aeronautics and Astronautics, Jan. 2006, pp. –.

[23] Bohon, H. L., Sawyer, J. W., and Miserentino, R., "Deployment and Performance Characteristics of 1.5-Meter Supersonic Attached Inflatable Decelerators," Tech. rep., NASA TN D-7550, 1974.

[24] Edward Fallon, J, I., "Supersonic stabilization and deceleration - Ballutes revisited," *Aerodynamic Decelerator Systems Technology Conferences*, American Institute of Aeronautics and Astronautics, May 1995, pp. –.

[25] Baker, D., "Investigation of an Attached Inflatable Decelerator with Mechanically Deployed Inlets at Mach Numbers from 2.25 to 4.75," Tech. rep., ARO Inc. Technical Report, AEDC TR-69-132, June, 1969.

[26] Bohon, H. L. and Miserentino, H. L., "Deployment and Performance Characteristics of 5-Foot-Diameter (1.5 m) Attached Inflatable Decelerators from Mach Number 2.2 to 4.4," Tech. rep., NASA TN D-5840, 1970.

[27] Corso, J. D., Cheatwood, F., Bruce, W., Hughes, S., and Calomino, A., "Advanced High-Temperature Flexible TPS for Inflatable Aerodynamic Decelerators," *Aerodynamic Decelerator Systems Technology Conferences*, American Institute of Aeronautics and Astronautics, May 2011, pp. –.

[28] Corso, J. D., Bruce, W., Liles, K., and Hughes, S., "Thermal Analysis and Testing of Candidate Materials for PAIDAE Inflatable Aeroshell," *Aerodynamic Decelerator Systems Technology Conferences*, American Institute of Aeronautics and Astronautics, May 2009, pp. –.

[29] Player, C., "PAIDAE Thermal Protection System Testing Final Report FY2008," Tech. rep., PAI-DAE-3.3-012, NASA Langley Research Center, 2008.

[30] GUY, L., "Structural design options for planetary entry," *Structures, Structural Dynamics, and Materials and Co-located Conferences*, American Institute of Aeronautics and Astronautics, April 1968, pp. –.

[31] Kyser, A. C., "Deployment Mechanics For An Inflatable Tension-Cone Decelerator," Tech. rep., NASA CR- 929, November, 1967.

[32] Stroud, W. J. and Zender, G. W., "Experimental Investigation to Determine Utility of Tension Shell Concept," Tech. rep., NASA TM-X-1211, March, 1966.

[33] Jurewicz, D., Lichodziejewski, L., Tutt, B., Gilles, B., and Brown, G., "Application of inflatable aeroshell structures for Entry Descent and Landing," *Aerospace Conference, 2013 IEEE*, 2013, pp. 1–10.

[34] Swanson, G., Cassell, A., Johnson, R. K., Hughes, S. J., Calomino, A. M., and Cheatwood, F. M., "Tension Measurements of Hypersonic Inflatable Aerodynamic Decelerator Structural Straps under Static and Dynamic Loading," *Aerodynamic Decelerator Systems Technology Conferences*, American Institute of Aeronautics and Astronautics, March 2013, pp. –.

[35] Harris, C., "Transonic Aerodynamic Investigation of Tension Shell and Blunted 100 Conical Shapes for Unmanned Entry Vehicles," Tech. rep., NASA TN D-3700.

[36] Anderson, M. S., Robinson, J. C., Bush, H. G., and Fralich, R. W., "A Tension Shell Structure for Application to Entry Vehicles," Tech. rep., NASA TN D-2675, 1965.

[37] Robinson, J. C. and Jordan, A. U., "Exploratory Experimental Investigation at Mach 7 of Tension Shell Shapes for Entry Vehicles," Tech. rep., Proposed NASA TN.

[38] Deveikis, W. D. and Sawyer, J. H., "Experimental Investigation at Mach Number 3 Of Tension Shell Entry Body Shapes," Tech. rep., Proposed NASA TN.

[39] Zender, G. W. and Stroud, W. J., "Plastic Model Tests of a Tension Shell Structure for Entry Vehicles," Tech. rep., Proposed NASA TN.

[40] Schairer, E., Heineck, J., Walker, L., and et al., "Simultaneous, unsteady PIV and photogrammetry measurements of a tension-cone decelerator in subsonic flow," 15th Int. Symp. on Applications of Laser Techniques to Fluid Mechanics, Lisbon, Portugal, 0508 July 2010.

[41] Cassell, A., Swanson, G. T., Quach, B., Kushner, L. K., Brown, J. D., Kazemba, C. D., Kruger, C., Johnson, R. K., Hughes, S. J., Littell, J., Calomino, A. M., and Cheatwood, F. M., "Design and Execution of the Hypersonic Inflatable Aerodynamic Decelerator Large-Article Wind Tunnel Experiment," *Aerodynamic Decelerator Systems Technology Conferences*, American Institute of Aeronautics and Astronautics, March 2013, pp. –.

[42] Li, L., Gonyea, K., and Braun, R. D., "Finite Element Analysis of the Inflatable Re-Entry Vehicle Experiment (IRVE)," *AIAA SciTech*, American Institute of Aeronautics and Astronautics, Jan. 2015, pp. –.

[43] "NASA Launches New Technology: An Inflatable Heat Shield," NASA Mission News, August 2009.

[44] "Inflatable Reentry and Descent Technology (IRDT)," Tech. rep., IRDT fact-sheet, ESA, 2005.

[45] Wilde, D. and Walther, S., "Flight Test and ISS Application of the Inflatable Reentry and Descent Technology (IRDT)," *Acta Astronautica*, Vol. 51, No. 1-9, 2002, pp. 8388.

[46] Marraffa, L., e. a., "IRDT 2R Mission, First Results," Thermal Protection Systems and Hot Structures, Proceedings of the 5th European Workshop, ESTEC, Noordwijk, The Netherlands., 17-19 May 2006.

[47] BOHON, H., "A summary of supersonic decelerators with emphasis on problem areas in aerodynamics and structures," *Aerospace Sciences Meetings*, American Institute of Aeronautics and Astronautics, Jan. 1967, pp. –.

[48] HOUTZ, N., "Optimization of inflatable drag devices by isotensoid design," *Annual Meeting*, American Institute of Aeronautics and Astronautics, June 1964, pp. –.

[49] Barton, R. R., "Development of Attached Inflatable Decelerators for Supersonic Applications," Tech. rep., NASA CR-66613, 1968.

[50] Mikulas, Martin M., J. and Bohon, H. L., "Development Status of Attached Inflatable Decelerators," *J. Spacecraft Rockets*, Vol. 6, No. 6, June 1969, pp. 654–660.

[51] COMER, R. L. and LEVY, S., "DEFLECTIONS OF AN INFLATED CIRCULAR-CYLINDRICAL CANTILEVER BEAM," *AIAA Journal*, Vol. 1, No. 7, July 1963, pp. 1652–1655.

[52] Fichter, W. B., "A Theory for Inflated Thin-Wall Cylindrical Beams," Tech. rep., NASA TN D-3466, NASA Langley Research Center, June 1966.

[53] Weeks, G. E., "Buckling of a Pressurized Toroidal Ring Under Uniform External Loading," Tech. rep., NASA TN-D-4124, August, 1967.

[54] Timoshenko, S., "Theory of Elastic Stability," *McGraw-Hill Book Co., Inc.*, 1936, pp. 285–286.

[55] Ratzersdorfer, J., "The Buckling of a Thin Circular Arch. Engineering," Vol. 150, Oct. 11 1940, pp. 284–285.

[56] Boresi, A. P., "A Refinement of the Theory of Buckling of Rings Under Uniform Pressure," *J. Appl. Mech.*, Vol. 22, No. 1, March 1955, pp. 95–102.

[57] Thomas, J. C. and Wielgosz, C., "Deflections of Highly Inflated Fabric Tubes," *Thin-Walled Structures*, Vol. 42, No. 7, July 2004, pp. 1049–1066.

[58] Van, A. L. and Wielgosz, C., "Bending and Buckling of Inflatable Beams: Some New Theoretical Results," *Thin-Walled Structures*, Vol. 43, No. 8, August 2005, pp. 1166–1187.

[59] Apedo, K. L., Ronel, S., Jacquelin, E., Massenzio, M., and Bennani, A., "Theoretical Analysis of Inflatable Beams made from Orthotropic Fabric," *Thin-Walled Structures*, Vol. 47, No. 12, August 2009, pp. 1507–1522.

[60] LEVY, S. and HESS, T., "TENSION SHELL DESIGN CONSIDERATIONS FOR PLANETARY ENTRY," *Structures, Structural Dynamics, and Materials and Co-located Conferences*, American Institute of Aeronautics and Astronautics, April 1966, pp. –.

[61] Prada y Nogueira, I. A.and Forlivesi, F. and Morel, Q., "The FEM Applicability for the First-Stage Design of Inflatable Bodies. Iterative Methodology Between FD and FEM for the Inherently Safe Re-Entry Capsule for YES2. The Breogan Leakage Protection System," IAC Paper 03-U.3.04, Sept.Oct. 2003.

[62] Wang, J., Chen, T., Sleight, D., and Tessler, A., "Simulating Nonlinear Deformations of Solar Sail Membranes Using Explicit Time Integration," *Structures, Structural Dynamics, and Materials and Co-located Conferences*, American Institute of Aeronautics and Astronautics, April 2004, pp. –.

[63] Tessler, A., Sleight, D., and Wang, J., "Nonlinear Shell Modeling of Thin Membranes with Emphasis on Structural Wrinkling," *Structures, Structural Dynamics, and Materials and Co-located Conferences*, American Institute of Aeronautics and Astronautics, April 2003, pp. –.

[64] Su, X., Abdi, F., Taleghani, B., and Blandino, J., "Wrinkling Analysis of a Kapton Square Membrane Under Tensile Loading," *Structures, Structural Dynamics, and Materials and Co-located Conferences*, American Institute of Aeronautics and Astronautics, April 2003, pp. –.

[65] Blandino, J. R., Johnston, J. D., and Dharamsi, U. K., "Corner Wrinkling of a Square Membrane due to Symmetric Mechanical Loads," *J. of Spacecraft and Rockets*, Vol. 39, No. 5, Sep.Oct. 2002, pp. 717–724.

[66] Young, A. C., *Large Payload HIAD Systems: Development of Computationally Efficient Modeling Strategies and Structural Investigations*, Ph.D. thesis, 2017.

[67] Young, A. C., Davids, W. G., Goupee, A. J., and Clapp, J. D., "Computationally Efficient Finite-Element Modeling of Braided Inflatable Structural Members with Axial Reinforcing," *Journal of Engineering Mechanics*, 2017.

[68] Young, A. C., Davids, W. G., Whitney, D. J., Clapp, J. D., and Goupee, A. G., "Structural Testing and Analysis of a Braided, Inflatable Fabric Torus Structure," *Acta Astronautica*, 2017.

[69] GUY, L., "Tension shell structures for low density entry vehicles," *Annual Meeting*, American Institute of Aeronautics and Astronautics, July 1965, pp. –.

[70] Brown, G., "Estimating Minimum Inflation Pressure for Inflatable Aerodynamic Decelerators," *Aerodynamic Decelerator Systems Technology Conferences*, American Institute of Aeronautics and Astronautics, May 2009, pp. –.

[71] Sims, L. A., "Concept, Aerodynamics and Design Details of Hyperflow Parachutes - A Summary," *Presented at the Summer Course on Aerodynamic Deceleration, University of Minnesota, July 6-15*, 1965.

[72] Anderson, M. S., Bohon, H. L., and Mikulas, J. M. M., "A Structural Merit Function for Aerodynamic Decelerators," Tech. rep., NASA TN D-5535, 1969.

[73] Anon, "Performance of and Design Criteria for Deployable Aerodynamic Decelerators," Tech. rep., ASD-TR-61-579, U.S. Air Force, Dec., 1963.

[74] Alexander, W. C. and Lau, R. A., "State-of -the-Art Study for High-Speed Deceleration and Stabilization Devices," Tech. rep., NASA CR-66141, 1966.

[75] McShera, J. T., "Aerodynamic Drag and Stability Characteristics of Towed Inflatable Decelerators at Supersonic Speeds," Tech. rep., NASA TN D-1601, 1963.

[76] Dwyer Cianciolo, A. M., Davis, J. L., Komar, D. R., Munk, M. M., Samareh, J. A., Powell, R. W., Shidner, J. D., Stanley, D. O., W., A. W., Kinney, D. J., McGuire, M. K., Arnold, J. O., Howard, A. R., Sostaric, R. R., Studak, J. W., Zumwalt, C. H., Llama, E. G., Casoliva, J., Ivanov, M. C., Clark, I., and Sengupta, A., "Entry, Descent and Landing Systems Analysis Study: Phase 1 Report," Tech. rep., NASA/TM-2010-216720, March, 2010.

[77] Dwyer Ciancolo, A., Davis, J., Engelund, W., Komar, D. R., Queen, E. M., Samareh, J. A., Way, D. W., Zang, T. A., Murch, J. G., Krizan, S. A., Olds, A. D., Powell, R. W., Shidner, J. D., Kinney, D. J., McGuire, M. K., Arnold, J. O., Covington, M. A., Sostaric, R. R., Zumwalt, C. H., and Llama, E. G., "Entry, Descent and Landing Systems Analysis Study: Phase 2 Report on Exploration Feed-Forward Systems," Tech. rep., NASA-TM-2011-217055, March, 2011.

[78] Samareh, J. and Komar, D., "Parametric Mass Modeling for Mars Entry, Descent and Landing System Analysis Study," *Aerospace Sciences Meetings*, American Institute of Aeronautics and Astronautics, Jan. 2011, pp. –.

[79] Mikhail, E. M., Bethel, J. S., and McGlone, J. C., *Introduction to Modern Photogrammetry*, John Wiley & Sons, New York, 2001.

[80] Atkinson, K. B., editor, *Close Range Photogrammetry and Machine Vision*, Whittles Publishing Company, 2001.

[81] Shortis, M. R. and Beyer, H. A., "Sensor Technology for Digital Photogrammetry and Machine Vision," , pp. 106–155.

[82] Cooper, M. A. R. and Robson, S., "Theory of Close Range Photogrammetry," , pp. 9–51.

[83] El-Hakim, S. F., editor, *Videometrics and Optical Methods Jot 3D Shape Measurement*, No. 4309, SPIE Proceedings, Jan 2001.

[84] Danehy, P. M., Jones, T. W., Connell, J. W., Belvin, W. K., and Watson, K. A., "Photogrammetry Method for Transparent, Reflective, or Dark Surfaces," Tech. Rep. LAR-16426-1-ND, NASA Disclosure of Invention and New Technology, December 2001.

[85] Lin, G., Tan, H., and Wang, C., "Pressure Airship Model Structural Analysis and Deformation Measurement Using Photogrammetry," *International Conference on Experimental Mechanics 2008*, 2009.

[86] Seely, L. and Smith, M., "A Realistic View of the Future of Scientific Balloning," *Adv. Space Res.*, Vol. 30, No. 5, 2002, pp. 1128–1133.

[87] Gaspar, J., Mann, T., Sreekantamurthy, T., and Behun, V., "Structural Test and Analysis of a Hybrid Inflatable Antenna," *Structures, Structural Dynamics, and Materials and Co-located Conferences*, American Institute of Aeronautics and Astronautics, April 2007, pp. –.

[88] Kuhn, T., Berger, U., Lang, M., and Baier, H., "Advanced Tailplane Designs and Repair Mechanisms for the Semirigid Airship Zeppelin NT," *Aviation Technology, Integration, and Operations (ATIO) Conferences*, American Institute of Aeronautics and Astronautics, Sept. 2005, pp. –.

[89] Agnes, G. and Davis, D., "Environmental Disturbance Modeling for Inflatable Space Structures," *Structures, Structural Dynamics, and Materials and Co-located Conferences*, American Institute of Aeronautics and Astronautics, April 2002, pp. –.

[90] Hinson, W. F. and Keafer, L. S., "Large Inflated Antenna Systems," Tech. rep., NASA Report N84-17234, 1984.

[91] Freeland, R. E., Bilyeu, G. D., and Veal, G. R., "Large Inflatable Deployable Antenna Flight Experiment Results," *48th Congress of the International Astronautical Federation*, 1997.

[92] Freeland, R. E. and Helms, R. G., "lnflatable space structures technology development for large radar antennas," *24th International Symposium on Space Technology and Science*, Vancouver, Canada, October 4-8 2004.

[93] Jenkins, C. H. M., editor, *Gossamer Spacecraft: Membrane And Inflatable Structures Technology For Space Applications*, Vol. 191, American Institute of Aeronautics and Astronautics, Reston, VA, 2001.

[94] Pappa, R., Geirsch, L., and Quagliaroli, J., "Photogrammetry of a 5-m Inflatable Space Antenna with ConsumerGrade Digital Cameras," *Experimental Techniques*, July/August 2001, pp. 21–29.

[95] Pappa, R. S., Woods-Vedeler, J. A., and Jones, T. W., "In-Space Structural Validation Plan for a StretchedLens Solar Array Flight Experiment," *Proceedings of the 20th International Modal Analysis Conference*, Feb 2002, pp. 461–471.

[96] Watson, J. J., "Static-Test Results for the Characterization of Inflatable Rigidizable Columns," *AIAA Paper 2001-1269*, April 2001.

[97] Pappa, R. S., Lassiter, J. O., and Ross, B. P., "Structural Dynamics Experimental Activities in Ultralightweight and Inflatable Space Structures," *Journal of Spacecraft and Rockets*, Vol. 40, No. 1, Jan. 2003, pp. 15–23.

[98] Jones, T. and Pappa, R., "Dot projection photogrammetric technique for shape measurements of aerospace test articles," *Aerospace Sciences Meetings*, American Institute of Aeronautics and Astronautics, Jan. 2002, pp. –.

[99] Shortis, M. R. and Snow, W. L., "Videometric Tracking of Wind Tunnel Aerospace Models at NASA Langley Research Center," *The Photogrammetric Record*, Vol. 15, No. 85, 1997, pp. 673–689.

[100] Slade, K., Belvin, K., and Behun, V., "Solar Sail Loads, Dynamics, and Membrane Studies," *Structures, Structural Dynamics, and Materials and Co-located Conferences*, American Institute of Aeronautics and Astronautics, April 2002, pp. –.

[101] Giersch, L. R., "Pathfinder Photogrammetry Research for Ultra-Lightweight and Inflatable Space Structures," Tech. rep., NASA CR-2001-211244, November 2001.

[102] Pappa, R. S., Jones, T. W., Black, J. T., Walford, A., Robson, S., and Shortis, M. R., "Photogrammetry Methodology Development for Gossamer Spacecraft Structures," *Sound and Vibration*, Vol. 36, No. 8, August 2002, pp. 12–21.

[103] Dharamsi, U., Evanchik, D., and Blandino, J., "Comparing Photogrammetry with a Conventional Displacement Measurement Technique on a 0.5m Square Kapton Membrane," *Structures, Structural Dynamics, and Materials and Co-located Conferences*, American Institute of Aeronautics and Astronautics, April 2002, pp. –.

[104] Shortis, M. R., Robson, S., Pappa, R. S., Jones, T. W., and Goad, W. K., "Characterization and Tracking of Membrane Surfaces at NASA Langley Research Center," *Proceedings of ISPRS Commission V Symposium on Close-Range Imaging, Long-Range Vision*, September 2002.

[105] Adetona, O., Keel, L., Horta, L., Cadogan, D., Sapna, G., and Scarborough, S., "Description of New Inflatable/Rigidizable Hexapod Structure Testbed for Shape and Vibration Control," *Structures, Structural Dynamics, and Materials and Co-located Conferences*, American Institute of Aeronautics and Astronautics, April 2002, pp. –.

[106] Tanner, C. L., *Aeroelastic Analysis and Testing of Supersonic Inflatable Aerodyanmic Decelerators*, Ph.D. thesis, Georgia Institute of Technology, 2012.

[107] O'Keefe, S. and Bose, D., "IRVE-II Post-Flight Trajectory Reconstruction," *Guidance, Navigation, and Control and Co-located Conferences*, American Institute of Aeronautics and Astronautics, Aug. 2010, pp. –.

[108] Abraham, N., Buehrle, R., Templeton, J., Lindell, M., and Hancock, S., "Modal Test of Six-Meter Hypersonic Inflatable Aerodynamic Decelerator," *IMAC Conference and Exposition on Structural Dynamics*, Society for Experimental Mechanics, February 2014.

[109] Swanson, G. T., Cassell, A. M., Hughes, S. J., Johnson, R. K., and Calomino, A. M., "The Challenges of Integrating Instrumentation with Inflatable Aerodynamic Decelerators," *Aerospace Conference*, Institute of Electrical and Electronics Engineers, March 2013.

[110] Cassell, A., Swanson, G., Johnson, R., Hughes, S., and Cheatwood, F., "Overview of Hypersonic Inflatable Aerodynamic Decelerator Large Article Ground Test Campaign," *Aerodynamic Decelerator Systems Technology Conferences*, American Institute of Aeronautics and Astronautics, May 2011, pp. –.

[111] Kushner, L. and Schairer, E., "Planning Image-Based Measurements in Wind Tunnels by Virtual Imaging," *Aerospace Sciences Meetings*, American Institute of Aeronautics and Astronautics, Jan. 2011, pp. –.

[112] Kazemba, C. D., Tran, K., Quach, B., Kushner, L. K., Cassell, A., Li, L., Braun, R., Littell, J., Norman, J. V., Johnson, R. K., Hughes, S. J., Calomino, A. M., and Cheatwood, F. M., "Determination of the Deformed Structural Shape of HIADs from Photogrammetric Wind Tunnel Data," *Aerodynamic Decelerator Systems Technology Conferences*, American Institute of Aeronautics and Astronautics, March 2013, pp. –.

[113] Kushner, L. K., Littell, J., and Cassell, A., "Photogrammetry of a Hypersonic Inflatable Aerodyanmic Decelerator," *Aerodynamic Decelerator Systems Technology Conference*, American Institute of Aeronautics and Astronautics, March 2013.

[114] Ashter, S. A., *Thermoforming of Single and Multilayer Laminates: PPlastic Films Technologies, Testing, and Applications*, Eslevier Inc., 2014.

[115] Nyquist, H., "Certain factors affecting telegraph speed," *Bell System Technical Journal*, Vol. 3, 1924, pp. 324–346.

[116] Nyquist, H., "Certain topics in telegraph transmission theory," *Trans. AIEE*, Vol. 47, April 1928, pp. 617644.

[117] Swanson, G., Kazemba, C., Johnson, K., Calomino, A., Hughes, S., Cassell, A., and Cheatwood, N., "Overview of the 6 Meter HIAD Inflatable Structure and Flexible TPS Static Load Test Series," *11th International Planetary Probe Workshop; 16-20 Jun. 2014; Pasadena, CA; United States*, 2014.

[118] Swanson, G. T., Kazemba, C. D., Johnson, R. K., Hughes, S. J., Calomino, A. M., Cheatwood, F. M., Cassell, A. M., Anderson, P., and Lowery, A., "Overview of the 2nd Gen 3.7m HIAD Static Load Test," *12th International Planetary Probe Workshop; 15-19 Jun. 2015; Cologne; Germany*, 2015.

[119] Olds, A., Beck, R., Bose, D. M., White, J., Edquist, K. T., Hollis, B. R., Lindell, M., Cheatwood, F. M., Gsell, V., and Bowden, E. L., "IRVE-3 Post-Flight Reconstruction," *Aerodynamic Decelerator Systems Technology Conferences*, American Institute of Aeronautics and Astronautics, March 2013, pp. –.

[120] Cheatwood, N., "Hypersonic Inflatable Aerodynamic Decelerator (HIAD) Technology," *NASA's Game Changing Technology Industry Day*, 2016.

[121] Ragab, M., Cheatwood, F. M., Hughes, S., DiNonno, J., Bodkin, R., Lowry, A., Kelly, J., and Reed, J. G., "Performance Efficient Launch Vehicle Recovery and Reuse," *AIAA SPACE 2016*, American Institute of Aeronautics and Astronautics, sep 2016.